Advanced methods for structural characterization and structure-property correlation for functional materials of layered compounds

Dissertation
der Mathematisch-Naturwissenschaftlichen Fakultät
der Eberhard Karls Universität Tübingen
zur Erlangung des Grades eines
Doktors der Naturwissenschaften
(Dr. rer. nat.)

vorgelegt von
Michael Thomas Dürrschnabel
aus Rastatt

Tübingen
2013

Tage der mündlichen Qualifikation:	11.03.2014
Dekan:	Prof. Dr. Wolfgang Rosenstiel
1. Berichterstatter:	Prof. Dr. Oliver Eibl
2. Berichterstatter:	Prof. Dr. Reinhold Kleiner
3. Berichterstatter:	Prof. Dr. Lorenz Kienle

Contents

Summary

A large number of functional materials have layered structures yielding anisotropic physical properties and an exciting physics of extended defects. For the understanding of both phenomena extensive computational methods are necessary for calculating anisotropic physical properties in an ab-initio approach. Calculating high-energy electron scattering is essential to yield quantitative results on defect structures by electron microscopy and spectroscopy. In this thesis superconducting $ReBa_2Cu_3O_{7-x}$ (ReBCO, Re=rare earth) coated conductors and thermoelectric Bi_2Te_3-related device-relevant materials were analyzed in detail. For both compounds various computational methods were applied to yield a quantitative structure-property correlation. The microstructure and the chemical composition of a material affecting its macroscopic physical properties is referred to as structure-property correlation.

Coated conductors consist of multilayer thin film structures and are high-temperature superconducting (HTS) wires of the second generation. The analyzed coated conductors were grown by two methods: (i) chemical solution deposition (CSD) and (ii) inclined substrate deposition (ISD). In this work both materials were analyzed and compared to each other, yielding a structure-property correlation.

The analysis of Bi_2Te_3-related materials focused on thin films and bulk materials. Bi_2Te_3-related materials have the highest thermoelectric figure-of-merit ZT at room temperature and are used in energy conversion devices. Additionally, these materials are topological insulators, a hot topic in current research. Alloying reduces thermal conductivity by enhancing phonon scattering and yields an enhanced ZT value for the alloys as compared to the binary compound.

Electron microscopy is the method of choice to establish a structure-property correlation. In this thesis a combination of scanning electron microscopy (SEM) and transmission electron microscopy (TEM) was applied to cover a broad range of length scales. Several quantitative analytical methods that require computational methods have been implemented for device relevant analytics: (i) quantitative energy-dispersive X-ray (EDX) analysis in the SEM including quantitative EDX spectrum simulation and (ii) aberration corrected scanning transmission electron microscopy (STEM) analysis including the corresponding image simulation.

Film thicknesses directly relate to critical currents and are therefore crucially important for coated conductors. In this work a method for determining the film thickness based on thickness calibration curves was developed. For electron energies of up to 30 keV electron scattering was calculated in the excitation volume by a Monte Carlo approach, which allowed also to implement quantitative EDX spectrum simulation. Simulation of electron trajectories and X-ray intensities on the micrometer scale also yields optimized acquisition conditions with respect to lateral resolution, precision of quantitative analysis, and minimum detectable mole fractions. Furthermore, Monte Carlo simulations for the electron trajectories was used to calculate the electron penetration depth and to rule out stray radiation generated in the substrate of thin films. This method was applied for high-precision wavelength-dispersive X-ray spectrometry (WDX) determining antisite defect densities in Bi_2Te_3-related thermoelectric materials.

High-angle annular dark-field (HAADF) STEM imaging is the method of choice to reveal the nanostructure of materials, since it provides easily interpretable, quantifiable atomic number (Z) contrast images. In aberration corrected STEM the probe diameter can be reduced to less than 1 Å and single atomic imaging and spectroscopy is simultaneously possible. Simulation of e.g. HAADF images allow confirm, discard, or modify structural and chemical models for extended defects. Atomically resolved HAADF images of Bi_2Te_3-related thermoelectric materials as well as of $DyBa_2Cu_3O_{7-x}$ (DyBCO) coated conductors were simulated for different sample thicknesses and compared to experimentally acquired images. It

was shown that alloying can be imaged in real space on the atomic scale. In case of the DyBCO coated conductors atomic resolution could be proven at various interfaces.

Structure-property correlations are of key importance for improving material or device relevant performances by tailoring the microstructure and the chemistry. Ab-initio density functional theory (DFT) calculations implemented in the Wien2k code yield the band structure for electrons depending on the crystal structure of a material, which in turn can be determined by the analytical methods used here. With the band structure, temperature-dependent electron transport coefficients were calculated by solving the linearized Boltzmann equation. The Wien2k and the BoltzTraP simulation packages were setup and yielded the transport properties for various modifications of the crystal structure.

For Bi_2Te_3, transport coefficients were calculated depending on the chemical potential and temperature, the chemical potential being directly related to the charge carrier density. The calculated thermopower strongly depended on the charge carrier density and satisfactorily fitted to experimental values obtained in bulk and thin films.

In summary, the computational methods implemented in this thesis treat scattering of Bloch waves for different electron energies. For simulating electron microscopy data, high electron energies have to be used, primary energies are in the 5-300 keV range. For calculating transport coefficients in crystals electron energies are in the eV range and below. The computational methods applied in this work yield an enhanced, quantitative understanding of the physical phenomena being involved and an important contribution to the structure-property correlation of materials.

CSD coated conductors were grown from liquid precursors under ambient pressure. These films were analyzed by SEM and TEM methods to reveal their microstructure. It was found that the layers in CSD coated conductors yield strongly varying film thicknesses, large film roughnesses, and an inhomogeneous chemical composition on the micrometer scale.

For coated conductors prepared by ISD biaxially-textured MgO buffer layers can be deposited on untextured Hastelloy substrates by electron evaporation. The biaxial texture of the MgO buffer layer is of crucial importance for achieving high critical currents in the superconducting layers and was quantitatively measured by electron diffraction in cross-section for MgO films revealing strong and poor texture depending on the deposition conditions. These measurements are the key for controlling the texture and understanding the physics of texture formation by the ISD method.

Growing superconducting layers with thicknesses exceeding 1 µm yields a dramatic reduction in critical current densities for all applied technologies except the ISD technology. In contrast, an almost linear increase of the critical current with the DyBCO film thickness was observed in ISD grown coated conductors due to a highly biaxially-textured film at all thicknesses. A record value of the critical current of 1018 $A\,cm^{-1}$ was measured for a DyBCO film with 5.9 µm thickness. Therefore, the ISD technology offers a unique possibility to overcome thickness limitations in coated conductor technology.

This thesis clearly documents the limitations of CSD grown coated conductors: (i) the film thickness is poorly controlled due to the large surface roughnesses yielding a limitation for the critical current of such films; (ii) biaxially-textured YBCO films can only be grown to thicknesses significantly smaller than 1 µm, in thicker films the biaxial texture is lost in the top part of the film. Very different to these findings ISD films yield (i) very smooth surfaces and (ii) biaxial texture up to more than 6 µm film thickness. The surface smoothness is a direct consequence of the biaxial texture that yields low-energy, small-angle grain boundaries with large critical current densities.

Zusammenfassung

Eine große Anzahl funktioneller Materialien hat eine Schichtstruktur, welche eine Anisotropie der physikalischen Eigenschaften und eine spannende Physik ausgedehnter Defekte ergibt. Für das Verständnis beider Phänomene sind umfangreiche Rechenmethoden notwendig, um die anisotropen, physikalischen Eigenschaften in einem Ab-initio Ansatz zu berechnen. Die Berechnung hochenergetischer Elektronenstreuung ist essentiell, um mittels Elektronenmikroskopie und -spektroskopie quantitative Ergebnisse zu Defektstrukturen zu erhalten. In dieser Dissertation wurden supraleitende $SeBa_2Cu_3O_{7-x}$ (SeBCO, Se = Seltenerd) Bandleiter und Bi_2Te_3-basierte, bauteilrelevante, thermoelektrische Materialien im Detail untersucht. Für beide Verbindungen wurden verschiedene Rechenmethoden angewendet, um quantitative Struktur-Eigenschaftsbeziehungen zu erhalten. Die Mikrostruktur und die chemische Zusammensetzung eines Materials beeinflusst seine makroskopischen, physikalischen Eigenschaften, dies wird als Struktur-Eigenschaftskorrelation bezeichnet.

Bandleiter bestehen aus einer Multilagenstruktur und sind supraleitende Drähte der zweiten Generation. Die untersuchten Bandleiter wurden durch zwei Methoden hergestellt: (i) Chemische Abscheidung aus der Lösung (chemical solution deposition, CSD) und (ii) Elektronenstrahlverdampfung bei gleichzeitiger Schrägstellung des Substrates (inclined substrate deposition, ISD). In dieser Arbeit wurden beide Materialien analysiert und mit Hinblick auf Struktur-Eigenschaftsbeziehungen verglichen.

Bei der Analyse der Bi_2Te_3-basierten Materialien lag der Fokus auf dünnen Filmen sowie Volumenmaterialien. Bi_2Te_3-basierte Materialien haben bei Raumtemperatur den höchsten thermoelektrischen Gütefaktor ZT und werden deshalb in Energieumwandlern verwendet. Des Weiteren sind Bi_2Te_3-basierte Materialien topologische Isolatoren, welche gerade ein hochaktuelles Forschungsfeld sind. Legieren reduziert die Wärmeleitfähigkeit durch Erhöhung der Phononenstreuung, was einen höheren ZT-Wert der Legierung verglichen zu binären Verbindungen zur Folge hat.

Elektronenmikroskopie ist die Methode der Wahl, um eine Struktur-Eigenschaftsbeziehung zu erhalten. In dieser Arbeit wurde eine Kombination aus Rasterelektronenmikroskopie (REM) und Transmissionselektronenmikroskopie (TEM) verwendet, um einen weiten Bereich an Längenskalen abzudecken. Verschiedene quantitative Analysemethoden, die Rechenmethoden benötigen, wurden zur Analytik von Bauelementen angewendet: (i) Energiedispersive Röntgenmikroanalyse (EDX) im Rasterelektronenmikroskop in Kombination mit quantitativer Simulation von EDX-Spektren, (ii) aberrationskorrigierte Rastertransmissionselektronenmikroskopie (STEM) mit zugehöriger Bildsimulation.

Für supraleitende Bandleiter stehen Filmdicken in direkter Beziehung zu kritischen Strömen und sind deshalb von entscheidender Bedeutung. In dieser Arbeit wurde eine Methode zur Filmdickenbestimmung basierend auf Dickenkalibrierungskurven entwickelt. Dafür wurde die Elektronenstreuung im Wechselwirkungsvolumen für Elektronenenergien bis 30 keV mit Hilfe eines Monte Carlo Ansatzes berechnet, welcher ebenfalls quantitative EDX-Spektrensimulation erlaubt. EDX-Spektren konnten so für komplexe Probengeometrien berechnet werden und in einer einfachen Weise mit experimentell erhaltenen EDX-Spektren verglichen werden. Die Simulation von Elektronentrajektorien und Röntgenintensitäten auf der Mikrometerskala ergibt optimierte Akquisitionsbedingungen mit Hinblick auf die laterale Auflösung, die Genauigkeit der quantitativen Analyse und der Nachweisgrenze. Des Weiteren wurde die Simulation von Elektronentrajektorien verwendet, um die Eindringtiefe der Elektronen zu berechnen und Störstrahlung mit Ursprung im Substrat bei den Dünnfilmen auszuschließen. Diese Methode wurde für hochpräzise wellenlängendispersive Röntgenspektrometrie (WDX), welche eine Bestimmung der Substitutionsatomdefektdichten (antisite defects) in Bi_2Te_3-basierten Materialien ermöglicht, angewandt.

Dunkelfeldbilder, erhalten mit großen Streuwinkeln, (HAADF) im STEM ist die Methode der Wahl, wenn die Nanostruktur von Materialien abgebildet werden soll, da sie einfach zu interpretierende und quantifizierbare Z-Kontrastbilder liefert. Bei aberrationskorrigierten Rastertransmissionselektronenmikroskopen kann der Sondendurchmesser auf weniger als 1 Å reduziert werden und gleichzeitige atomar aufgelöste Bildgebung und Spektroskopie erreicht werden. Die Simulation von z. B. HAADF-Bildern ermöglicht die Struktur- und chemische Zusammensetzung ausgedehnter Kristalldefekte zu bestimmen. Atomar aufgelöste HAADF-Bilder von Bi_2Te_3-basierten Materialien sowie von $DyBa_2Cu_3O_{7-x}$ (DyBCO) wurden für verschiedene Probendicken simuliert und mit experimentell aufgenommenen Bildern verglichen. Es wurde gezeigt, dass das Legieren im Realraum auf atomarer Ebene abgebildet werden kann. Im Falle von DyBCO-Bandleitern wurde die atomare Auflösung an verschiedenen Grenzflächen gezeigt.

Struktur-Eigenschaftsbeziehungen sind von herausragender Bedeutung, um die Leistungsfähigkeiten von Materialien in Bauelementen durch Maßschneidern der Mikrostruktur bzw. der Chemie zu verbessern. Die Ab-initio Dichtefunktionaltheorie (density functional theory, DFT), welche im Wien2k-Code implementiert ist, erlaubt die Berechnung der elektronischen Bandstruktur auf Basis der Kristallstruktur eines Materials. Diese wurden mit den analytischen Methoden, die in dieser Arbeit benutzt wurden, bestimmt. Mit der Bandstruktur können temperaturabhängige Transportgrößen durch Lösen der linearisierten Boltzmann-Gleichung berechnet werden. Die Softwarepakete BoltzTraP und Wien2k wurden im Rahmen dieser Arbeit eingerichtet und erlaubten die Berechnung von Transporteigenschaften für verschiedene Modifikationen der Kristallstruktur. Für Bi_2Te_3 wurden die Transportkoeffizienten in Abhängigkeit vom chemischen Potential und der Temperatur berechnet, wobei das chemische Potential direkt mit der Ladungsträgerdichte verbunden ist. Der berechnete Seebeck-Koeffizient hängt stark von der Ladungsträgerdichte ab und stimmte in zufriedenstellender Weise mit den gemessenen Werten überein.

Zusammenfassend betrachtet behandeln die hier angewandten Rechenmethoden Streuung von Bloch-Wellen bei verschiedenen Elektronenenergien. Für die Simulation elektronenmikroskopischer Daten müssen hochenergetische Elektronen im Bereich von 5 bis 300 keV Primärelektronenenergie betrachtet werden. Für die Berechnung von Transportkoeffizienten in Kristallen sind die Elektronenenergien im Elektronenvoltbereich und darunter. Die angewandten Rechenmethoden liefern ein erweitertes, quantitatives Verständnis der beteiligten physikalischen Phänomene sowie einen wichtigen Beitrag zur Struktur-Eigenschaftskorrelation von Materialien.

CSD-Bandleiter wurden aus flüssigen Ausgangsmaterialien unter Umgebungsdruck hergestellt. Diese Filme wurden mit REM- und TEM-Methoden bzgl. Mikrostruktur untersucht. In CSD-Bandleitern wurde eine stark schwankende Filmdicke, eine hohe Filmrauhigkeit und eine inhomogene chemische Zusammensetzung im Mikrometerbereich gefunden.

Für mittels ISD hergestelle Bandleiter können biaxial texturierte MgO-Pufferschichten auf untexturierten Hastelloy-Substraten mittels Elektronenstrahlverdampfung abgeschieden werden. Die biaxiale Textur ist von entscheidender Bedeutung, um hohe kritische Ströme in supraleitenden Schichten zu erreichen und wurde mit Hilfe von Elektronenbeugung an MgO-Querschnittsproben quantitativ bestimmt. Diese Messungen sind der Schlüssel zur Kontrolle der Texturierung und des Verständnisses der Texturentstehung in der ISD-Methode.

Das Wachstum von supraleitenden Schichten mit mehr als einem Mikrometer Schichtdicke ergibt für alle angewandten Abscheidungsverfahren außer ISD einen dramatischen Rückgang in den kritischen Stromdichten. Im Gegensatz dazu wurde in DyBCO-Bandleitern ein linearer Anstieg des kritischen Stromes mit der DyBCO-Filmdicke aufgrund einer hochtexturierten Schicht bei allen Filmdicken beobachtet. Für einen DyBCO-Film mit 5.9 µm Filmdicke wurde ein Rekordwert des kritischen Stromes von 1018 $A\,cm^{-1}$ gemessen. Deshalb bietet die ISD-Technologie eine einzigartige Möglichkeit, Dickenbeschränkungen des kritischen Stromes in der Bandleitertechnologie zu überwinden.

Diese Dissertation zeigt klar die Grenzen der CSD-Bandleiter-Technologie: (i) die Filmdicke wird wegen der hohen Oberflächenrauhigkeit schlecht kontrolliert, was den kritischen Strom in solchen Filmen

begrenzt; (ii) biaxial texturierte YBCO-Filme können nur für Filmdicken wesentlich kleiner als 1 µm hergestellt werden, da in dickeren Filmen die biaxiale Textur im oberen Teil der Filme verloren geht. In großem Unterschied zu diesen Erkenntnissen wurde in ISD-Schichten (i) eine sehr glatte Oberfläche und (ii) eine biaxiale Textur bis zu mehr als 6 µm Filmdicke beobachtet. Die glatte Oberfläche ist eine direkte Folge der biaxialen Textur, welche niederenergetische Kleinwinkelkorngrenzen mit hohen kritischen Stromdichten ergibt.

Chapter preview

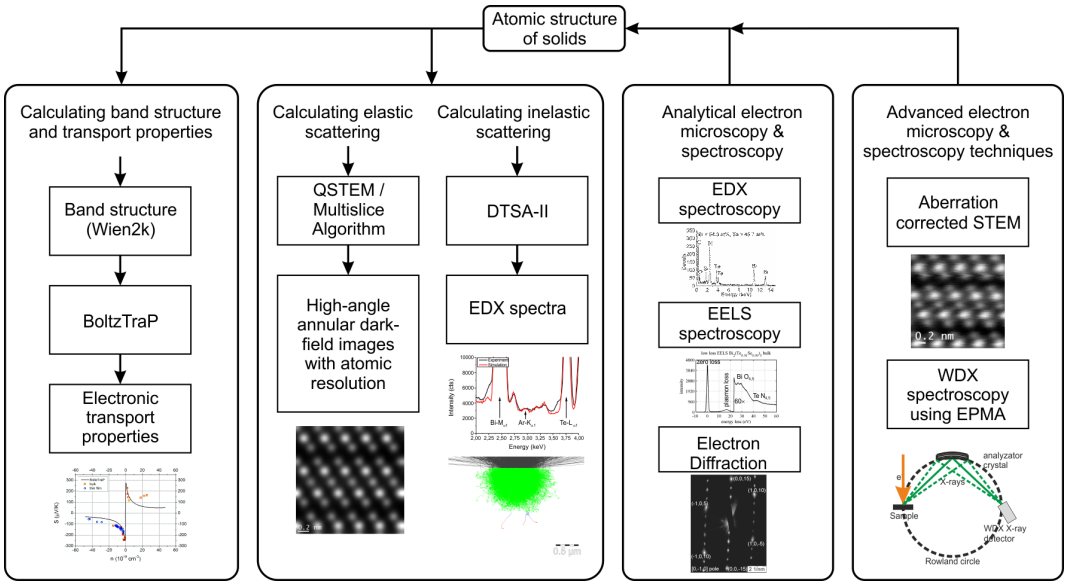

This thesis is unique in the sense that it covers several disciplines ranging from scanning electron microscopy (SEM) over aberration-corrected scanning transmission electron microscopy (STEM) to ab-initio calculations of transport properties. The interconnection of the single disciplines can be seen in the above figure. It is divided into three parts:

- Part I Basics contains two chapters dealing with the theory and methodology of electron microscopy and superconductivity, respectively.
- Part II Simulation of elastic and inelastic electron scattering, divided into three chapters (3-5).
- Part III Structure-property correlation by electron microscopy techniques, divided into three chapters (6-9) dealing with structure-property correlations in coated conductors.

Chapter 1 deals with the basics of electron microscopy in inorganic crystalline samples. Crystallographic basics, the theory of elastic and inelastic electron scattering as well as the imaging theory of high-resolution phase contrast imaging and scanning transmission electron microscopy is presented.

Chapter 2 is an introduction to superconductivity. It covers crystallographic aspects of high-temperature superconductors (HTS) as well as the Ginzburg-Landau theory for understanding type-II HTS. Furthermore, technically important aspects like critical current, critical current density, and current limitations in (high-temperature) superconductors are treated. Finally, a summary of two HTS growth processes, i.e. chemical solution deposition (CSD) and inclined substrate deposition (ISD), used in this work is presented.

Chapter 3 summarizes the theories necessary for energy-dispersive X-ray spectra (EDX) simulation. It also contains important results on film thickness determination via experimental and simulated EDX spectra in coated conductor materials.

Chapter 4 deals with the study of layered, anisotropic structures of Bi_2Te_3 and DyBCO by aberration-corrected STEM. The theory of contrast formation in high-angle annular dark-field (HAADF) images

is explained. The experimentally obtained HAADF images were compared to simulated ones for both compounds. In Bi_2Te_3-related materials the StripeSTEM technique is used by integrating the electron energy-loss (EEL) spectra parallel to the van-der-Waals gaps present in the material yielding layer-by-layer EEL spectra.

Chapter 5 explains how to carry out calculations of electronic transport properties by solving the linearized Boltzmann equation, which can then be linked to the nanostructure of a material. The chapter focuses on how to setup the code and to explain important subroutines, since no proper documentation was available. It also contains calculations of temperature-dependent transport coefficients of Bi_2Te_3, which in a final step are compared to experimentally measured values.

Chapter 6 deals with inclined substrate deposition (ISD) and the unique evolution the biaxial texture inside the MgO buffer layer in dependence on the applied growth conditions. The structure of the MgO buffer layer was analyzed by SEM and TEM. This growth behavior can be explained by directional diffusion and the van-der-Drift theory.

Chapter 7 contains basic structural and electrical analyses of DyBCO coated conductors. The results are then compared to those found in coated conductors grown by other techniques like rolling-assisted biaxial texturing (RABiTS) and pulsed laser deposition (PLD).

Chapter 8 presents the results of structure-property correlations in thick DyBCO coated conductors. It was shown that in ISD coated conductors the critical current increases linearly with the DyBCO film thickness. Electron diffraction revealed that the DyBCO film is completely biaxially textured even in the top parts explaining the linear increase in the critical current.

Chapter 9 summarizes the results obtained in the analyses of CSD coated coated conductors. The homogeneity of the films was determined on different length scales and correlates well with the superconducting properties. The highlight of the chapter is the O2p spectroscopy applied the first time to CSD coated conductors yielding statements about the local oxygen concentration and, therefore, about the local superconducting properties.

Part I.

Basics

1. Electron microscopy and spectroscopy

Electron microscopy is an essential method for structural and chemical analysis of coated conductors. For industrial applications several orders of magnitude of length scales are of relevance since the macroscopic properties are governed by microscopic quantities. Second generation coated conductors have lengths up to 1 kilometer but the most critical limiting factor are grain boundaries on the nanometer scale. It is very challenging to cover all these length scales. Scanning electron microscopy (SEM) was used to determine surface, interface, chemical properties or the film thickness of the samples up to the micrometer level. Transmission electron microscopy (TEM) was used to determine structural and chemical properties on the nanometer scale. A profound understanding of structure-chemistry-property correlations is needed to enhance the quality of today's coated conductor technology.

1.1. Sample preparation

SEM samples need only a minimum of treatment since they need not to be electron transparent. Plan-view SEM samples can be analyzed often without any preparation. TEM samples on the other hand need sophisticated sample preparation methods since they have to be electron transparent. Depending on the issue to be analyzed and the sample itself there are several possibilities for TEM sample preparation. Here, conventional grinding and polishing as well as the focused ion beam method were used. For details please have a look at chapter 2 in the thesis of Z. Aabdin [1]. In this work three sample types were used for SEM and TEM of coated conductors: (i) plan-view, (ii) cross section, and (iii) longitudinal section.

1.2. Electron interactions with solids

In general there are two possibilities for an electron to interact with the atoms of a specimen. It can either be scattered inelastically or elastically, i.e. it looses energy or not.

1.2.1. Elastic scattering and electron diffraction

1.2.1.1. The two-beam case

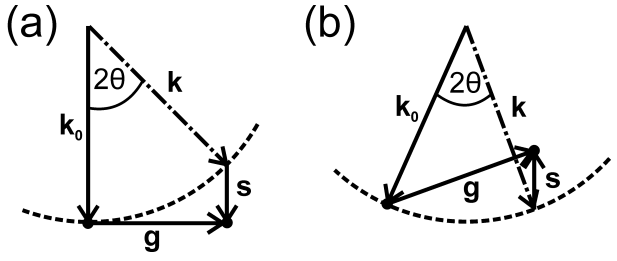

Figure 1.1.: Geometrical definition of the excitation error s [2] using a Ewald sphere construction. (a) s<0 (**g** outside the Ewald sphere) and (b) s>0 (**g** inside the Ewald sphere).

Conventional TEM diffraction contrast imaging is conducted in a two-beam condition and uses two types of imaging modes: (i) bright-field and (ii) dark-field. In (i) the objective aperture of the microscope is centered on the direct beam and in (ii) the objective aperture is centered on the diffracted beam. For any TEM characterization done with the Zeiss 912Ω this technique was used to image the samples. The contrast seen in this type of images can be explained for

crystalline samples without dislocations in general by the dynamical diffraction theory. The basis of this theory is the description of electron waves in a crystal potential as Bloch waves. For thin samples the dynamical theory can be approximated by the kinematical theory. The kinematical theory is only valid if intensity backscattering from the direct into diffracted beam can be neglected. In many cases this cannot be assumed. The more general formulation is the dynamical diffraction theory, which includes the intensity backscattering. The starting point are two coupled differential equations called Howie-Whelan equations, having the following form if absorption is neglected and the incident electron wave is propagating in z direction [3, 4, 2]:

$$\frac{d}{dz}\begin{pmatrix}\Psi_0\\ \Psi_g\end{pmatrix} = \begin{pmatrix}\frac{i\pi}{\xi_0} & \frac{i\pi}{\xi_g}e^{2\pi isz}\\ \frac{i\pi}{\xi_g}e^{-2\pi isz} & \frac{i\pi}{\xi_0}\end{pmatrix}\cdot\begin{pmatrix}\Psi_0\\ \Psi_g\end{pmatrix} \tag{1.1}$$

where Ψ_0 and Ψ_g are the amplitudes of the direct and the diffracted beam, respectively. The second term of the first equation describes the backscattering into the direct beam. ξ_0 and ξ_g are the extinction distances of the direct and the diffracted beam, respectively. The extinction distance can be calculated via

$$\xi_{hkl} = \frac{\pi V_{uc}\cos\theta_B}{\lambda F_{\mathbf{g}}} \tag{1.2}$$

where V_{uc} is the volume of the unit cell, λ is the wavelength of the electrons, θ_B is the Bragg angle and $F_{\mathbf{g}}$ is the kinematical structure factor for the reciprocal lattice vector $\mathbf{g}$. The quantity s is called excitation error. In general it is a vector and being defined as

$$\mathbf{s} = \mathbf{k_0} - \mathbf{k} - \mathbf{g}. \tag{1.3}$$

Fig. 1.1 is the geometric representation of the excitation error as deviation from the perfect Bragg condition. The value of s is a real number. The geometry for s>0 and s<0 are both shown in Fig. 1.1.

The Howie-Whelan equations in Eq. 1.1 can be transformed and simplified [3] via

$$\Psi_0' = \Psi_0\exp\left(-\frac{\pi iz}{\xi_0}\right) \tag{1.4}$$

$$\Psi_g' = \Psi_g\exp\left(2\pi isz - \frac{\pi iz}{\xi_0}\right) \tag{1.5}$$

into a single differential equation of the second order (which is similar to the differential equation of the harmonic oscillator)

$$\frac{d^2\Psi_0}{dz^2} - 2\pi is\frac{d\Psi_0}{dz} + \frac{\pi^2}{\xi_g^2}\Psi_0 = 0. \tag{1.6}$$

Eq. 1.6 can be solved by a linear combination of sine and cosine functions in dependence on the sample thickness z and by introducing the dimensionless parameter the effective excitation error $s_{eff} =$

$\sqrt{s^2+\xi_g^{-2}}$. The solution for the direct and the diffracted intensity in dependence on sample thickness t and s_{eff} is then given by [3]

$$|\Psi_0|^2 = 1-|\Psi_g|^2 \tag{1.7}$$

$$|\Psi_g|^2 = \left(\frac{\pi t}{\xi_g}\right)^2 \frac{\sin^2(\pi t\, s_{eff})}{(\pi t\, s_{eff})^2}. \tag{1.8}$$

From that it is immediately clear that both functions are limited for $s=0$ unlike those in the kinematical approximation. The equations explain image contrast originating from thickness variations and bending contours due to variations of the excitation error. However, absorption and inelastic scattering are not considered and the Eq. 1.7 and Eq. 1.8 fail to describe real two-beam images experimentally acquired in a TEM. By introducing two complex quantities, i.e. $\frac{i}{\xi_0'}$ and $\frac{i}{\xi_g'}$ into the Howie-Whelan equations (Eq. 1.1), absorption effects can be described and the Howie-Whelan equations have the form

$$\frac{d}{dz}\begin{pmatrix}\Psi_0\\ \Psi_g\end{pmatrix} = \pi\begin{pmatrix} \frac{i}{\xi_0}-\frac{1}{\xi_0'} & \left(\frac{i}{\xi_g}-\frac{1}{\xi_g'}\right)e^{2\pi i s z} \\ \left(\frac{i}{\xi_g}-\frac{1}{\xi_g'}\right)e^{-2\pi i s z} & \frac{i}{\xi_0}-\frac{1}{\xi_0'}\end{pmatrix}\cdot\begin{pmatrix}\Psi_0\\ \Psi_g\end{pmatrix}. \tag{1.9}$$

The corresponding intensity values of Eq. 1.9 are according to Hashimoto et al. [5]:

$$|\Psi_0(z)|^2 = \frac{e^{-2\kappa_0 t}\left\{\left[\sqrt{1+w^2}+w\right]^2 e^{2\Delta\kappa t}+\left[\sqrt{1+w^2}-w\right]^2 e^{-2\Delta\kappa t}\right\}}{4(1+w^2)} + \frac{e^{-2\kappa_0 t}\cos(2\pi\Delta k t)}{2(1+w^2)} \tag{1.10}$$

$$|\Psi_g(z)|^2 = \frac{e^{-2\kappa_0 t}\left\{\cosh(2\Delta\kappa t)-\cos(2\pi\Delta k t)\right)\}}{2(1+w^2)} \tag{1.11}$$

with $\kappa_0=\frac{\pi}{\xi_0'}$, $\Delta\kappa=\frac{\pi}{\xi_g'\sqrt{1+w^2}}$, $\Delta k=\frac{\sqrt{1+w^2}}{\xi_g}$, and t as the sample thickness, respectively. The exponential term describes the absorption. Both equations (Eq. 1.10 and Eq. 1.11) can only be used for a defect free translationally symmetric crystal. If crystalline defects are present the Howie-Whelan equations need to contain a term for the displacement field $\mathbf{R}(z)$ yielding bending of lattice planes

$$\frac{d}{dz}\begin{pmatrix}\Psi_0\\ \Psi_g\end{pmatrix} = \pi\begin{pmatrix} \frac{i}{\xi_0}-\frac{1}{\xi_0'} & \left(\frac{i}{\xi_g}-\frac{1}{\xi_g'}\right)e^{2\pi i s z+2\pi i\mathbf{g}\cdot\mathbf{R}} \\ \left(\frac{i}{\xi_g}-\frac{1}{\xi_g'}\right)e^{-2\pi i s z-2\pi i\mathbf{g}\cdot\mathbf{R}} & \frac{i}{\xi_0}-\frac{1}{\xi_0'}\end{pmatrix}\cdot\begin{pmatrix}\Psi_0\\ \Psi_g\end{pmatrix} \tag{1.12}$$

By introducing the transforms $\Psi_0' = \Psi_0 \exp\left(-\frac{i\pi z}{\xi_0}\right)$ and $\Psi_g' = \Psi_g \exp\left(2\pi i s z - \frac{i\pi z}{\xi_0} + 2\pi i \mathbf{g}\cdot\mathbf{R}\right)$ Eq. 1.12 can be simplified to

$$\frac{d}{dz}\begin{pmatrix}\Psi_0\\ \Psi_g\end{pmatrix} = \pi\begin{pmatrix} -\frac{1}{\xi_0'} & \frac{i}{\xi_g} - \frac{1}{\xi_g'} \\ \frac{i}{\xi_g} - \frac{1}{\xi_g'} & -\frac{1}{\xi_0'} + 2isz + 2i\mathbf{g}\cdot\frac{d\mathbf{R}}{dz}\end{pmatrix}\cdot\begin{pmatrix}\Psi_0\\ \Psi_g\end{pmatrix} \tag{1.13}$$

Eq. 1.13 can only be solved by numerical methods and is the starting point for image simulation of defects in the two-beam case in TEM as shown in thesis of N. Peranio [6].

1.2.2. Imaging theory

1.2.2.1. Electron optics and lens aberrations

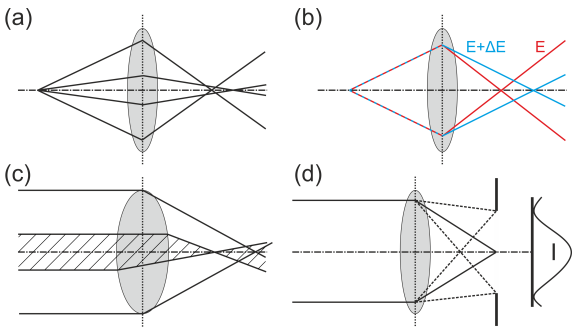

Figure 1.2.: Graphical representation of the most important lens aberrations. (a) Spherical aberration, (b) Chromatic aberration, (c) two fold axial astigmatism, and (d) diffraction.

Spherical aberration is the most crucial one if you want to acquire high resolution images. It means that electrons that pass the lens closer to the optical axis are focused at a larger distance from the lens than electrons that pass the lens in greater distance to the optical axis as sketched in Fig. 1.2a. Thus, in the Gaussian image plane of the lens concentric circles of radius r_S

$$r_S = C_{s,3}\,\alpha^3 \tag{1.14}$$

can be detected, where $C_{s,3}$ is the image-sided third-order spherical aberration constant and α is the aperture semi-angle. Higher orders of spherical aberration are neglected here because they are smaller than the third-order ones. In the plane of least confusion, located before the Gaussian image plane, the concentric circles have the smallest radius $r_{S,min}$

$$r_{S,min} = \frac{C_{s,3}}{4}\,\alpha^3. \tag{1.15}$$

Hence, it is convenient to use small apertures to minimize the effect of spherical aberration, but at the same time the total amount of current passing through the lens will be reduced yielding low image intensities at high magnifications. Over the years several attempts have been made to correct the speherical and the chromatic aberration[7]. Recent microscopes overcome this problem by using a C_s-image-corrector based on hexapole elements placed before and after the objective lens [8].

Another important quantity is the chromatic aberration. It has its origin in the energy spread ΔE of the electrons emitted at the electron source, the stability of high tension and lens currents causing focal variations of the lens in time, and inelastic scattering of electrons within the sample. These effects generate electrons of different "color", i.e. electrons with slightly different energies and velocities. Moving through the magnetic lens, slower electrons (E, red line in Fig. 1.2b) are more strongly refracted than faster electrons (E+ΔE, blue line in Fig. 1.2b). For visible light this is just reverse. The radius of the disc r_C in the Gaussian image plane is [3]

$$r_C = \frac{C_C}{2}\frac{\Delta E}{E}\alpha \tag{1.16}$$

$$\frac{\Delta E}{E} = \frac{\Delta f}{f} + 2\frac{\Delta I}{I} \tag{1.17}$$

where C_C is the image-sided chromatic aberration constant, E is the total electron energy, α is the aperture semi-angle, f is the focal length of the lens and I is the (objective) lens current. Δf, and ΔI are fluctuations in the focal length and the (objective) lens current, respectively. The chromatic aberration can be minimized by using cold field-emission guns, i.e. high brightness and minimal energy spread, or a monochromator.

Astigmatism occurs if electron lenses have no perfect cylindrical symmetry. If two rays travel in orthogonal planes through the lens they will be focused in two different points on the optical axis. Every modern microscope is able to correct astigmatism of the condenser and objective lenses by introducing a pair of magnetic quadrupole coils after a magnetic lens.

Every real lens has only a limited aperture as indicated in Fig. 1.2d. On every edge that electron waves pass, they get diffracted and a parallel beam gets transformed into an Airy disc. The radius r_D of the disc is defined as radius of the central intensity maximum and can be expressed as [3]

$$r_D = 0.61\frac{\lambda}{\alpha}. \tag{1.18}$$

The resolution r_{total} of a TEM can then be calculated by adding the quadratic radii of each aberration disc to

$$r_{total} = \sqrt{r_S^2 + r_C^2 + r_D^2}. \tag{1.19}$$

For SEM and STEM the finite size of the electron source has to be considered during the calculation of r_{total}.

1.2.2.2. High-resolution phase contrast imaging

In electron microscopy high-resolution phase contrast images are a superposition of the direct beam with a couple of diffracted beams ($\geq$1). The more beams are used the higher the resolution. For this imaging mode not only the amplitudes of the beams are of relevance but also their phase. High-resolution phase contrast imaging can be used to image the atomic structure of a material. However, the interpretation of these kind of images is by no means easy. This is due to a couple of reasons [3]:

1. The image contrast varies with slight changes in the specimen thickness,
2. the objective lens defocus and astigmatism,
3. and changes in the sample orientation or its scattering factor.

The experimental procedure can be implemented very easily. The crystalline sample has to be tilted into the desired orientation, mostly a low indexed pole. This yields a superposition of a large amount of beams contributing to the image. In microscopes not having a C_S-image-corrector one has to additionally use the objective aperture to limit the used beams to a certain diffraction angle. The effect of lens aberrations

on the image will thus be limited. Depending on the actual issue one has to optimize the image quality, i.e. the number of used beams vs. lens aberrations and thus the right objective aperture has to be selected.

High-resolution phase contrast images can be understood using Fresnel diffraction and propagation, because the best images are not obtained in the Gaussian focus [9]. The following paragraphs are summarizing the results of Spence [9]. The electron amplitude at the object plane of the objective lens $\Psi'(x,y)$ can be written as a convolution of the exit electron amplitude $\Psi_{ex}(x,y)$ at the lower side of the specimen $T(x,y)\cdot\Psi_{ex}(x,y)$ and the Fresnel-Propagator in z direction $\mathscr{P}_z(x,y)$:

$$\Psi'(x,y) = A\left(\Psi_{ex}(x,y)\right)\otimes\mathscr{P}_z(x,y) \tag{1.20}$$

with A is a complex amplitude and $T(x,y)$ is the sample transmission function. However, not yet considered are the effect of the objective aperture and the objective lens itself. If both effects are included one can write for the image amplitude $\Psi_i(x',y')$:

$$\begin{aligned}\Psi_i(x',y') &= -\frac{A}{M\lambda^2 f^2}\left[FT\left(\Psi_{ex}(x,y)\right)P\left(\frac{X}{\lambda f},\frac{Y}{\lambda f}\right)\right.\\ &\left.\exp\left(i\chi\left\{\frac{X}{\lambda f},\frac{Y}{\lambda f}\right\}\right)\right]\otimes\mathscr{P}(X,Y)\end{aligned} \tag{1.21}$$

where FT denotes a Fourier transformation, P is the objective aperture pupil function, and χ is the aberration phase shift. The distances X and Y are lying in the back-focal plane of the objective lens and are defined as follows: $X = f\theta$ and $Y = f\beta$ where θ and β are the angles at which rays leave the object. This can also be further modified:

$$\Psi_i(x',y') = \frac{1}{M}\Psi_{ex}(-x',-y')\otimes FT\left[P(u,v)\exp\left(i\chi\{u,v\}\right)\right] \tag{1.22}$$

where $u = \dfrac{X}{\lambda f}$ and $v = \dfrac{Y}{\lambda f}$. The term $P(u,v)\exp\left(i\chi\{u,v\}\right)$ can also be called microscope transfer function or contrast transfer function (CTF). In the case of radial symmetry the relation $\theta = \lambda\sqrt{u^2+v^2}$ holds and one can write for Eq. 1.22

$$\Psi_i(x',y') = \frac{1}{M}\Psi_{ex}(-x',-y')\otimes FT\left[P(\theta)\exp\left(i\chi\{\theta\}\right)\right]. \tag{1.23}$$

If only defocus and spherical aberration are considered in the function $\chi(\theta)$ it has the following form:

$$\chi(\theta) = \frac{2\pi}{\lambda}\left\{\frac{\Delta f\,\theta^2}{2}+\frac{C_s\theta^4}{4}\right\} \tag{1.24}$$

where Δf and C_s are the defocus and the spherical aberration constant, respectively.

The optimum defocus is obtained by balancing the spherical aberration constant C_s against Δf . The CTF yielding the fewest zero values is the optimum one. The corresponding defocus value is called Scherzer defocus Δf_{Sch}. Its value can be calculated using [3]

$$\Delta f_{Sch} = -\sqrt{\frac{4}{3}C_s\lambda}. \tag{1.25}$$

The magnitude of the first zero of the CTF defines the point resolution of the microscope in Fig. 1.3. In reality the CTF is limited by the damping envelope damping the CTF at high scattering angles such that it goes asymptotically to zero. The point where no practically usable information gets transferred anymore is called information limit (see Fig. 1.3). The damping envelope describes the instabilities of the microscope including the chromatic aberration of the objective lens, angular spread of the electron source, specimen drift, specimen vibration, and the signal-to-noise ratio of the detector (usually a CCD camera) [3]. In general the CTF can be described as a function of the scattering vector **K** using Bragg's law. Spence [9] used the following expression to mathematically describe the CTF in absence of axial astigmatism including the partial coherence and electronic instabilities

$$CTF(\mathbf{K}) = P(\mathbf{K}) \exp\left[i\chi(\mathbf{K})\right] \exp\left[-\frac{\pi^2\delta^2\lambda^2\mathbf{K}^4}{2}\right] \exp\left[-\left(\frac{\pi\theta_c}{\lambda}\right)^2 \ln 2\mathbf{q}\right] \tag{1.26}$$

$$\chi(\mathbf{K}) = \pi\left(\Delta f\lambda\mathbf{K}^2 + \frac{C_s}{2}\lambda^3\mathbf{K}^4\right) \tag{1.27}$$

$$\delta = C_c\sqrt{\left(\frac{\Delta U}{U}\right)^2 + 4\left(\frac{\Delta I}{I}\right)^2 + \left(\frac{\Delta E}{E}\right)^2} \tag{1.28}$$

$$\mathbf{q} = \left(C_s\lambda^3\mathbf{K}^3 + \Delta f\lambda\mathbf{K}\right)^2 + \pi^2\lambda^4\Delta^4\mathbf{K}^6 - 2\pi^4 i\lambda^3\Delta^2\mathbf{K}^3 \tag{1.29}$$

where λ is the electron wavelength, θ_c is the illumination semi-angle, $\frac{\Delta U}{U}$ is the stability of the acceleration voltage, $\frac{\Delta I}{I}$ is the stability of the objective lens current, and ΔE is the energy-spread of the electron source. Fig. 1.3 shows the phase contrast transfer function $\mathrm{Im}\left[CTF(\mathbf{K})\right]$ (PCTF) for a Jeol 3000F.

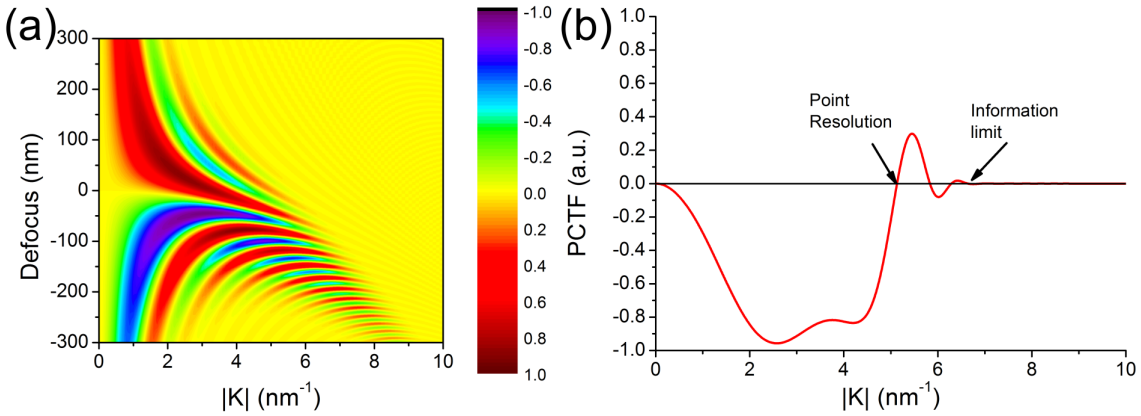

Figure 1.3.: PCTF for a Jeol 3000F using λ = 300 kV, C_s = 1 mm, C_c = 1.8 mm , θ_c= 1 mrad, $\frac{\Delta U}{U} = 10^{-7}$, $\frac{\Delta I}{I} = 10^{-7}$, and ΔE = 0.7 eV. The objective aperture pupil function is assumed to be unity over the total plotted range. Negative defocus values denote underfocusing. (a) Defocus range -300 nm to 300 nm and (b) Scherzer defocus Δf_{Sch} = -51.25 nm.

Phase contrast image interpretation is not straight forward since the contrast seen in the image depends according to Williams and Carter [3] on several factors like lens aberration, microscope alignment, specimen thickness etc. Thus, it is convenient to simulate phase contrast images for several thickness and defocus values to identify the atomic columns more easily. Two methods are available: (i) the Bloch wave and (ii) the multislice method. Both methods have their advantages and their use depends on the exact problem that needs to be solved. Both use the fact that a collision of a fast electron with a crystal

can be described by the time-independent Schrödinger equation, i.e. it is assumed that no momentum is transferred from the electron to the crystal.

$$\Delta\Psi(\mathbf{r}) + \frac{8\pi^2 me}{h^2}\left[E + V(\mathbf{r})\right]\Psi(\mathbf{r}) = 0 \tag{1.30}$$

1.2.2.3. Scanning Transmission Electron Microscopy (STEM)

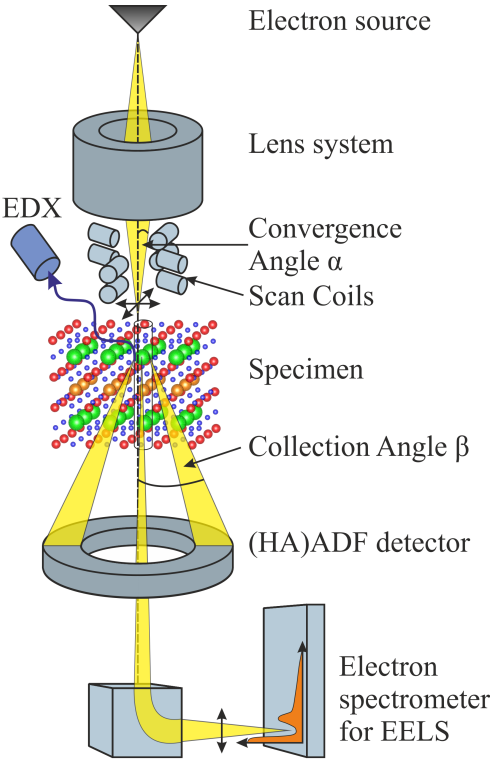

Figure 1.4.: The principle of STEM and a selection of signals that can be used [10, 11].

In a STEM a fine electron probe is focused on the sample and scanned across a predefined rectangular scan field analogous to the SEM. This can be achieved by putting additional scan coils in front of the sample as shown in Fig. 1.4. Typical convergence angles α in STEM are large (α > 10 mrad) compared to CTEM. The electrons contained in the probe scatter when traveling through the sample and create at each scan position a site-specific convergent electron diffraction pattern [12].

An important type of image signal in STEM is collected by the high-angle annular dark-field (HAADF) detector, yielding called Z-contrast images. The HAADF image is formed by incoherent elastically scattered electrons, i.e. the intensity observed in the HAADF image is a sum of superimposed single scattering events where heavy atoms scatter more electrons into high angles than lighter ones. The intensity in HAADF images is roughly proportional to Z^2. Collections angles β of 70 to 150 mrad are used for HAADF images. Annular detectors are used to maximize the signal-to-noise ratio due to the large amount intensity being captured by these detectors. A description of the image formation can be found for example in [13]. However, the striking benefit of high-resolution HAADF images compared to high-resolution phase contrast images is that the intensity observed in the image is almost independent of the sample thickness and the atom columns are always bright spots simplifying the image interpretation enormously.

The incoherency in HAADF images is mainly due to thermal diffuse scattering (TDS), i.e. at temperatures larger than 0 K phonons are present in the crystal lattice. Another possibility for the incoherency is the detector geometry [13]. This particular issue is of great interest for HAADF image simulation since it is not easy to implement electron-phonon scattering since it is very time consuming [11]. The electron-phonon scattering can be calculated by modifying the atomic scattering factors. In the past this was accomplished using isotropic Debye-Waller factors [14]. More recent programs like QSTEM [11] and STEMSim [15] use the more accurate frozen phonon approximation [16] for the HAADF image simulation.

Besides the imaging techniques STEM also offers atomically-resolved spectroscopic techniques like EDX and EELS as schematically shown in Fig. 1.4.

1.2.2.4. Diffraction theory: the many beam case

The Bloch wave method was developed by Bethe [17] using the fact that electrons traveling through a translational symmetric crystal potential behave as Bloch waves ($\Psi(\mathbf{r},\mathbf{k})$):

$$\Psi(\mathbf{r},\mathbf{k}) = B_{\mathbf{k}}(\mathbf{r})\, e^{2\pi i \mathbf{k}\cdot\mathbf{r}} \tag{1.31}$$

where the $B_{\mathbf{k}}(\mathbf{r})$ are the Bloch functions. The Bloch functions $B_{\mathbf{k}}(\mathbf{r})$ and the crystal potential $V(\mathbf{r})$ can be both expanded into a Fourier series:

$$B_{\mathbf{k}}(\mathbf{r}) = \sum_{\mathbf{g}} C_{\mathbf{g}}(\mathbf{k})\, e^{2\pi i \mathbf{g}\cdot\mathbf{r}} \tag{1.32}$$

$$V(\mathbf{r}) = \frac{h^2}{2me} \sum_{\mathbf{g}} U_{\mathbf{g}}\, e^{2\pi i \mathbf{g}\cdot\mathbf{r}}. \tag{1.33}$$

where the plane-wave amplitudes $C_{\mathbf{g}}(\mathbf{k})$ depend on $\mathbf{k}$ but not on $\mathbf{r}$. It is assumed that only those electron wave functions will solve the Schrödinger equation (Eq. 1.30), which scatter into direction $\mathbf{k}+\mathbf{g}$:

$$\Psi(\mathbf{r},\mathbf{k}) = \sum_{\mathbf{g}} C_{\mathbf{g}}(\mathbf{k})\, e^{2\pi i (\mathbf{k}+\mathbf{g})\cdot\mathbf{r}}. \tag{1.34}$$

If both the electron wave function $\Psi(\mathbf{r})$ and the potential $V(\mathbf{r})$ are inserted into the Schrödinger equation (Eq. 1.30) one has to evaluate the product of two infinite sums (see Appendix). Since it is being summed over all terms one is free to set the center of the variables.

$$\begin{aligned} \Psi(\mathbf{r})\cdot V(\mathbf{r}) &= \frac{h^2}{2me} \sum_{\mathbf{g}} U_{\mathbf{g}} \sum_{\mathbf{h}} C_{\mathbf{h}}(\mathbf{k})\, e^{2\pi i (\mathbf{k}+\mathbf{g}+\mathbf{h})\cdot\mathbf{r}} \\ &= \frac{h^2}{2me} \sum_{\mathbf{g}} e^{2\pi i (\mathbf{k}+\mathbf{g})\cdot\mathbf{r}} \left(U_0 C_{\mathbf{g}}(\mathbf{k}) \sum_{\mathbf{h}\neq 0} U_{\mathbf{h}} C_{\mathbf{g}-\mathbf{h}}(\mathbf{k}) \right). \end{aligned} \tag{1.35}$$

If this is inserted into the Schrödinger equation (Eq. 1.30) one gets

$$\left[-|\mathbf{k}+\mathbf{g}|^2 + \frac{2meE}{h^2} + U_0 \right] C_{\mathbf{g}}(\mathbf{k}) + \sum_{\mathbf{h}\neq 0} U_{\mathbf{h}} C_{\mathbf{g}-\mathbf{h}}(\mathbf{k}) = 0. \tag{1.36}$$

Note that this equation has to be fulfilled for every diffraction vector $\mathbf{g}$ since they are independent of each other. U_0 is the mean inner potential of the crystal. Eq. 1.36 can be further simplified by collecting all g independent terms by introducing the scalar quantity $K = \sqrt{\frac{2meE}{h^2} + U_0}$ (absolute value of the wave-vector of the electrons in the mean inner potential of the crystal):

$$\left[K^2 - |\mathbf{k}+\mathbf{g}|^2 \right] C_{\mathbf{g}}(\mathbf{k}) + \sum_{\mathbf{h}\neq 0} U_{\mathbf{h}} C_{\mathbf{g}-\mathbf{h}}(\mathbf{k}) = 0 \tag{1.37}$$

where g is the index over all beams and h is the index of all excited beams g-h. Eq. 1.37 is the starting point for all Bloch wave calculations. It tells how the Bloch wave amplitudes C are connected to each other via the potential terms U. This is called the dynamical coupling concept [3]. Eq. 1.37 can also be written as in matrix form [18]:

$$\begin{pmatrix} M_{-\mathbf{g}-\mathbf{g}} & \cdots & M_{\mathbf{g}-\mathbf{0}} & \cdots & M_{-\mathbf{g}-\mathbf{g}} \\ \vdots & \ddots & \vdots & & \vdots \\ M_{\mathbf{0}-\mathbf{g}} & \cdots & M_{\mathbf{00}} & \cdots & M_{\mathbf{0}-\mathbf{g}} \\ \vdots & & \vdots & \ddots & \vdots \\ M_{\mathbf{g}-(-\mathbf{g})} & \cdots & M_{\mathbf{g}-\mathbf{0}} & \cdots & M_{\mathbf{gg}} \end{pmatrix} \cdot \begin{pmatrix} C_{-\mathbf{g}}(\mathbf{k}) \\ \vdots \\ C_{\mathbf{0}}(\mathbf{k}) \\ \vdots \\ C_{\mathbf{g}}(\mathbf{k}) \end{pmatrix} = \mathbf{0} \tag{1.38}$$

where $M_{\mathbf{gg}} = K^2 - |\mathbf{k}+\mathbf{g}|^2$ and $M_{\mathbf{gh}} = U_{\mathbf{g}-\mathbf{h}}$. The rows correspond to the used **g** vectors and the columns to the allowed **h** vectors. The solution of this N×N linear equation system is only found if suitable boundary conditions are applied.Then the N eigenvalues of M define the **k** vector of each Bloch wave and the corresponding eigenvector defines its amplitude C [18]. For practical reasons, i.e. if absorption needs to be included, the eigenvalue approach is not feasible since much more computation time is needed for solving complex eigenvalue problems. Therefore, Self et al. [18] introduced the scattering matrix approach which is faster and can be applied also for thick (~100 nm) crystals. However, truncation and rounding errors enter during the numerical calculation, i.e. it is necessary to perform calculation checks to guarantee correct results. The Bloch wave method is for example implemented in the EMS software package [19].

1.2.2.5. Diffraction theory: The Multislice method

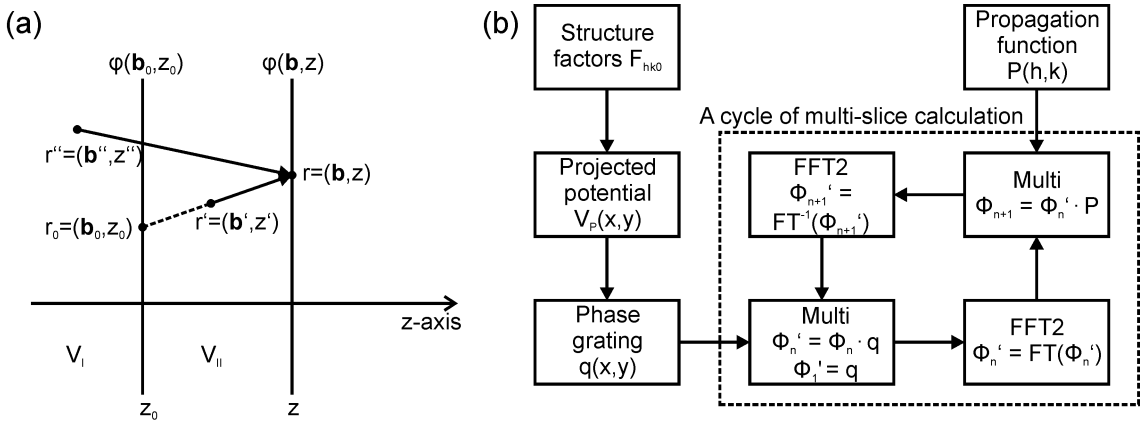

Figure 1.5.: (a) A derivation of the multi-slice formula from an integral form of the Schrödinger equation. The region of integration in the forward-scattering approximation will be divided into two parts: V_I in front of and V_{II} inside the slice. (b) A flow chart of the procedure for the multi-slice calculation. Here the capital letters Φ and P denote the Fourier transforms of the corresponding functions φ and p, respectively. The phase grating q and propagation function P are computed in advance of the multi-slice iteration. [20]

The multi-slice method is faster than the Bloch wave calculation. It uses numerical integration to solve the Schrödinger equation. It was described first by Cowley and Moodie [21] in 1957. The theoretical approach in case of fast electrons was given by Ishizuka and Ueda [20], which will be summarized in the following paragraphs. They derived the multi-slice formula by integrating the Schrödinger equation. The integral form of the equation is then replaced by a function similar to the infinite Born series and solved by applying the method of stationary phase to each term.

The integral form of the Schrödinger equation (Eq. 1.30) is given by:

$$\begin{aligned}\Psi(\mathbf{r}) &= \exp(i\mathbf{kr})\,\varphi(\mathbf{r}) \\ &= \exp(i\mathbf{kr})\left[1-\frac{2m}{4\pi\hbar}\int\frac{\exp\{i\,(|\mathbf{k}|\,|\mathbf{r}-\mathbf{r}'|-\mathbf{k}\cdot(\mathbf{r}-\mathbf{r}'))\}}{|\mathbf{r}-\mathbf{r}'|}\right. \\ &\times \left. V(\mathbf{r}')\cdot\varphi(\mathbf{r}')\,d\mathbf{r}'\right]\end{aligned} \tag{1.39}$$

where $\Psi(\mathbf{r})$ is the wave function, $\mathbf{k}$ is the wavevector, m is the electron mass, $V(\mathbf{r})$ is the potential energy, and $\mathbf{r}=(x,y,z)$. The direction of incident electrons is assumed to be parallel to the z-axis or in terms of the unit cell along the c-direction. Assuming small-angle electron scattering at high electron energies Eq. 1.39 can be transformed into:

$$\begin{aligned}\varphi(\mathbf{b},z) &= 1-\int\int_{z'=-\infty}^{z'=z}\frac{i}{\hbar v}V(\mathbf{b}',z')\cdot\varphi(\mathbf{b}',z')\times \\ &\left[\underbrace{\frac{1}{i\lambda(z-z')}\exp\left\{i|\mathbf{k}|\frac{|\mathbf{b}-\mathbf{b}'|}{2(z-z')}\right\}}_{=p(\mathbf{b},z)}\right]dz'd\mathbf{b}'\end{aligned} \tag{1.40}$$

where v and λ are the incident electron velocity and wavelength, respectively. The two vectors **b** and **b'** are perpendicular to the incident electrons (see Fig. 1.5). The propagation function $p(\mathbf{b},z)$ in the square bracket of Eq. 1.40 has the form of a Huygens wavelet in the paraboloidal approximation. If $p(\mathbf{b},z)$ is normalized, $\varphi(\mathbf{b},z)$ can be written as

$$\begin{aligned}\varphi(\mathbf{b},z) &= \int\varphi(\mathbf{b}_0,z_0)\,p(\mathbf{b}-\mathbf{b}_0,z-z_0)\,d\mathbf{b}_0 \\ &+ \left(\frac{i}{\hbar v}\right)\int_{V_{II}}\int_{z'=z_0}^{z'=z}V(\mathbf{b}',z')\cdot\varphi(\mathbf{b}',z')\times p(\mathbf{b}-\mathbf{b}',z-z')dz'd\mathbf{b}'.\end{aligned} \tag{1.41}$$

The integral in Eq. 1.41 can be solved by an infinite series expansion:

$$\varphi(\mathbf{b},z)=\sum_{n=0}^{\infty}\left(\frac{i}{\hbar v}\right)^n f_n(\mathbf{b},z). \tag{1.42}$$

By assuming a slowly varying potential and applying the stationary-phase method described in the appendix of [20] one obtains:

$$f_n(\mathbf{b},z)=\int\frac{1}{n!}\left\{\int_{z'=z_0}^{z'=z}V(\mathbf{b}_0,z')\,dz'\right\}^n\times\varphi(\mathbf{b}_0,z_0)\,p(\mathbf{b}-\mathbf{b}_0,z-z_0)\,d\mathbf{b}_0. \tag{1.43}$$

Therefore, $\varphi(\mathbf{b},z)$ has the form

$$\varphi(\mathbf{b},z) = \int \exp\left\{-\frac{i}{\hbar v}\int_{z'=z_0}^{z'=z} V(\mathbf{b}_0,z')\,dz'\right\} \times \varphi(\mathbf{b}_0,z_0)\,p(\mathbf{b}-\mathbf{b}_0,z-z_0)\,d\mathbf{b}_0 \tag{1.44}$$

or in a more simple form by using a convolution integral (denoted by $*$)

$$\varphi_{n+1}(\mathbf{b}) = [\varphi_n(\mathbf{b})\cdot q_n(\mathbf{b})] * p(\mathbf{b},z_{n+1}-z_n) \tag{1.45}$$

with the following simplifications

$$\varphi_n(\mathbf{b}) = \varphi(\mathbf{b},z_n) \tag{1.46}$$

$$q_n(\mathbf{b}) = \exp\left\{-\frac{i}{\hbar v}\int_{z'=z_n}^{z'=z_n+1} V(\mathbf{b},z')\,dz'\right\} \tag{1.47}$$

$$p(\mathbf{b},z) = \frac{1}{i\lambda(z-z')}\exp\left\{i|\mathbf{k}|\frac{|\mathbf{b}-\mathbf{b}'|}{2(z-z')}\right\} \tag{1.48}$$

where $q_n(\mathbf{b})$ is the phase grating calculated from the projected potential using Eq. 1.47. The projected potential $V_P(x,y)$ along the c-axis of the unit cell is calculated by using the following Fast Fourier Transforms (FFT):

$$V_P(x,y) = \frac{1}{a\cdot b}\sum_h\sum_k F(h,k,0)\exp\left[2\pi i(hx+ky)\right] \tag{1.49}$$

with a,b as the 2D unit cell dimensions, h,k Miller indices, F as structure factor calculated from the atomic scattering factors.The propagation function in reciprocal space $P(h,k)$ has the form

$$P(h,k) = \exp\left\{-2\pi i\Delta z\frac{\lambda}{2}\left[\left(\frac{h}{a}\right)^2+\left(\frac{k}{b}\right)^2\right]\right\} \tag{1.50}$$

with the electron wave length λ, slice thickness Δz, and a,b as the unit cell dimensions. The convolution integral in Eq. 1.45 is calculated in the multi-slice method by successive application of 2D FFT's (Fig. 1.5b) and applying the Fourier convolution theorem such that:

$$\varphi_{n+1} = FT\{\varphi_n\cdot q\}\cdot P. \tag{1.51}$$

The computation time of one multi-slice cycle (Fig. 1.5b) scales with $2N\log_2 2N$ (N: number of beams), whereas for a direct Bloch wave calculation the computation time scales with N^2 if only matrix multiplications are used or with N^3 if also a Eigenvalue problem is solved [22]. For a large number of beams (> 1000) being used, the multi-slice method is much more efficient than the Bloch wave calculation. For a good resolution the number of sampling points (beams) should be large enough to avoid artifacts in the resulting image.

1.2.3. Inelastic electron scattering

1.2.3.1. Electron Energy-Loss Spectroscopy (EELS)

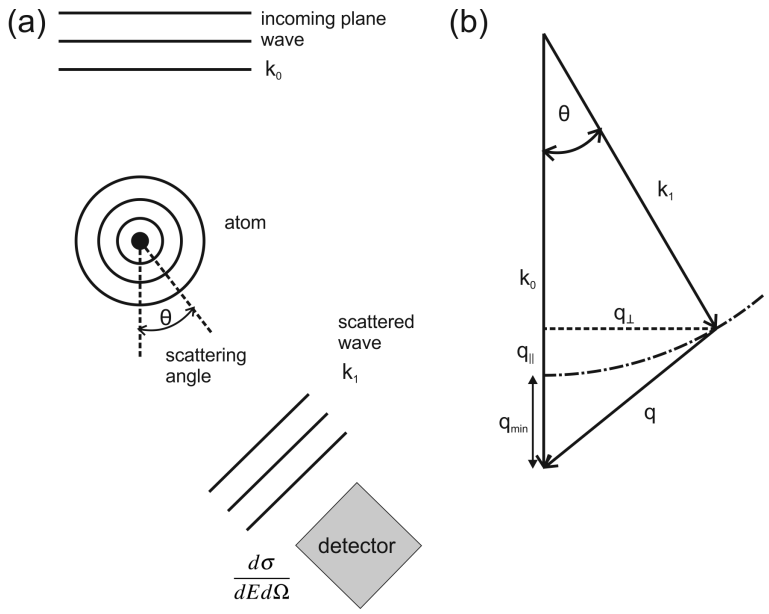

Figure 1.6.: (a) Schematic diagram of inelastic scattering of a plane wave on a single atom. (b) Scattering triangle for inelastic scattering events. This figure is reproduced according to Fig. 2.4 in [23].

Inelastic scattering occurs due to the electrostatic interaction of fast primary electrons with inner and outer shell atomic electrons [24]. For the understanding of EEL spectra generation it is important to deal with relativistic mechanics and quantum mechanics to derive inelastic cross sections as schematically shown in Fig. 1.6. The two fundamental equations in inelastic scattering are conservation of energy and momentum. Since in an electron microscope mostly high-energy electrons are used, relativistic effects have to be considered. The total energy and momentum of a relativistic electron are given by

$$W = \gamma m_0 c^2 \tag{1.52}$$

$$p = \gamma m_0 v^2 = \hbar k_0. \tag{1.53}$$

where $\gamma = 1 + \frac{E_0}{mc^2}$ is a relativistic factor, m_0 is the electron rest mass, v is the electron velocity, and $k_0 = |\mathbf{k}_0|$ is the incident electron wave number. The total relativistic energy W can be written in dependence of the incident electron wave number

$$W^2 = m_0^2 c^4 + p^2 c^2 = m_0^2 c^4 + \hbar^2 k_0^2 c^2. \tag{1.54}$$

Then the energy conservation formula has the form

$$W - E = W' = \sqrt{m_0^2 c^4 + \hbar^2 k_1^2 c^2} \tag{1.55}$$

where W and W' are the energies before and after the collision event and E is the energy-loss. Furthermore, one can write for the wave number $k_1 = |\mathbf{k}_1|$ after the collision

$$k_1^2 = k_0^2 - 2\frac{\gamma m_0 E}{\hbar^2} + \frac{E^2}{\hbar^2 c^2}. \tag{1.56}$$

Eq. 1.56 clearly shows that the wave number after the collision depends on the wave number before the collision and the energy-loss. Thus, $k_0^2 > k_1^2$. From Fig. 1.6b one can extract an equation for the conservation of momentum

$$q^2 = k_0^2 + k_1^2 - 2k_0 k_1 \cos\theta. \tag{1.57}$$

One can introduce a new wave vector having the same length as $\mathbf{k_1}$ but lying in the direction of $\mathbf{k_0}$. The difference to $\mathbf{k_0}$ is called $\mathbf{q}_{min}$ as shown in Fig. 1.6b. The scattering vector $\mathbf{q}$ can be written according to Fig. 1.6 as

$$q^2 = q_{||}^2 + q_{\perp}^2. \tag{1.58}$$

In the case of small scattering angles ϑ one can assume for the quantity $\mathbf{q}_{min}$ and the characteristic scattering angle θ_E [24]

$$q_{min} \approx k_0 \theta_E \tag{1.59}$$

$$\theta_E \approx \frac{E}{2E_0}. \tag{1.60}$$

θ_E is used to select the best suitable objective aperture in EELS experiments.

The intensity being present in an EEL spectrum is related to the energy-loss E and the solid angle Ω or what is known as the double differential cross section $\frac{d^2\sigma}{dEd\Omega}$. For the determination of inelastic cross sections in general quantum mechanics is needed. The form of $\frac{d^2\sigma}{dEd\Omega}$ can be derived for example via time-dependent perturbation theory describing the transition rate between initial and final states of the interacting electrons. This is also known as Fermi's Golden Rule [25]. The transition probability can then be written as

$$\frac{d^2\sigma}{dEd\Omega} \propto \langle f, \mathbf{k_1} | V | i, \mathbf{k_0} \rangle \tag{1.61}$$

where $|i, \mathbf{k_0}\rangle$ are the initial and final $|f, \mathbf{k_1}\rangle$ states wave vectors. V is the interaction potential, i.e. a Coulomb potential.

If it is assumed that the incoming electron energies are much greater than those of the excited electron states, one can write the total wave function of the system as product of an electron plane wave and atomic states [25]. The double differential cross section can be written by introducing the "Generalized Oscillator Strength" (GOS) $\frac{df(q,E)}{dE}$ according to Inokuti [26] as

$$\frac{d^2\sigma}{dEd\Omega} = \frac{4\gamma^2 R}{Eq^2}\frac{k_1}{k_0}\frac{df(q,E)}{dE}. \tag{1.62}$$

where R is the Rydberg energy. The first approach for the calculation of the GOS was developed by Bethe [27] and is used to calculate K-shell ionization cross sections for EELS. The base is the wave mechanics of the hydrogen atom.

For high electron energies retardation effects become important and the double differential cross section should be modified according to Møller [28]

$$\frac{d^2\sigma}{dEd\Omega} = 4\gamma^2 a_0^2 R^2 \frac{k_1}{k_0}\left[\frac{1}{Q^2} - \frac{2\gamma-1}{\gamma^2 Q(E_0-Q)} + \frac{1}{(E_0-Q)^2} + \frac{1}{(E_0+m_0c^2)^2}\right]|\eta(q,E)|^2. \tag{1.63}$$

The quantity Q has dimensions of energy and its exact definition can be found in [24] and $|\eta(q,E)|^2$ is an energy-differential relativistic form factor similar to the non-relativistic case ($|\varepsilon(q)|^2$) and its definition can be looked up in [26].

Using the approximation of Fano [29] that the differential cross section can be written within in the dipole approximation, i.e. regions where $\frac{df}{dE} = const$ as three independent terms and integrating up to a collection angle β the single differential cross section has the following form

$$\frac{d\sigma}{dE} = \frac{4\pi a_0^2 R^2}{ET}\frac{df}{dE}\left[\ln\left(1+\frac{\beta^2}{\theta_E^2}\right) + G(\beta,\gamma,\theta)\right] \tag{1.64}$$

where

$$G(\beta,\gamma,\theta) = 2\ln\gamma - \ln\left(\frac{\beta^2+\theta_E^2}{\beta^2+\frac{\theta_E^2}{\gamma^2}}\right) - \frac{v^2}{c^2}\left(\frac{\beta^2}{\beta^2+\frac{\theta_E^2}{\gamma^2}}\right) \tag{1.65}$$

The single differential cross sections can be directly compared to experimentally acquired EEL spectra. A further integration over all energy losses can be carried out resulting in the Bethe asymptotic formula for the total ionization cross section for inner shells. The obtained result shown in Eq. 1.66 can be used, e.g. for calculating X-ray production

$$\sigma_K = \frac{4\pi a_0^2 R^2 N_K b_K}{E_K T}\left[\ln\left(\frac{c_K T}{E_K}\right) + 2\ln\gamma - \frac{v^2}{c^2}\right] \tag{1.66}$$

where N_K is number of electrons per shell (K, L, M), b_K and c_K are parameters fitted to experimental data [30].

In an experimentally acquired EEL spectrum there are also other features present besides ionization edges of inner shell electrons described by the ionization cross section. Fig. 1.7 shows a schematic EEL spectrum. Several important features are indicated at several energy-losses. The most prominent feature of an EEL spectrum is the zero-loss peak. Only quasi-elastically scattered electrons contribute to it. Neglecting artifacts introduced by the filter or spectrometer, the FWHM of the zero-loss peak is the energy spread of the electron source. The low-loss region extending from 0 to about 50 eV is the next interesting spectral area. Peaks or edges located in this area are due to collective oscillations of valence electrons (plasmons) or due to ionizations of the outermost atomic shells. The number of plasmon peaks depends on the sample thickness in relation to the ineleastic mean free path. If the sample thickness exceeds the ineleastic electron mean free path the incident electron can undergo multiple scattering creating

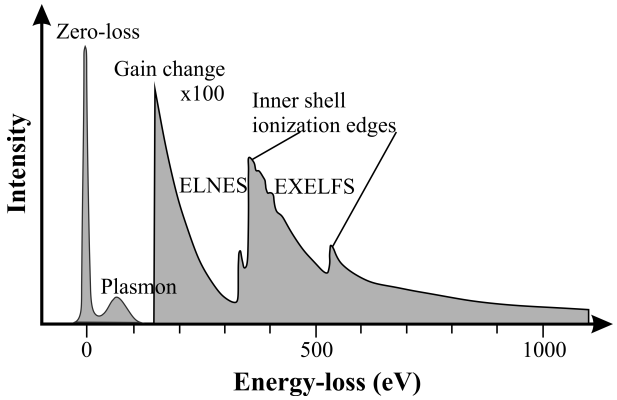

Figure 1.7.: Schematic EEL spectrum with indicated features. Reproduced from [25].

more than one plasmon. The high-loss region is located above 50 eV. Since the EEL spectrum is highly dynamic a gain change was introduced at 150 eV in Fig. 1.7. Here the ionization edges of inner shell electrons are mostly found. The integral intensity of the ionization edge is proportional to the amount of atoms covered by the electron beam. The kinetic energy transferred to the excited electron is not fixed. Thus, the signal found at a specific ionization edge may extend above the threshold energy. 30 to 40 eV above the ionization edge the Electron-Loss Near-Edge Structure (ELNES) is being observed. Its origin is due to empty electronic states near the Fermi edge modified in solids by the chemical bindings of atoms resulting in a complex Density Of States (DOS). Above this region the EXtended Electron-Loss Fine Structure (EXELFS) is being observed. The electron can now act as quasi-free electron. The excess energy can be interpreted as an electron wave scattered once on the atomic neighborhood of the ionized atom. Oscillations are generated on a smooth DOS. These are called EXELFS [3].

1.2.3.2. Energy-Dispersive X-ray Analysis

A second way for an incident electron to inelastically scatter and lose part of its energy is the generation of characteristic X-rays or Auger electrons. Characteristic X-rays are generated by creating an atomic electron vacancy in one of the inner shells and filling it up by outer shell electrons. Due to quantum mechanics only certain transitions are allowed. The selection rules are $\Delta l = \pm 1$ and $\Delta j = 0, \pm 1$. For light elements (Z<10) the probability of X-ray emission is close to zero, a second process emitting an electron is dominant. This is called Auger electron emission. Both emission probabilities are coupled such that $A + X = 1$. Besides characteristic X-rays also Bremsstrahlung is found in X-ray spectra. Bremsstrahlung originates from deceleration of fast electrons in the Coulomb field of a nucleus.

In electron microscopes (SEM or TEM) X-rays are detected either wavelength dispersive (WDX) or energy dispersive (EDX). Both have advantages and disadvantages. WDX has the advantage of a high energy resolution (~10 eV) and low detection limits (~15 ppm), but the disadvantage is that it takes up to several hours for acquisition. EDX is much faster, it only needs several minutes to generate a X-ray spectrum, but the energy resolution and the detection limit are a factor of 10-13 larger than in WDX. The incident electrons create X-rays that leave the sample behind and are Bragg reflected and focused by a single crystal of Johannsson geometry onto a proportional counter. The spectrometer can only record one wavelength at a time. All parts of the spectrometer sample, analyzing crystal, and proportional counter have to be placed on the Rowland circle to generate a X-ray spectrum.

The principle of EDX is very different. The X-ray quantum generated in the sample hits a semiconductor diode and generates electron-hole pairs. The number of electron-hole pairs is proportional to the energy of the incident X-ray quantum. A field effect transistor coupled to the diode generates an electrical output signal that can be further processed and converted into an X-ray spectrum. The energy resolution of the spectrum depends on the statistics of the electron-hole pair generation and the noise of the preamplifier. Both types of spectrometers are shielded in commercially available products by a window from the sample chamber to avoid contamination. This window typically consists of ~500 nm diamond-like carbon, boron compounds, or metal-coated plastic films (e.g. ~300 nm pyrolene plus 20-40 nm Al) [31]. It absorbs especially low energy X-ray quanta hampering light element (Z<10) analysis.

The quantification of EDX and WDX spectra can be done as described below. The element concentrations are proportional to the measured integral intensities of the characteristic X-ray lines. The quantification procedure compares the actual measured intensity I_A to an intensity I_S obtained on a standard sample. However, the measured intensity is not the generated intensity, so that the concentration cannot be directly calculated. Three correction factors need to be introduced:

1. Z: the atomic number correction
2. A: the X-ray absorption correction
3. F: the X-ray fluorescence correction

The final quantification equation has the following form [3]

$$\frac{c_A}{c_S} = Z \cdot A \cdot F \frac{I_A}{I_S}. \tag{1.67}$$

Nowadays every X-ray analysis software has implemented this equation. Eq. 1.67 is valid for all types of samples, i.e. bulk and thin film samples, but for thin film samples used in the TEM an approximation called Cliff-Lorimer method exists to quantify EDX spectra. For thin films absorption and fluorescence can be neglected. If for example an EDX spectrum of a two element sample needs to be quantified in TEM Eq. 1.67 can be modified to [3]

$$\frac{c_A}{c_B} = k_{AB} \frac{I_A}{I_B}. \tag{1.68}$$

k_{AB} are called Cliff-Lorimer factors and it holds in this case $c_A + c_B = 1$. They are related to the atomic number correction factor and can be calculated by

$$k_{AB} = \frac{Q_B \omega_B a_B A_B \eta_B}{Q_A \omega_A a_A A_A \eta_A} \tag{1.69}$$

where Q_i are ionization cross sections, ω_i are fluorescence yields, a_i are the relative transition probabilities, i.e. $a = \frac{I_{K\alpha}}{I_{K\alpha}+I_{K_\beta}}$, A_i are the atomic weights, and η_i are detector efficiencies. The Cliff-Lorimer equation (Eq. 1.67) can also be easily generalized to multiple element systems.

Another important quantity in X-ray spectra is the minimum detectable mole fraction, since it determines the accuracy of the measurement. The X-ray emission during electron bombardment obeys a Poisson statistics. A X-ray peak is considered to be 99% real if it exceeds three times the standard deviation $\sigma = \sqrt{N_B}$ of the background counts N_B present under the peak. Thus, the minimum detectable mole fraction c_{min} is defined as

$$\frac{c_{min}}{c} = \frac{3\sqrt{N_{Back}}}{N_{Peak}} = \frac{3\sqrt{I_{Back}}}{\sqrt{t} I_{Peak}} \tag{1.70}$$

where c is the actual concentration, N_{Back} are the background counts under the peak, N_{Peak} are the background-corrected peak counts, I_{Back} is the background intensity, I_{Peak} is the peak intensity, and t is the spectral live time. Combined with the Cliff-Lorimer equation for two elements the detectable mole fraction c_A for element A can be calculated in terms of the actual concentration c_B of element B as

$$\frac{c_{A,min}}{c_B} = k_{AB} \frac{3\sqrt{N_{A,Back}}}{N_{B,Peak}} = k_{AB} \frac{3\sqrt{I_{A,Back}}}{\sqrt{t} I_{B,Peak}}. \tag{1.71}$$

If a scanning unit is being available in the microscope, not only EDX spectra can be acquired but also an element mapping. Chemical mapping is very useful to determine secondary phases without destroying the original sample in any type of material. Chemical mapping is mainly used in SEM in this work but the same aspects are also true for STEM. For the SEM work a Jeol 6500F equipped with an Oxford Pentafet EDX detector was used. Typical acceleration voltages are in the range from 5 to 30 kV depending on the sample and the actual issue. In order to estimate the intensity I per pixel obtained in a specific elemental map several parameters need to be considered:

1. The acquisition rate A in counts per sec,
2. The total acquisition time T (normally in the order of 1000 s),
3. The peak counts N_{Peak} of a specific element extracted from the EDX sum spectrum,
4. The total number of counts N_{Total} contained in the EDX sum spectrum,
5. The number of frames F summed up in the individual elemental map,
6. and the elemental map size S in Pixels.

The Oxford INCA software used for this work offers 4 different fixed map sizes (128×88 px, 256×176 px, 512×352 px, and 1024×704 px). The process time, i.e. the time required by the electronics to process each pulse can be varied in 6 arbitrary steps ranging from 1 to 6 inside INCA at which 1 is the fastest and 6 is the slowest. The process time controls the total acquisition time and the energy resolution. For EDX point spectra a process time of 5 was always used whereas for the elemental mapping it was always reduced to 2 to minimize drift and charging effects. Taking above points an equation for the intensity per pixel can be set up

$$\frac{I}{pixel} = \frac{A \cdot T \cdot \frac{N_{Peak}}{N_{Total}} \cdot F}{S}. \tag{1.72}$$

The final map in INCA is composed by superimposing the secondary electron image and three X-ray maps of interest to a ”mix” image. To each map a color (red, green, or blue) is assigned. Single element sample areas have a single color in the mix image whereas multi-elemental areas show a mixed color. The image combination principle is the same as for the plasmon imaging technique described above. It can be used to identify secondary phases inside a matrix.

2. Physical properties and synthesis of high-temperature superconducting wires

2.1. Introduction

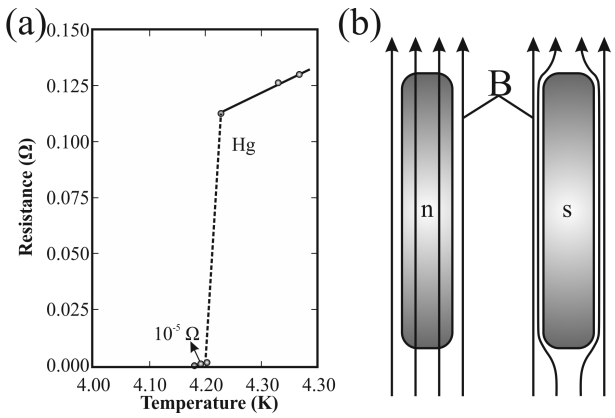

Figure 2.1.: (a) Resistivity curve of mercury and (b) schematic drawing of the Meissner-Ochsenfeld effect. In the normal state (on the left side) the solid is fully penetrated by the magnetic field B whereas in the superconducting state (on the right side) the magnetic field is completely removed inside the solid. Reproduced from [32].

Since Heike Kamerlingh Onnes discovered a hundred years ago the phenomenon that Hg looses all measurable resistance (Fig. 2.1a) at liquid helium temperatures [33] the effect of superconductivity came into view of scientists. This was not predicted by the Matthiessen theory [34, 35, 36] which assumed that with decreasing temperature the electrical resistivity of metals also decreases. For the liquefaction of He, which is essential to observe superconductivity in Hg H. Kamerlingh Onnes received the physics Nobel prize in 1913. Great effort had been made since those days to explain this new effect by theory and new experiments were designed. However, the loss of resistance is not enough to identify the superconductive state. Another effect discovered by Meissner and Ochsenfeld known as Meissner-Ochsenfeld effect [37] is needed to assure that a material has really entered in a superconductive state. The Meissner-Ochsenfeld effect is the removal of the magnetic field from the inside of a superconductor, i.e. a superconductor is a perfect diamagnet (Fig. 2.1b).

On the theory side the most important findings were the London theory [38], the Ginzburg-Landau theory [39], and finally the BCS theory [40] of superconductors. The London theory is a phenomenological theory based upon the Maxwell equations. It describes for example the penetration of the magnetic field in a superconductor. The Ginzburg-Landau theory tries to handle superconductivity as a thermodynamic problem. Both theories were unable to deal with microscopic properties of superconductors. Hence, Bardeen, Cooper, and Schrieffer developed their theory which is still broadly used today. The first two theories are still used for certain aspects, e.g. the Ginzburg-Landau coherence length. The last two theories were awarded with the physics Nobel prize.

Experimentalists were on a steady search for new superconducting materials since 1911. Many metals and alloys were found to be superconducting as can be seen from the selection presented in Tab. 2.1. However, their transition temperatures are limited to a maximum of about 40 K and technical applications are only possible at liquid helium temperatures. Many of today's applications for example NMR magnets or even the Large Hadron Collider (LHC) still use one of those materials. This is due to the fact that the material science and the industrial up-scale process of these materials have been investigated thoroughly in the past 40 to 50 years. However, the use of liquid He is very expensive.

Metal	T_c [K]	Alloy	T_c [K]
Al	1.140	Nb_3Sn	18.05
Ti	0.39	Nb_3Ge	23.2
V	5.38	Nb_3Al	17.5
Ga	1.091	NbN	16.0
Nb	9.50	V_3Ga	16.5
Hg	4.153	V_3Si	17.1
Pb	7.193	MgB_2	39
Sn	3.722		

Table 2.1.: Superconducting metals and alloys and their transition temperature T_c [41, 42].

Therefore, Bednorz and Müller used their knowledge of the existence of superconductivity in oxides [43] to look for oxides that have the following two properties:

1. A large density of charge carriers
2. A large electron-phonon coupling constant

One class of materials fulfilling these properties are those showing a large Jahn-Teller effect, i.e. a spontaneous distortion to remove the degeneration of electron states. In 1986 they found $Ba_xLa_{5-x}Cu_5O_z$[44] which has at x=0.75 the onset of T_c at 30 K. Shortly afterwards superconductivity at liquid nitrogen temperatures was discovered in the Y-Ba-Cu-O system [45]. This was the beginning of the era of High-temperature Superconductors (HTS). Several HTS compounds have been found up to now as indicated in blue in Fig.2.2. Though many other elements and compounds like MgB_2 show superconducting behavior. The pnictide class of superconducting materials, very recently discovered, shows T_c values up to 55 K.

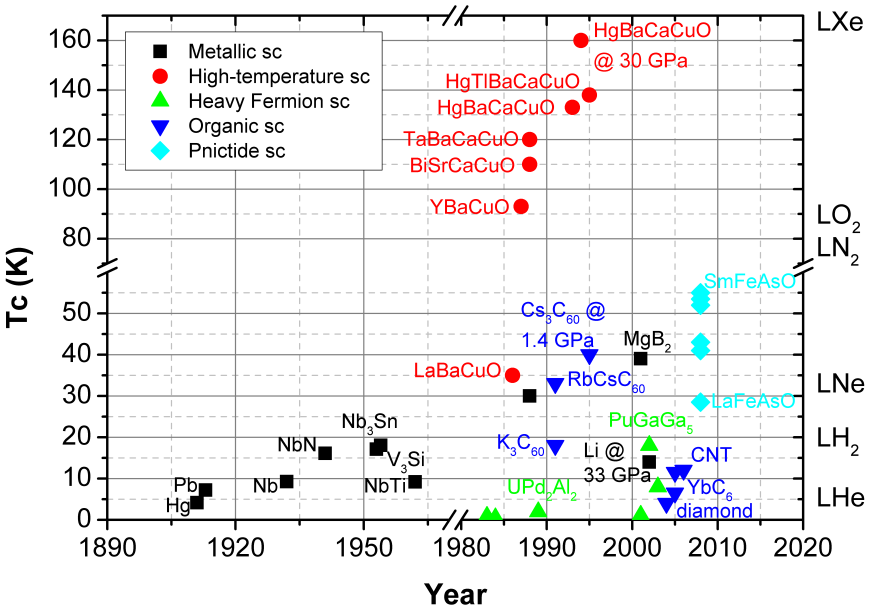

Figure 2.2.: Time of discovery and the transition temperature T_c of superconductors (sc). Note that not all data points are identified by their name.

The goal of material scientists working on HTS materials is to optimize the material such that it can easily be commercialized. One major problem of HTS materials is that they are ceramics. Their superconducting properties are governed by their micro and nanostructure. The challenge for material scientists was and actually is to understand how the micro and nanostructure influences physical properties like the current transport capability. Precise control of phase, grain, and defect formation in these materials is of crucial importance for any application. In order to become relevant for any type of energy technology like motors, generators, transformers, power transmission lines, and magnetic energy storage devices several requirements have to be fulfilled. Among these requirements are a high current transport capability, low AC and DC losses, decrease of the critical current density with increasing magnetic field strength, and

the ease and cost efficiency of industrial fabrication. A good review of materials and requirements is presented by Larbalestier et al. [46].

Currently, the rare earth barium copper oxides (ReBCO) like $YBa_2Cu_3O_{7-x}$ (YBCO) are in the focus of interest. In form of so-called second generation coated conductors, i.e. ReBCO material in thin films on flexible metal substrates they meet all requirements mentioned above. Fig. 2.3a shows a comparison of different superconductors at 4.2 K with respect to the decrease of the critical current density with increasing magnetic field. The outstanding benefit of YBCO is that it can carry a current density (j_c) of 10^5 A cm^{-2} at magnetic fields up to 30 T whereas the metallic superconductors show a strong decrease of j_c with increasing magnetic field. Only the bismuth strontium calcium copper oxides (BSCCO) compete with YBCO at 4.2 K. However, for applications at liquid nitrogen temperatures (Fig. 2.3b) the j_c of BSCCO decreases significantly due to thermally activated flux flow and cannot compete with YBCO anymore.

The superior properties of nano-engineered ReBCO coated conductors makes them to material of choice for any practical superconducting application at liquid nitrogen temperatures. The insertion of pinning relevant nano-particles such as $BaZrO_3$ (BZO) even increases the performance of ReBCO coated conductors in magnetic fields [47].

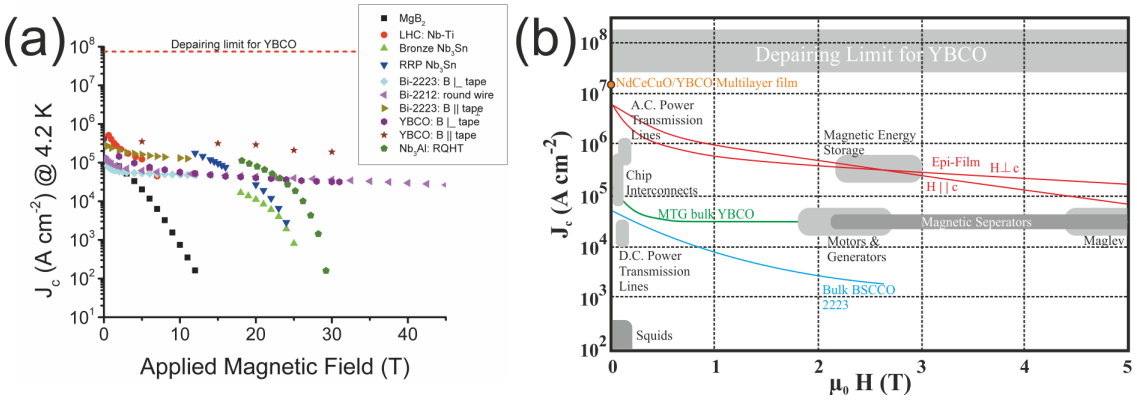

Figure 2.3.: Diagram showing the critical current density (j_c) as a function of the applied magnetic field at (a) 4.2 K for several superconducting materials [48] and (b) at 77 K plus possible applications [49]. Some abbreviations used in (b) were Maglev = Magnetically Levitated Train, MTG = Melt Textured Growth, and BSCCO 2223 = $Bi_2Sr_2Ca_2Cu_3O_{10}$.

2.2. Structural properties of YBCO and DyBCO

$DyBa_2Cu_3O_{7-x}$ (DyBCO) is related to $YBa_2Cu_3O_{7-x}$ (YBCO), i.e. the central Y atom is replaced by a Dy atom. Both are ceramic compounds having an orthorhombic symmetry in the superconducting state. The space group of DyBCO is Pmmm. However, this depends on the oxygen doping which will be discussed further down. Similar to YBCO the DyBCO unit cell consists of three c-axis stacked perovskite-like cells and has the Dy atom in its center as shown in Fig. 2.4. The only difference between a perovskite structure and the actual structure is the oxygen coordination. There is no octahedral oxygen coordination, only a pyramidal one, i.e. the central rare earth atom has no oxygen bonding. The result are CuO_2 planes acting as charge carrier reservoir. DyBCO has its superconducting transition at T_c = 92.1 K [51]. The Rare earth Barium Copper Oxide (REBCO) lattice parameters were determined using X-ray diffraction and a Rietveld refinement [52]. For YBCO they were a = 3.8178(1) Å, b = 3.8845(1) Å, and c = 11.6817(3) Å and for DyBCO a = 3.8244(1) Å, b = 3.8890(1) Å, and c = 11.6885(3) Å.

Similar to YBCO the superconducting property of DyBCO also depends on the oxygen concentration and the unit cell structure. By varying the oxygen partial pressure during the growth Jorgensen et al.

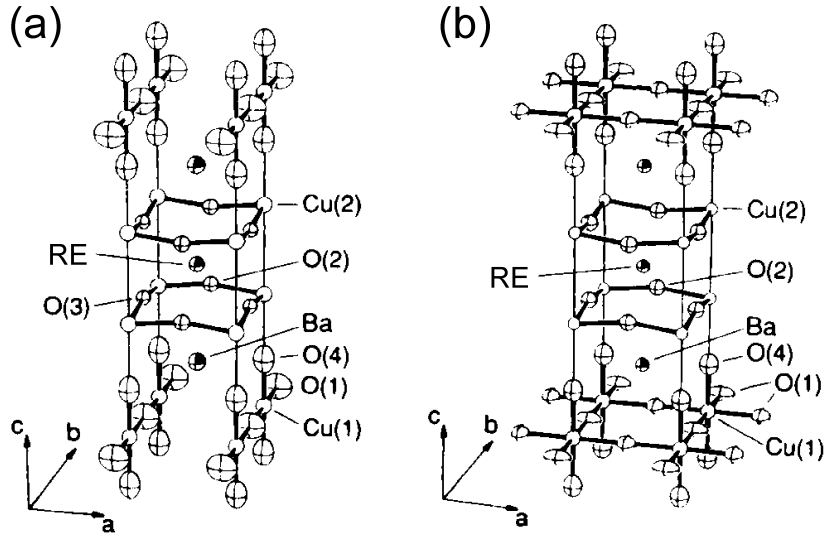

Figure 2.4.: Structure of $REBa_2Cu_3O_{7-x}$ (RE = Rare Earth: Y, Dy). (a) The superconducting orthorhombic Pmmm phase. (b) The antiferromagnetic tetragonal P4/mmm phase. Please note that in the tetragonal phase (b) the O(1) site is not fully occupied. [50]

[50] showed that YBCO has a structural phase transition from orthorhombic (space group Pmmm) to tetragonal (space group P4/mmm) depending on the oxygen deficiency δ ($0 \leq \delta \leq 1$). According with the structural phase transition there is also a transition between superconductor and anti-ferromagnetic insulator depending on oxygen content and temperature (see Fig. 2.14 in [32]). The transition point lies at δ = 0.65 as shown in Fig. 2.5. Extensive electron microscopic research has been done by van Tendeloo and Krekels on that particular issue [53]. They found out that the phase transition is due to the oxygen ordering on the CuO planes.

Within YBCO several secondary phases and crystal defects exist for example twin boundaries. Crystalline defects in YBCO had been thoroughly studied by Cai and Zhu [54]. Twin boundaries in the orthorhombic phase are responsible for the spot splitting in electron diffraction patterns. The amount of splitting determines the oxygen content. In ReBCO materials twins have two equivalent crystallographic directions ([110] and $[\bar{1}10]$). They form during growth to accommodate the strain energy of the tetragonal to orthorhombic phase transition.

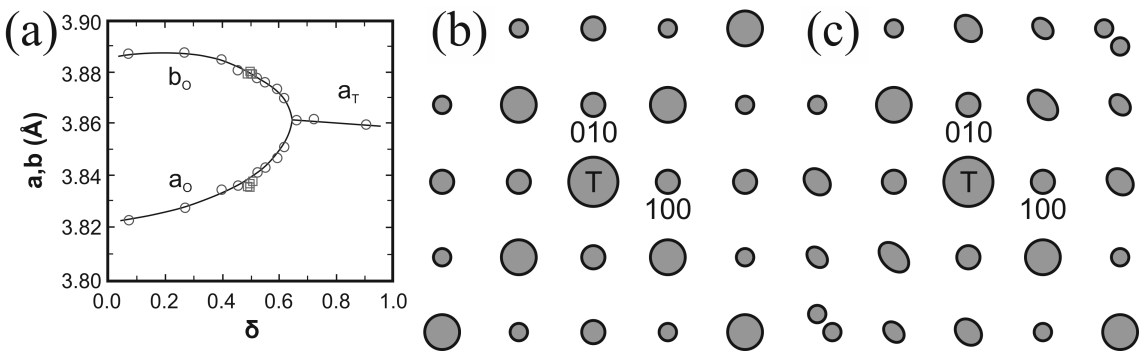

Figure 2.5.: (a) Phase transition due to oxygen doping [50]. Schematic electron diffraction pattern in the TEM (b) tetragonal and (c) orthorhombic phase.

2.3. Superconducting properties of ReBCO coated conductors

The London theory [38] assumed the density of superconducting particles, i.e. Cooper pairs, to be spatially constant. Therefore, only one type of superconductor should exist. However, this is not the case. Ginzburg and Landau [39] proposed in a phenomenological theory that superconductors can split up into two types: Type I and type II. They assumed that the phase transition from the normal to the superconducting state should be a phase transition of second order. The base of their theory was the definition of an order parameter $\Psi(\mathbf{r})$ for the superconducting phase. This order parameter has at T = 0 K a value of one and at T = T_c a value of zero. The absolute square $|\Psi(\mathbf{r})|^2$ is the density of superconducting particles. The important quantities they finally derived are the London penetration depth λ_L and the Ginzburg-Landau coherence length ξ_{GL}. Typical values of both parameters are listed in Tab. 2.2. The Ginzburg-Landau theory is only valid near T_c. However, both parameters (λ_L and ξ_{GL}) are important for the pinning behavior of crystalline defects. Both paramters λ_L and ξ_{GL} can be combined to a single one $\kappa = \lambda_L/\xi_{GL}$ also called as "Ginzburg-Landau parameter" [32]. If $\kappa \leq 1/\sqrt{2}$ the material is a type-I superconductor, whereas for $\kappa > 1/\sqrt{2}$ it is a type-II one.

Type-I superconductors try to shield the outer magnetic field until superconductivity breaks totally down at the thermodynamic critical field B_{cth}. The behavior of type-II superconductors is quite different. They act as type-I superconductors up to the first critical field B_{c1}. Then magnetic flux can enter into the superconductor in form of flux lines if the outer magnetic field is larger than B_{c1}. This creates a new state which is called mixed state, critical state, or Shubnikov phase. In magnetization curves this new state is also visible. These flux lines repel each other due to the Lorentz force and arrange themselves in a periodic structure called Abrikosov lattice. Normally, the Abrikosov lattice has a hexagonal closed packed structure offering the flux lines a maximum distance from each other. Superconductivity breaks also down for type-II superconductors if the outer magnetic field is larger than B_{c2}. Typical values for B_{c1} and B_{c2} are listed in Tab. 2.2. Most high-temperature superconductors are type-II superconductors.

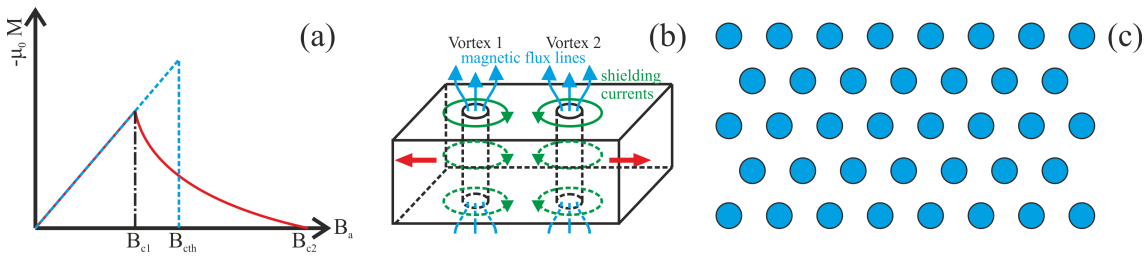

Figure 2.6.: (a) Schematic magnetization curve for superconductors of type I (dashed blue curve) and II (solid red curve). (b) Principle of flux line repulsion due to Lorentz force and (c) schematic arrangement of flux lines.

As shown above HTS materials have an orthorhombic structure. The consequence is that those materials cannot be treated as isotropic materials like for example Nb which has a base-centered cubic (bcc) unit cell. The effective electron mass m^* is significantly different for the (a,b)-plane and the c-axis direction of the material. Since the effective electron mass m^* enters in λ_L and ξ_{GL} superconducting properties are affected by this anisotropy (see Tab. 2.2). Fig. 2.7 shows the magnetic field dependence of the critical current density for $Bi_2Sr_2CaCu_2O_x$ (BSCCO) thin films. It can be seen that if the external magnetic field **B** is parallel to the c-axis, the critical current density drops significantly faster than if the external magnetic field is applied perpendicular to the c-axis. In ReBCO coated conductors this effect is also being present but less strong.

Parameter	Nb [55]	Nb_3Sn [55]	Nb-Ti [55]	MgB_2[56]	$Bi_2Sr_2Ca_2Cu_3O_{10}$ (BSCCO-2223) [55]	YBCO [55]
T_c [K]	9.2	18.3	9.5	39	110	92
λ [nm]	40	80	60		$200^{a,b}$, 1000^{c}	$150^{a,b}$, 600^{c}
ξ [nm]	38	3.5	45	2-10	$1.3^{a,b}$, 0.2^{c}	$1.5^{a,b}$, 0.4^{c}
B_{c2} [T]	0.2	24	14	2.5 - 32	$250^{a,b}$, 30^{c}	$150^{a,b}$, 40^{c}

Table 2.2.: Typical values for the most important superconducting materials. The index a,b denotes a quantity parallel the (a,b)-plane and the index c a quantity parallel the c-axis of the material.

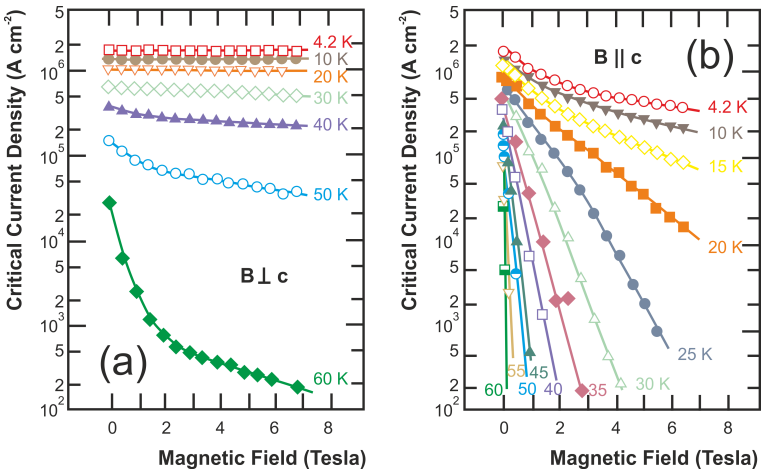

Figure 2.7.: Magnetic field dependence of the critical current density for the direction (a) **B** perpendicular to the c-axis and (b) **B** parallel to the c-axis of $Bi_2Sr_2CaCu_2O_x$ thin films [57].

2.4. Important superconductor issues for technical applications

2.4.1. Critical current density (j_c)

For technical superconductor applications one characteristic curve is of crucial importance: the I-V curve. From the shape of the I-V curve for example the flux pinning quality of the superconductor can be determined which is of great importance for technical applications. One should remember that the critical current density j_c is a function of temperature T and external magnetic field **B**. The critical current density j_c is reached if at a fixed external magnetic field **B** a voltage drop of 1 µV cm^{-2} is measured in the superconductor. The order of magnitude for j_c varies between 10^4 and 10^7 A cm^{-2}, i.e. a large range. There are three methods used in an industrial environment allowing to determine j_c:

1. Transport current measurements (resistive)
2. Cryoscan (inductive) [58]
3. Tapestar (inductive) [59]

Fig. 2.8a shows the setup for transport current measurements. It is just a four point measurement, but the most critical issue is that the contacts have to be stable enough to transmit several hundred Ampères into the superconducting tape. The measured data points will form an I-V-curve as shown in Fig. 2.8b and the critical current I_c will be reached per definition if the voltage exceeds 1 µV cm^{-2}. An important quantity of

such I-V curves as shown in Fig. 2.8b are the n-values. They describe the steepness of the curve, i.e. $\frac{U}{U_0} = \left(\frac{I_{meas}}{I_C}\right)^n$. The values of n range from $n = 1$ (ohmic conductor) to $n \to \infty$ (perfect superconductor). This relation can be derived, e.g. by modeling current distributions in imperfect samples and was proven over many years empirically [60]. A major drawback of this method is that the superconducting tape cannot be used for further applications. Thus, non-destructive contactless methods like Cryoscan or Tapestar for determining critical currents are needed.

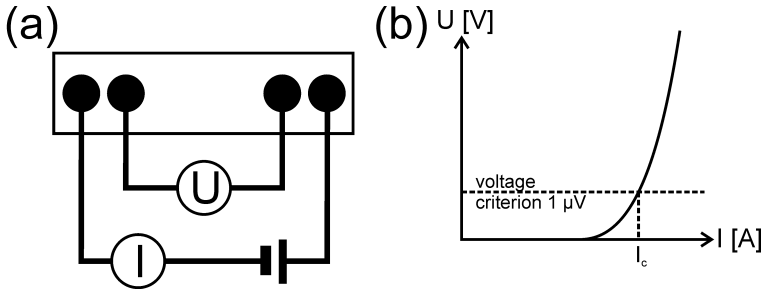

Figure 2.8.: (a) Setup for transport current measurements and (b) resulting I-V curve.

2.4.2. Current limitations

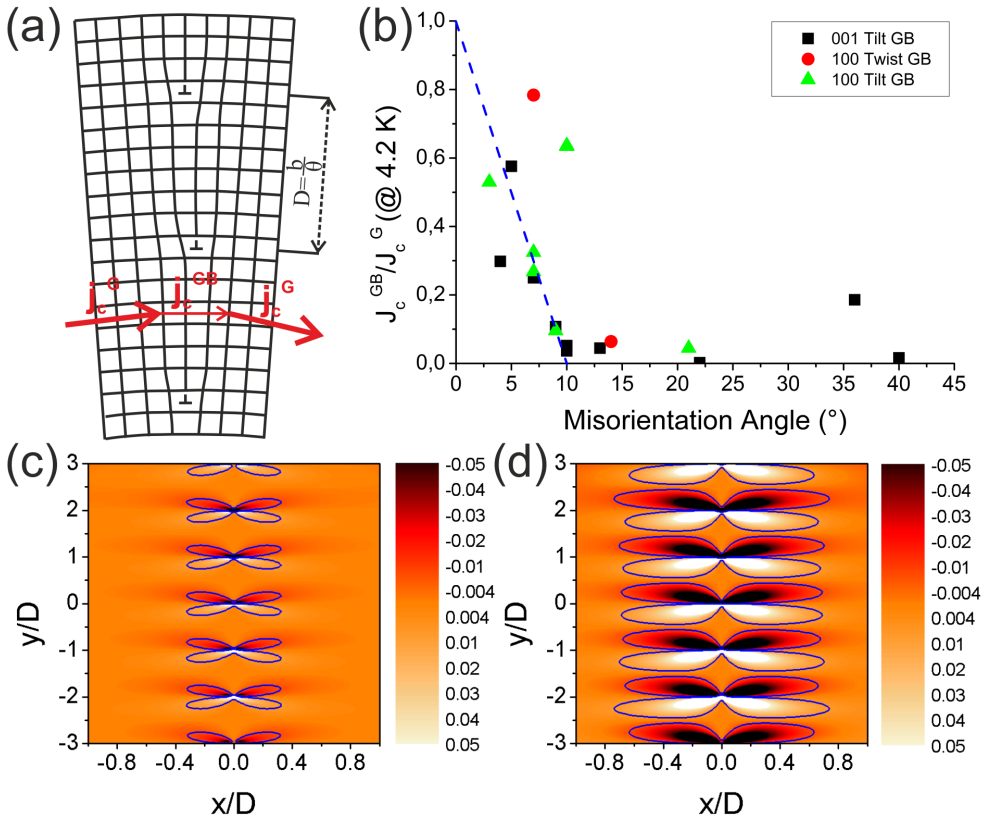

Figure 2.9.: (a) Schematic of a grain boundary consisting of single edge dislocations [61]. (b) Normalized critical current density as a function of the misorientation angle [62]. Calculated strain field ε_{xx} for an infinite array of edge dislocations at (c) 2° and (d) 10° tilt grain boundary. The solid blue line denotes the 1 % strain level.

Technical applications in energy technology require materials that can carry high currents at high magnetic fields [63]. Superconductors and especially coated conductors are able to fulfill these requirements. However, there are limitations depending on the material. There are four main limitations known:

1. Grain boundaries as weak links e.g. in YBCO
2. Thermal activated flux flow e.g. in BSCCO
3. Percolation e.g. in MgB_2
4. Depairing

Superconducting YBCO is a granular material. The current transport within YBCO grains is much larger than the current transport through YBCO grain boundaries as indicated in Fig. 2.9a. As shown by Chisholm and Pennycook [64] the critical current transported across a grain boundary strongly depends on the grain misorientation angle (Fig. 2.9b). They explain the physical origin of this behavior by the sensitivity of YBCO to the strain present at YBCO grain boundaries. Cava [65] explained the superconductivity in layered copper oxide superconductors like YBCO by doping the CuO_2 planes either by holes or electrons. Chisholm and Pennycook [64] stated if strain of only 1% is present at for example grain boundaries the charge reservoir, i.e. the copper oxide chains are disrupted and a significant volume around each dislocation core of the grain boundary is non-superconducting. For a 2° and a 10° tilt grain boundary this volume is indicated by a blue line (see Fig. 2.9c and d). The goal of coated conductor growth is to minimize the influence of grain boundary strain field effects on the critical current density.

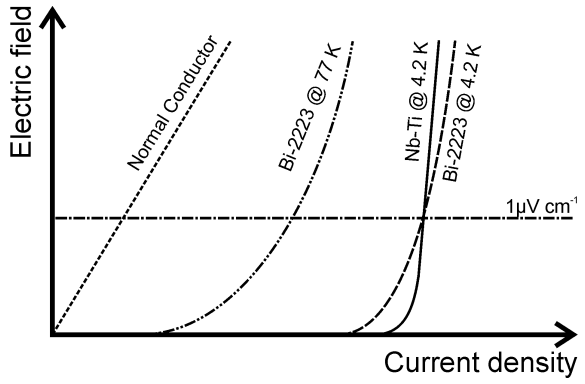

Figure 2.10.: Effect of flux flow resistance for BSSCO [66].

In type-II superconductors magnetic flux penetrates if the applied magnetic fields exceed B_{c1}. The Lorentz force acts on the magnetic flux lines if a transport current is flowing through the superconductor. It will move the flux lines since it is perpendicular to the transport current and the magnetic field. This process dissipates energy and yields a detectable resistance called "flux-creep resistance" or "flux-flow resistance" depending on the strength. Crystal defects that have a size in the order of the coherence length ξ create energetic favorable sites for the flux lines and "pin" them. The superconductor will be useless for practical issues if the pinning force is small. Fig. 2.10 shows the effect of thermally activated flux creep for BSCCO high-temperature superconductors. For 77 K the curve is almost near the ohmic one of a normal conductor.

Percolation is only of interest if the superconductor contains larger fractions of non-superconducting secondary phases as in the MgB_2 system.

The mechanism of depairing appears only at very high critical current densities ($j_{DP} > 10^7$- 10^8 A cm^{-2} [55]). Only at these current densities the self-field in the superconductor is strong enough to separate the Cooper pairs back into two individual electrons, i.e. the material becomes normal conducting. This phenomenon is rare because other current limitations are active at lower current densities.

2.5. Fabrication of second generation coated conductors

Actually there are three methods to fabricate second generation coated conductors. First there is Chemical Solution Deposition (CSD) on RABiTS substrates, second there is Inclined Substrate Deposition

(ISD) on non-magnetic, polycrystalline Hastelloy substrates, and third there is Ion Beam-Assisted Deposition (IBAD) on polycrystalline substrates [67, 68]. In general a coated conductor consists of a metallic substrate, one or more buffer layers, and the superconducting layer itself. Large angle grain boundaries in the superconductor hamper the current transport capability of the superconductor. Therefore, they have to be avoided, i.e. the superconductor needs to be biaxially textured. The three techniques mentioned before are able to achieve this by different methods. CSD and ISD will be explained in detail since the films analyzed here were grown by one of both methods.

2.5.1. CSD grown coated conductors on RABiTS substrates

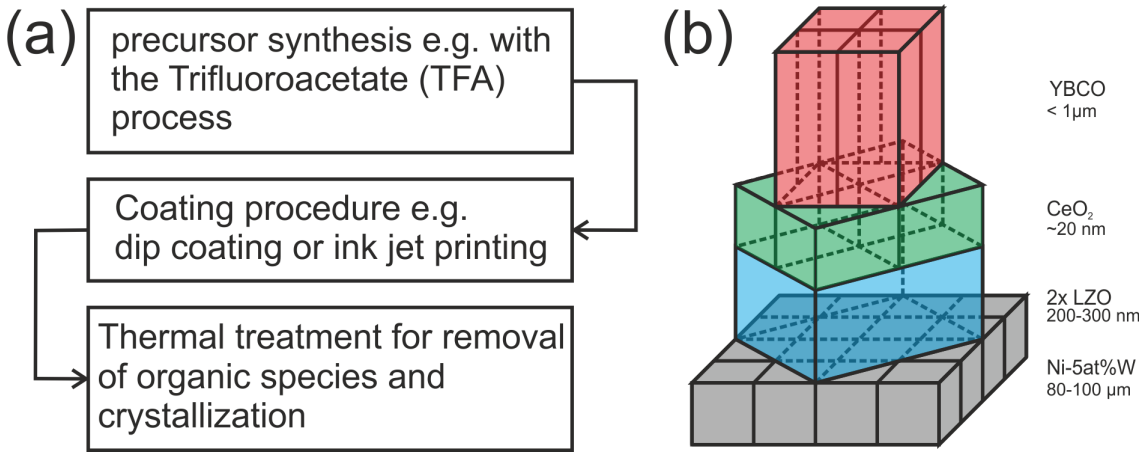

Figure 2.11.: (a) Schematics of the growth of CSD coated conductors. (b) Schematic layer structure and the orientation of each layer with respect to the substrate [69].

The basic RABiTS process was developed by Goyal et al. [70] in 1996 to obtain long lengths of flexible, biaxially oriented substrates with smooth, chemically compatible surfaces for epitaxial growth of high-temperature superconductors. The metal substrate production uses already well established, industrially scalable, thermomechanical processes to impart a strong biaxial texture to a base metal followed by vapor deposition of epitaxial buffer layers. Buffer layers can be ceramics and/or metals. The YBCO grows epitaxially on this kind of substrates yielding critical current densities exceeding 10^5 A cm^{-2} at 77 K in zero field and have field dependencies similar to epitaxial films on single crystal ceramic substrates.

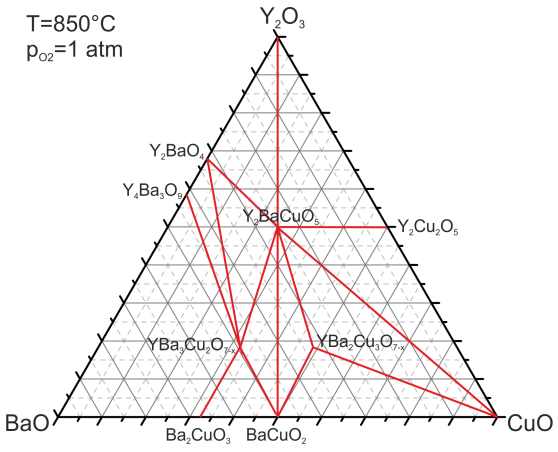

Figure 2.12.: Pseudoternary Y_2O_3-BaO-CuO phase diagram at typical CSD growth conditions [71].

The CSD approach for growing coated conductors is one of the most potentially economic approaches, since it includes inexpensive non-vacuum equipment, high deposition rates on large areas, and potentially near 100% utilization of the precursor material [72]. Furthermore, the production of CSD HTS tapes has the following advantages for commercial applications such as power cables or coils for magnets: high reproducibility, high production rate, high performance of j_c and I_C ($\geq$ 300 A/cm-width), long lengths (about 100-1000 m), and the fulfillment of mechanical and dimensional requirements [69]. However, RABiTS based coated conductors have a major drawback

for commercial applications: the Ni based substrate is magnetic, i.e. hysteretic losses are present during operation.

The starting point for the CSD coated conductor growth are the RABiT substrates on which buffer layers are grown. The exact steps to derive biaxially textured Ni substrates were for example shown by Specht et al. [73] or Eickemeyer et al. [74]. The CSD route chemically deposits layers, i.e. a precursor solution is needed. The basic steps for CSD are shown in Fig. 2.11a. They include (i) precusor synthesis for both buffer layer and superconductor, (ii) the substrate coating process by for example dip coating or ink jet printing, and (iii) the annealing step inside a tube furnace to remove the organic species and to crystallize each layer. Details of the CSD precursor process are listed by Knoth [69] for the buffer layer process and by Falter et al. [75] for YBCO TFA process. The resulting layer structure and the orientation of the single layers with respect to each other of the CSD process is schematically shown in Fig. 2.11. Therein also typical layer thicknesses are provided. The CSD technology or at least modified versions seem still to be used as quoted in chapter 11.5 in [76].

CSD processed YBCO coated conductors contain due to their complicated growth a bunch of secondary phases. These secondary phases are remains of incomplete reacted educts. PVD grown samples do not show this great variety of secondary phases since the chemistry during the growth can be better controlled. Fig. 2.12 shows a pseudoternary Y_2O_3-BaO-CuO phase diagram at typical CSD growth conditions. The thermodynamically allowed phases are indicated within the phase diagram.

2.5.2. ISD grown coated conductors on Hastelloy substrates

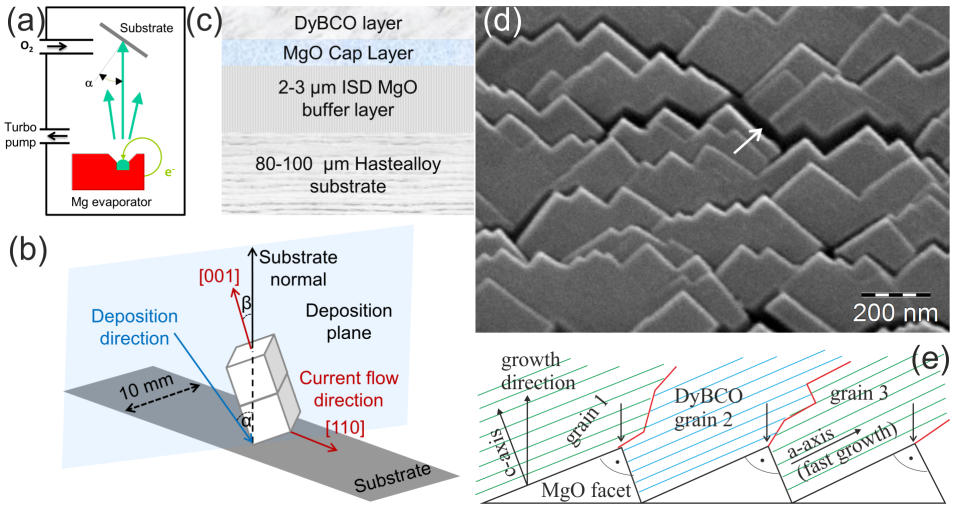

Figure 2.13.: (a) Growth principle of ISD coated conductors [77]. (b) ISD growth geometry [Quelle Theva] and (c) schematic layer structure. (d) ISD MgO surface. (e) Orientation relation of buffer layer with the superconductor.

Another promising method to long length biaxially textured superconductors is the ISD method [78, 77]. It is used to deposit the MgO buffer layer on polycrystalline Hastelloy substrates by e-beam evaporation. The Hastelloy substrate is tilted by an angle α towards the incoming MgO vapor as schematically shown in Fig. 2.13a. This forces the MgO to grow in columns with [001] axis tilted by an angle β with respect to the substrate normal. The deposition direction vector, the MgO [001] vector, and the substrate normal all lie in one plane, the deposition plane as can be seen from Fig. 2.13b. The angles α and β are not equal but related to each other. In the past some research on this particular issue was done for example by Bauer et al. [78] or Xu et al. [79]. During the MgO growth process the MgO crystallites orient themselves such that only [001] oriented crystals survive. This happens in the first few hundred nm of film thickness due to surface energy and shadowing. Typical ISD layers have thickness of two to three microns and

consist of 100 nm wide, [001] oriented MgO columns that are divided by voids. Some of the voids can be seen by SEM as cracks on the ISD MgO surface (look at the white arrow in Fig. 2.13d). The surface of the ISD buffer layer has roof-tile-like structure as can be seen in Fig. 2.13d. Normally, the next step is to close the cracks of the MgO surface to achieve a better orientation of the superconductor. Therefore, the substrate is tilted back into normal condition, i.e. vapor incidence along the substrate normal and an additional several 100 nm thick MgO layer is deposited at elevated temperatures. This yields a dense, sharply roof-tile-like structured MgO surface. Afterwards, the superconducting layer is grown on top of MgO layers. The MgO facets will force the superconductor to grow in c-axis orientation and forming small-angle grain boundaries between single superconductor grains as schematically shown in Fig. 2.13e. The grain boundaries are tilted because the a-axes grow faster than the c-axes. The result is a curved and inclined grain boundary as shown in Fig. 2.13e.

The striking benefit of this method is that it uses a non-magnetic, poly-crystalline Hastelloy substrate minimizing AC losses and its simple layer structure compared to the IBAD method. Also, no extensive substrate treatment is needed in order to biaxially texture the substrate as for RABiTS substrates or an assisting ion beam as needed for IBAD increasing the production costs. However, as in any vapor deposition technique a vacuum needs to be maintained around the deposition area; otherwise the method would not work unlike the CSD method described above. This can be seen as the only drawback of the method increasing process costs. It can be also easily upscaled to large superconducting single film thicknesses reaching up to 8 µm [80]. These films are able to carry currents exceeding 1000 A/cm. It can be also upscaled to reach long tape lengths. Prusseit et al. [81] already reported lengths up to 40 m back in 2006. A further increase to more than 100 m was also scheduled for 2006 in [81]. The only method yielding similar values is IBAD. Values of 300 A/cm transported over a tape length of 600 m at 77 K in self-field were reported for IBAD samples [82].

Part II.

Simulation of elastic and inelastic electron scattering

3. Electron scattering and X-ray generation in coated conductor related materials

3.1. Introduction

Application relevant second-generation (2G) coated conductor tapes have to carry high critical currents I_c. The amount of total current carried by a "perfect" tape depends on the film thickness and the film roughness of the superconducting layer. In Rolling-Assisted Biaxially Textured Substrate (RABiTS) coated conductors for example the film thickness is limited by fundamental issues of the growth process [83], e.g. a-axis growth and porosity leading to a dead layer. In chemical solution deposited coated conductors the surface roughness is an inherent problem of the growth method crucially affecting the amount of current being carried by a tape. Therefore, thickness and roughness control of the superconducting layers is of utmost importance for coated conductors grown by this technique. In contrast, the I_c capacity of coated conductors grown by the Inclined Substrate Deposition Technique (ISD) is neither affected by the surface roughness nor a dead layer nor porosity since none of these problems exist in ISD coated conductors [84]. However, it is necessary to control the thickness of the buffer layers since they are generating the biaxial texturing in dependence on the layer thickness.

Ideally, thickness and roughness quantification should be done in-situ and destruction-free directly after the film growth with a high spatial accuracy. Energy-dispersive X-ray (EDX) analysis the method of choice to do this and was not used for this purpose so far. The amount of X-ray quanta leaving the film surface towards the detector is determined by the film thickness. The surface roughness strongly affects this depending on the acquisition conditions especially at low energies.

Since 2G coated conductors have non-trivial layer geometries, a profound understanding of X-ray generation and transport in the single layers is hard to achieve. Monte Carlo simulation programs like DTSA-II [85] dealing with electron transport in solids are also capable to simulate X-ray transport. They offer the unique possibility to study on an idealized model structure both electron and X-ray transport and to set up the right acquisition conditions for the experiment. Moreover, the combination with the experiment also offers the possibility to explain electron and X-ray transport in the real material and finally to set up a X-ray count-thickness relation.

Understanding the theoretical basis of DTSA-II means in particular understanding the Bethe theory [27]. However, the theory of the Monte Carlo algorithm, ionization cross sections, characteristic X-ray radiation, Bremsstrahlung, X-ray absorption, and stopping power is filling books. Therefore, a theory section summarizing these issues is integrated into this chapter. A list of files where the single functions of DTSA-II are implemented in the EPQ library is given in the appendix.

3.2. Theoretical considerations

3.2.1. The Monte Carlo Method

The basis of all calculations is the Monte Carlo method as described in D.C. Joy's book [86] and in Scott and Love's book [87]. The following paragraphs summarize the fundamental issues of the Monte Carlo method. The first step is to choose the starting energy, the starting position, and the starting direction of a

primary electron. Then a first random number $RND1$ ($RND1 \in [0, 1]$) is generated and the elastic mean free path λ is calculated to determine the distance s between two elastic scattering events.

$$s = -\lambda \ln(RND1) \tag{3.1}$$

Next the two scattering angles φ and Ψ necessary for a three-dimensional simulation need to be calculated. For Ψ, the azimuthal scattering angle the expression is

$$\Psi = 2\pi RND2 \tag{3.2}$$

with $RND2 \in [0, 1]$. For the deflecting angle φ the situation is more complicated since both the differential σ' and the total elastic cross section σ are involved. Both are needed to describe the scattering probability of an electron into the angle φ. For simplicity the Rutherford cross section can be used but for more sophisticated models Mott cross sections should be used since they yield higher accuracy. The calculation of φ with a random number $RND3$ ($RND3 \in [0, 1]$) is done as follows

$$RND3 = \int_0^{2\pi} \int_0^{\phi} \frac{\sigma'(\phi)}{\sigma} \sin\phi \, d\phi d\Psi \tag{3.3}$$

After completing the scattering events the new coordinates and the energy-loss of the primary electron have to be calculated. Details are given in the stopping power paragraph. The last step is to replace the old coordinates by the new ones and repeat the steps described above as long as the energy of the primary electron is larger than some certain threshold value (e.g. 50 eV).

DTSA-II simulates electron trajectories and can also model the generation of characteristic X-ray radiation and Bremsstrahlung and their transport through solids. The intensity of the characteristic radiation $dI_{i,A}$ and the Bremsstrahlung $dI_{B,A}$ per unit length ds for element A are calculated according to [85]

$$\frac{dI_{i,A}}{ds} = F_A \, p_{i,A} \, Q_A(E) \tag{3.4}$$

$$\frac{dI_{B,A}}{ds} = F_A \, Q_{B,A}(E) \tag{3.5}$$

where F_A is material dependent factor, $p_{i,A}$ is the probability that the excited atom will use the i'th allowed transition for relaxation, $Q_A(E)$ is the characteristic ionization cross section for the atomic shell for which transition i is allowed and $Q_{B,A}(E)$ is the total Bremsstrahlung cross section for element A. Both $Q_A(E)$ and $Q_{B,A}(E)$ depend on the primary electron energy E.

3.2.2. Calculation of ionization cross sections

DTSA-II includes two models for choosing the characteristic ionization cross section: (1) The semi-empirical K-shell ionization cross section of Casnati et al. [88] and (2) a more sophisticated analytical formula for K, L and M ionization cross sections from Bote et al. [89] based upon distorted-wave and plane-wave Born calculations. Model (1) fits an exponential curve to experimental values using that the ionization cross section vs. ionization energy per Rydberg energy is linear on a bilogarithmic scale. Their final result is Eq. 3.6. Model (2) in equation Eq. 3.7 is an analytical expression dependent on the

overvoltage ratio U and 5 parameters (a_1, a_2, a_3, a_4, a_5). The values of the 5 parameters were obtained by least-square fitting of the cross sections to a numerical database. The values are listed for atomic numbers Z=1-99 in 1 within [89] and are included also in DTSA-II.

$$\sigma_K = n_K a_0^2 \xi \left(\frac{R}{E_K}\right)^2 \left(\frac{E_K}{R}\right)^{-0.0318+\frac{0.3160}{U}-\frac{0.1135}{U^2}} \times \left[10.57 \exp\left(-\frac{1.736}{U}+\frac{0.317}{U^2}\right)\right] \frac{\ln U}{U} \tag{3.6}$$

$$\sigma = 4\pi a_0 \frac{U-1}{U}\left(a_1 + a_2 U + \frac{a_3}{1+U} + \frac{a_4}{(1+U)^3} + \frac{a_5}{(1+U)^5}\right) \tag{3.7}$$

where a_0 is the Bohr radius, n_K is the number of electrons in the K-shell, ξ is a relativistic correction factor dependent on the over voltage ratio U and the ionization energy E_K, and R is the Rydberg energy.

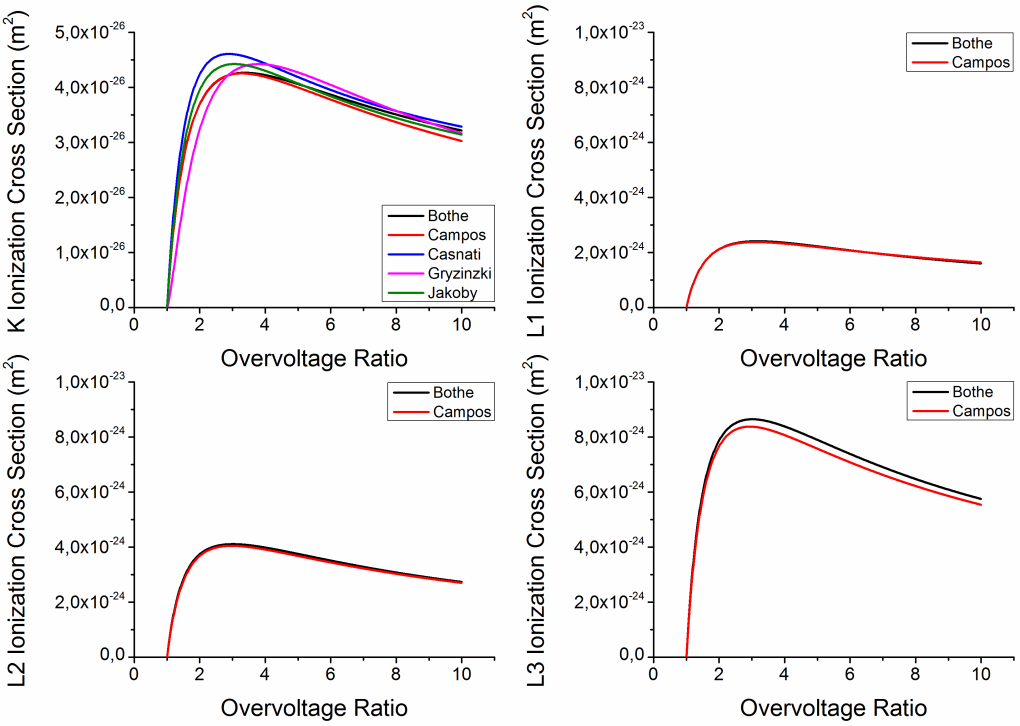

Figure 3.1.: K and L shell ionization cross sections for Cu as function of the overvoltage ratio for the different models [89, 90, 88, 91, 92, 93].

3.2.3. X-ray emission, fluorescence yield, and depth distribution of X-rays

After having introduced the ionization cross section it is necessary to discuss the probability of X-ray emission, i.e. the fluorescence yields. In scanning electron microscopy (SEM) mainly two emission processes are dominant (1) Auger electron emission and (2) X-ray photon emission. Both processes depend on the atomic number Z. The dominating process for small atomic numbers Z is Auger electron production whereas it is X-ray production for large Z. In DTSA-II several tables for K, L and M X-ray fluorescence yields are included. For the K-shell following references were found: [94, 95, 96, 97, 98].

For L-shell fluorescence two papers could be identified [99, 94] and for M-shells only [100] is available up to present time.

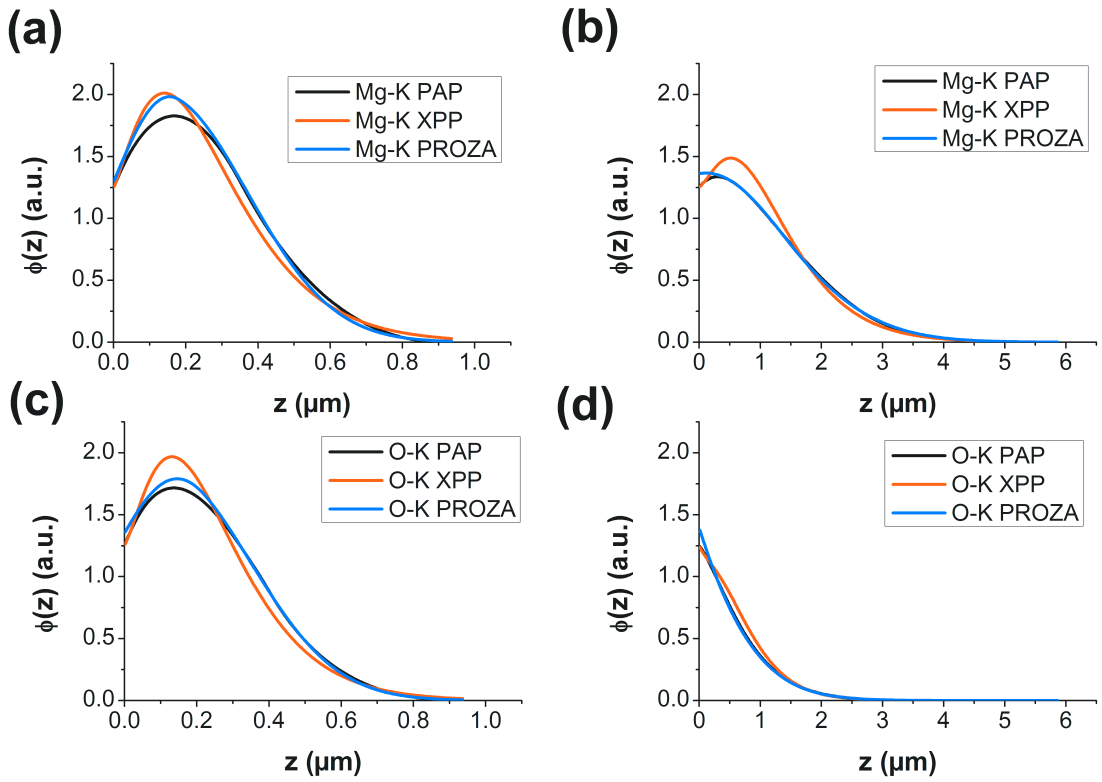

Figure 3.2.: MgO bulk depth distribution curves of emitted X-rays in MgO ($\rho = 3.58\ \frac{g}{cm^3}$) calculated for 3 different models with DTSA-II. Primary energies for Mg-K were (a) 10 keV and (b) 30 keV. In (c) and (d) the same is shown for O-K.

$\varphi(\rho z)$ curves, i.e. the depth distribution of X-rays within a sample of density ρ are one approach to calculate the generated X-ray intensity in quantitative X-ray microanalysis. $\varphi(\rho z)$ curves can be determined experimentally for example via the tracer method [101]. These experimental measurements were the basis of several models implemented within DTSA-II namely PAP, XPP [102], and PROZA96 [103, 104]. Monte Carlo modeled $\varphi(\rho z)$ curves were extensively used in the ZAF method [87] but they are also essential for understanding X-ray intensity vs. thickness calibration curves. Fig. 3.2 shows the three models in comparison for a bulk MgO sample simulated for the Mg-K and O-K line with 10 keV and 30 keV primary electron energy, respectively. Deviations up to about 15% between the single models can be observed, e.g. in Fig. 3.2c. They occur in the region of the maximum of the $\varphi(\rho z)$ function and are attributed to deviations in the modeling of backscattered electrons emerging from deeper sample regions being responsible for this surface ionization maximum. In deeper sample regions the curves of all three models are close to each other. For thin film simulations the surface ionization region in the $\varphi(\rho z)$ curves is the relevant region. Deviations are expected especially for compositions with large differences in the mean atomic number and for film thicknesses below 100 nm.

3.2.4. X-ray absorption

Material	X-ray line	Energy [keV]	t_{crit} [µm]
MgO	O-K	0.525	0.78
	Mg-K	1.254	2.12
DyBCO	Ba-L	4.466	0.27
	Cu-K	8.048	4.39
	O-K	0.525	6.53
LZO	O-K	0.525	0.23
	Zr-L	2.042	1.03
	La-L	4.651	4.68

Table 3.1.: Critical absorption lengths for different X-ray lines in MgO, DyBCO and LZO calculated according to the database of Chantler [105].

However, $\varphi(\rho z)$ curves themselves only describe the amount of generated X-rays in a certain depth. X-ray absorption within the sample decreases the number of X-rays emerging from the sample and being finally detected. Absorption in general is described by the Lambert-Beer law

$$I = I_0 e^{-\mu t} = I_0 e^{-\frac{\mu}{\rho}\rho t} \tag{3.8}$$

$$t_{crit} = \frac{1}{\mu} \tag{3.9}$$

where I_0 is the initial intensity, I is the final intensity after a distance t through a material, μ is the linear attenuation coefficient, $\frac{\mu}{\rho}$ is the mass absorption coefficient, and ρ is the mass density. Values for the mass attenuation coefficients are available for example in Zschornack's book [106] or in Chantler's database [105]. DTSA-II uses Chantler's values. Critical absorption lengths t_{crit} can be defined as shown in Eq. 3.9. It determines the maximum film thickness that can be detected by EDX. Tab. 3.1 shows values relevant for this work calculated from Zschornack's book.

3.2.5. Stopping power

As introduced in the Monte Carlo paragraphs primary electrons undergo inelastic scattering events i.e. they lose part of their energy. The stopping power is a quantity describing how much energy an electron loses per unit length when traveling through a solid. Bethe [27] first made a theoretical description of the problem. However, his formula is only correct for energies larger than at least 1 keV; below that energy Bethe's model fails. Joy and Luo [107] modified the Bethe model to overcome this problem. They derived for the non-relativistic case

$$\frac{dE}{ds} = \frac{2\pi e^4 N Z}{E} \ln\left(\sqrt{\frac{\varepsilon}{2}}\frac{E+kJ}{J}\right) \tag{3.10}$$

where e is the elementary charge, N is the number of atoms per (unit) volume, Z is the atomic number, E is the primary electron energy, $\varepsilon = 2.71828...$ (Euler's number), k is a material dependent constant, and J is the mean ionization potential. The square root term considers the indistinguishability of electrons [108]. DTSA-II includes several datasets of J [109, 110, 111, 112, 113, 114]. Joy and Luo's formula with tabulated values of J from Seltzer and Berger were used by default in DTSA-II. The implementation in DTSA-II is provided in the following program listing:

```
1  package gov.nist.microanalysis.EPQLibrary;
2  import java.util.Arrays;
3  import java.util.List;
4  import java.util.Random;
5  /**
6  <p> This class provides various different implementations for the electron energy loss
       expression in the form first described by Bethe. The units of the result of compute are
       energy/length or Joules/meter </p>
7  <p> Copyright: Pursuant to title 17 Section 105 of the United States Code this software is not
        subject to copyright protection and is in the public domain </p>
```

```
8  <p> Institution: National Institute of Standards and Technology </p>
9  @author Nicholas W. M. Ritchie
10 @version 1.0  */
11
12 abstract public class BetheElectronEnergyLoss extends AlgorithmClass
13 {
14         private static final AlgorithmClass[] mAllImplementations =
15         {
16                 BetheElectronEnergyLoss.Bethe1930,
17                 BetheElectronEnergyLoss.Bethe1930Strict,
18                 BetheElectronEnergyLoss.JoyLuo1989
19         };
20
21         /** Constructs a BetheElectronEnergyLoss */
22         protected BetheElectronEnergyLoss(String name, Reference ref)
23         {
24                 super("Stopping power", name, ref);
25         }
26
27         @Override
28         public List<AlgorithmClass> getAllImplementations()
29         {
30                 return Arrays.asList(mAllImplementations);
31         }
32
33         @Override
34         protected void initializeDefaultStrategy()
35         {
36                 addDefaultAlgorithm(MeanIonizationPotential.class,
37                 MeanIonizationPotential.Berger83);
38         }
39
40         /** compute - Computes dE/ds in Joules/meter per kg/meter^3
41         @param elm An element
42         @param eB The electron energy (in Joules)
43         @return dE/ds in Joules per meter per kg/meter^3
44         */
45         abstract public double compute(Element elm, double eB);
46
47         /** JoyLuo1989 - Joy & Luo's modification to the Bethe expression to improve the
               applicability at low-beam energies. (As described in Scanning Electron Microscopy
               and X-ray Microanalysis (3rd edition))     */
48
49         static public class JoyLuoBetheElectronEnergyLoss extends BetheElectronEnergyLoss
50         {
51                 // Some minor caching optimizations
52                 transient private final double[] mK = new double[Element.elmEndOfElements];
53                 JoyLuoBetheElectronEnergyLoss()
54                 {
55                         super("Joy-Luo", Reference.Goldstein);
56                         for(int z = Element.elmH; z < Element.elmEndOfElements; ++z)
                                                                mK[z] = 0.731 + 0.0688 * Math.
                               log10(z);
57                 }
58
59                 private final double K = -(785 * ToSI.EV * Math.pow(ToSI.CM, 3.0)) / (ToSI.
                       ANGSTROM * ToSI.GRAM);
60
61                 @Override
62                 public double compute(Element el, double eB)
63                 {
64                         final int z = el.getAtomicNumber();
65                         final MeanIonizationPotential mip = (MeanIonizationPotential)
                               getAlgorithm(MeanIonizationPotential.class);
66                         final double j = mip.compute(el);
67                         final double j_star = j / (1.0 + (mK[z] * j / eB));
68                         return ((K * z) / (el.getAtomicWeight() * FromSI.eV(eB))) * Math.log
                               ((1.166 * eB) / j_star);
69                 }
70     };
71
72     static public BetheElectronEnergyLoss JoyLuo1989 = new JoyLuoBetheElectronEnergyLoss();
73
```

```
74          /** Bethe1930 - The original expression of Bethe for the stopping power  adjusted so
                that even when the electron energy falls below about J/1.166, the electron
                continues to decelerate (albeit slowly). */
75          static public class Bethe30ModElectronEnergyLoss        extends BetheElectronEnergyLoss
76          {
77                  Bethe30ModElectronEnergyLoss()
78                  {
79                          super("Bethe(Modified)", new Reference.CrudeReference("Bethe H. Ann.
                                Phys. (Leipzig) 1930; 5: 325"));
80                  }
81                  private final double K = -(785 * ToSI.EV * Math.pow(ToSI.CM, 3.0)) / (ToSI.
                        ANGSTROM * ToSI.GRAM);
82
83                  @Override
84                  public double compute(Element el, double eB)
85                  {
86                          final MeanIonizationPotential mip = (MeanIonizationPotential)
                                getAlgorithm(MeanIonizationPotential.class);
87                          final double e_eV = FromSI.eV(eB);
88                          final double j = FromSI.eV(mip.compute(el));
89                          double f = 1.166 * e_eV / j;
90                          // The low energy modification...
91                          if(f < 1.1)
92                                  f = 1.1;
93                          return ((K * el.getAtomicNumber()) / (el.getAtomicWeight() * e_eV)) *
                                Math.log(f);
94                  }
95          }
96
97          static public final BetheElectronEnergyLoss Bethe1930 = new
                Bethe30ModElectronEnergyLoss();
98
99          /** Bethe1930Strict - The original expression of Bethe for the stopping power. Below
                eB = J/1.166 the energy loss goes positive (the electron shows  unphysical
                acceleration.) */
100         static public class Bethe30ElectronEnergyLoss extends BetheElectronEnergyLoss
101         {
102                 Bethe30ElectronEnergyLoss()
103                 {
104                         super("Bethe", new Reference.CrudeReference("Bethe H. Ann. Phys. (
                                Leipzig) 1930; 5: 325"));
105                 }
106
107                 private final double K = -(785 * ToSI.EV * Math.pow(ToSI.CM, 3.0)) / (ToSI.
                        ANGSTROM * ToSI.GRAM);
108
109                 @Override
110                 public double compute(Element el, double eB)
111                 {
112                         final MeanIonizationPotential mip = (MeanIonizationPotential)
                                getAlgorithm(MeanIonizationPotential.class);
113                         final double e_eV = FromSI.eV(eB);
114                         final double j = FromSI.eV(mip.compute(el));
115                         final double f = 1.166 * e_eV / j;
116                         return ((K * el.getAtomicNumber()) / (el.getAtomicWeight() * e_eV)) *
                                Math.log(f);
117                 }
118         }
119
120         static public BetheElectronEnergyLoss Bethe1930Strict = new Bethe30ElectronEnergyLoss
                ();
121
122         /**
123         <p> Modifies an existing BetheElectronEnergyLoss model to add variation in the amount
                of energy lost per step. The class takes the nominal energy loss  and modifies it
                by a certain randomized fractional amount to emulate the way sometimes an electron
                 may loose slightly more than average or slightly less than average. </p>
124         <p> Copyright: Pursuant to title 17 Section 105 of the United States Code this
                software is not subject to copyright protection and is in the public domain </p>
125         <p> Institution: National Institute of Standards and Technology </p>
126         @author nritchie
127         @version 1.0 */
128         static public class StragglingModified extends BetheElectronEnergyLoss
```

```
129         {
130                 private final BetheElectronEnergyLoss mBethe;
131                 private final double mPercent;
132                 private final Random mRandom;
133
134                 public StragglingModified(BetheElectronEnergyLoss base, double percent)
135                 {
136                         super("Straggling[" + base.getName() + "]", base.getReferenceObj());
137                         mBethe = base;
138                         mPercent = percent;
139                         mRandom = new Random();
140                 }
141
142                 @Override
143                 public double compute(Element elm, double eB)
144                 {
145                         final double bee = mBethe.compute(elm, eB);
146                         return Math.min(0.0, bee * (1.0 + mRandom.nextGaussian() * mPercent));
147                 }
148         }
149 }
```

3.3. Experimental

3.3.1. Thin film investigation

Coated conductor thin films were investigated with respect to their film thickness by EDX. Monte Carlo simulations were performed to understand electron transport in each layer of the coated conductors, to choose optimal acquisition conditions, and to predict layer thicknesses.

Sample series	Acceleration voltage [kV]	Acquisition time [s]
LZO	10, 20, 30	200
YBCO	20	200
MgO	10, 30	60, 200
DyBCO	30	50

Table 3.2.: Experimental acquisition parameters for each sample series.

Experiments were carried out in a Jeol 6500F field emission SEM equipped with an Oxford Pentafet EDX detector. Four sample types namely $La_2Zr_2O_7$ (LZO) buffer layers on RABiTS, YBCO grown on LZO buffered Ni substrates (RABiTS), ISD-deposited MgO buffer layers on Hastelloy substrates, and MgO buffered $DyBa_2Cu_3O_{7-x}$ (DyBCO) layers on Hastelloy substrates were analyzed. These four types can be divided into two classes: (i) Films grown by Chemical Solution Deposition (CSD) and (ii) films grown by Physical Vapor Deposition (PVD). Acquisition details are listed in Tab. 3.2. Cross-sectional SEM samples were prepared by the Focused Ion Beam (FIB) method. Transmission Electron Microscope (TEM) cross-sectional images were acquired with an analytical Zeiss 912Ω TEM.

Descriptions of CSD film growth can be found for LZO in [115] and for YBCO in (Falter et al., 2003). For the PVD case further information about the growth processes can be found in case of the ISD MgO in [116] and for the DyBCO in [117].

3.3.2. EDX setup and spectrum acquisition

Four LZO samples were analyzed by EDX analysis in the SEM using three electron primary energies (10, 20, and 30 keV). Sample details are listed in Tab. 3.3. With the same parameters Monte Carlo simulations were carried out for all four samples. From the EDX spectra net counts per nA of Zr-$L_{\alpha 1}$ and La-$L_{\alpha 1}$ were extracted and plotted vs. the LZO film thickness. The amount of X-ray counts measured in EDX spectra is proportional to the film thickness if the composition is assumed to be constant. A

Sample	Growth method	Buffer Layer thickness [nm]	Superconducting Layer thickness [nm]	Measurement method
LZO1	CSD	80	–	TEM
LZO2	CSD	134	–	Ellipsometry
LZO3	CSD	252	–	TEM
LZO4	CSD	325	–	TEM
MgO1	PVD	100	–	Nominal
MgO2	PVD	200	–	Nominal
MgO3	PVD	400	–	Nominal
MgO4	PVD	800	–	Nominal
MgO5	PVD	1000	–	Nominal
MgO6	PVD	1600	–	Nominal
MgO7	PVD	2000	–	Nominal
MgO8	PVD	3000	–	Nominal
MgO9	PVD	5000	–	Nominal
DyBCO1	PVD	2500	330	Nominal
DyBCO2	PVD	2200	500	Nominal

Table 3.3.: Sample details: Sample name, growth method, layer thicknesses, and their method of determination.

similar procedure was applied on the nine ISD MgO thin films listed in Tab. 3.3 using Mg-K and O-K net counts per nA. Here only 30 keV electrons were used for both experiment and simulation. For the roughness determination in MgO films 10 and 30 keV primary electron energies were used at different sample tilting angles. EDX spectra were acquired for each electron primary energy and tilting angle. Afterwards they were compared to Monte Carlo simulation results.

From experimental EDX point spectra in YBCO acquired at 20 keV primary energy Ba-L and Cu-K peak counts were extracted, normalized to the current, and plotted against each other to document the influence of YBCO roughness on EDX spectra. For a series of increasing YBCO thicknesses EDX spectra were simulated using the same acquisition conditions as in the experiment. YBCO thicknesses ranging from 25 to 500 nm were simulated. Cu-Kα net counts were extracted and plotted vs. YBCO film thickness to obtain a calibration curve. Afterwards, the simulated values were compared to experimentally determined thickness values.

A similar procedure as in the YBCO was applied on MgO buffered DyBCO thin films using 30 keV primary electrons. Sample details are summarized in Tab. 3.3. From experimental EDX point spectra in DyBCO Ba-L and Cu-K normalized peak counts were extracted and plotted into a correlation diagram. For determining the DyBCO film thickness EDX spectra of DyBCO thin films with thicknesses ranging from 100 nm to 1000 nm were simulated. From there Ba-$L_{\alpha 1}$, Dy-$L_{\alpha 1}$ and Cu-K_{α} net counts per nA were extracted and compared to experimentally obtained values.

3.3.3. EDX spectrum simulation

Simulation of EDX spectra was carried out using DTSA-II. However, some detector properties especially detector crystal parameters were not known exactly and thus the standard values provided by DTSA-II were used. Simulated spectra normally did not yield the same number of X-ray counts as experimental ones. Therefore, experimental and simulated spectra were scaled such that their integral counts were equivalent. The fitting error was estimated using a χ^2 method as described for example in [118].

Thickness calibration curves were obtained by using the following functions to fit the data by least square fitting:

$$y = f(x) = m \cdot x + c \tag{3.11}$$

$$y = f(x) = b_1 \left[1 - \exp\left(-\frac{x - b_2}{b_3} \right) \right] \tag{3.12}$$

m, c, b_1, b_2, and b_3 are fitting parameters, respectively. Consequently, the thickness offset can be calculated as $(y-c)/m$ for Eq. 3.11 and is represented by the parameter b_2 Eq. 3.12. Eq. 3.12 takes absorption effects at low electron primary energies into account. For very thin layers the minimum detectable counts N_{MDC} of the contained elements is an important quantity. It can be defined due to Poisson statistics the following way:

$$N_{MDC} = 3\,\sigma_{Bgd} = 3\,\sqrt{N_{Bgd}} \tag{3.13}$$

where N_{Bgd} are the counts belonging to the background.

3.4. Results

3.4.1. CSD coated conductors

3.4.1.1. LZO buffer layers of CSD coated conductors

A crucial issue for CSD buffer layers is the control of film thickness, surface roughness, and chemical homogeneity. The film thickness determines barrier efficiency to prevent the diffusion of metal ions into the superconductor. In an industrial environment where tape lengths up to one km are not uncommon a quick and non-destructive method is needed to assess the film quality on the µm scale. EDX spectroscopy in the SEM is a clever method to achieve this goal. Only Monte Carlo simulations of EDX spectra yield quantitative understanding of the spectra and yield larger thickness and homogeneity.

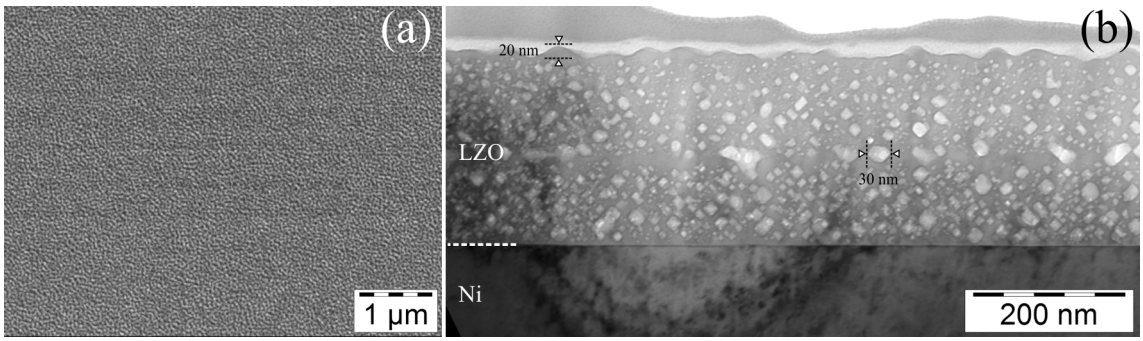

Figure 3.3.: LZO thin film grown on a Ni substrate. (a) SEM plan-view image of a CSD grown LZO layer. (b) TEM cross-sectional bright-field image of the same sample. Nano voids are present with a high density, one is marked (30 nm).

Fig. 3.3 shows the surface and the volume morphology of LZO thin films on Ni substrates (RABiTS). On the micrometer scale the surface is homogeneously rough as can be seen in Fig. 3.3a. From the TEM cross-section shown in Fig. 3.3b a surface roughness of 20 nm was determined. Further, it can be seen that LZO samples are porous. Pore sizes up to 30 nm were found. The LZO/Ni interface was found to flat, i.e. its roughness is below 5 nm.

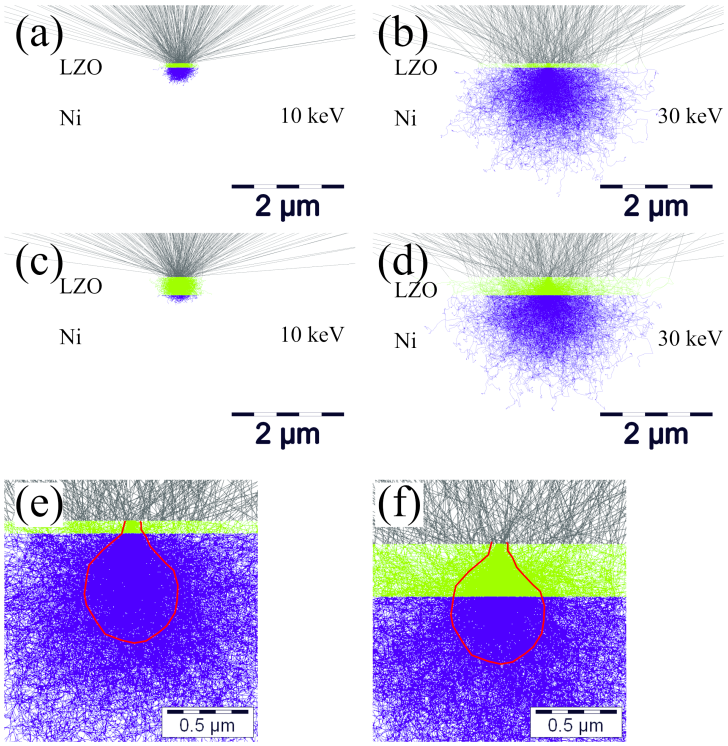

Figure 3.4.: LZO thin films grown on Ni substrates. Simulated electron trajectories at 10 keV primary electron energy for (a) sample LZO1 and (c) sample LZO4. Simulated electron trajectories at 30 keV for (b) sample LZO1 and (d) sample LZO4. (e) and (f) Magnified views of the interaction volume of sub (b) and (d), respectively.

Trajectory images visualize the sample regions being penetrated by electrons and are contributing to X-ray production. Electron transport Monte Carlo simulations treat solids as amorphous, homogeneously dense, and flat structures. Hence, channeling effects, interface roughness, and voids were ignored by the standard configuration of DTSA-II. They have to be modeled separately if necessary, we used the standard configuration here. Fig. 3.4a,b show electron trajectories for a 80 nm thick LZO film on a Ni substrate at 10 and 30 keV primary electron energy, respectively. Most of the electron trajectories are lying in the substrate. In Fig. 3.4c the situation is different. Here the main part of the trajectories lies within the 325 nm thick LZO film at 10 keV electron energy. In Fig. 3.4d significantly more electrons penetrate the substrate at 30 keV electron energy than at 10 keV. Fig. 3.4e and Fig. 3.4f are enlarged regions of Fig. 3.4b and Fig. 3.4d where the main part of the interaction volume of 30 keV electrons is indicated roughly by the red, solid line. It is assumed that the main part of emitted X-rays is emerging from this region. 10 keV primary electrons are hardly able to fully penetrate a 325 nm thick LZO film (Fig. 3.4c). Only few electrons reach the Ni substrate. Consequently, there will be no significant contribution of X-rays generated by the Ni substrate to the obtained EDX spectrum. At 30 keV primary electron energy the major fraction of the interaction volume lies within the substrate region for all analyzed sample thicknesses.

Fig. 3.6 shows a comparison of simulated (red) and experimental (black) EDX spectra of LZO acquired with the different acquisition conditions summarized in Tab. 3.2. The EDX spectra in Fig. 3.5a-d correspond to the trajectory images shown in Fig. 3.4. Simulated and experimental spectra were always scaled to equal integral counts. It can be seen that significant differences between experiment and simulation are being present especially in the Zr-L series and the Ni-L series. A general trend was observed in all spectra: the fitting errors in the low energy region of EDX spectra were found to be larger than at higher energies. The χ^2 values listed in Tab. 3.4 prove this quantitatively. The χ^2 values are large compared to

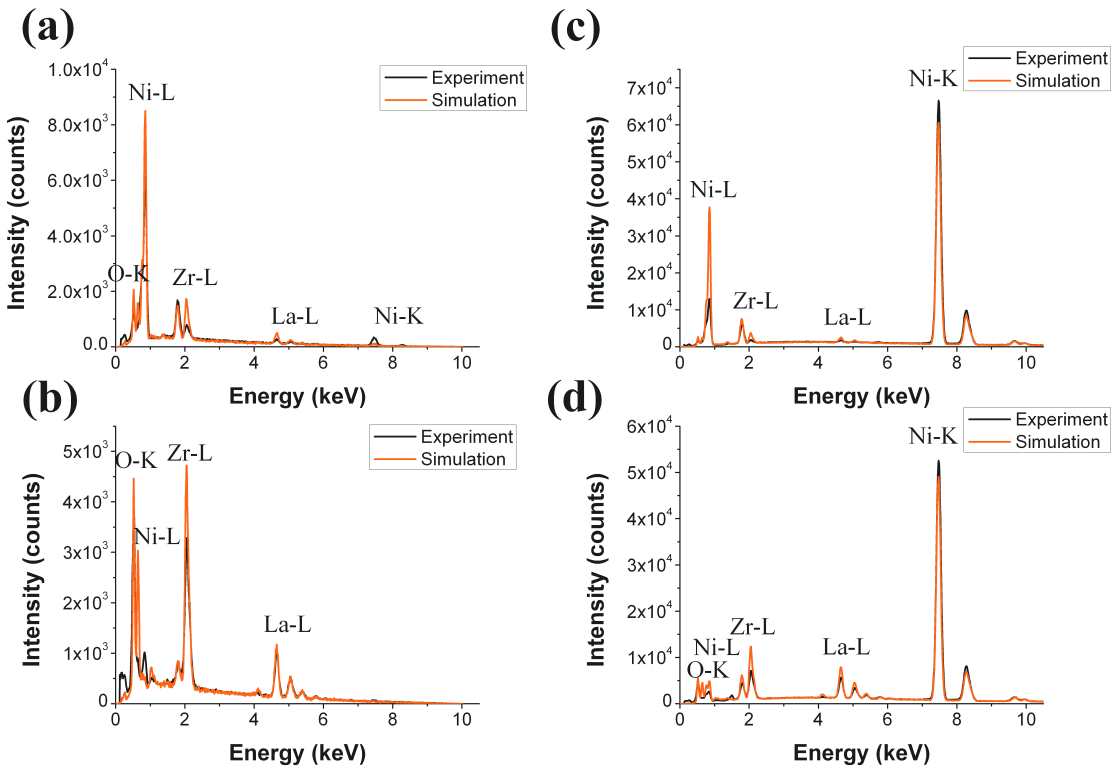

Figure 3.5.: For LZO thin films grown on Ni substrates experimental and simulated EDX spectra were compared. The acquisition conditions were 10 keV for (a) sample LZO1 and (b) sample LZO4 and 30 keV for (c) sample LZO1 and (d) sample LZO4.

Si single crystal values showing significant deviations of simulation and experiment especially in the low energy region.

Sample	χ^2 (0-2 keV)			χ^2 (0-20 keV)		
	10 keV	**20 kev**	**30 keV**	**10 keV**	**20 kev**	**30 keV**
Si bulk	4.02	12.49	22.97	0.88	2.50	3.83
LZO1	96.88	758.39	1666.62	18.04	98.62	197.53
LZO2	146.15	849.27	1862.83	18.92	100.39	210.28
LZO3	227.72	300.77	214.47	25.39	44.75	33.19
LZO4	211.92	348.70	471.84	24.69	58.16	83.17

Table 3.4.: χ^2 values determining the agreement of experiment and simulation for LZO thin films grown on Ni substrates. The Si bulk values are given for comparison.

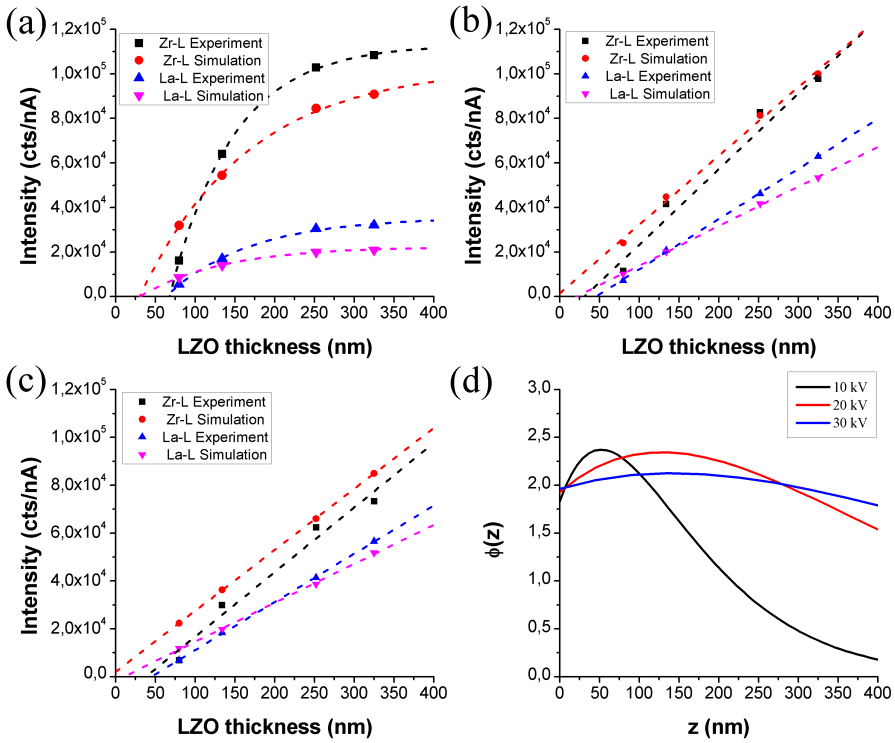

Figure 3.6.: LZO thin films grown on Ni substrates. LZO thickness plotted vs. La- $L_{\alpha 1}$ and Zr-$L_{\alpha 1}$ net counts per nA acquired at (a) 10 keV, (b) 20 keV, and (c) 30 keV primary electron energy. The dashed lines are the fitted thickness calibration curves. (d) Calculated $\varphi(\rho z)$ curves of Zr-$L_{\alpha 1}$ emitted intensity for 10, 20 and 30 keV in LZO bulk according to the PAP model.

X-ray line	Primary energy [keV]	Type	minimum detectable [counts/nA]	minimum detectable film thickness [nm]
La-L	10	E	386 ± 62	63 ± 6
	10	S	286 ± 53	30 ± 5
	20	E	567 ± 59	46 ± 4
	20	S	431 ± 56	21 ± 4
	30	E	652 ± 55	45 ± 3
	30	S	525 ± 55	10 ± 5
Zr-L	10	E	678 ± 87	68 ± 1
	10	S	459 ± 76	30 ± 8
	20	E	748 ± 78	30 ± 25
	20	S	519 ± 74	-5 ± 10
	30	E	652 ± 55	45 ± 3
	30	S	501 ± 70	-8 ± 1

Table 3.5.: Minimum detectable counts and corresponding LZO thickness calculated from least square fitting for experimental (E) and simulated (S) EDX spectra.

For thin films the X-ray intensity is linearly correlated to the film thickness. If several EDX spectra were acquired from films of known thicknesses a calibration curve can be obtained. With this calibration curve unknown film thicknesses can be determined. Monte Carlo simulations provide additional information

to understand the experiment since an ideal sample is assumed. In the case of LZO, e.g. the La-$L_{\alpha 1}$ and the Zr-$L_{\alpha 1}$ net counts per nA can be used to obtain calibration curves. In Fig. 3.6 the La-$L_{\alpha 1}$ and Zr-$L_{\alpha 1}$ net counts per nA were plotted vs. the LZO film thickness for both, experiment and simulation. Each set of data points was fitted by either an exponential function (10 keV electron energy) or a linear function (20 and 30 keV electron energy). In Fig. 3.6a (10 keV primary electron energy) all curves start to increase linearly with thickness but at 250 nm they saturate. The 20 keV and 30 keV curves (Fig. 3.6b,c) increase linearly within the displayed thickness range. This can be explained by the finite size of the excitation volume at 10 keV. Fig. 3.6d shows the calculated emitted X-ray depth distribution or $\varphi(z)$ function according to the PAP model [102] for 10, 20 and 30 keV primary electron energy in a LZO bulk sample. At an electron energy of 10 keV the $\varphi(z)$ curve is reduced to 1/e of its initial value at 250 nm LZO thickness. This is exactly the thickness where the X-ray counts begin to saturate in Fig. 3.6a. The $\varphi(z)$ curves for 20 and 30 keV electron energy are almost constant. Thus, the intensity in counts per nA increases linearly with LZO film thickness as can be seen in Fig. 3.6b and Fig. 3.6c. Another major observation was that all calibration curves show a thickness offset. This offset is due to the minimum detectable number of X-ray counts. This minimum number of X-ray counts can be converted into a thickness. The results are shown in Tab. 3.5. Negative values might appear if the simulation overestimates the X-ray counts or two peaks are overlapping.

3.4.1.2. Fully-processed CSD coated conductors

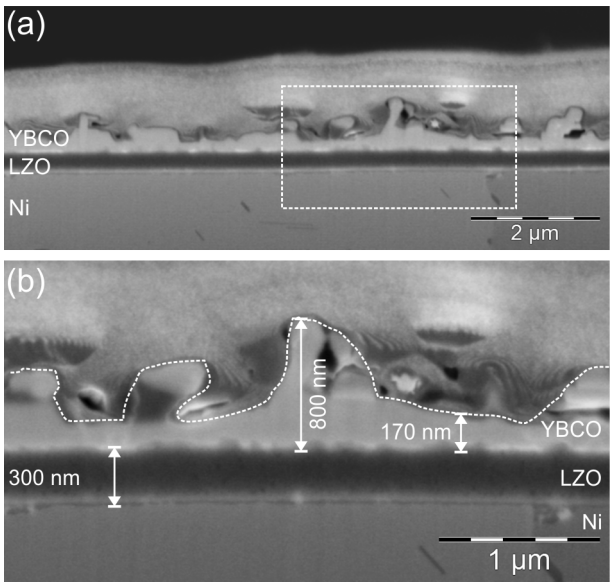

Figure 3.7.: (a) Cross sectional secondary electron image of a fully-processed CSD YBCO coated conductor. The dashed area indicates the area magnified in (b). (b) Magnified view of (a). Note the YBCO roughness denoted by the dashed line. The thickness of the LZO layer and typical YBCO thicknesses are indicated in the image.

Fully-processed CSD samples consist of three thin films namely LZO, CeO_2, and YBCO on top of a Ni substrate. The first two layers act as diffusion barriers preventing metal atoms from the substrate from diffusion into the superconductor. Therefore, EDX analysis and simulation of electron transport in this thin film system is not an easy job. The effective YBCO thickness governs the amount of current carried by the tape and needs to be measured. EDX offers the possibility to do this damage-free. The roughness in CSD type of samples is due to the process, i.e. thin films are deposited as liquid solution of precursor that needs to react and form the film at temperatures of about 700-800°C. Surface roughness mainly originates from fast growing a-axis grains, secondary phases, the roughness of the LZO layer, removal of gaseous species, and non-uniform drying. In a rough film a significant amount of material does not contribute to the current transport. A precise control of roughness and film thickness increases the total amount of current carried by each tape and decreases the material costs per tape at the same time. Non-destructive methods are of great importance in an industrial environment since no material needs to be wasted.

Fig. 3.7 shows the microstructure of a typical CSD grown coated conductor in cross section. A maximum YBCO thickness of 800 nm was observed in Fig. 3.7b whereas the minimum measured thickness was only 170 nm, i.e. a thickness variation of 470 % on a micrometer scale. As mentioned above EDX can be used to determine the local film thickness. Since the roughness features of the YBCO have about 1 µm

in size, i.e. about the size of the excitation volume, EDX point measurements are well suited to quantify the roughness. However, only one sample was available so that excessive Monte Carlo simulations were performed to obtain a thickness calibration curve for the Cu-K counts.

Fig. 3.8a shows normalized Cu-K peak counts vs. Ba-L peak counts extracted from EDX point spectra. The normalized Cu-K peak counts varied from 0.35 to 1.00 this equals to a scatter of 65%. Since a linear relation of normalized Cu-K peak counts to film thickness exists this documents the YBCO surface roughness that was observed in Fig. 3.7. However, this is only an indirect way to quantify the amount of the YBCO thickness variation. Thus, EDX spectra of different YBCO thicknesses were simulated to obtain the thickness calibration curve shown in Fig. 3.8b. The Cu-K net counts per nA were chosen because the Cu-K peak had no overlap with any other element and had the least absorption yielding an approximately linear relationship with the YBCO film thickness up to about 500 nm.

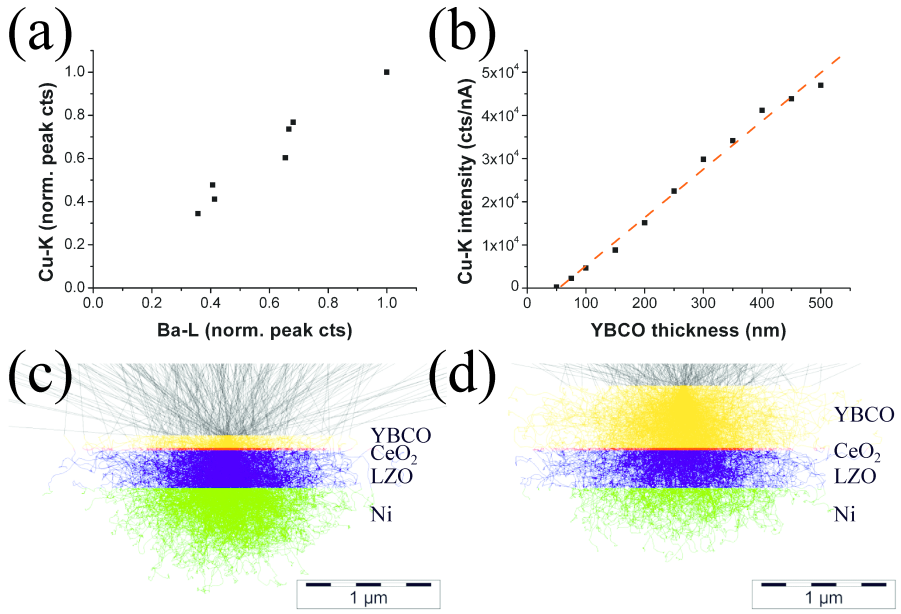

Figure 3.8.: YBCO coated conductor (Ni substrate, LZO buffer layer, and YBCO). (a) Experimental EDX correlation diagram of normalized Cu-K vs. Ba-L peak counts. The individual data points are determined for each acquired spectrum and local film thickness. (b) Simulated thickness calibration curve of Cu-K net counts per nA vs. YBCO thickness. The red dashed line is the fitted thickness calibration curve. Simulated electron trajectories at 20 keV primary electron energies for YBCO layer thicknesses of (c) 100 nm and (d) 500 nm, respectively.

Other X-ray peaks for example Y-L and Ba-L were strongly overlapping with Zr-L and La-L from the underlying LZO buffer layer and thus could not be used. K lines of Zr and Y were also not used since their intensities were beyond the detection limit.

X-ray line	Primary energy [keV]	Type	minimum detectable [counts/nA]	minimum detectable film thickness [nm]
Cu-K	20	S	358 ± 61	54 ± 10

Table 3.6.: Minimum detectable counts and corresponding YBCO thickness calculated from least square fitting for simulated (S) EDX spectra.

However, again a thickness offset due to the minimum detectable limit was observed as shown in Tab. 3.6. In principle the minimum detectable film thickness could be decreased by decreasing the primary electron energy. However, one has to keep in mind that Cu-K then might not be excited any more and one has to use one of the overlapping lines what can cancel the desired effect by a worse peak fit. Fig. 3.8c and d show two trajectory images of 20 keV electrons penetrating a 100 nm and a 500 nm YBCO film,

respectively. It can be seen that all layers of CSD coated conductor were penetrated by the electrons in both cases. Thus, the interaction volume is not the limiting factor if the YBCO thickness is smaller than 500 nm and a linear relationship of Cu-K net counts vs. YBCO thickness is observed. Cu-K net counts were extracted from experimentally acquired EDX point spectra and local YBCO thickness was calculated with the help of the calibration Fig. 3.8b fit matching with values obtained from SEM cross-section measurements.

3.4.2. ISD coated conductors

3.4.2.1. MgO buffer layers of ISD coated conductors

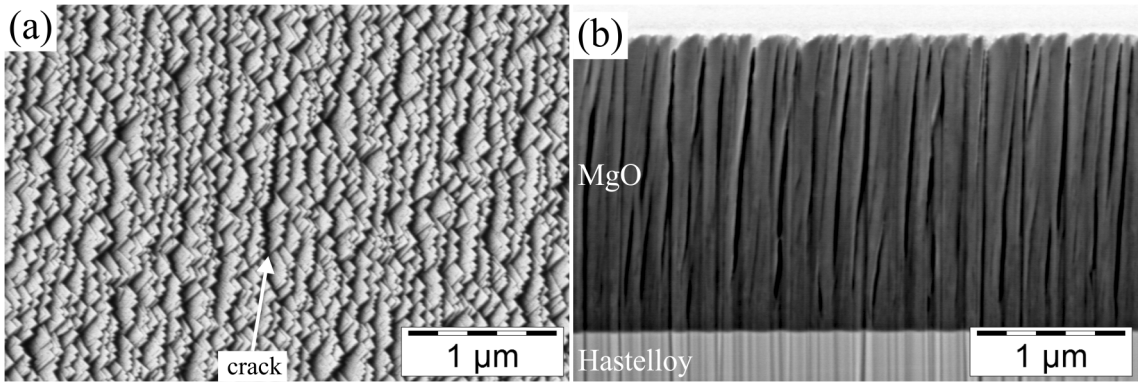

Figure 3.9.: MgO thin films grown on Hastelloy substrates. Secondary electron images of sample MgO7 (a) SEM plan-view and (b) SEM cross-sectional image.

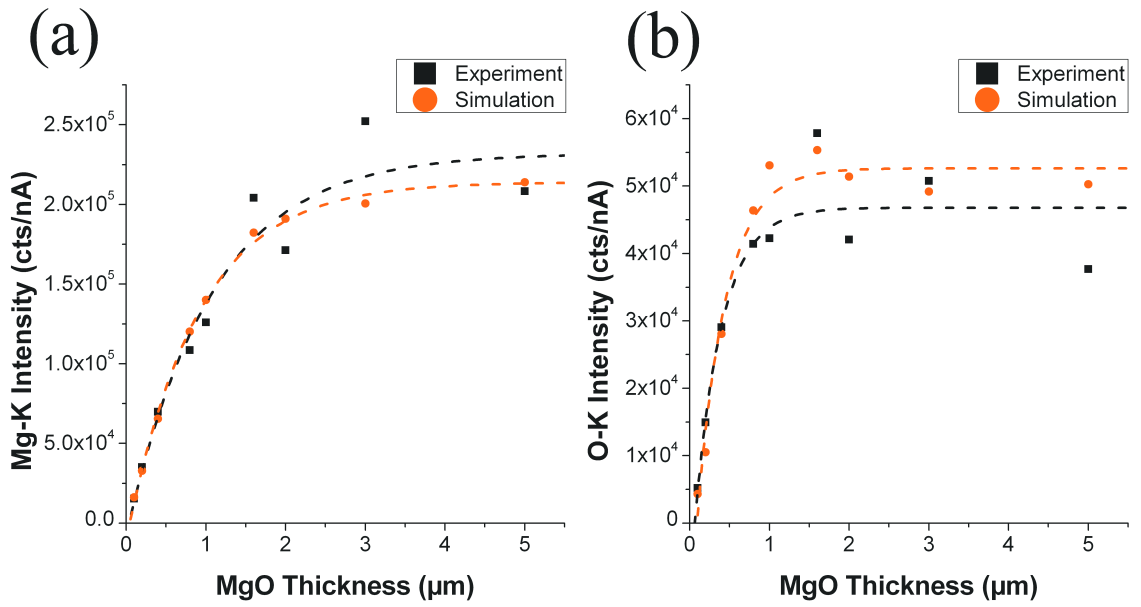

Figure 3.10.: MgO thin films grown on Hastelloy substrates. MgO thickness vs. (a) Mg-K and (b) O-K net counts per nA in simulation (red circles) and experiment (black squares). The dashed lines are the fitted thickness calibration curves. The experimental data was extracted from EDX area scans.

X-ray line	Primary energy [keV]	Type	minimum detectable [counts/nA]	minimum detectable film thickness [nm]
Mg-K	30	E	223 ± 99	90 ± 36
		S	178 ± 101	45 ± 15
O-K		E	173 ± 71	64 ± 55
		S	96 ± 64	90 ± 23

Table 3.7.: Minimum detectable counts and corresponding MgO thickness calculated from least square fitting for experimental (E) and simulated (S) EDX spectra.

Sample	χ^2 0-2 keV	χ^2 0-20 keV
Si bulk	22.97	3.83
MgO1	22.33	7.62
MgO2	34.84	9.31
MgO3	42.78	10.01
MgO4	42.43	8.67
MgO5	43.64	8.81
MgO6	59.67	10.92
MgO7	54.69	10.02
MgO8	63.43	12.47
MgO9	27.98	6.44

Table 3.8.: χ^2 values determining the agreement of experiment and simulation for MgO thin films grown on Hastelloy substrates. The Si bulk values are given for comparison.

ISD MgO layer were deposited by electron-beam evaporation, i.e. a PVD method. The motivation to analyze these films by EDX was study the evolution of texture and the influence of the film density on EDX measurements since the MgO film consists of single columnar grains having a more-ore-less faceted surface depending on the overall film thickness. Additionally, EDX could also be used to determine the MgO film thickness.

Fig. 3.9a shows a typical ISD MgO surface in plan-view. Regular facets and cracks are visible. AFM experiments (not shown here) revealed that the facets have an average height of 20 to 70 nm depending on the total MgO film thickness. The FIB-prepared SEM cross-section image in Fig. 3.9b shows single MgO columnar grains. The dark regions are voids forming the cracks observed in plan-view images.

An EDX thickness calibration curve can also be determined for PVD layers. Only 30 keV electron energy was used for this issue since films up to 5 µm were analyzed. EDX spectra were acquired and simulated by Monte Carlo simulation for the nine ISD MgO samples listed in Tab. 3.3. Afterwards, the Mg-K and O-K net counts per nA were extracted from each spectrum and plotted vs. the MgO film thickness, the results are shown in Fig. 3.10. For Mg-K the relationship was linear in the first 2 µm of MgO , for O-K in the first µm. Afterwards, the X-ray counts for both lines saturate. Experiment and Monte Carlo simulation show in both cases the same saturation behavior. This can be explained by the limited X-ray excitation volume. The calculated $\varphi(z)$ function of MgO bulk material was plotted in Fig. 3.2b and d. At the critical depth of 2 µm for Mg-K and 1 µm for O-K the $\varphi(z)$ function drops below e^{-1} of the initial value so that deeper MgO parts do not contribute to the EDX spectrum detected at the sample surface. From Fig. 3.10 it appears that the thickness offset due to the minimum detectable limit seems small as compared to the LZO samples. However, if exponential fits were performed determining the minimum detectable thickness the values were very similar to those found in LZO for both experiment and simulation. The exact values are listed in Tab. 3.7.

As a last point the accuracy of simulation in ISD MgO samples was analyzed using the χ^2 method. The results are listed in Tab. 3.8. They are a factor 8 to 10 better than the LZO values but still three times worse than those for a Si single crystal.

3.4.2.2. Fully-processed ISD coated conductors

X-ray line	Primary energy [keV]	Type	minimum detectable [counts/nA]	minimum detectable film thickness [nm]
Ba-L	30	S	229 ± 38	31 ± 6
Dy-L			198 ± 30	-94 ± 20
Cu-K			189 ± 35	78 ± 17

Table 3.9.: Minimum detectable counts and corresponding DyBCO thickness calculated from least square fitting for simulated (S) EDX spectra.

For MgO buffered DyBCO layers also the thickness determination by non-destructive methods is important. Due to the chemical complexity of the sample Monte Carlo simulations may provide a better understanding of electron and photon transport. In sample DyBCO2 the MgO film was intentionally grown at wrong growth conditions to study the effect on the DyBCO layer grown on top.

The morphology of DyBCO films is presented in Fig. 3.11. Fig. 3.11a and b show the surfaces of sample DyBCO1 and DyBCO2, respectively, both have rough surfaces. However, sample DyBCO1 was regularly faceted at the MgO-DyBCO interface whereas sample DyBCO2 had an irregular facet shape. Secondary electron images from FIB-prepared SEM cross-sections shown in Fig. 3.11c revealed an almost homogeneous DyBCO thickness for sample DyBCO1. Darker regions within the DyBCO film where identified by EDX in the TEM as secondary phases or voids. Sample DyBCO2 was inhomogeneous compared to sample DyBCO1. The interface roughness's measured in Fig. 3.11d were with about 200 nm twice as large as those measured in Tab. 3.10c with about 120 nm.

The influence of these structural features on EDX point spectra is shown in Fig. 3.11e and f in X-ray scatter diagrams of normalized Cu-K peak counts vs. normalized Ba-L peak counts. Sample DyBCO1 showed a small scattering of data points in the 10-15% range whereas sample DyBCO2 showed a large one in the 35-40 % range. Fig. 3.11g and h show a representative comparison of experimental and simulated EDX spectra for sample DyBCO1 and DyBCO2, respectively.

It can be clearly seen that for both samples the DyBCO peaks fit quite well whereas peaks from the buried layers show partly tremendous deviations from experiment and simulation. This increases of course the χ^2 values and finally the accuracy of simulation mentioned in Tab. 3.9.

Sample	χ^2 0-2 keV	χ^2 0-20 keV
Si bulk	22.97	3.83
DyBCO1	212.38	31.57
DyBCO2	120.89	19.04

Table 3.10.: χ^2 values determining the agreement of experiment and simulation for DyBCO coated conductors. The Si bulk values are given for comparison.

Also for DyBCO samples it is important to assess the DyBCO film quality and thickness without destroying the coated conductor tape. Hence, a DyBCO thickness series was simulated in DTSA-II and compared to the experimentally acquired spectra. The Ba-L, Dy-L and Cu-K net counts per nA were extracted from experimental and simulated spectra and were plotted against the corresponding DyBCO thickness. The result is shown in Fig. 3.12a. A linear increase of the X-ray counts per nA with thickness was observed in the displayed thickness range for all lines. In addition, thickness offsets due to the minimum detectable limit were determined. The values are listed in Tab. 3.9. This can be explained by calculating the $\varphi(z)$ function for all three X-ray lines. Fig. 3.12b shows the $\varphi(z)$ functions for emitted X-rays (solid line) and total generated X-ray photons (dashed line). This shows that the critical absorption depth of X-rays in DyBCO is beyond 1.5 µm film thickness. Fig. 3.12c and Fig. 3.12d show simulated electron trajectories of sample

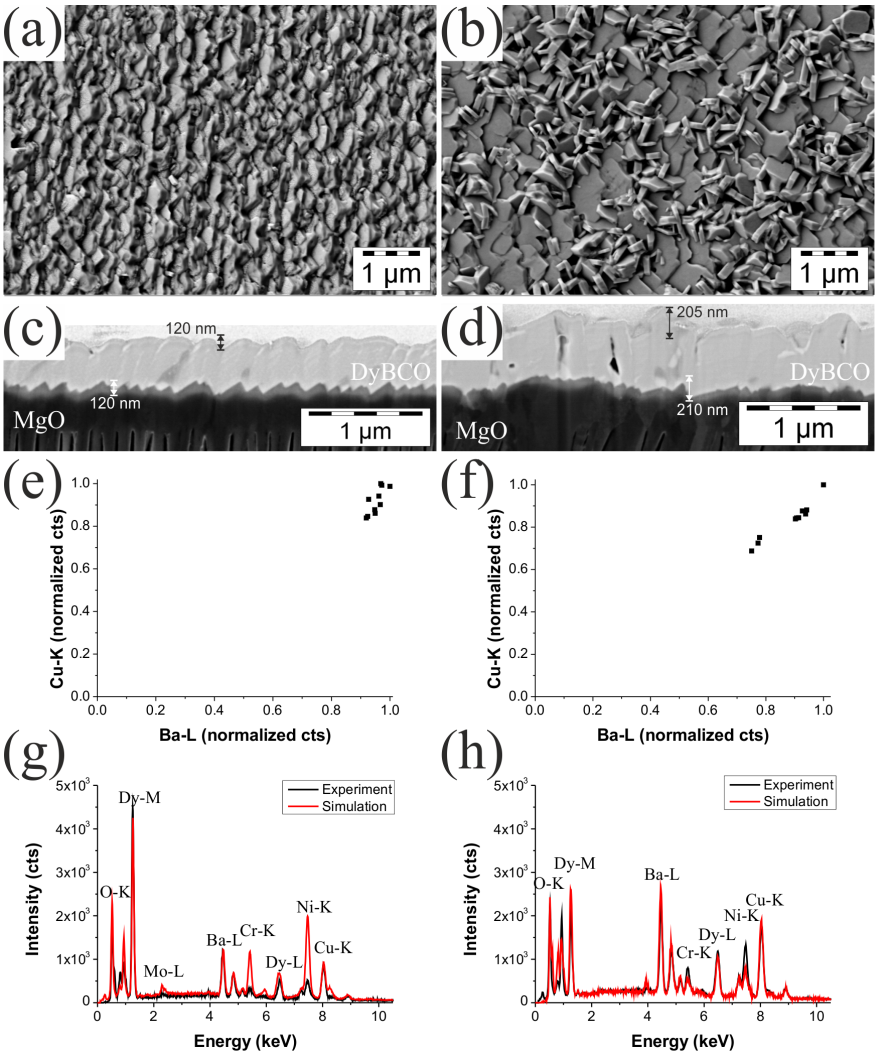

Figure 3.11.: DyBCO coated conductors (Hastelloy substrate, MgO buffer layer, and DyBCO). SEM plan view images of (a sample DyBCO 1 and (b) sample DyBCO 2. SEM cross-sectional images of (c) sample DyBCO 1 and (d) sample DyBCO 2. EDX correlation diagrams of normalized Ba-L vs. Cu-K net counts for (e) sample DyBCO 1 and (f) sample DyBCO 2. Comparison of experimental and simulated EDX spectra of (g) sample DyBCO 1 and (h) sample DyBCO 2.

DyBCO1 and DyBCO2 at 30 keV primary electron energy. It can be seen that all layers of the sample are penetrated by electrons.

As final point the accuracy of simulation in DyBCO samples was analyzed by the χ^2 method. The results are listed in Tab. 3.10. They are by a factor of 2 larger than the MgO values in the energy range 0-20 keV. In the low energy range (0-2 keV) the values deviate by a factor of 4. Compared to single crystalline Si the DyBCO values are by a factor of 10 larger.

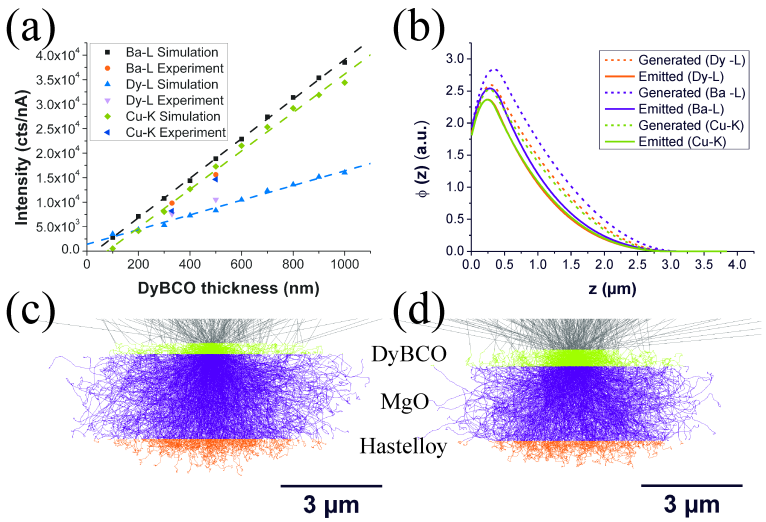

Figure 3.12.: DyBCO coated conductors (Hastelloy substrate, MgO buffer layer, and DyBCO). (a) Simulated and experimental net counts per nA of Dy, Ba, and Cu in dependence on the DyBCO thickness. The dashed lines are the fitted thickness calibration curves. (b) Calculated X-ray depth distribution according to the PAP model for a bulk DyBCO sample. Simulated trajectory image for (c) sample DyBCO 1 and (d) sample DyBCO 2.

3.5. Discussion

3.5.1. Methodology highlights

The propagation of electrons in single and multilayer thin films could be calculated for coated conductor materials. Electron transport was simulated and the electron trajectories were tracked for different primary electron energies. The resulting images of electron trajectory images yield information how far electrons penetrate into a material and in which region of a multilayer structure X-rays are being generated. The experimentally detected and the simulated X-ray spectra of coated conductor thin films were matching well to each other.

In thin film technology in general but in coated conductor technology in particular, the determination of the local film thickness is of great interest without destroying the film. Since the X-ray intensity is linearly related to the film thickness if the critical absorption length is not reached, EDX analysis can be used to determine the local film thickness. However, thickness calibration curves are needed to determine the film thickness from the measured counts per nA of a film of unknown thickness. Within this chapter experimental thickness calibration curves were obtained for LZO, MgO, and DyBCO. Thickness calibration curves on basis of simulated EDX spectra represent an ideal behavior. Depending on the acquisition conditions and sample complexity significant differences between experimental and simulated thickness calibration curves were observed. The origin of these differences is discussed in the last paragraph of this discussion. Besides the film thickness also the film roughness can be determined, which is a local thickness variation. Ideal candidates for this were the YBCO films prepared by CSD with their large roughness on the micrometer scale. It was shown that the large scattering of X-ray intensities acquired at various positions on the film surface originated from the film roughness and could be explained using simulated thickness calibration curves.

In this thesis (multilayer) thin film structures were analyzed. The thinnest films had a thickness of a few ten nanometers, e.g. 20 nm CeO_2, 80 nm LZO, or 100 nm MgO. However, as the films get thinner the number of X-rays being generated decreases, since the number of X-ray counts being generated depends on the film thickness. A minimum detectable mole fraction always exists for X-ray quantification due to the Bremsstrahlungs background. It depends on the sensitivity, i.e. on the minimum detectable mole fraction of the element, therefore, also a minimum detectable film thickness exists and was determined for all samples. The exact values are listed in Tab. 3.5 for LZO, in Tab. 3.6 for YBCO, in Tab. 3.7 for MgO,

and in Tab. 3.9 for DyBCO, respectively. Practically, peak-overlapping and poor background fits may decrease the minimum detectable mole fraction and, therefore, the minimum detectable film thickness. Thus, high-energy X-ray lines are preferred to low-energy lines, since the background is more linear and the lines are better separated at the high-energy part of the EDX spectrum (> 3 keV). If X-ray lines of the low-energy part of the EDX spectrum are used, negative film thickness might occur. The primary energy of the electrons should be chosen such that the transversal length of electron interaction volume is slightly larger than the nominal film thickness. The minimum detectable film thicknesses measured in this work were in the range of several ten nanometers corresponding to a few hundred counts per nA.

In a Monte Carlo calculation the number of primary electrons being simulated is limited to a several thousands. Therefore, the simulated intensity needs to be adjusted. DTSA-II contains several possibilities to do this. Here the simulated spectra were scaled such that both spectra have the same integral counts. On a qualitative level reasonable results were produced for all samples. However, a quantitative figure of merit is needed describing the quality of the fit. For example the χ^2 method [118] is suited for that issue. It was found that χ^2 increases with the chemical complexity of the sample and with increasing primary electron energy. In addition, the χ^2 value of the low energy part (0-2keV) of EDX spectra is about a factor 10 larger than that in the total spectrum (0-20 keV). This behavior is due to the more precise knowledge of K ionization cross section and fluorescence yields. The literature on both issues is quite substantial [94, 95, 96, 97, 98, 90, 89, 88, 91, 92, 93]. Most of the K peaks found in EDX spectra also have high energies. In contrast, for the L- and M ionization cross sections and fluorescence yields only few studies exist [99, 94, 100, 89, 90] dealing with this non-trivial issues and the L and M peaks are mostly located in the low energy part (0-2 keV) of the EDX spectrum. Nevertheless, a good overall fitting behavior was observed for all simulated spectra.

3.5.2. Computing performance

The computing performance of DTSA-II is one key point. At present DTSA-II can only use a single core of the processor, i.e. it is not parallelized. However, several instances of the program can run in parallel if required. We tested the computing performance of DTSA-II by simulating EDX spectra of two sample types for an increasing number of electrons while logging the time: (i) bulk Si and (ii) an MgO-buffered DyBCO thin film on a Hastelloy substrate. Simulations were carried out using 10 keV and 30 keV electron energies on the three hardware systems having the properties listed in Tab. 3.11.

A linear relation for simulation time vs. simulated electrons was always obtained. The simulation time increases with the complexity of samples and the layers penetrated by the interaction volume (the interaction volume increases if the electron energy is increased). If the simulation time for 10000 electrons on System1 is compared to System3 for the two electron energies and the two sample types, System3 was always about 25% faster. System2 lies in terms of computation time always in between System1 and System3. If the computation time of the bulk Si is compared to the DyBCO thin film on System3, the simulation time increased for the DyBCO thin film by a factor of 4-5 compared to the Si for both electron energies. The fastest simulation for 10000 electrons (55 min) was found for the Si sample at 10 keV on System3. The longest simulation time (about 11 h) was observed for the DyBCO thin film sample on System1 using 30 keV electrons.

	CPU	RAM [GB]	Java runtime environment
System1	AMD 3700+ x64@2.2GHz	1	x86
System2	Intel Core2Duo E4600@2.5 GHz	3	x86
System3	Intel Core2Quad Q6600@2.4 GHz	4	x64

Table 3.11.: Features of the used computer systems for EDX spectrum simulation.

3.6. Summary

Quantitative EDX spectrum simulation was implemented, which calculates the electron scattering in the excitation volume by a Monte Carlo approach, yielding calculation of electron trajectories, X-ray emission, X-ray fluorescence, and X-ray absorption. EDX Spectra can be calculated for samples with complex geometries and can be compared in a straight-forward manner to experimentally obtained spectra. Simulations of electron trajectories and X-ray intensities on the micrometer scale were carried out yielding optimized acquisition conditions with respect to lateral resolution, precision of quantitative analysis, and minimum detectable mole fractions. Experimental and simulated EDX calibration curves were obtained for determining of film thicknesses and roughnesses in ReBCO coated conductors, both being important in thin film technology.

4. Large-angle electron scattering for layered functional materials

4.1. Introduction

The nanostructure and chemistry of materials have a great influence on their physical properties. The optimization of these macroscopic properties by nanostructure engineering is a hot topic in research nowadays. High-angle annular dark-field scanning transmission electron microscopy (HAADF-STEM) imaging is the method of choice to reveal the atomic structure of materials since it provides easily interpretable, quantifiable Z-contrast (Z: atomic number) images in contrast to phase contrast based imaging in high-resolution transmission electron microscopy (HRTEM). Furthermore, a simultaneous acquisition of electron energy-loss spectra (EELS) and of HAADF images was demonstrated for the first time for $YBa_2Cu_3O_{7-x}$ [119, 120]. Most modern STEMs are able to explore the chemical composition, interdiffusion, and electronic structure on the atomic scale for almost any type of material or nanodevice [10]. A number of spectacular atomic resolution HAADF-STEM experiments conducted on various materials have been published over the last 20 years proving the capability of the method [119, 121, 122]. In case of Bi_2Te_3-related materials only few studies using HAADF-STEM techniques have been carried out [123, 124]. We used HAADF-STEM imaging combined with image simulation to identify the elemental layers and to trace the influence of Se or Sb alloying on the image contrast in n- and p-type Bi_2Te_3-related materials, respectively. Similar aspects also hold for $DyBa_2Cu_3O_{7-x}$ (DyBCO) superconductors since they are also layered structures. In this thesis the focus lies for DyBCO materials on crystalline defects and grain boundaries, which influence the critical current of these materials to a great extent. In addition, a layer-by-layer EELS analysis (StripeSTEM) might reveal the oxygen doping on the atomic scale.

The motivation to apply HAADF-STEM methods was to use the atomic number sensitivity of electrons scattered into angles larger than those used in conventional TEM [125]. The striking advantages of HAADF-STEM Z-contrast based imaging over conventional HRTEM phase contrast imaging are that (i) no contrast reversal or delocalization occurs in dependence on defocus or sample thickness [2] and that (ii) simultaneous imaging and spectroscopy with atomic resolution are possible. In HAADF-STEM the image contrast stems mainly from thermal diffuse (incoherent) scattering. Pennycook and Jesson [125] showed by using a Bloch wave approach that the image contrast in HAADF images is mainly due to tightly bound s-states. Thus, the emerging electron intensity is localized on the atomic columns. The final HAADF image can be understood as a convolution of both, the electron probe and the object function, which consist just of thickness-integrated s-states at each atomic column. Due to this type of image formation quantitative analysis of the image intensity is possible with respect to mass densities on the atomic scale. However, the probe needs to be carefully adjusted in terms of defocus and convergence angle to guarantee optimum imaging conditions.

HAADF image simulation in Bi_2Te_3-related materials was applied to prove that

1. in HAADF images the Z-contrast is hardly affected by the TEM sample thickness. In contrast, in HRTEM phase contrast images often varies systematically with the ratio of sample thickness to extinction distance (Fig. 10.31 in [2]), which is short for compounds containing heavy elements (see chapters 13.5, 14.4, and 14.5 in [3] and chapter 10.5 in [2]).
2. Image simulation can be used to quantitatively explore the alloying in real space.

Furthermore, the simulations offer a new unique way of understanding, how the HAADF image is formed, how an electron wave propagates through a crystal lattice, and how the final contrast is linked to the atomic structure of the crystal. For such simulations the open source program QSTEM [11] written by C.T. Koch was used. First comparative studies of STEM experiments and simulations on the atomic scale of $La_{0.7}Sr_{0.3}MnO_3$-$SrTiO_3$ multilayer structures were already carried out by van Aert et al. [126].

The StripeSTEM technique [127] allows simultaneous acquisition of HAADF-STEM Z-contrast images and EEL spectra with atomic resolution. However, the acquisition is carried out line-wise (StripeSTEM) not pixel-wise (EELS mapping). As quoted by Heidelmann et al. [127] the line-wise StripeSTEM technique is superior to conventional pixel-wise EELS mapping due to the better control of specimen drift and the better signal-to-noise ratio of the recorded EEL spectra. The inelastic cross section important for EELS decreases much faster with the scattering angle as compared to the elastic cross-section determining the Z-contrast in HAADF images [24]. This allows high-quality HAADF imaging also for relatively thick sample areas. The inelastic to elastic cross-section ratio is almost linearly decreasing with increasing atomic number Z [24]. The StripeSTEM technique is ideally suited for the analysis of materials with layered crystal structures or superlattices.

4.2. Experimental

4.2.1. Sample details and sample preparation

Bi_2Te_3-related materials have a layered pseudo-hexagonal crystal structure (space group $R\bar{3}m$, a = 4.395 Å, c = 30.44 Å) with quintuple sequences Te1-Bi-Te2-Bi-Te1, stacked along the pseudo-hexagonal c-axis and with weak van-der-Waals-like bondings between the Te1-Te1 layers [128]. The n-type $Bi_2(Te_{0.91}, Se_{0.09})_3$ and p-type $(Bi_{0.26}, Sb_{0.74})_2Te_3$ bulk compounds presented in this chapter were already pre-characterized to a great extend. Details about the growth method, the TEM sample preparation, and the analyses already done can be found in [129, 130, 131, 132, 133]. The chemical composition of the bulk compounds was determined with high accuracy by Eyidi et al. [134] using wavelength-dispersive X-ray spectroscopy (WDX) in an electron probe microanalyzer.

n-type $Bi_2(Te_{0.91}, Se_{0.09})_3$ and p-type $(Bi_{0.26}, Sb_{0.74})_2Te_3$ TEM samples were prepared from pellets synthesized by the Bridgman technique with the c-axis lying in the plane of the TEM sample [131]. The samples were analyzed in a probe-corrected TITAN 80-300 (S)TEM at Ernst-Ruska Centre in Juelich. The StripeSTEM method [127] was used to simultaneously acquire HAADF images and EEL spectra of single Bi(Sb) and Te(Se) layers in p- and n-type materials, respectively. The StripeSTEM spectra were obtained by integrating the measured column-by-column EELS map parallel to the van-der-Waals gaps of p-type $(Bi_{0.26}, Sb_{0.74})_2Te_3$. Low-Loss EEL spectroscopy was used to determine the local thickness of the samples in terms of the electron mean free path (mfp) determined by EELS.

The DyBCO coated conductors were grown by the ISD method [135] and the layers, their thicknesses, and growth parameters were the same as described by Aabdin et al. [136]. Samples were prepared conventionally by mechanical thinning and subsequent Ar ion milling in a Fischione 1010 ion milling machine such that the sample normal was aligned along the [110] direction of the DyBCO. HAADF images were acquired using the FEI Titan^3 at the University of Antwerp equipped with a HAADF detector and operated at 120 kV to prevent knock-on damage on the sample. The microscope had a builtin C_s probe corrector. Further parameters can be extracted from Tab.4.1.

All experimentally acquired HAADF images were Fourier-filtered [137] to reduce the noise within the image. Since there can be an error in the 10% range in the scaling in high-magnifaction experimental images, the experimental line profiles were adjusted such that they were matching (in length) the simulated line profiles.

4.2.2. Atomically-resolved HAADF image simulation

Parameter	Value Bi_2Te_3	Value DyBCO
Acceleration Voltage [kV]	300	120
C_{S3} [mm]	0.001	0.001
C_C [mm]	1	1
Energy spread [eV]	0.5	0.5
(Scherzer) Defocus [nm]	-1.7	-2.2
Astigmatism [nm]	0	0
Temperature [K]	300	300
Convergence angle [mrad]	25	17.5
Gun Brightness [A cm^{-2} sr]	0.6×10^{10}	0.6×10^{10}
Probe size [Å]	1.2	2
Dwell time [µs]	20	4.5
Thermal diffuse scattering used	no	no
Size of the used supercell [$Å^3$]	43.950 × 38.062 × 750.000	76.488 × 77.780 × 584.425
Size of the scan field [$Å^2$]	20×20	40×40
Number of scan points	64×64	128×128
Slice thickness [Å]	1.25	1.17
HAADF detector inner radius [mrad]	50	50
HAADF detector outer radius [mrad]	150	150

Table 4.1.: Parameters used for atomic resolution HAADF image simulation.

The QSTEM software [11] was used to simulate a thickness series of HAADF images to perform a quantitative analysis of the experimental images. Atomically-resolved HAADF images were simulated for the [110] zone axis of the Bi_2Te_3-related materials and the DyBCO coated conductor, respectively. The simulation parameters are summarized in Tab.4.1.

In case of Bi_2Te_3 alloys alloying was included in the simulations by setting a fractional occupation of Se on Te sites and of Sb on Bi sites in the structure file yielding a random distribution of the alloyed atoms in the final supercell. Typical calculation times were about 1.2 h for Bi_2Te_3 images on a Dell Precision T7500 workstation having two 3.4 GHz Intel Xeon Hex-core processors and 64 GB RAM. Furthermore, the simulation was configured such that at every 10th slice an image was saved to hard-disk. An example for a QSTEM structure input file as well as a screenshot of QSTEM's home screen, where simulation details can be configured, are provided in the Appendix.

Atomically resolved HAADF images were simulated for n-type $Bi_2(Te_{0.91},Se_{0.09})_3$ and p-type $(Bi_{0.26},Sb_{0.74})_2Te_3$ materials. In the simulation alloying was realized by statistically replacing Te by Se (n-type) or Bi by Sb (p-type) in 75 nm thick supercells, respectively. The supercell was divided into 600 slices having a thickness of 1.25 Å shifted such that the atomic layers are in the center of the slices. The number of scan points was 64×64 covering an area of 20×20 Å. The probe array had 128×128 entries. Thermal diffuse scattering (TDS) was neglected during the multislice calculation.

For DyBCO a thickness series was simulated and fitted to one experimental image. A 58.4 nm thick $DyBa_2Cu_3O_{7-x}$ supercell was simulated with respect to atomically resolved HAADF imaging. The supercell was divided into 500 slices having a thickness of 1.17 Å shifted such that the atomic layers are in the center of the slices. The number of scan points was 128×128 covering an area of 40×40 Å. The probe array had 400×400 entries. TDS was neglected during the multislice calculation.

4.3. Results

4.3.1. High-angle annular dark-field imaging in Bi_2Te_3 alloys

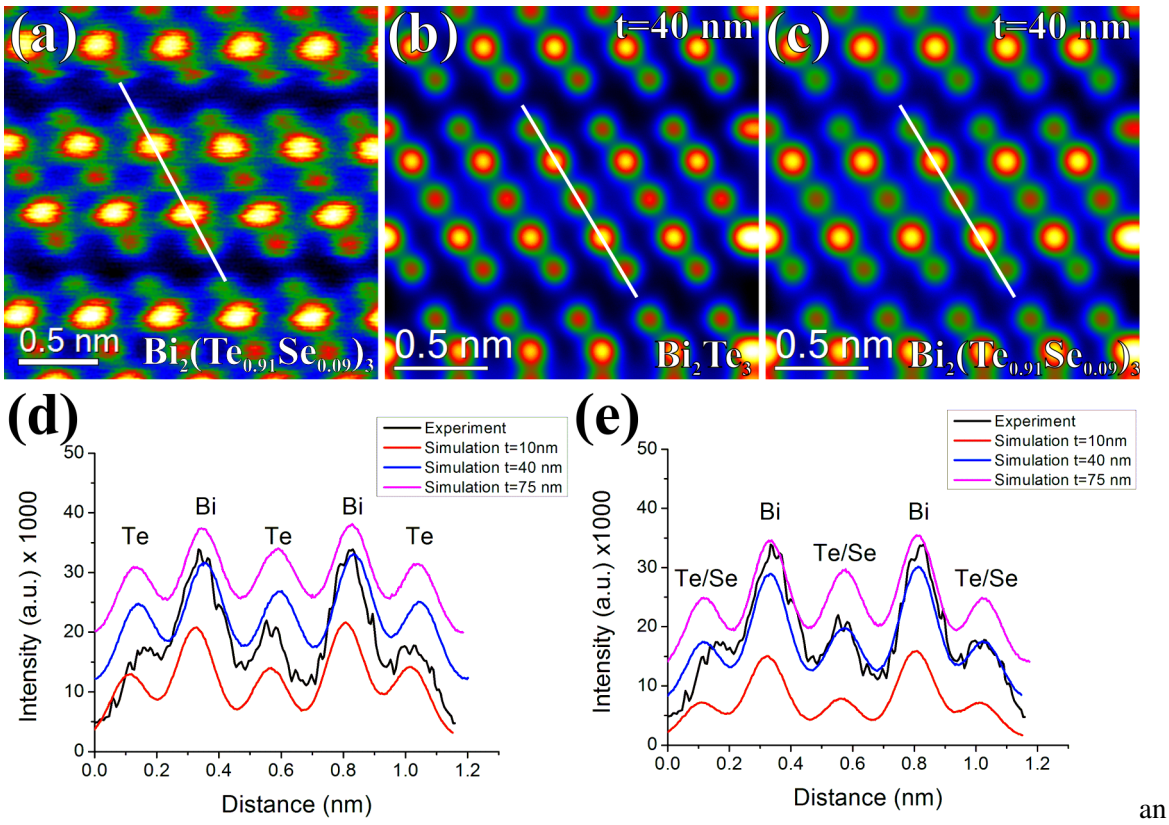

an

Figure 4.1.: High-resolution HAADF images in [110] zone-axis orientation. Images are shown in false colors. (a) Experimental image acquired in $Bi_2(Te_{0.91},Se_{0.09})_3$ at a sample thickness of 0.5 mfp. Simulated images for (b) pure Bi_2Te_3 and (c) the alloy $Bi_2(Te_{0.91},Se_{0.09})_3$ for a sample thickness of 40 nm. The white lines indicate intensity line profiles for (d) Bi_2Te_3 and (e) $Bi_2(Te_{0.91},Se_{0.09})_3$.

Experimental HAADF images in $Bi_2(Te_{0.91},Se_{0.09})_3$ were acquired at thicknesses of 0.25 mfp (20 nm), 0.5 mfp (40 nm), and 0.8 mfp (63 nm) on bulk samples. The mean free path (mfp) was determined by EELS and converted to nm according to Malis et al. [138]. Fig.4.1 shows the comparison of an experimental HAADF image acquired in $Bi_2(Te_{0.91},Se_{0.09})_3$ (Fig.4.1a) to the simulated HAADF images of pure Bi_2Te_3 (Fig.4.1b) and of $Bi_2(Te_{0.91},Se_{0.09})_3$ (Fig.4.1c). All HAADF images are displayed in false color. The white lines being present within Fig.4.1a-c indicate the line profiles extracted from the images. Fig.4.1d shows line profiles extracted from simulated HAADF images for different sample thicknesses in pure Bi_2Te_3 together with the experimental line profile. Fig.4.1e shows the same for the alloyed material.

Experimental HAADF images in $(Bi_{0.26},Sb_{0.74})_2Te_3$ were acquired at thicknesses of 0.25 mfp, 0.6 mfp, and 0.86 mfp corresponding to 21 nm, 50 nm, and 71 nm, respectively. Fig.4.2 shows the comparison of experimental and simulated HAADF images for $(Bi_{0.26},Sb_{0.74})_2Te_3$. Intensity lines profiles are presented in Fig.4.2 for $Bi_2(Te_{0.91},Se_{0.09})_3$.

4.3.2. StripeSTEM in p-type $(Bi_{0.26}, Sb_{0.74})_2Te_3$

Fig.4.3 shows low-loss StripeSTEM data acquired at sample thicknesses between 0.25 mfp and 0.86 mfp. The color coded EELS data (on the right) is correlated with the STEM data (on the left) for each

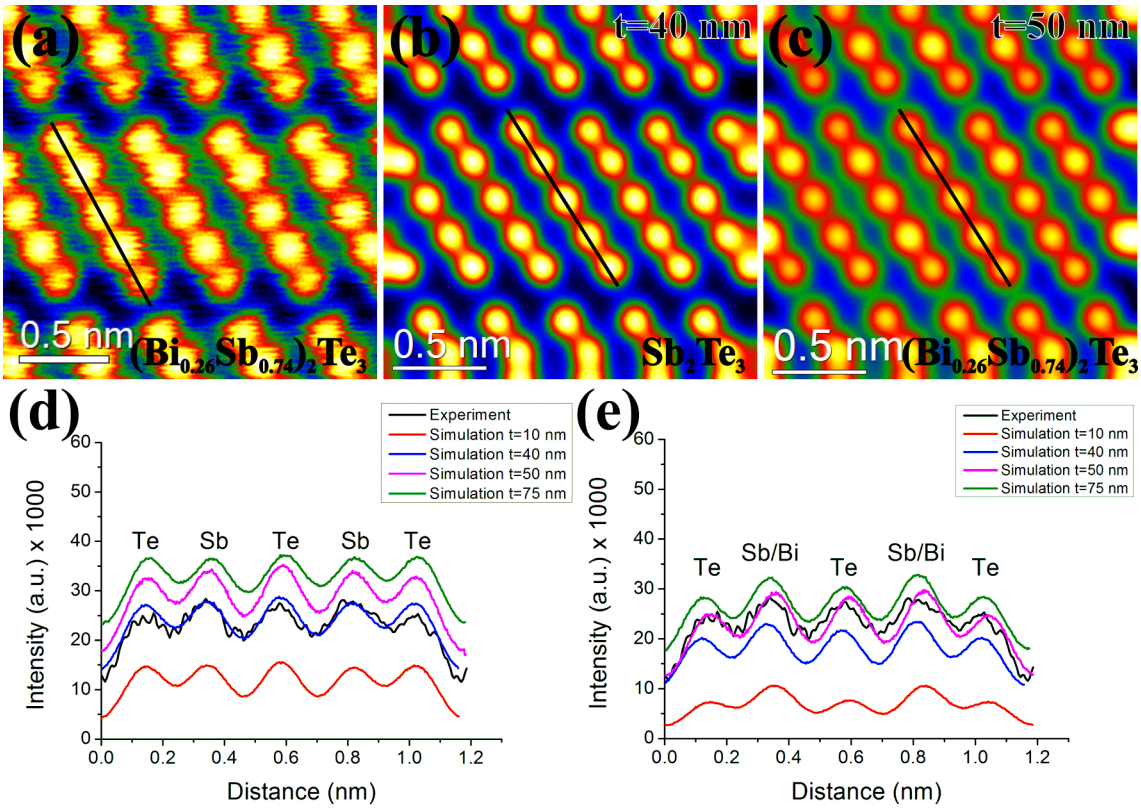

Figure 4.2.: High-resolution HAADF images in [110] zone-axis orientation. Images are shown in false colors. (a) Experimental image acquired in $(Bi_{0.26},Sb_{0.74})_2Te_3$ at a thickness of 0.6 mfp. Simulated images for (b) Sb_2Te_3 and (c) $(Bi_{0.26},Sb_{0.74})_2Te_3$ for a sample thickness of 40 nm. The black lines indicate intensity line profiles for (d) Sb_2Te_3 and (e) $(Bi_{0.26},Sb_{0.74})_2Te_3$.

thickness. Vertical and horizontal line profiles were extracted from the EELS data. The vertical ones were taken at the Sb-$N_{4,5}$ and the Te-$N_{4,5}$ edge, respectively. The horizontal ones were extracted within the van-der-Waals gap between the Te1-Te1 layers.

Fig. 4.4 shows core-loss StripeSTEM data acquired at the Sb/Te-$M_{4,5}$ edge. The sample thickness was determined to be 0.46 mfp. The data evaluation was same as for the low-loss case. These data prove that the individual atomic layers can also be resolved by EELS spectroscopy.

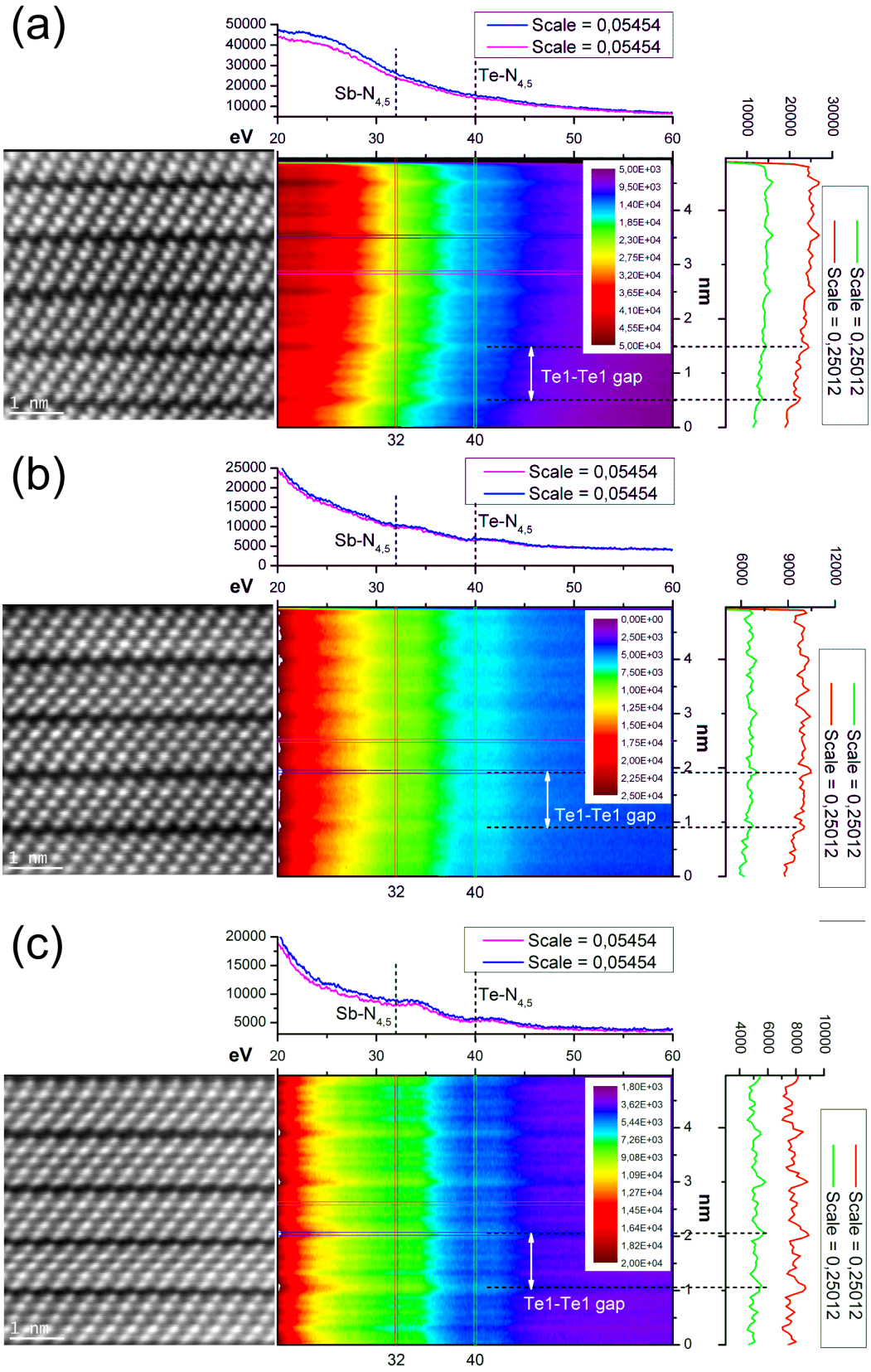

Figure 4.3.: Low-loss StripeSTEM data of $(Bi_{0.26},Sb_{0.74})_2Te_3$ for different sample thicknesses (a) 0.25 mfp, (b) 0.6 mfp, and (c) 0.86 mfp. For each subfigure (i) the HAADF STEM image is shown on the left and (ii) the color coded EELS data together with lines profiles extracted in horizontal and vertical direction on the right. The white arrows indicate the distances between subsequent van-der-Waals gaps.

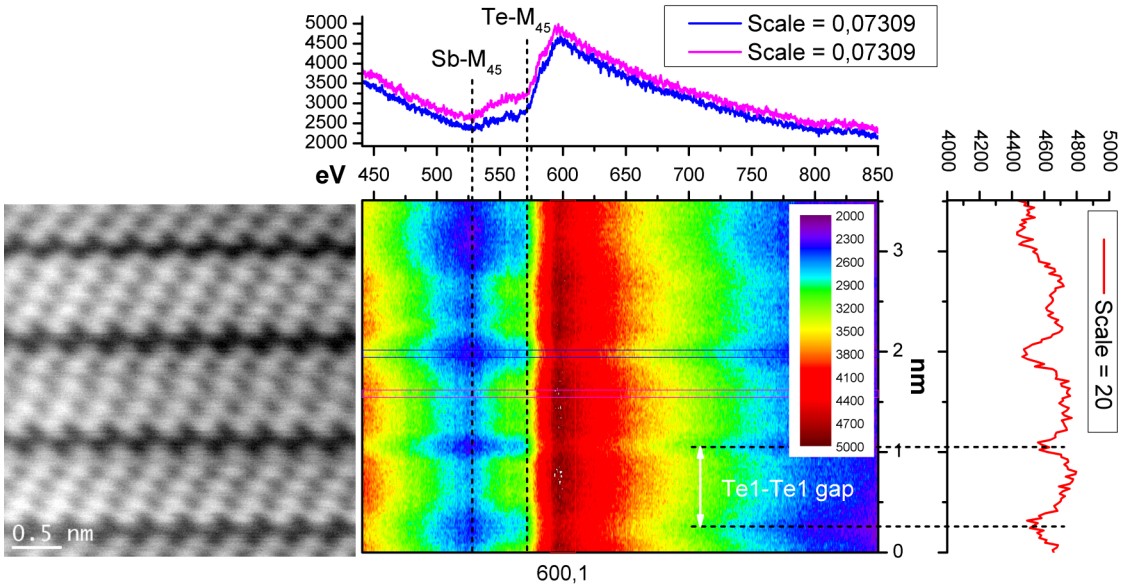

resolution

Figure 4.4.: Te-M_{45} core-loss StripeSTEM data of $(Bi_{0.26}, Sb_{0.74})_2Te_3$ for a sample thickness of 0.46 mfp. The HAADF STEM image is shown on the left and the color coded EELS data together with lines profiles extracted in horizontal and vertical direction on the right.

4.3.3. High-angle annular dark-field imaging in $DyBa_2Cu_3O_{7-x}$ coated conductors

HAADF images were acquired in an ISD coated conductor sample prepared in cross-section. For this type of samples the sample thickness was not determined for the different images and the probe size was estimated to about 2 Å from the diffractogram of Fig. 4.5a. The exact simulation parameters are listed in Tab. 4.1.

Fig. 4.5a shows an experimentally acquired HAADF images of a DyBCO coated conductor in [110] zone-axis orientation. The displayed area is located near (about 5 nm) the MgO-DyBCO interface. The image is displayed in false color to emphasize changes in the gray values. The maximum number of gray values is decreasing in Fig. 4.5 from the left to the right edge indicating a decrease in sample thickness.

Fig. 4.5b, c and d show simulated HAADF images of a DyBCO coated conductor in [110] zone-axis orientation for increasing sample thicknesses. The maximum simulated sample thickness yielding useful output was 23.1 nm. In all images the CuO chain layers appeared as dark gaps if one goes along the vertical image direction. Furthermore, significant differences in terms of gray values and resolution between experiment and simulation were observed for all thicknesses indicating that the experimental sample thickness is larger than 23.1 nm.

Fig. 4.5e shows horizontally integrated line profiles of Fig. 4.5a to d emphasize the findings in the images. It can also be observed that the intensity peaks of the single atomic columns are more homogeneous in the simulation.

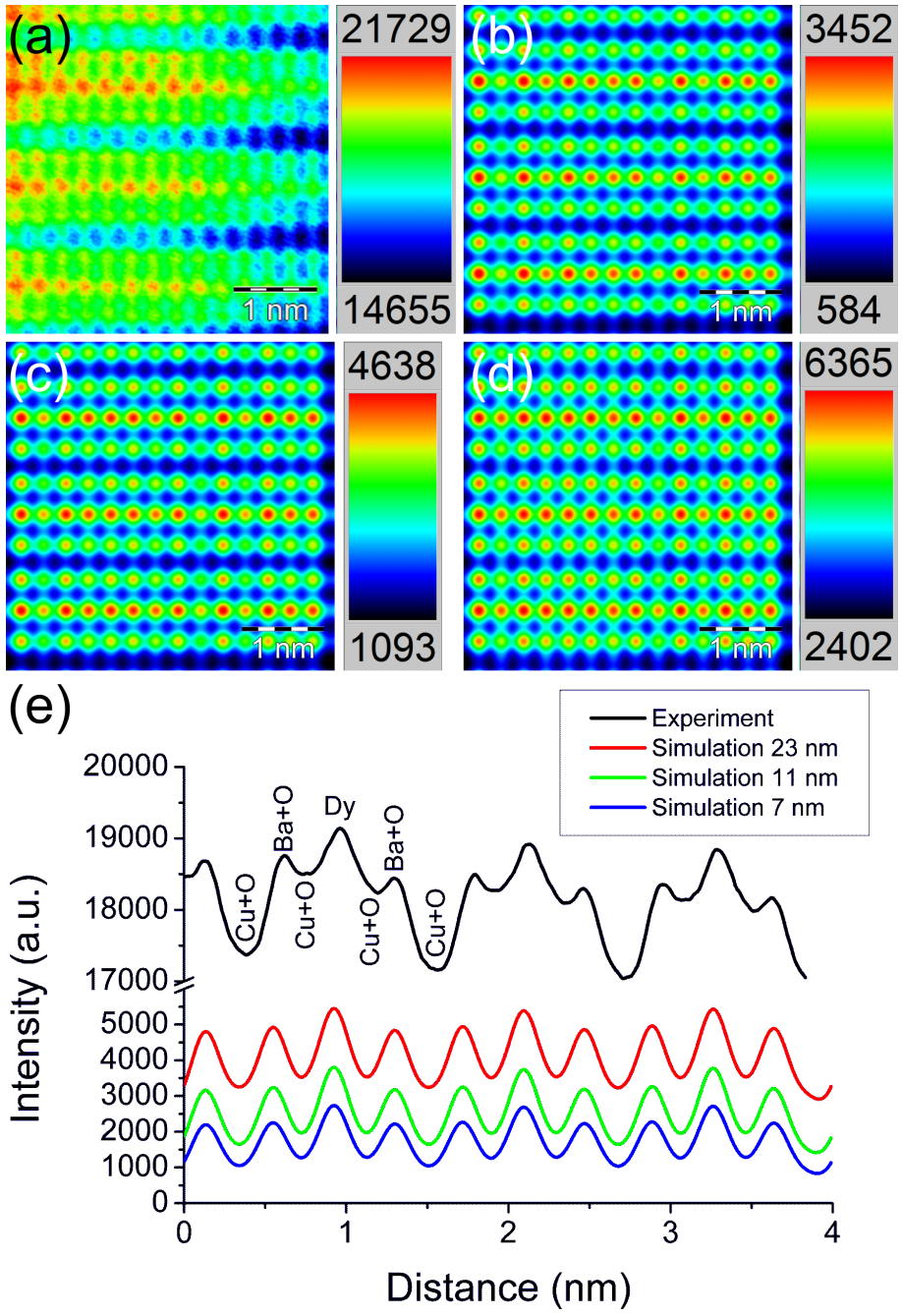

Figure 4.5.: High-resolution HAADF images of a DyBCO coated conductor in [110] zone-axis orientation. Images are shown in false colors. (a) Experimentally acquired, simulated for a sample thickness of (b) 6.8 nm, (c) 11.5 nm, and (d) 23.1 nm. (e) Vertically integrated intensity profiles of (a), (b), (c), and (d).

4.4. Discussion

4.4.1. Quantitative analysis of alloying in Bi_2Te_3 compounds in real space

Both n-type$Bi_2(Te_{0.91}, Se_{0.09})_3$ and p-type $(Bi_{0.26}, Sb_{0.74})_2Te_3$ are semi-conductors and their physical properties can be adjusted by alloying. The pseudo-hexagonal unit cell of Bi_2Te_3 (Fig.4.6a) was shown in [110] orientation to prove atomic resolution of the HAADF images. In the HAADF images (Fig.4.6b and c) the qualitative Z^2 dependence of the intensities of the atomic columns can clearly be seen: In $Bi_2(Te_{0.91}, Se_{0.09})_3$ material the heavy Bi atomic columns (Z=83) appear significantly brighter than the

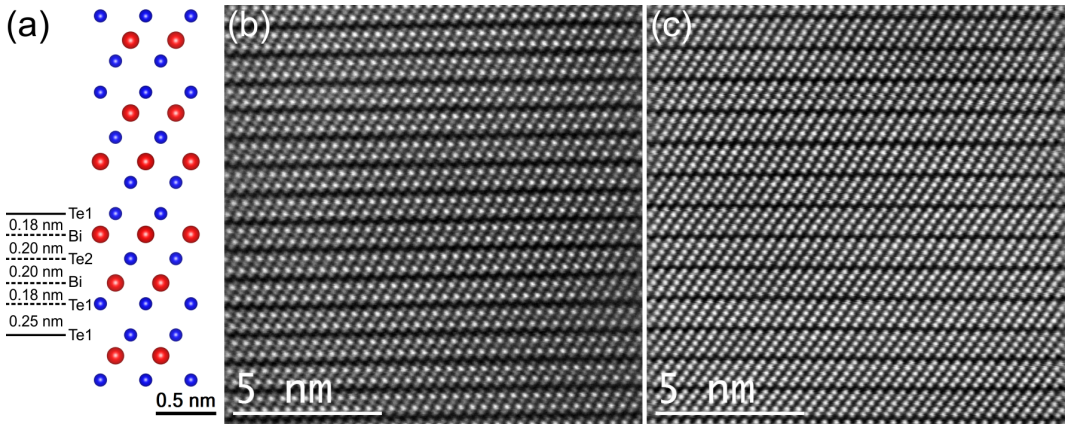

Figure 4.6.: (a) Hexagonal unit cell of Bi_2Te_3-related materials in [110] zone axis orientation. Atomically resolved HAADF image of (b) n-type $Bi_2(Te_{0.91}, Se_{0.09})_3$ and (c) p-type $(Bi_{0.26}, Sb_{0.74})_2Te_3$.

lighter Te/Se (Z=52 / Z=34) atomic columns (Fig.4.6b). In $(Bi_{0.26}, Sb_{0.74})_2Te_3$ the Bi/Sb (Z=83 / Z=34) atomic columns appear almost with the same intensity as the Te (Z=52) columns since the mean atomic number of both columns is similar. Finally, the van-der-Waals gap between the Te1-Te1 layers appeared as dark gap.

In literature HAADF images resolving individual Sb dopant atoms in Si [122] or different types of artificial atomic scale multilayer structures [126] have been reported. Therefore, quantification of alloying in Bi_2Te_3 compounds in real space should be possible by comparing experimental and simulated intensity line profiles to each other (Fig.4.1d and e, Fig.4.2d and e).

In $Bi_2(Te_{0.91}, Se_{0.09})_3$ material the best fit was obtained for a sample thickness of 40 nm (Fig.4.1d and e). The simulated line profile of the alloyed material (Fig.4.1e) fits better to the experimental one than the simulated line profile of Bi_2Te_3 (Fig.4.1d). In particular, for the Te atomic columns alloying with Se yields reduced intensities. Note that for simulation of the alloyed material the high-accuracy chemical composition as obtained by WDX spectrometry was used [134] and, thus, proving the accuracy of this method. In $(Bi_{0.26}, Sb_{0.74})_2Te_3$ material the best fit in pure material Sb_2Te_3 was obtained for a sample thickness of 40 nm (Fig.4.2d) and for $(Bi_{0.26}, Sb_{0.74})_2Te_3$ at 50 nm (Fig.4.2e). Thus, one has either to know the sample thickness or material composition to perform an unambiguous comparison between experiment and simulation. In our case the composition, i.e. $(Bi_{0.26}, Sb_{0.74})_2Te_3$, was precisely known from WDX spectrometry [134]. Note that substitution of Sb by Bi yields a slightly higher intensity at the Bi/Sb atomic columns than at the Te columns.

Another aim of the experiments was to prove that even for compounds with heavy elements HAADF Z-contrast imaging is superior to HRTEM phase contrast imaging. The acquisition of HAADF images acquired in Bi_2Te_3 materials at various thicknesses have shown that the image contrast does only slightly change with sample thickness. This is particularly beneficial for real-life TEM samples with thicknesses in the range between 10 nm to 100 nm as used here. In contrast, in HRTEM phase contrast images a reversal of contrast is already observed at sample thicknesses larger than 10 nm [2]. However, thin TEM samples are difficult or impossible to prepare due to practical reasons.

Our calculations of atomically resolved HAADF images did not include thermal diffuse scattering (TDS), i.e. inelastic scattering of electrons on phonons. They can be enhanced by including this scattering mechanism to more accurately match the experimental images, since TDS is responsible for most of the high-angle scattering. Bi_2Te_3-related materials have an ideal potential for high-accuracy quantitative HAADF image analysis on the atomic scale and only few (quantitative) STEM studies exist for this material class.

4.4.2. Simultaneous atomic resolution imaging and EEL spectroscopy in p-type $(Bi_{0.26},Sb_{0.74})_2Te_3$

The StripeSTEM experiments, i.e. simultaneous acquisition of atomically resolved HAADF images and EEL spectra at the elemental layers, allow to correlate the atomic structure with the chemistry or the atomic bindings. According to Heidelmann et al. [127] the spatial resolution is as good as in a column-by-column measurement. However, specimen drift and the signal-to-noise ratio are much better in StripeSTEM measurements. The results presented here are the first ones obtained in Bi_2Te_3 materials.

The StripeSTEM experiments conducted at low electron energy-losses yielded for all thicknesses a layered structure as seen in the color coded EELS map (Fig.4.3). The van-der-Waals gaps between the Te1-Te1 layers could be identified for all thicknesses since the vertical line profiles within the spectral data matched exactly with the gaps seen in the HAADF images. However, individual elemental layers could not be identified in the EELS data. Specimen drift limited the spatial resolution. A clear dependence of the spectral data on specimen thickness was not observed in Fig.4.3.

Also, the core-loss StripeSTEM experiments yielded a layered structure, in particular, the van-der-Waals gap as seen in the EELS data matched with the gaps seen in the HAADF image. Again, individual elemental layers could not be identified in the EELS data. The core-loss EELS data were altogether noisier than in the low-loss case due to the high dynamics in EEL spectra. Specimen drift and charging effect were quite severe for this case.

The van-der-Waals gaps in Bi_2Te_3 materials were unambiguously identified by the StripeSTEM method. These gaps yield important materials properties: (i) Bi_2Te_3 materials can easily be cleaved along the basal plane due to the weak bondings at this gap. (ii) Highly mobile gliding dislocations in the basal plane were observed, which are assumed to yield enhanced scattering of phonons and thus low thermal conductivities [132]. (iii) Impurity atoms might be easily introduced and diffuse along this gap. In particular, the natural nanostructure (nns) [139] is believed to have its origin in Ar atoms introduced by ion-milling and diffusing along the van-der-Waals gaps. The nns is a pure structural modulation with a strong strain field which significantly scatters phonons and reduces the thermal conductivity in these materials [131]. This opens an essentially new way to implement a phonon-glass / electron-crystal (PGEC) [140, 128] type of material, which is the key to optimize the thermoelectric materials properties for a high thermoelectric figure-of-merit ZT. So far, however, a StripeSTEM analysis of TEM sample with a nns has not been carried out.

4.4.3. Quantitative image simulation in $DyBa_2Cu_3O_{7-x}$ coated conductors

Fig.4.7a shows the orthorhombic unit cell of DyBCO in [110] orientation to prove the atomic resolution obtained in Fig.4.7b. In experimental atomically-resolved HAADF images of DyBCO coated conductors (Fig.4.7b) the Dy columns are the brightest atomic columns followed by the Ba/O columns. The Cu/O columns could not be resolved in the HAADF image as individual peaks, they are rather valleys in between the Dy and Ba peaks. Pennycook and Boatner [119] did similar experiments on $ErBa_2Cu_3O_{7-x}$. The intensity they observed was also brightest for the Er atomic columns, less for the Ba columns, and least for the Cu columns. They also acquired a thickness series of atomically-resolved HAADF images in $YBa_2Cu_3O_{7-x}$ finding that the relative contrast of the single layers does not change with the sample thickness only the overall contrast due to electron absorption. For the atomically-resolved HAADF images of DyBCO coated conductors we would expect a similar behavior, which was observed in the experiment, but not in the simulation. There are the following reasons why this is the case: (i) Technical difficulties during the image acquisition occurred and the exact acquisition conditions are not fully known, (ii) the coated conductor grains are not single crystalline areas like in the Bi_2Te_3 but rather containing lots of crystal defects, and (iii) the analyzed sample area was quite thick (about 100 nm). For the simulation of atomically-resolved HAADF images of the DyBCO coated conductors crystalline defects were not considered.

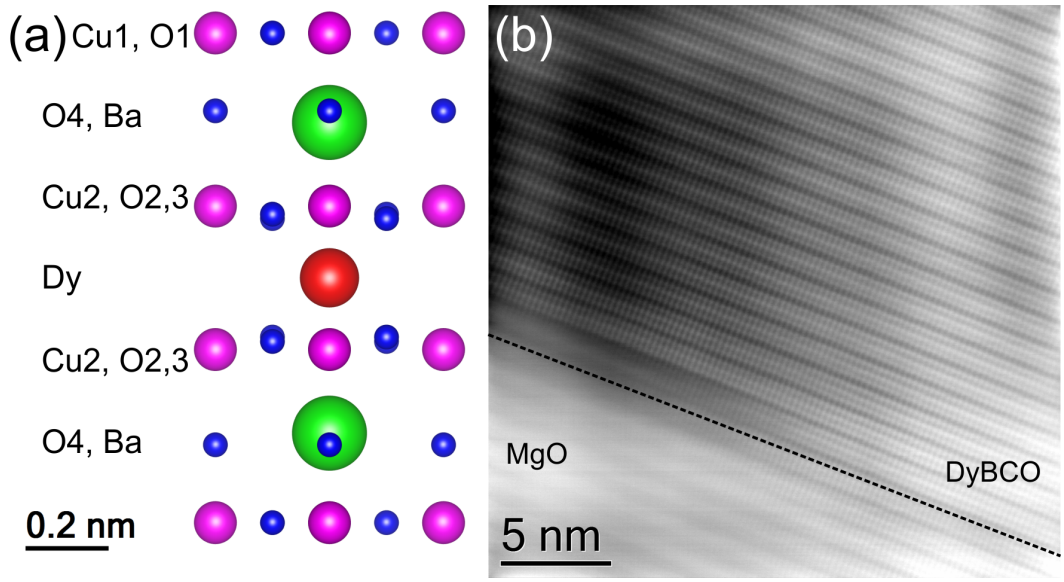

Figure 4.7.: (a) Orthorhombic unit cell of DyBCO in [110] zone axis orientation. (b) Atomically resolved HAADF image of the MgO/DyBCO interface.

4.5. Summary

Atomically resolved HAADF images of thermoelectric n-type$Bi_2(Te_{0.91}, Se_{0.09})_3$ and p-type $(Bi_{0.26}, Sb_{0.74})_2Te_3$ and of DyBCO coated superconductors were simulated for different sample thicknesses and compared to experimental images. It was shown that the influence of alloying on the HAADF image intensity could be proven for Bi_2Te_3-related compounds. An very good fit of experimental and simulated images was found by including the alloying in the simulation, therefore, we were able to image alloying in real space. The van-der-Waals gap between Te1-Te1 layers were identified in the StripeSTEM experiments by correlating the EELS data with the simultaneously acquired atomically resolved HAADF images. In case of the DyBCO coated superconductors atomic resolution could be demonstrated.

5. Electron scattering and electronic transport quantities in thermoelectric materials

5.1. Introduction

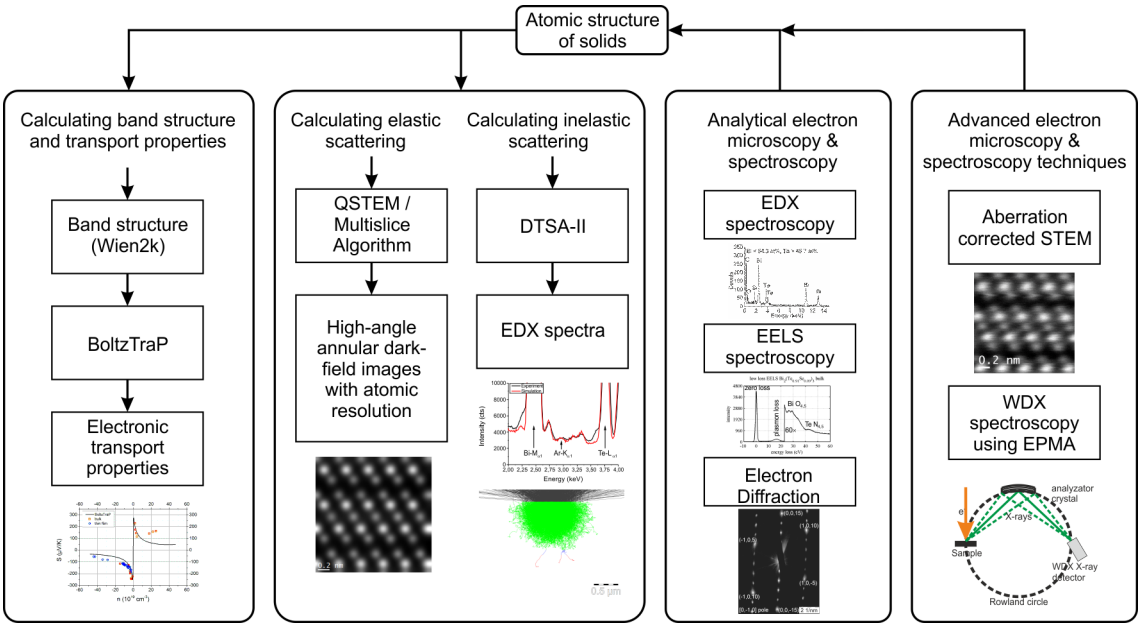

Figure 5.1.: Linking microscopy and spectroscopy results obtained by analytical TEM with calculations of the electronic transport properties and scattering of high-energy electrons.

The overall goal is to link the physical properties with the nanostructure of a material. The link of this chapter with the others might not be obvious to the reader on the first instance. The link will be explained using Fig. 5.1 in thefollowing way: The starting point is the atomic structure and the chemistry of a solid. The atomic structure of a solid is determined by electron diffraction, high-resolution (scanning) transmission electron microscopy (HR(S)TEM). The chemical composition is determined by analytical methods like energy-dispersive X-ray (EDX) analysis and electron energy-loss spectroscopy (EELS) up to the atomic level. Wavelength-dispersive X-ray (WDX) analysis applied in an electron-probe microanalyzer is used due to the superior energy resolution and detection limit compared to EDX. In a next step, the obtained results are integrated into a model structure, which is the basis for the simulation of microscopic sample properties like Z-contrast images and EDX spectra. The atomic structure and the chemical composition of a material are necessary to determine its band structure by e.g. density functional theory methods implemented for example in the Wien2k code [141]. The band structure itself is the basis for calculating macroscopic (electronic) transport properties like electrical conductivity σ, thermopower S, and the thermal conductivity κ by solving the linearized Boltzmann equation. These quantities can be finally compared to macroscopic, experimental measurements of transport quantities.

The software package BoltzTraP (**Boltz**mann **Tra**nsport **P**roperties) [142] is one possibility to calculate the transport coefficients by solving the linearized Boltzmann equation. BoltzTraP uses a Fourier sum to fit energy bands, which provides a simple basis for the following integrations for obtaining transport

coefficients. Since energy bands are given as Fourier sums, their derivatives yield the velocities and their second derivatives yield the curvature or inverse effective masses. Both quantities are used for calculating the electronic transport coefficients. The idea of this procedure was developed in 1986 by Koelling and Wood [143] and was implemented into code by the work of Madsen and Singh in 2006 [142]. However, BoltzTraP up to version 1.2.1 does not consider phononic contributions to e.g. the thermal conductivity $\varkappa$ and assumes an energy independent relaxation time τ. However, phononic contributions to the transport coefficients are in general not negligible.

The implementation of BoltzTraP is briefly explained. The key equations are mentioned and the subroutines in which they are being calculated are given. The reader can follow step by step the most important formulas and check the corresponding code. It starts with the definition of the star function and ends with the transport coefficients. More than 10 output files are being generated. They allow the user to check the results on a more detailed level. BoltzTraP operates in three spaces: real space, reciprocal space, and energy space. The transfer from k space to energy space via the density of states is of particular importance.

5.2. Implementation of semi-classical transport equations

The BoltzTraP code is based on the Fourier expansion of band energies, maintaining the space group symmetry using star functions. The program structure is shown in Fig. 5.2. The band structure provided, e.g. by a Wien code [144] file is read via the subroutine "read_input". The mode "CALC" is used for calculating the Fourier expansion coefficients. In case of "NOCALC" the expansion coefficients have to be loaded from the binary file "case.engre". The calculation of the energies $\bar{\varepsilon}_i$ in Rydberg (Eq. 5.1) and the star functions S (Eq. 5.2) are done in BoltzTraP according to Pickett et al. [145, 142] and are carried out in the files "fite4.f90", "bands.f90" (subroutine "bands"), and "stern1.f90" (subroutine "stern1").

$$\bar{\varepsilon}_i(\mathbf{k}) = \sum_{\mathbf{R}} c_{\mathbf{R},i} S_{\mathbf{R}}(\mathbf{k}) \tag{5.1}$$

$$S_{\mathbf{R}}(\mathbf{k}) = \frac{1}{n} \sum_{\Lambda} e^{i\mathbf{k}\Lambda\mathbf{R}} \tag{5.2}$$

R is a direct lattice vector, **k** is a reciprocal lattice vector, and Λ are the n point group rotations in the space group (they can be found at the end of the "*.struct" file). Please note that BoltzTraP always uses primitive instead of conventional lattices, in particular, for Bi_2Te_3 rhombohedral direct and reciprocal base vectors instead of hexagonal ones have to be used (see appendix for transformation). For other crystal systems such as fcc (face-centered cubic) and bcc (base-centered cubic) similar transformations are implemented (see p. 145 in [146]). Correct band energies ε_i are obtained by fitting the $\bar{\varepsilon}_i$ such that $\bar{\varepsilon}_i = \varepsilon_i$ holds, more star functions than band energies are used, and a roughness function is minimized [142, 145]. The expansion coefficients $c_{\mathbf{R},i}$ are calculated in subroutine "fite4" in file "fite4.f90".

The first and the second derivatives in k-space of the band structure $\varepsilon_i(\mathbf{k})$ required for the group velocity $v_\alpha(i,\mathbf{k}) = \frac{1}{\hbar}\frac{\partial \varepsilon_{i,\mathbf{k}}}{\partial k_\alpha}$ and the inverse mass tensor $M^{-1}_{\beta u}(i,\mathbf{k}) = \frac{1}{\hbar^2}\frac{\partial^2 \varepsilon_{i,\mathbf{k}}}{\partial k_\beta \partial k_u}$, respectively, are calculated in the subroutine "setfft" in file "setfft.f90" (see Listing 5.1). The related grids are named energygrid, velocitygrid, and curevaturegrid. Please note that all grids in subroutine "setfft" are still in real space. The transformation to reciprocal space is done in subroutine "dos" in file "dos.f90" via fast fourier transformations. The density of states is also calculated in the subroutine "dos" and saved in the second column of the file "*.transdos".

The conductivity tensors $\sigma_{\alpha\beta}(i,\mathbf{k})$ and $\sigma_{\alpha\beta\gamma}(i,\mathbf{k})$ are calculated according to eq. 9 and 10 in [142] in the subroutine "dos_histogram" using the energy grid, velocity grid, and curvature grid calculated

Listing 5.1: Source code of the BoltzTraP subroutine setfft.

```
SUBROUTINE setfft(energygrid,velocitygrid,curvaturegrid,ifft,value)
  USE defs
  USE bandstructure
  USE lattice_points ! lattice points without stars generated in latgen2; contains only integer values
  IMPLICIT NONE
  INTEGER, INTENT(IN)      :: ifft(3) ! max. array sizes
  REAL(8), INTENT(IN)      :: value(nwave) ! engre values
  COMPLEX(8), INTENT(OUT) :: energygrid(ifft(1),ifft(2),ifft(3)) ! bandstructure
  COMPLEX(8), INTENT(OUT) :: velocitygrid(ifft(1),ifft(2),ifft(3),3) ! group velocity
  COMPLEX(8), INTENT(OUT) :: curvaturegrid(ifft(1),ifft(2),ifft(3),6) ! inverse effective mass
  INTEGER                  :: i,nw,nst
  INTEGER                  :: ii,jj,i1,i2,i3,index
  REAL(8)                  :: vec(3,1),mat(3,3),stg(3,nsym)
  REAL(8)                  :: br(3,3)

  br=MATMUL(aac_dir,p2c_dir) ! real space primitive (in case of Bi2Te3 rhombohedral) base vectors in column form; units: bohr
  energygrid=CZERO    ! initialize with zero
  velocitygrid=CZERO  ! initialize with zero
  curvaturegrid=CZERO ! initialize with zero
  DO nw=1,nwave
     CALL stern1(latt_points(1,nw),nsym,symop,nst,stg) ! star function
     DO i=1,nst ! number of stars
        i1=INT(stg(1,i)+SIGN(test,stg(1,i)))
        i2=INT(stg(2,i)+SIGN(test,stg(2,i)))
        i3=INT(stg(3,i)+SIGN(test,stg(3,i)))
        IF(i1.LT.0) i1=i1+ifft(1)
        IF(i2.LT.0) i2=i2+ifft(2)
        IF(i3.LT.0) i3=i3+ifft(3)
        energygrid(i1+1,i2+1,i3+1)=value(nw)/nst
        vec(1:3,1)=MATMUL(br,stg(1:3,i)) ! star vector as function of primitive base vectors in bohr units (s = n1*a1+n2*a2+n3*a3)
        mat=MATMUL(vec,TRANSPOSE(vec))
        index=0
        DO ii=1,3
           velocitygrid(i1+1,i2+1,i3+1,ii)=IMAG*vec(ii,1)*value(nw)/nst ! assign the group velocities
           DO jj=1,ii
              index=index+1
              curvaturegrid(i1+1,i2+1,i3+1,index)=-mat(ii,jj)*value(nw)/nst ! assign the inverse effective masses
           ENDDO
        ENDDO
     ENDDO
  ENDDO
END SUBROUTINE setfft
```

previously. The conductivity tensors are being energy projected (switch from k-space to energy space) according to eq. 11 in [142] inside subroutine ”noculc” (in file “noculc.f90”) and then used to calculate the Fermi integrals inside the subroutine ”fermiintegrals” (in file “fermiintegrals.f90”). The conductivity tensors are saved into the files “*.sigxx” and “*.sigxxx”.

The output of the subroutine ”fermiintegrals” are the transport tensors calculated according to equations 12-17 in [142]. The transport tensor traces are written in dependence on the chemical potential μ in Rydberg and the temperature T in K into the file “*.trace”, whereas the all transport tensor components can be found explicitly in the files “*.condtens” and “*.halltens”. For the complete file structure of both files see Tab.5.1. A complete list of in and output files as well as the source code files including a description is given in Tab.5.2 and Tab.5.3.

(a) *.trace

Column	Quantity	Unit
1	Chemical potential μ	Ry
2	Absolute temperature T	K
3	Number of carriers per unit cell	$\frac{e}{u.c.}$
4	Density of states n(μ)	
5	Seebeck coefficient	$\frac{V}{K}$
6	Electrical conductivity σ divided by the relaxation time τ	$\frac{1}{\Omega m s}$
7	Hall coefficient R_H	$\frac{m^3}{C}$
8	Electronic thermal conductivity ϰ divided by the relaxation time τ	$\frac{W}{mKs}$
9	Electronic specific heat c	$\frac{J}{mol\,K}$
10	Pauli magnetic susceptibility χ	$\frac{m^3}{mol}$

(b) *.condtens.

Column	Quantity	Unit
1	Chemical potential μ	Ry
2	Absolute temperature T	K
3	Number of carriers per unit cell	$\frac{e}{u.c.}$
4-13	Electrical conductivity σ divided by the relaxation time τ; component order: xx, xy, xz, yx, yy, yz, zx, zy, zz	$\frac{1}{\Omega m s}$
14-23	Seebeck coefficient; component order: xx, xy, xz, yx, yy, yz, zx, zy, zz	$\frac{V}{K}$
24-33	Electronic thermal conductivity ϰ divided by the relaxation time τ; component order: xx, xy, xz, yx, yy, yz, zx, zy, zz	$\frac{W}{mKs}$
34-61	27 Hall coefficients R_H	$\frac{m^3}{C}$

Table 5.1.: File structure of the *.trace and *.condtens file.

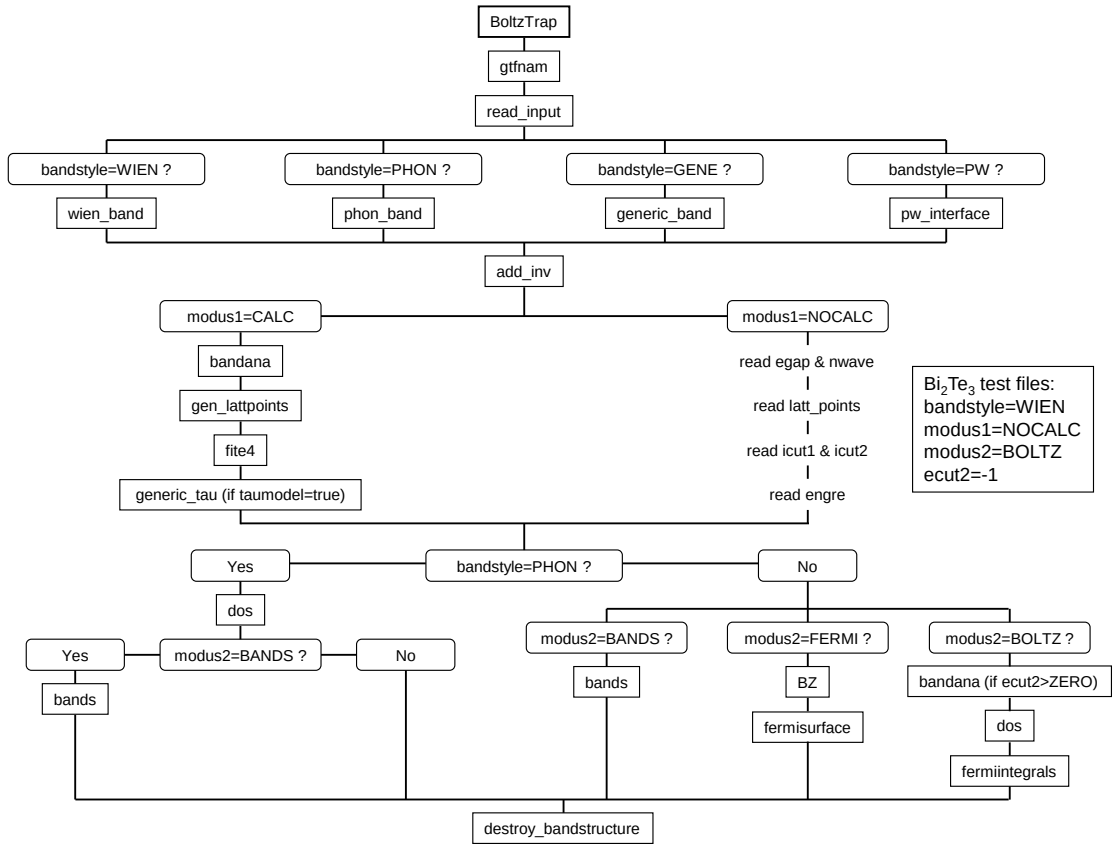

Figure 5.2.: Scheme of the different modules being invoked in BoltzTraP.

Table 5.2.: In and output files used by BoltzTraP including their description.

File	File name	status	format	subroutine	comment
5	Bi2Te3.intrans	old	formatted	read_input	stores the input variables of BoltzTraP
6	Bi2Te3.outputtrans	unknown	formatted	bandana	stores the output generated by BoltzTraP
10	Bi2Te3.energyso	old	formatted	gene_energy files_symms(), wien_structfile	energy-file, reading nkpt and nband
20	Bi2Te3.struct	old	formatted	gene_energy files_symms(), wien_structfile	Read the WIEN2k crystal structure file
21	Bi2Te3.trace	unknown	formatted	fermiintegrals	Trace values of the transport tensors
22	Bi2Te3.condtens	unknown	formatted	fermiintegrals	individual components of the transport tensors (3+9+9+9 columns)
24	Bi2Te3.halltens	unknown	formatted	fermiintegrals	individual components of the Hall tensors (3+27 columns)
25	Bi2Te3.trace	unknown	formatted	fermiintegrals	same as file 21 if doping is considered
26	Bi2Te3.condtens	unknown	formatted	fermiintegrals	same as file 22 if doping is considered
30	Bi2Te3_BZ.dx	unknown	formatted	write_CUBE_FS; write_dx_BZ	Fermi surface? Wigner construction of Brillouin zones?
31	Bi2Te3_fermi.dx	unknown	formatted	fermisurface, write_dx_fs	not accessible without modification of the source code
32	Bi2Te3_sigxx.dx	unknown	formatted	fermisurface, write_dx_fs	not accessible without modification of the source code
33	Bi2Te3_sigyy.dx	unknown	formatted	fermisurface, write_dx_fs	not accessible without modification of the source code

37				bands	First derivative of the band structure E(k)
34	Bi2Te3_sigzz.dx	unknown	formatted	fermisurface, write_dx_fs	not accessible without modification of the source code
35	Bi2Te3_band.dat	unknown	formatted	bands	Band structure E(k)
36	Bi2Te3_band.gpl	unknown	formatted	gplbands	plot band structure?
38				bands	Second derivative of the band structure E(k)
48	Bi2Te3.engre	unknown	formatted	fite4	Fourier coefficients of the bandstructure eq. 1 [142]
49	Bi2Te3.transdos	unknown	formatted	dos	Energy, density of states (dos1)
50	Bi2Te3.sigxx	unknown	formatted	dos	transport distribution
51	Bi2Te3.sigxxx	unknown	formatted	dos	transport distribution

Table 5.3.: Complete list of sources files included into BoltzTraP version 1.2.3.

File #	File name	File Size [kB]	File description
1	add_inv.F90	1	Add center off symmetry for non-centrosymmetric lattices
2	bandana.F90	4	Sets the range of bands used by BoltzTraP to calculate transport coefficients
3	bands.F90	5	Calculates the bands used for the transport coefficients and their derivatives. Output in files 35, 37, 38
4	BoltzTraP.F90	11	Main program
5	boseintegrals.F90	13	Phonon contribution to transport coefficients
6	bz.F90	3	Brillouin zone according to Wigner-Seitz construction.
7	c3fft.F90	71	3D Fast Fourier Transform.
8	crystal_band.F90	10	Lattice data from CRYSTAL interface
9	dos.F90	8	Calculates the density of states, i.e. transforms the k space into the energy space
10	dosvv.F90	5	Calculates unit density of states

11	dos_histogram.F90	4	Calculates the conductivity tensors sigma eqs. 9 - 11 in [142] using the histogram method.
12	dos_tetra.F90	7	Calculates the conductivity tensors sigma eqs. 9 - 11 in [142] using the tetrahedron method.
13	fermiintegrals.F90	14	Calculates the electronic transport coefficients; eqs. 12-15 in [142]
14	fermisurface.F90	5	Calculates Fermi surfaces
15	fite4.F90	6	Implements the eqs. 1 - 5 of [142]
16	generic_band.F90	5	Reads Siesta Abinit and PWSCF band structure data.
17	generic_lifetime.F90	1	Implements a life time dependency of the transport coefficients
18	gen_lattpoints.F90	5	Fills all lattice vectors with length shorther than gmax into the array latt_points
19	gmlib2.F90	10	Physical constants and utility functions e.g. cross product calculation etc.
20	gplbands.F90	3	bandstructure plot
21	gtfnam.F90	2	Gets the file names
22	ifflim.F90	1	??
23	gtfnam.F90	2	Gets the file names of the in and output files of BoltzTraP
24	kdelta.F90	0	Tests if k is in star of g
25	latgen2.F90	4	Calculates real and reciprocal space lattice vectors, transformation into "primitive" lattice vectors according to ch. 1-2 of [146].
26	Makefile	2	Makefile for a Linux Fortran compiler, e.g. gefortran
27	m_bandstructure.F90	5	Initializes or destroys the band structure
28	m_bspline.F90	73	B-spline interpolation in one, two, and three dimensions. Used by Abinit.
29	m_fermimod.F90	4	??
30	m_input.F90	4	Reads the input variables from the case.intrans file
31	m_interfaces.F90	14	Contains different interfaces.
32	noculc.F90	8	Inspired from a noculc.f in WIEN2k

33	phonondrag.F90	15	Routine to calculate the phonon drag contribution to the Seebeck coefficient. Requires electron and phonon group velocities, and the estimation of 2 relaxation times, for el-ph and ph-ph processes. The momentum transfer to electrons is determined by the fraction of electrons which are scattered to higher momentum states by not-yet-equilibrated phonons coming from the hot side. Currently (19/3/2013) implements formula from Cantrell J Phys C 20, pp. 1985-1992 (1987) equation 42, with the matrix element P replaced by a constant times N_Q times delta functions for energy and k conservation.
34	phon_band.F90	3	PHON-WIEN interface, reads band structure data
35	pw_interface.F90	2	Interface for pwsic band structure style.
36	readvv.F90	2	Read group velocities?
37	reallocate.F90	3	Dynamic extension of FORTRAN arrays
38	setfft.F90	2	Initializes the energy grid, velocity grid and curvature grid
39	setfft2.F90	1	Initializes the energy grid, velocity grid and curvature grid
40	sortag.F90	4	To sort a vector into increasing order from A(1) to A(N), a may be type real or type integer. Vector TAG is permuted the same as vector A.
41	stern1.F90	2	Calculates the star of g
42	wien_band.F90	8	Reads the band structure data from Wien2k
43	write_cube_fs.F90	1	??
44	write_dx_bz.F90	3	??
45	write_dx_fs.F90	2	??
46	x_trans	9	Linux console script to organize the BoltzTraP input files

5.3. Compiling and running BoltzTraP

The BoltzTraP code is freely available on the ICAMS website [147] and was compiled on a Dell Precision T7500 workstation with the properties listed in Tab. 5.4. For this work BoltzTraP version 1.2.1 was used. The compilation can be conducted either on Linux or on Windows. Both possibilities were tested. The operating systems and the used compiler software as well as additional packages needed are also summarized in Tab. 5.4.

Property description	Property
Processors	2x Intel Xeon X5690 @ 3.47 GHz
RAM	64 GB
Operating system	openSuse Linux 12.1, Windows Server 2008 R2
Fortran Compiler	Gnu Fortran compiler 4.6 (Linux), Intel Composer XE 2011 integrated into Microsoft Visual Studio 2010 (Windows)
Additional packages needed	csh, LaPack and Blas (Linux), Intel MKL library (Windows)

Table 5.4.: Properties of the Dell Precision T7500 workstation. Please note that the additional libraries are available via the standard openSuse repositories. The Intel MKL library is part of the Intel Composer XE 2011.

5.3.1. Linux

In Linux Makefiles are used to organize the compilation of the Fortran code. In case of BoltzTraP a Makefile is already provided inside the "*/src*" folder. Please note that all paths quoted in the text are inside the BoltzTraP program folder. The Makefile (see List. Listing 5.2) was slightly modified since the latlas library is not present in the openSuse standard repositories and the program also works without using it but might be less efficient. The compilation and linking process is started if you change inside the terminal window to the "*/src*" directory and type "make -f Makefile". This executes the gfortran compiler with the selected options and links the files. Finally a BoltzTraP executable is generated. BoltzTraP can be used now.

The csh package is needed to run the "*x_trans*" shell script located in the "*/src*" folder which generates a file called "*BoltzTraP.def*" and runs the BoltzTraP executable. The "*BoltzTraP.def*" files associates the Fortran file number with the file name used by the operating system. The input test files as well as some reference output files of, e.g. Bi_2Te_3 can be found in the folder "*/tests/Bi2Te3*" and "*/tests/Bi2Te3/Reference*", respectively. At present time (BoltzTraP v. 1.2.1) only transport properties can be calculated since the modes "FERMI" and mode "BANDS" are not supported yet, i.e. the output of files #30-#38 is empty.

BoltzTraP can be called via command-line by typing "*BoltzTraP ../../src/x_trans*" if the BoltzTraP executable and the "*x_trans*" shell script are located inside the "*/src*" folder. This will automatically take care of the necessary file actions. Please note that the folder containing the input files has to have the same name as the input files otherwise an error will be thrown. The output files are in text form and can be imported in, e.g. Matlab for further processing.

5.3.2. Windows

In Windows the situation is different than under Linux. No Makefiles and console scripts are needed since with the Microsoft Visual Studio a completely Graphical User Interface based software is available. The only drawback is that you need to install the commercial Intel Fortran Compiler (included e.g. in Intel Parallel Studio XE 2011), which integrates easily into Microsoft Visual Studio. However, the great benefit is that you can debug in Visual Studio in an intuitive way and track the variable values. This was one key for understanding the code of BoltzTraP. The procedure is as follows:

Listing 5.2: BoltzTraP Makefile for the gfortran compiler.

```
SHELL = /bin/sh
gfortran
FC = gfortran
FOPT = -g -Wall -pedantic -march=native -funroll-loops -O3 -ffast-math -fgcse-lm -fgcse-sm -ffast-math -ftree-vectorize -fexternal-blas -fbounds-check -finit-integer=-666 -finit-real=nan
LDFLAGS =
LIBS = -llapack -lblas

EXECNAME = BoltzTraP

############################################################
FFLAGS = $(FGEN) $(FOPT) EXEC = $(DESTDIR)/$(EXECNAME)
#.....................................................#

# Object files common to both REAL and COMPLEX type subroutines #

OBJS = reallocate.o gmlib2.o latgen2.o m_bandstructure.o m_input.o gtfnam.o gen_lattpoints.o BoltzTraP.o wien_band.o phon_band.o generic_band.o add_inv.o bandana.o stern1.o kdelta.o fite4.o sortag.o gplbands.o dos.o ifflim.o setfft.o c3fft.o fermiintegrals.o bands.o kcomp.o bz.o fermisurface.o setfft2.o write_dx_fs.o write_dx_bz.o write_cube_fs.o dos_histogram.o dos_tetra.o noculc.o

$(EXEC): $(OBJS) $(LINKER) $(LFLAGS) -o $(EXEC) $(OBJS) $(LDFLAGS) $(LIBS) $(LFLAGS)

clean: rm -f *.o *.mod *.pc *.pcl *~
.SUFFIXES: .F90 .o
.F90.o: $(FC) $(FFLAGS) -c $<
```

1. Generate a new Fortran project
2. Add the BoltzTraP source files to the project
3. Go to the project property page (“Eigenschaftsseite”) and set under “Konfigurationseigenschaften/-Fortran/Libraries” the option “Use Intel Math Kernel Library” to “Parallel (/Qmkl:parallel)”. If this option is not set a Linker error will occur indicating that in file “fite4” the external subroutines “DGEMM”, “DGETRF”, and “DGETRS” cannot be resolved.
4. The compilation process can be started via “Erstellen/Projektmappe erstellen” or by just pressing F7.he band structure of Bi_2Te_3 is used to calculate its macroscopic transport properties.
5. Generate a “BoltzTraP.def” file for your simulation. Please note that all files have the same name as the directory they are stored in. Example: if the folder is named “case” then the files have to named “case.intrans”, “case.struct”, “case.energy(so)”, and “case.engre”.
6. Last point before BoltzTraP can be executed is that you need to set the command line argument in ”Konfigurationseigenschaften/Debugging” to the value ”BoltzTraP.def” if it is already in your Visual Studio project folder. It tells Visual Studio where to find the input files.
7. If you additionally want to debug please select the following points:
   a) Set in “Configuration/Fortran/Debugging” all available settings (3).
   b) Set in “Configuration/Linker” the property “Generate Debug Info” to “Yes”.
   c) Select the desired break points in the code by right-click and choosing set break point.
   d) Then, after you started the debugging by pressing F5 and the program ran into the first break-point, select the desired variable(s) for monitoring by right-click and ”Überwachung hinzufügen”. The variable value will then be shown in the ”Überwachen” window, which is usually placed below the editor window.

5.4. Results and Discussion

The results shown here were calculated for Bi_2Te_3 using the input files provided with the code. In a first step the obtained results were compared to the provided reference files. In a second step the obtained data was compared to experimental transport properties measured in bulk and thin films [148].

5.4.1. Verification of the obtained results with respect to reference data for the case of bulk Bi_2Te_3

Fig. 5.3a shows the density of states (DOS) depending on the chemical potential μ of Bi_2Te_3 in a range of ± 4 eV around the band gap. An almost perfect match of our calculation (solid black curve) with the reference (dashed red line) one was obtained. Furthermore, the form of the DOS and its values agree with those found in literature for Bi_2Te_3 [149, 150, 151].

The room-temperature (300 K) electrical conductivity σ parallel (labeled as "xx") as well as perpendicular (labeled as "zz") to the basal plane of Bi_2Te_3 is shown in Fig. 5.3b. For both directions calculated (solid black and red curve) and reference (dashed orange and blue curve) plots were compared yielding a perfect match of the calculated with the reference curves.

Fig. 5.3c shows the (solid black and red curve) and the reference (dashed orange and blue curve) in-plane ("xx") and out-of-plane ("zz") thermopower S of Bi_2Te_3 at 300 K in dependence of the chemical potential μ. Again all calculated curves match to their reference ones perfectly. The thermopower vs. μ plots found in literature [142, 150, 149] do also match in form and values with our calculation.

The electronic contribution to the thermal conductivity κ in dependence on μ is shown in Fig. 5.3d. The line and color coding is the same as for the electrical conductivity. Also here a perfect match between our calculation and the reference was found. Also a good agreement with the literature [142] was found where κ is compared to the Wiedemann-Franz law. However, if compared to experimental values one has to note that the phononic part of the thermal conductivity is not contained in the BoltzTraP calculations.

In Fig. 5.3e and f the power factor PF and the thermoelectric figure of merit ZT are shown in dependence on μ. Both are derived quantities:

$$PF = S^2\sigma \tag{5.3}$$

$$ZT = \frac{PF}{\kappa}T \tag{5.4}$$

The line and color convention was kept also for both plots. Since the original in-plane and out-of-plane quantities did not yield any deviation between calculation and reference, also PF and ZT yielding a perfect match for both directions, respectively. The PF plots also match with the ones found in literature [142, 150] quite well in form and values. However, for ZT our calculation and the literature [150] differ significantly. This can be explained with a different κ being used, since the PF values are matching quite well. In our calculation only the electronic part of κ is used whereas in the literature also the phononic part is considered since an experimentally acquired κ was used.

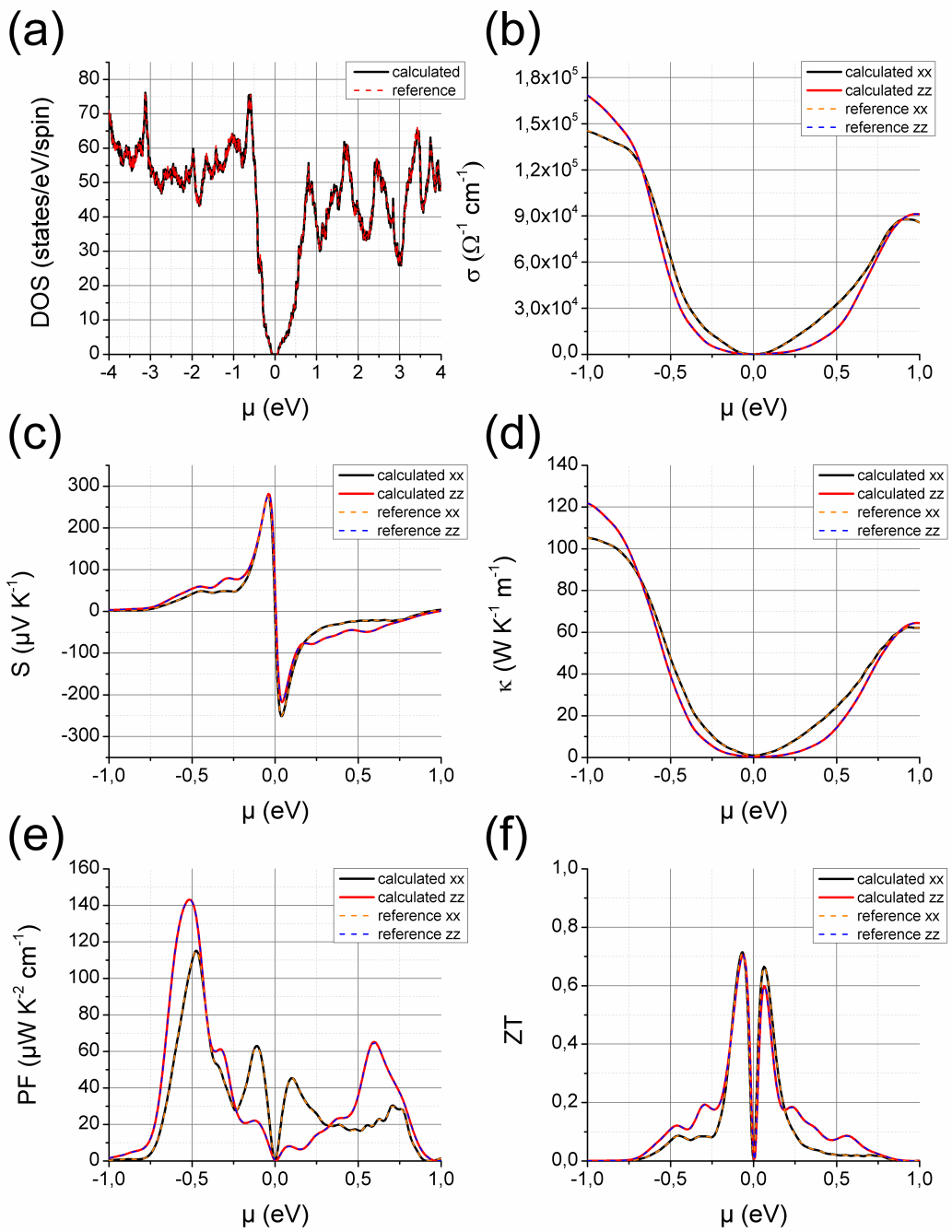

Figure 5.3.: Comparison of calculated Bi_2Te_3 transport data with reference data provided with the BoltzTraP code [147] in dependence of the chemical potential μ for a fixed temperature of 300 K. Calculated values are shown as solid and reference plots as dashed lines. (a) Density of states (DOS), (b) electrical conductivity σ, (c) Thermopower S, (d) electronic heat conductivity κ, (e) power factor ($PF = S^2\sigma$), and (f) the thermoelectric figure of merit ZT = $\frac{S^2\sigma}{\kappa}T$.

The BoltzTraP code can also calculate temperature dependent transport quantities as shown in Fig. 5.4. This figure shows the temperature dependent transport quantities for a fixed chemical potential μ of -0.0655 eV. This corresponds to the left ZT maximum in Fig. 5.3f. Fig. 5.4a shows the temperature dependence between 50 and 800 K of the electrical conductivity σ. Both, our calculated and the reference data match quite well. Interestingly, the electrical conductivity increases with temperature rather than it decreases as it could be found in literature [152, 149]. This behavior does not depend on μ since the σ-T behavior is similar for μ values close to the band gap. The only difference between our calculation and that of Huang and Kaviany [149] is that they are using a modified BoltzTraP version including an

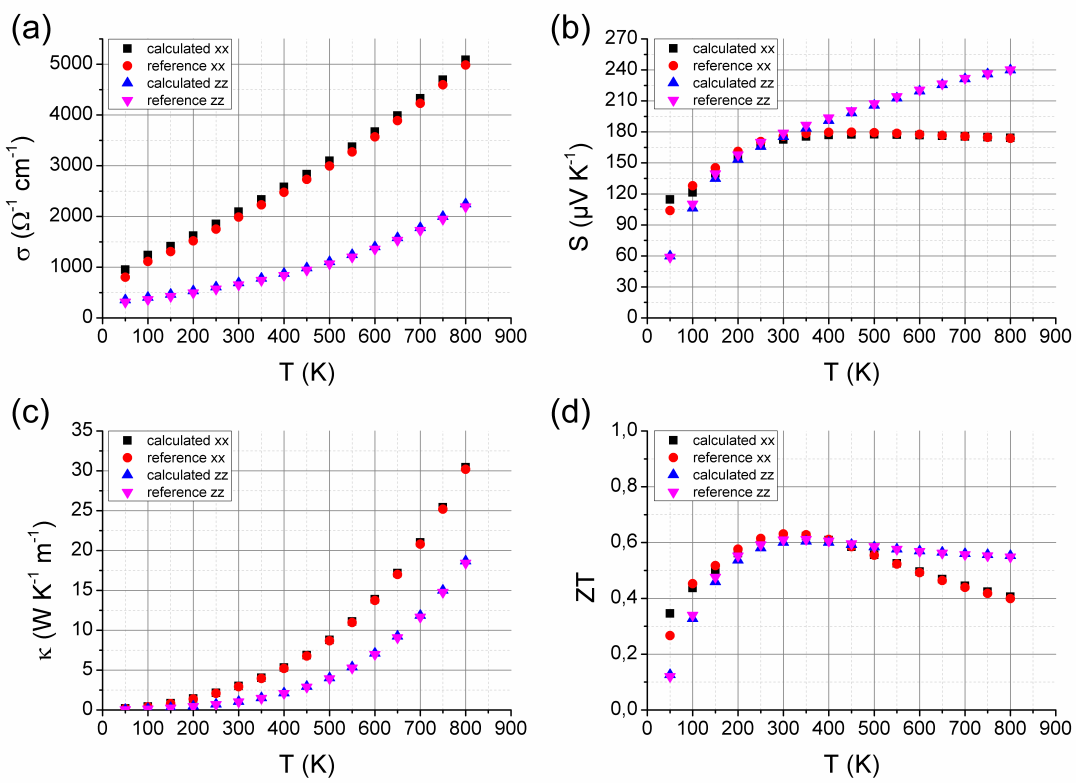

Figure 5.4.: Comparison of calculated Bi_2Te_3 transport data with reference data provided with the BoltzTraP code [147] in dependence of the temperature T for a fixed chemical potential μ of -0.0655 eV. (a) Electrical conductivity σ, (b) thermopower S (c) electronic heat conductivity κ, and (d) the thermoelectric figure of merit ZT = $\frac{S^2\sigma}{\kappa}T$.

energy-dependent relaxation time and also a temperature dependency of the band structure itself, which might explain the differences.

Fig. 5.4b shows the temperature dependency of the thermopower, where our calculation and the reference data again fitted quite well. For both directions an increase was observed up to 300 K. For higher temperatures the in-plane ("xx") component of the thermopower remained almost constant whereas the ou-of-plane ("zz") component increased further up to 800 K. In the low-temperature regime (T < 300 K) our results fit quite well to the literature [152, 149]. However, for temperatures larger than 300 K the results begin to differ from experimental values where a decrease of the thermopower was observed. Huang and Kaviany [149] showed clearly that if an energy-dependent relaxation time and also a temperature dependency of the band structure itself were used the simulated results fit quite precisely to experimental values up to 500 K whereas if a constant relaxation time and a fixed band structure are used the simulated thermopower values remain to large for temperatures larger than 300 K. Additionally, the in-plane thermopower values calculated by Huang and Kaviany [149] are about 30-40 % larger than our values for 300 K. However, it was not clear for which chemical potential they calculated their thermopower values.

Fig. 5.4c shows the temperature dependency of the electronic part of the heat conductivity κ. Again our calculation matches with the reference values in all cases. The κ data increases with the temperature up to 800 K for both cases (in-plane and out-of-plane). However, if compared to the results of Huang and Kaviany [149] they also find an increase of the electronic thermal conductivity with T up to 500 K if they use the BoltzTraP calculation, but their values are almost by a factor of 10 smaller than our values, which might again be attributed to an energy-dependent relaxation time and also a temperature dependency of the band structure itself.

The calculated ZT shown in Fig. 5.4d matches of course with the reference one due to its matching

components (σ, S, and κ). If we compare our ZT calculation to that of Huang and Kaviany [149], one immediately sees that the peaking behavior in our ZT values is less compared to the ZT values of Huang and Kaviany [149]. Also the absolute ZT values are overestimated in our case for high temperatures (T > 300 K), which is again attributed to the energy-dependent relaxation time and also a temperature dependency of the band structure itself used by Huang and Kaviany [149].

5.4.2. Comparison of calculated transport properties to experimental measurements of Bi_2Te_3 bulk and thin films

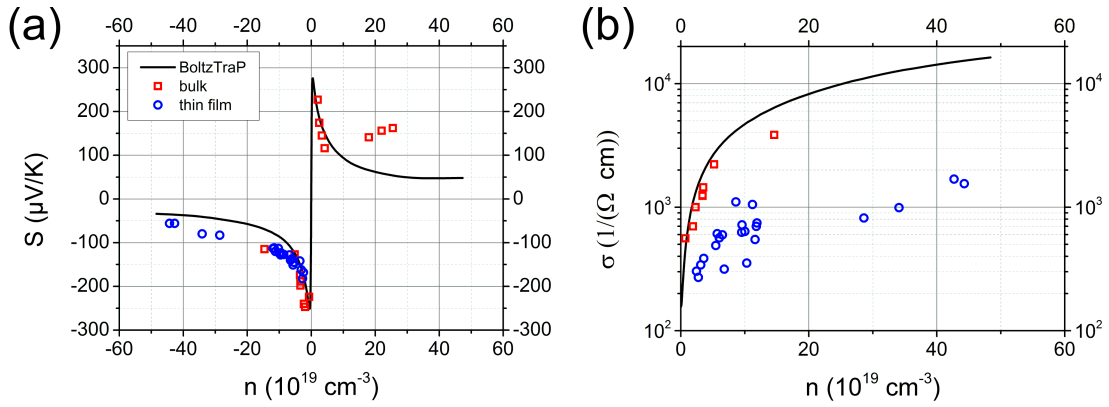

Figure 5.5.: Dependence of thermopower S (a) and electrical conductivity σ (b) on charge carrier density n for Bi-Te materials as presented by Peranio et al. [148]. Blue circles indicate in-plane values obtained from a stoichiometry series of MBE grown thin films with a Te content between 52.3 at.% to 61.8 at.% [153]. Red squares indicate basal plane values of bulk with a Te content between between 51.5 at.% to 70.5 at.% [128, 154]. Solid black lines indicate basal plane transport properties of Bi_2Te_3 as a function of the chemical potential calculated by solving the linearized Boltzmann equation [142, 150].

Transport theory predicts for Bi_2Te_3 a very sensitive dependence of the thermopower on the charge carrier density as shown in Fig. 5.5a. Results of Bi_2Te_3 bulk compounds [128, 154] show that Bi-rich samples are p-type and Te rich samples are n-type, these results are nicely matched by the BoltzTraP calculation (Fig. 5.5a). Note that p-type Bi_2Te_3 thin films were not obtained (Fig. 5.5a) by the thin film preparation technology although the Te content was varied from 52.3 at.% to 61.8 at.% [153]. Details are discussed by Peranio et al. [148].

In case of the electrical conductivity a good agreement of the BoltzTraP simulation and the Bi_2Te_3 bulk measurements was found (Fig. 5.5b). However, for the Bi_2Te_3 thin films a large deviation of electrical conductivity-charge carrier density interrelation was found. Peranio et al. [148] found in the microstructure oxygen rich secondary phases at grain boundaries being responsible for this behavior.

In summary, a good agreement of the BoltzTraP simulation with the Bi_2Te_3bulk materials was found indicating that the program does its job correctly. In the thin films experimental and simulated thermopower agreed well. However, the electrical conductivity was sensitively affected by oxidized secondary phases, yielding large variations between experimental and simulated values [148].

5.5. Conclusions

It could be shown that the BoltzTraP code could be successfully compiled in Windows as well as in Linux. It could be shown that in the case of Bi_2Te_3 the program does a correct job: Our calculated transport data agrees nicely with (i) the provided reference data, (ii) the literature, and (iii) experimental bulk values for quantities dependent on the chemical potential μ. In case of temperature dependent transport quantities differences were found with respect to literature data especially in the high temperature

regime. This is attributed to the fixed relaxation time and the temperature independence of the band structure in our case. The introduction of a relaxation time dependence into BoltzTraP code would be of great importance for future calculations.

Part III.

Structure-property correlation by electron microscopy techniques

6. Biaxially textured MgO buffer layers on randomly oriented substrates

6.1. Introduction

With the second generation of coated conductors grown on flexible metal tapes practical applications in the electric power industry came into reach [155, 156]. Large efforts were needed for texturing the superconducting layer consisting of $ReBa_2Cu_3O_{7-x}$ (Re=rare earth) layers. A common problem in early coated conductors was limited currents due to weak links created by large angle grain boundaries [64]. Major improvements on current current density were made by technologies such as RABiTS (Rolling Assisted biaxially Textured Substrates) [115] or IBAD (Ion Beam Assisted Deposition) [68] and, also, ISD [116, 157, 135].

After more than 30 years the ISD technique [158] was rediscovered and nowadays used by several groups and companies for coated conductor deposition [78, 159, 160]. An untextured substrate needs to be inclined under vacuum conditions vs. the incoming vapor. Anisotropy of diffusion will lead to a faceted surface structure and biaxially textured grains on a randomly orientated, polycrystalline substrate. Not all materials will yield a high-quality biaxial textured surface. Bauer [161] studied three materials grown by ISD, namely MgO, CeO_2 and yttria-stabilized zirconia (YSZ) on Hastelloy substrates. The results were compared to each other and it was found that YSZ and CeO_2 were not suitable for coated conductor growth due to bad texture transfer and crystallographic improper orientation. The different behavior of compounds during ISD deposition is mainly due to their anisotropy of surface energies.

6.2. Experimental

All MgO films included in this work were grown by the ISD technique. As a substrate material a non-magnetic HASTELLOY® C276 (a Ni-Mo-Cr alloy) tape was used. In a first step the substrate was cleaned and flattened by electro-polishing to get better adhesion of the subsequently grown MgO film. For the subsequent MgO growth the substrate was tilted by an angle α towards the incoming MgO vapor as shown in Fig. 6.1a. MgO was evaporated by e-beam evaporation and deposited at ambient temperature under vacuum conditions for semi-processed samples. The resulting film geometry is shown in Fig. 6.1b-c. For fully processed samples an additional MgO and a $REBa_2Cu_3O_{7-x}$ layer were grown in an untilted position at elevated temperatures as indicated in Fig. 6.1d. Further growth details can be found in [135].

Samples were characterized using a Jeol 6500F Scanning Electron Microscopy (SEM), a JPK Nanowizard Atomic Force Microscopy (AFM), and a Zeiss 912Ω Transmission Electron Microscopy (TEM) with an in-column omega energy filter operated at 120 kV. SEM and AFM were used to characterize the sample surfaces, whereas TEM was used to study volume properties of the samples. TEM samples were prepared in cross-section either by conventional grinding, polishing and ion beam milling techniques or by the Focused Ion Beam (FIB) method.

TEM images and diffraction patterns were acquired using a 5 or 10 eV energy slit aperture to reduce inelastically scattered electrons contributing to the image background. For bright and dark-field imaging a 3.5 mrad objective aperture was used. Diffraction patterns were acquired with a 700 nm selected

area electron diffraction (SAED) aperture. For analysis of radial and polar intensities within diffraction patterns the Gatan Digital Micrograph DiffTools script was used [162].

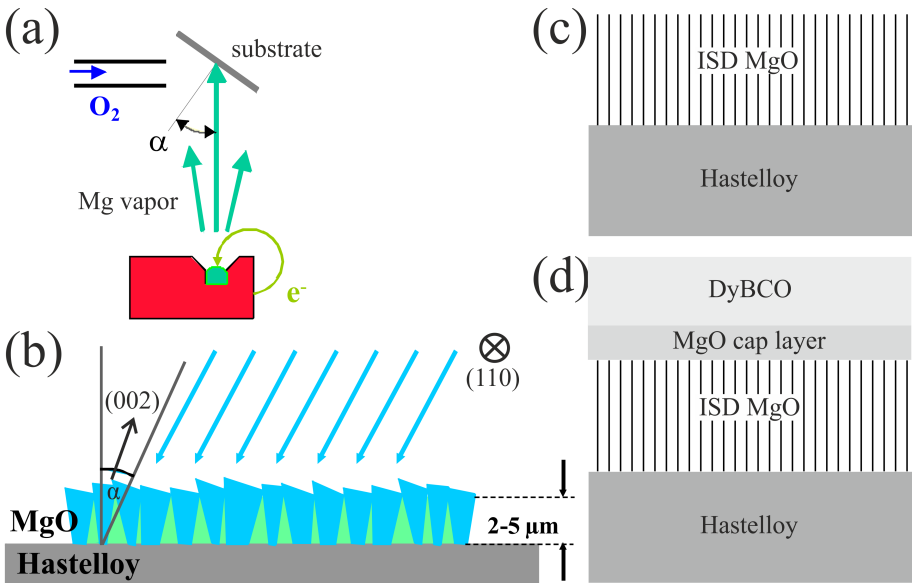

Figure 6.1.: (a) Schematic of Inclined Substrate Deposition [77], (b) sample geometry in a cross-sectional view (note that the tape direction is perpendicular to the paper plane and along the (110) direction), (c) layer structure of semi-processed samples and (d) same as (c) for fully-processed samples.

6.3. Results

6.3.1. Surface structure of ISD MgO films

The surface structure of ISD MgO is very important for subsequent High-Temperature Superconductor (HTS) growth. Hence, a detailed surface analysis is required. SEM and AFM images were acquired on a selected set of samples to characterize the MgO top surface morphology, i.e. to determine the facet length and facet height in dependence of the MgO film thickness. For the MgO nucleation layer AFM and SEM results are shown in Fig. 6.2a and b and for a well-textured 2 µm thick MgO film in Fig. 6.2c and d, respectively. Quantitative analysis of AFM and secondary electron images revealed that at 100 nm MgO layer thickness no faceted structure was visible (nucleation layer). Only in MgO films with layer thicknesses exceeding 800 nm, the surface appeared to be well-faceted (as can be seen Fig. 6.2c and d).

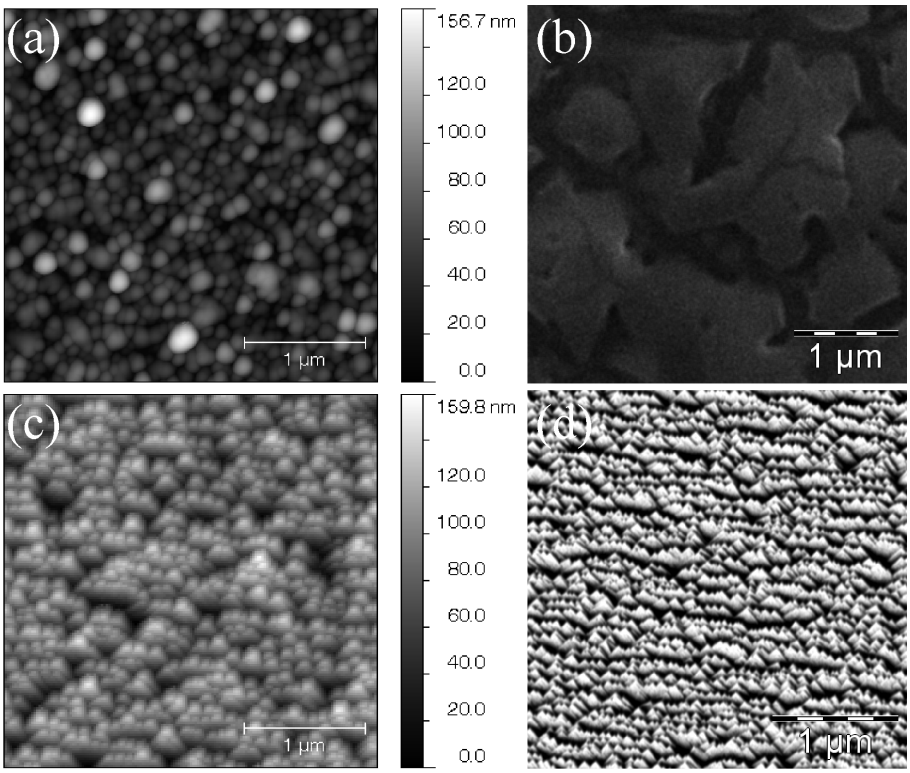

Figure 6.2.: Surface analysis of the MgO nucleation layer by AFM (a) and SEM (b) and of a well-textured 2 µm thick MgO film by AFM (c) and SEM (d).

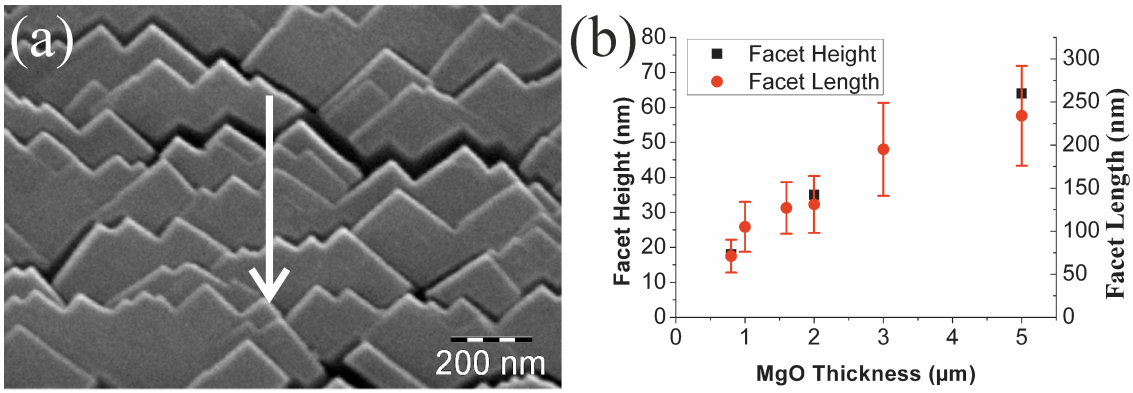

Figure 6.3.: (a) SEM plan-view image of an ISD MgO surface. The white arrow shows a typical area from which line scans were acquired to determine the facet length. (b) Facet height (extracted from AFM images not shown here) and facet length for different MgO layer thicknesses.

Along the white arrow inside Fig. 6.3a an intensity profile was acquired. From this intensity profile a mean facet length was determined. A similar procedure was applied to the AFM images from which a height profile was obtained to determine the facet height. Both results are plotted together inside Fig. 6.3b. Note that the profile direction in both cases was along the cross-sectional direction of the tape. The error bars in Fig. 6.3b denote the standard deviations determined from several facet length measurements.

For MgO film thicknesses less than 800 nm no facet structure was visible. At an MgO layer thickness of 800 nm a facet length of 71 nm and a facet height of 18 nm were measured, whereas at an MgO layer thickness of 5 µm a facet length of 230 nm and a facet height of 64 nm were found. Consequently, the MgO film roughness, i.e. facet height, and facet length both increase with the MgO film thickness as

can be seen in Fig. 6.3b. At MgO film thicknesses larger than 2 μm also a facetted fine structure was observed.

6.3.2. Volume structure of ISD MgO films

TEM cross-section analysis of MgO thin films was applied to understand the initial steps of MgO growth. For this a thin film of 100 nm thickness was selected that represents the MgO nucleation layer. Fig. 6.4a and b are dark-field images of the MgO nucleation layer obtained with (002) reflections (Fig. 6.4a) and (220) reflections (Fig. 6.4b) as in indicated in the corresponding diffraction pattern shown in Fig. 6.4c. From both dark-field images a grain size of 20 nm was determined. False colors were applied to enhance contrast and the visibility of the highly dynamic diffraction pattern shown in Fig. 6.4c. The diffraction pattern clearly shows a poly-crystalline MgO reflection rings. The radial and the (002) polar intensity profile are shown in Fig. 6.4d and e. The inhomogeneously distributed reflections show that the MgO nucleation layer is slightly textured. We also found an MgO grain size of 20 nm in a 100 nm thick semi-processed film. This suggests that the growth for all ISD MgO films follows a common model.

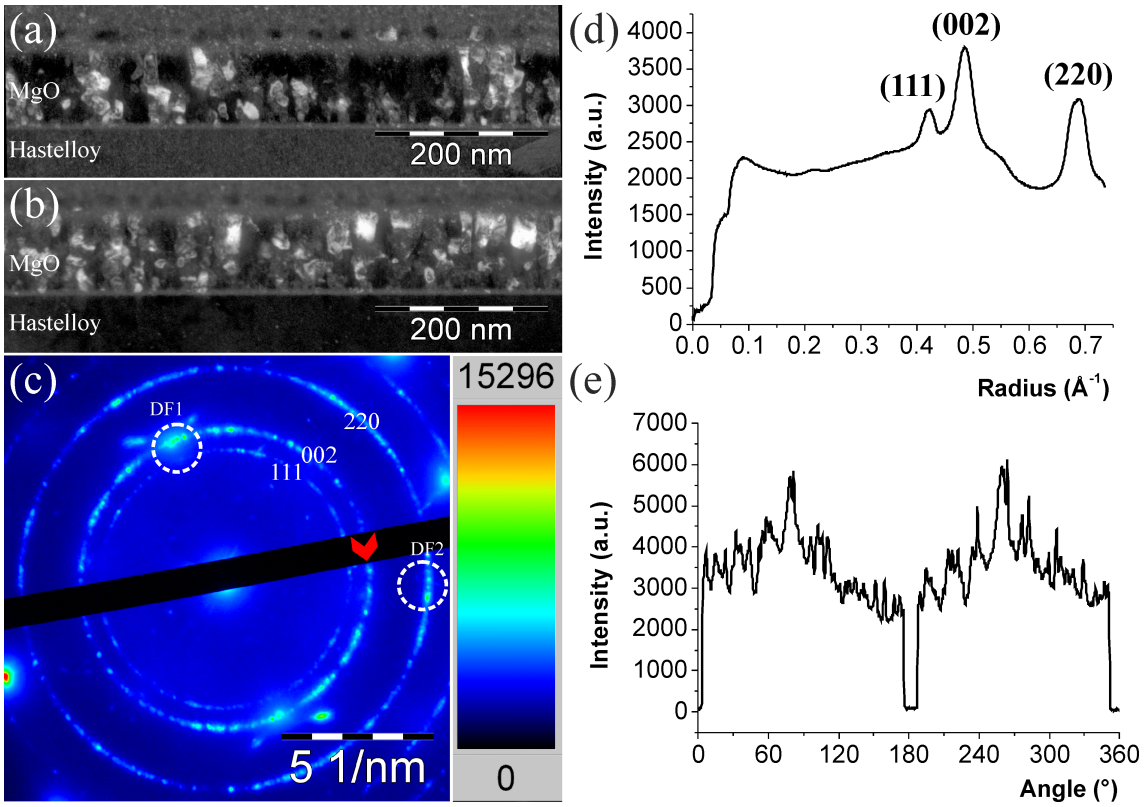

Figure 6.4.: TEM dark-field images of the MgO nucleation layer showing individual grains acquired with (a) (002) spots, (b) (220) spots, (c) corresponding diffraction pattern in false colors of the polycrystalline MgO layer, (d) radial intensity of the diffraction pattern shown in (c) and (e) polar intensity distribution of the (002) ring.

The MgO texture evolution is of crucial importance since it influences severely the subsequent superconductor growth. The choice of growth parameters controls totally the overall tape quality within the ISD buffer-layer growth. For texture analysis electron diffraction techniques were applied for both well-textured and poorly textured samples.

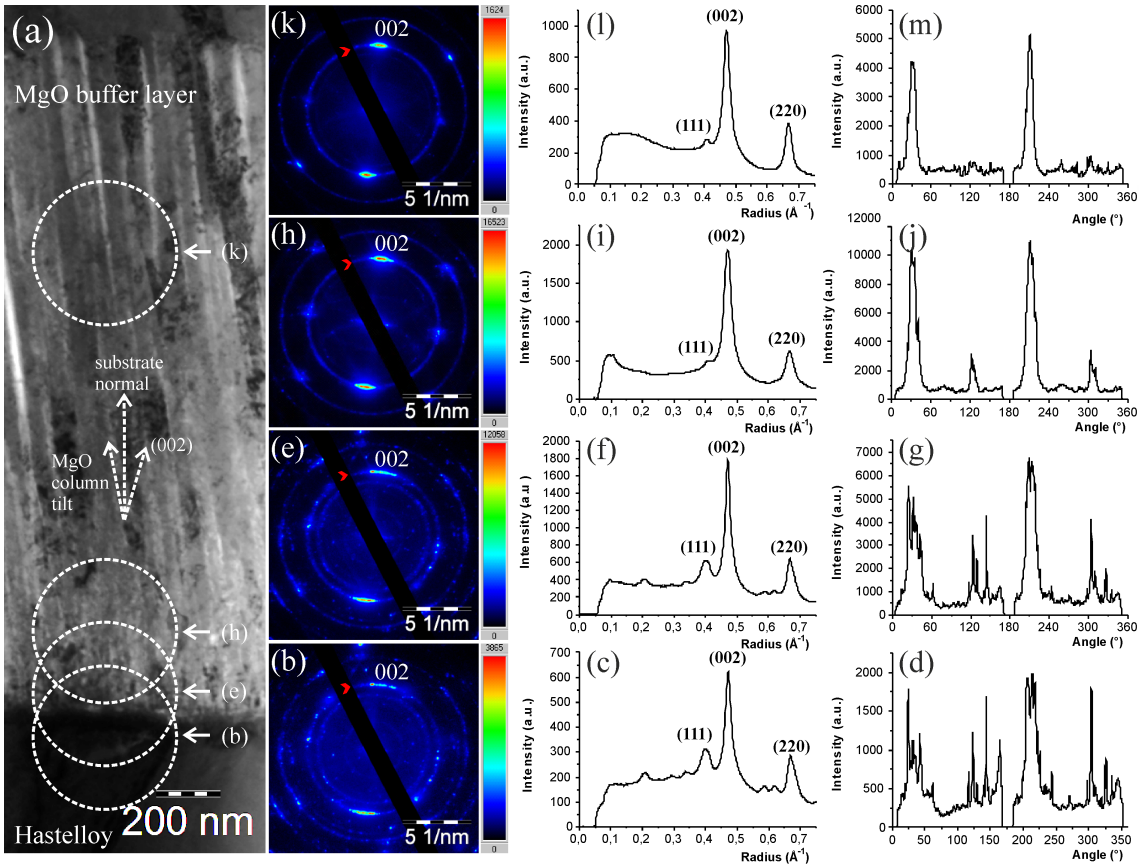

Figure 6.5.: Texture analysis of a well-textured sample by electron diffraction in the TEM. (a) Low magnification bright-field image. (b) Diffraction pattern displayed in false colors acquired at area (b). (c) Radial intensity profiles of (b) and (d) (002) polar intensity profiles of (b). Subfigures (e) to (g), (h) to (j) and (k) to (m) show similar images as subfigures (b) to (d). The red arrow indicates the starting point and direction of the polar intensity profiles.

Fig. 6.5a shows a cross sectional TEM bright-field image of the MgO buffer layer of a well-textured sample. The dashed white circles indicate the position and size of the selected area aperture used for acquiring the diffraction patterns shown in Fig. 6.5b, e, h, and k. All diffraction patterns were analyzed with respect to radial and (002) polar intensities. The results are shown in Fig. 6.5c-m. It was expected that with increasing distance from the Hastelloy/MgO interface the texture would increase. As a consequence the (002) reflection gets more and more pronounced in the diffraction patterns whereas the (111) reflection decreases in intensity. The radial intensity profiles in Fig. 6.5 nicely prove this. At the same time in the polar intensity profiles the intensity of all reflections except the (002) reflections decrease. This indicates that for a well-textured sample the only slightly textured structure in the nucleation layer changed into an almost single crystalline one. Fig. 6.5d, g, i and m show this transition very clearly.

Fig. 6.6 shows the same contents as Fig. 6.5 but for a poorly textured sample. These results were, however, very different from those shown in Fig. 6.5. The radial intensity profiles in Fig. 6.6 show a significant amount of (111) intensity still present at a distance of 1500 nm from the Hastelloy/MgO interface. In the (002) polar profiles more than two strong reflections were observed at the same thickness indicating a poor texturing. This is in contrast to the (002) polar profile acquired at the same MgO thickness in well-textured samples where only two strong reflections were present.

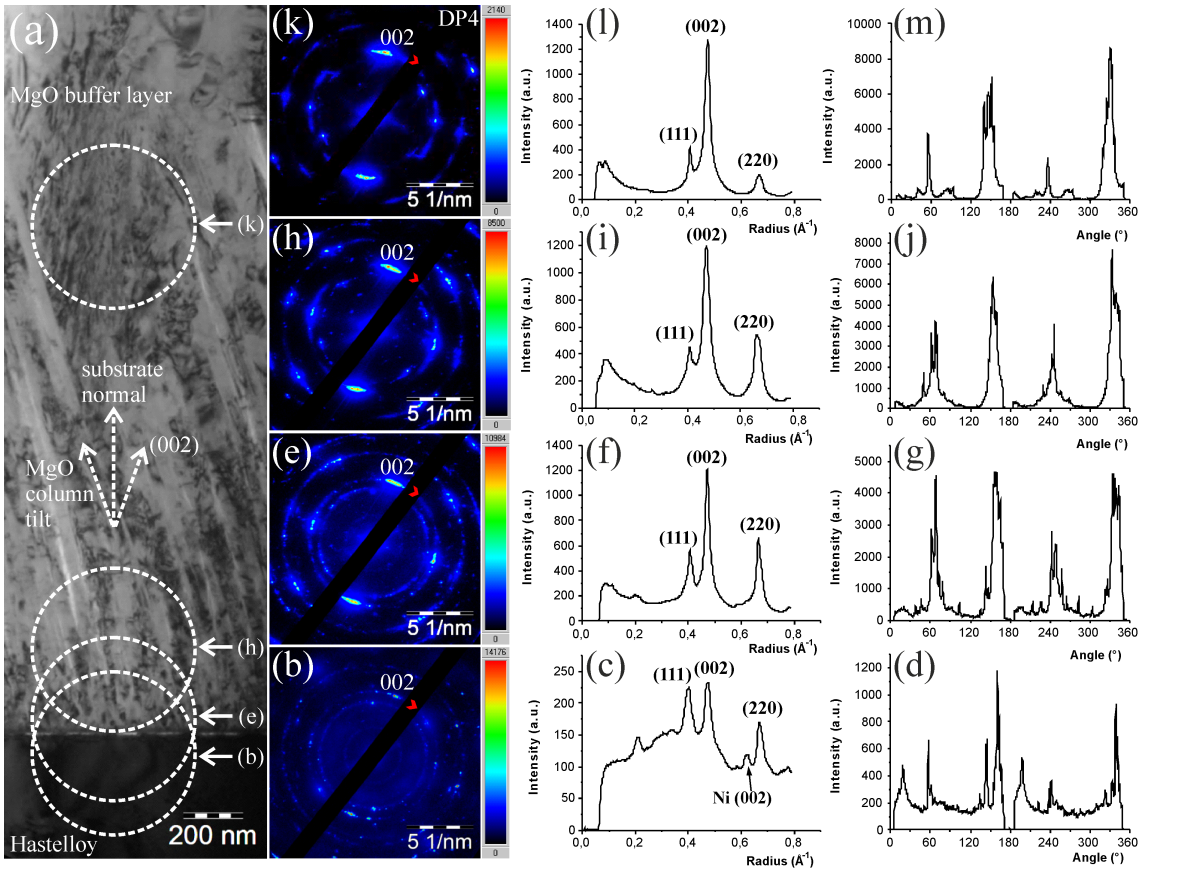

Figure 6.6.: Texture analysis of a poorly textured sample by electron diffraction in the TEM. a) Low magnification bright-field image. (b) Diffraction pattern displayed in false colors acquired at area (b). (c) Radial intensity profiles of (b) and (d) (002) polar intensity profiles of (b). Subfigures (e) to (g), (h) to (j) and (k) to (m) show similar images as subfigures (b) to (d). The red arrow indicates the starting point and direction of the polar intensity profiles.

MgO film thickness [nm]	Well-textured	Poorly textured
100	2.5	1.1
200	5.2	2.4
400	7.0	3.1
1500	9.1	3.3

Table 6.1.: Background corrected (002)/(111) ratios indicating the texture development with increasing MgO film thickness.

The (002)/(111) peak ratio was calculated as function of the distance from the interface and quantifies the MgO texture. It is large for well-textured MgO films and small for poorly textured MgO films. Tab.6.1 summarizes the (002)/(111) peak ratio results obtained from the well textured and the poorly textured sample. For the well-textured sample the (002)/(111) peak ratio increased with the distance from the interface from 2.5 to 9.1. In contrast for the poorly textured sample it increased only slightly from 1.1 to 3.3.

Diffraction contrast techniques were also applied to determine grain and defect structures within the MgO layer. Fig.6.7a shows a low-magnification bright-field image. The large crack is a preparation artifact. The small inset shows a diffraction pattern acquired in this sample area. Fig.6.7b shows the corresponding (002) dark-field image. In these images it was observed that the MgO layer consisted of (002) oriented columnar grains rotated by a maximum of 16° with respect to each other. Also a large amount of extended defects was observed within single columns due to the diffraction contrast present in Fig.6.7b.

Fig.6.7c and d show high magnification dark-field images of single MgO grains located in the MgO

cap layer. Several areas within Fig. 6.7c and d are indicated by numbers and will be addressed in the following: #1 denotes Moiré fringes present at grain boundaries. #2 shows dislocations within the MgO and #1+2 indicates Moiré contrast due to overlapping grains with overlying dislocation contrast, i.e. dislocations lie very close in this region. #3 shows dislocation loops with 5 nm in diameter and #4 denotes dislocations in weak-beam contrast. #5 shows MgO facets in cross-sectional view on the MgO top surface. As can be seen dislocations also run through the facet surface. #6 indicates grain boundaries. As can be seen from the images the grain boundaries are curved. They tend to tilt away from the [002] direction. From Fig. 6.7d a dislocation density of 2×10^9 cm^{-2} was determined.

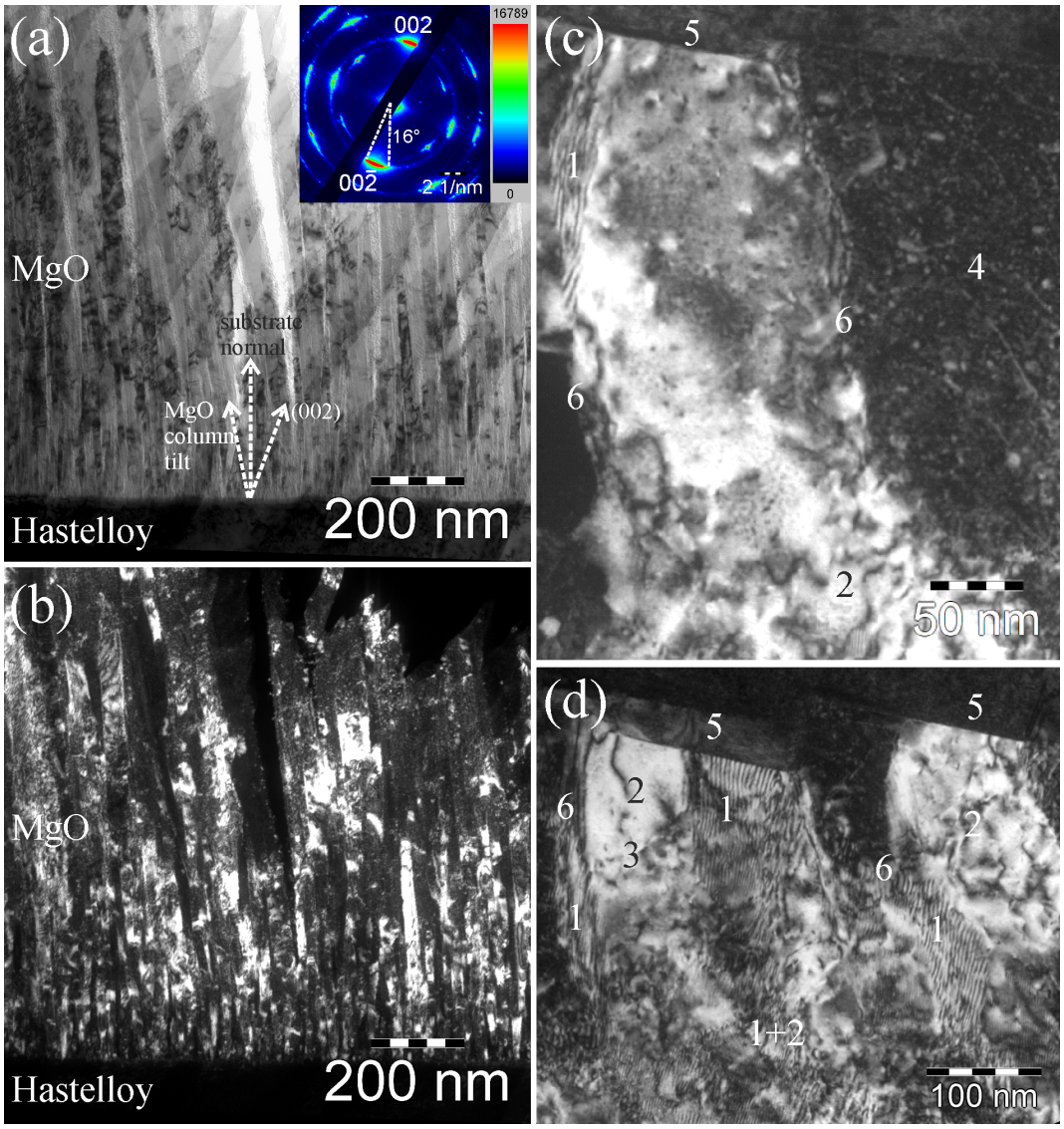

Figure 6.7.: TEM diffraction contrast images of the MgO ISD layer and the MgO cap layer. (a) Bright-field image with inset color-coded diffraction pattern, (b) corresponding (002) dark-field image to (a), (c) and (d) are high-magnification dark-field images in the MgO cap layer showing a large density of extended crystal defects.

6.4. Discussion

For coated conductor growth it is necessary to biaxially align the single ReBCO (Re = rare earth barium copper oxide) grains avoiding large angle grain boundaries, which dramatically reduce the amount of current being transported [64]. There are three major methods to obtain this biaxial texturing. First, there is the RABiTS method in which a Ni substrate is biaxially textured by thermo-mechanical process-

ing [163]. Second, there is IBAD method where a stack of buffer layers is deposited on an untextured substrate e.g. a Ni-based alloy with the help of an ion source [68]. The biaxial texture originates from the buffer layer and is transferred to the subsequently grown superconducting layer. A third way to obtain biaxially textured superconducting layers is the ISD method [160, 116, 135]. Here, MgO is thermally evaporated and then grown on an inclined untextured substrate. Thermally activated directional diffusion and shadowing of slowly growing crystallites creates a columnar-grown biaxially textured MgO buffer layer. The surface of this buffer layer is sharply faceted. On each MgO facet a biaxially oriented ReBCO grain can grow epitaxially yielding small-angle ReBCO grain boundaries and high critical currents. ReBCO thin films grown on (001) oriented MgO single crystals were reported in literature showing epitaxial growth. However, high critical currents can only be obtained if the deposition angle has the correct value. Too large or too small deposition angles yield no regularly faceted surface [79] and thus no biaxial texture and low critical currents. Each of the three methods described above has its advantages but also its disadvantages. The first two methods i.e. RABiTS and IBAD are unstable with respect to a-axis growth. The ReBCO growth direction has no component in the (a,b)-plane for both technologies. In ISD technology this issue is different. Due to the tilted geometry the ReBCO growth direction has a component in the (a,b)-plane suppressing a-axis growth. The driving force behind this growth type is the inclination of the MgO facets, which is due to the anisotropy of the MgO surface energies. A more detailed analysis of the MgO/DyBCO interface is present by Aabdin et al. [136].

From TEM diffraction patterns it is possible to extract crystal orientation data. For ISD grown MgO layers qualitative TEM data [79, 164] and also quantitative X-ray and AFM data [79, 165] already exist showing the texture development in the ISD MgO layer. Within this work it was possible to systematically quantify TEM diffraction data via the Digital Micrograph script DiffTools [162], i.e. it was possible to easily obtain radial and polar intensity profiles. The background subtracted (002)/(111) intensity ratio extracted from radial intensity plots increased with increasing distance from the Hastelloy/MgO interface for a well-textured sample (see Fig. 6.5). This is consistent with the observations of Xu et al. [79] and Koritala et al. [164]. Both found also an increase of MgO texturing with increasing distance from the substrate/MgO interface. Data evaluation of the same diffraction data by two different people yielded similar results for the (002)/(111) intensity ratio. Our AFM measurement of a MgO facet height of around 35 nm corresponding to a Root Mean Square (RMS) value of 12.8 nm which fits well to a RMS value of about 10 nm measured by Koritala et al. [165]. Both measurements were obtained for a 2 µm thick MgO film.

The nucleation layer is polycrystalline and consists of 20 nm sized nano-crystallites having arbitrary orientations as shown in Fig. 6.4. The surface of this nucleation layer is still unfaceted. Thermally activated directional diffusion of the MgO vapor and the fact that MgO (002) planes decrease the surface free energy [164] yielding a (002) faceted surface. The growth of other directions e.g. the (111) direction is suppressed as can be seen from Figs. 6 and 7. The facet inclination angle depends on the substrate-tilting angle α as shown by Xu et al. [79]. It linearly increases with α. As predicted by the van der Drift theory [166] the facet width (i.e. grain size) and facet height (i.e. surface roughness) increase both with the film thickness according to a power law as shown in Fig. 6.3b. The van-der-Drift theory predicts in three dimensions an exponent of 0.40 for both facet width and height on a uniformly smooth substrate and a flat geometry [167]. For tilted geometries theoretical exponential values of 0.5 were predicted [168]. However, we found in our experiments exponents of 0.63 and 0.67 being significantly larger than both theoretical values. As mentioned in the introduction part, the substrate surface and its roughness will influence the thin film growth i.e. also larger values than 0.5 for the exponents are possible depending on the substrate surface properties [169]. Especially the "noise level" present at the substrate surface will increase the exponents. The Hastelloy substrates used in this work have a RMS surface roughness of > 0.15 nm [157] forming this "noise level". Koritala et al. [164] experimentally observed an increase of MgO grain size from 20 nm in a 50 nm thick MgO film to 100-200 nm for a MgO film of 3 µm thickness. This fits very well to our own observations shown in Fig. 6.3 showing that ISD growth follows a common model.

Monte Carlo calculations of ISD growth were carried out by Bauer et al. [78]. It was found out that MgO columns with (002) terminated surfaces grew faster than any other. The influence of several parameters was carefully analyzed. It was found out that thermally activated directional diffusion is not necessary for a biaxially textured growth process but has a positive influence on it and thus cannot be neglected to explain the experimental observations. Within the Monte Carlo simulations following parameters were varied: (i) the layer thickness and (ii) the crystal orientation. For point (i) Bauer et al. [78] found a good agreement between simulation and experiment. In addition, our measurements confirm his findings. We also find the same column orientation and an increase in column diameter with increasing film thickness. In a second step (ii) Bauer et al. [78] varied the texture angle, the rotation of the texture around the substrate normal, and the rotation around the (001) texture axis. The simulations showed that for a substrate tilting angle of 40° which is the value used in our samples the texture angle has a maximum around 30°. This value was also observed for example in well-textured samples. Furthermore, the simulation predicted perpendicular growth of the columns for these values. Again the experimental column-tilting angle of 3-5° is very close to that prediction. For the rotation around the substrate normal the simulations showed for a substrate tilting angle of 40° a slight maximum for the [001](110) orientation which was observed in all our experiments. The same is valid for the rotation around the (001) texture axis.

6.5. Summary/Conclusions

The surface structure of ISD grown MgO films were studied by SEM, AFM, and TEM. Only for MgO films thicker than 800 nm surface faceting was observed by SEM and AFM. At a MgO layer thickness of 800 nm a facet length of 71 nm and a facet height of 18 nm were measured, whereas at a MgO layer thickness of 5 μm a facet length of 230 nm and a facet height of 64 nm were found. The MgO facet evolution could be explained by the van-der-Drift model. The (002)/(111) peak ratio obtained from TEM diffraction experiments revealed the amount of texture present in ISD MgO films. It was shown that all observations fit perfectly to the ISD growth model and the Monte Carlo simulations of Bauer et al.

7. $DyBa_2Cu_3O_{7-x}$ thin films grown on biaxially textured MgO buffer layers

7.1. Introduction

Coated conductors are the most promising material to meet the challenges imposed by energy technologies for applications at 77 K and higher magnetic fields [170]. In order to foster commercial applications of coated conductors the main focus of industrial research is directed towards increasing tape length, demonstrating perspectives of low production cost, improved superconducting properties (j_c, anisotropy of j_c etc.), and reduced AC losses. Coated conductors are today the most promising candidates for superconducting wires for magnet and energy technology. They will substitute Bi-2223 tapes and open the door for new applications of superconductivity.

During the last years several applications of HTS (high-temperature superconductors) were successfully realized in RABiTS or IBAD coated conductor technology [156, 155]. ISD is another promising technique for coated conductor fabrication offering both fast processing and excellent biaxial texture of the HTS [159, 78, 171]. Latest progress in ISD technology offers a serious and economic fabrication route for coated conductors. Together with specialized evaporation techniques ISD is a viable and economic way to produce second-generation HTS tapes for commercial applications [135]. The most important and technically challenging steps for the fabrication of coated conductors are the deposition of a biaxially textured buffer layer and the superconductor film in a reel-to-reel configuration. Since reference [78] was published great progress has been achieved.

TEM analysis of ReBCO (rare earth barium copper oxide) thin films has turned out to be of great importance for understanding structure-property correlations [172]. ISD grown coated conductors have not been investigated so far. Detailed studies on the growth of buffer layers for RABiTS coated conductors and a description of the used methodology were reported in [173]. Great progress has also been achieved in FIB preparation of coated conductor cross-sections ready for TEM [174]. The inclined orientation of the superconducting layer yields new microstructural features and, therefore, different superconducting properties as compared to RABiTS or IBAD grown films.

7.2. Experimental

7.2.1. Thin film deposition

The non-magnetic Ni-based alloy Hastelloy® C276 was used as substrate. After electro-polishing an ISD MgO layer was deposited as it is schematically shown in Fig. 7.1a using high deposition rates (> 5 nm s^{-1}). The tape was inclined by an angle α of 25°-30° towards the direction of the incoming MgO vapor. It is important to note especially for the interpretation of current measurements that the inclination angle is towards the side of the tape and not along its length. On top of the 2.4 µm thick ISD buffer layer, a 200 nm thick MgO cap layer was grown homoepitaxially at 720°C in an untilted configuration and with a smaller deposition rate. Subsequently, a DyBCO layer was deposited by continuous flash evaporation of granular stoichiometric material with a deposition rate of 1 nm s^{-1}. The substrate temperature was 650°C and an oscillating shuttle supplied the required oxygen for the cube-on-cube growth of the DyBCO phase.

In a final step, before the coated conductor was annealed in a tube furnace at 800 mbar oxygen pressure, a 500 nm thick Ag layer was deposited on top of the HTS. Further details of the processes are described in [175].

7.2.2. Basic characterization

Superconducting critical current densities were measured either resistively for short samples or by a reel-to-reel Hall sensor measurement [176] for longer samples applying a 1 $\mu V\,cm^{-1}$ criterion. The critical current density of the coated conductor was measured for different magnetic field strengths and directions. For this, a DyBCO bridge was chemically etched such, that it was 40 µm wide and 1 mm long. The critical current density j_c was measured by a 4-point method with a field criterion of 7.5 $\mu V\,cm^{-1}$ using a high-resolution two-axis goniometer [177]. It was mounted in a variable temperature insert placed in the bore of an 8 T superconducting magnet. By tilting the substrate, the critical current density can be determined for different angles between magnetic field and substrate normal. The current direction was always perpendicular to the magnetic field. The texture of the ISD-MgO was investigated by standard X-ray diffraction (XRD) and scanning electron microscopy (SEM) for examining of the surface structure.

7.2.3. TEM sample preparation and analysis

Element	X-ray line energy [keV]	X-ray line series	Cliff-Lorimer k-factor
Dy	6.495	L	2.304
Ba	4.446	L	2.050
Cu	8.048	K	1.457
Ag	2.984	L	1.756

Table 7.1.: Data used for the quantification of EDX spectra.

The TEM sample preparation was done in a FIB workstation (Zeiss Crossbeam 1540). A TEM lamella was cut out by the ion beam, lifted out, and finally attached to the TEM sample holder. The quality of the sample was documented by TEM images, but also by Energy Dispersive X-ray (EDX) spectra. FIB sample preparation for TEM of ISD grown coated conductors is demanding, because (i) they consist of materials with different sputtering rates, e.g. MgO and DyBCO (ii) large film thicknesses, especially of the MgO buffer layer, and (iii) strain present in the films. The TEM experiments were carried out in a Zeiss EM912 Omega transmission electron microscope, operating at 120 kV acceleration voltage, equipped with an Oxford EDX detector. For the analysis energy-filtered bright and dark-field images, selected area diffraction patterns, and EDX spectra were acquired. Bright and dark-field images were acquired under two-beam (systematic row) conditions 10-20° off the $[1\bar{1}0]$ zone axis of the DyBCO. The EDX acquisition time was 50 to 150 seconds. Spectra were quantitatively analyzed by the Cliff-Lorimer k-factor method. Details are listed in Tab. 7.1.

7.3. Results

7.3.1. MgO texture

The basic mechanism for texturing during the ISD process was already described in [78] and is schematically shown in Fig. 7.1a. Due to the high deposition rate (> 5 nm s^{-1}) and growth selection by shadowing

effects, only MgO grains with in-plane alignment yield a substantial growth rate, and thus the necessary texture for subsequent HTS crystal growth is formed. The result is a columnar structure with tilted end planes. The surface plane of each column is oriented towards the incoming MgO vapor, whereas the columns themselves tend to bend away from the deposition direction. The inclination angle α is yet not fully preserved, so that the [002] direction of the MgO is tilted by about β = 25° with respect to the substrate normal. This can also be seen in the X-ray pole figure of the MgO ISD layer (Fig. 7.1b). MgO cubes grow under 45° with respect to the tape direction yielding a faceted surface. The geometric scheme of the ISD MgO growth is shown in Fig. 7.1c.

With this technique well-textured buffer and HTS layers can be obtained. X-ray pole figures prove the in-plane texture of the ISD MgO and the HTS layer, respectively. The full width at half maximum (FWHM) was 10° and 8°, respectively.

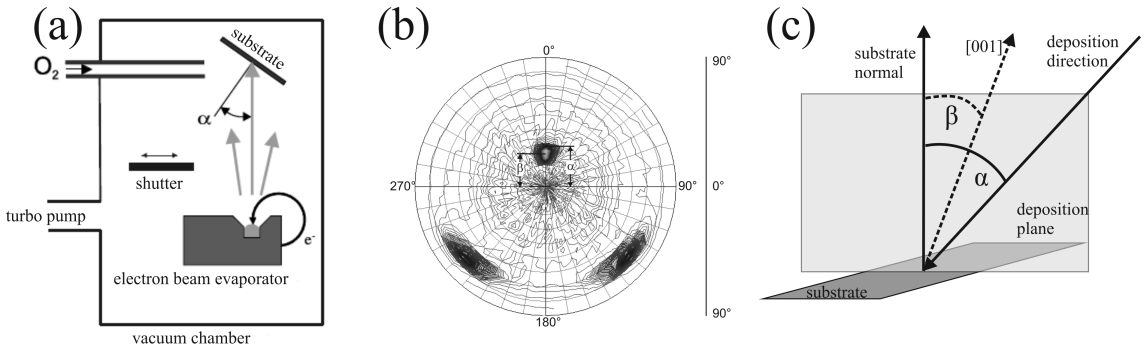

Figure 7.1.: (a) Geometry of the ISD deposition process, (b) a MgO (200) X-ray pole figure and (c) schematics of the MgO orientation on the substrate. Note that substrate normal, [001] direction of MgO and flux direction of evaporation lie in one plane.

7.3.2. Superconducting properties

Critical temperatures for DyBCO coated conductors can reach values up to 92 K. Critical current densities up to 2.5 MA cm^{-2} were reached at 77 K and zero external magnetic fields in short samples [178]. Fig. 7.2a shows a reel-to-reel Hall sensor measurement yielding a critical current density of 1.2 MA cm^{-2} at 77 K and in self-field for a 10 m long tape. In Fig. 7.2b the critical current density dependence on the angle between magnetic field and the substrate normal is shown for a sample grown under similar conditions. A peak was found in Fig. 7.2b at 70° tilt of the magnetic field direction with respect to the substrate normal. It corresponds to the measured inclination angle found in X-ray pole figures (see Fig. 7.1b). Additionally, the center of the maximum j_c value in Fig. 7.2b roughly coincides for all measured magnetic field values. Critical current densities were measured with the magnetic field being perpendicular to the c-axis of DyBCO and the following values were obtained at a temperature of 77 K and a 1 µV cm^{-1} criterion: 3.0×10^5 A cm^{-2} (1 T), 1.1×10^5 A cm^{-2} (4 T). This peak is related to intrinsic pinning and allows high critical current densities even for high magnetic fields as can be seen from Fig. 7.2b. Fig. 7.2c shows the pinning anisotropy with respect to the external magnetic field. It is found that the anisotropy in ISD films is strongly depending on the external magnetic field. The pinning anisotropy (pa) is defined here by Eq. 7.1.

$$pa = \frac{j_c^{max} - j_c^{min}}{j_c^{min}} \tag{7.1}$$

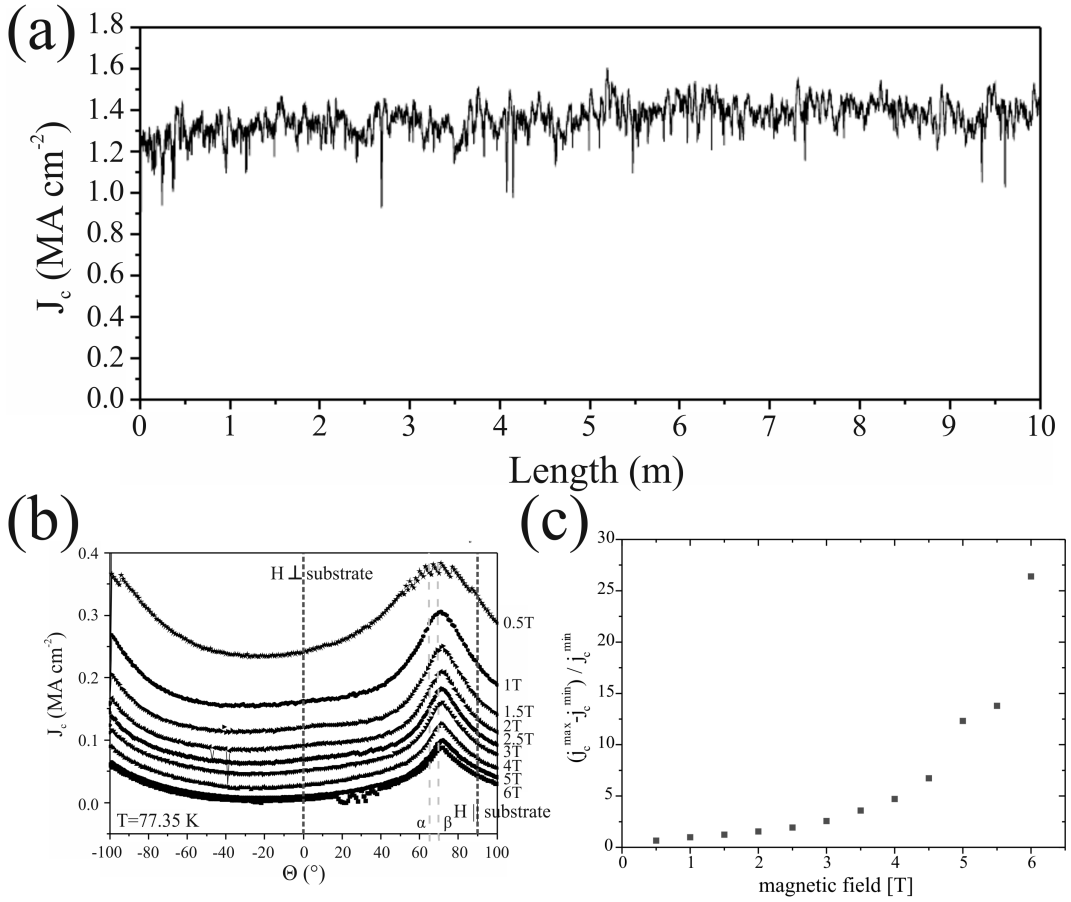

Figure 7.2.: (a) Critical current density at 77 K and self-field of a 10 m long ISD coated conductor measured by a continuous Hall sensor measurement. (b) Angular dependence of the critical current density j_c. (c) Amount of anisotropy in dependence of the external magnetic field determined from (b). The data presented here was acquired by J. Durrell (University of Cambridge, UK) in cooperation with Theva Duennschichttechnik GmbH (Ismaning, Germany).

According to Eq. 7.1 values were extracted from Holesinger et al. [170] and Gutierrez et al. [47] and summarized along with our ISD values in Tab. 7.2. The amount of anisotropy is for the ISD samples less than for RABiTS samples except for RABiTS grown by PLD. According to Tab. 7.2 the anisotropy of j_c increases from (i) YBCO films including nano-composites yielding the smallest anisotropy to (ii) ISD prepared pure DyBCO films and (iii) RABiTS prepared pure YBCO films showing the strongest anisotropy.

7.3.3. SEM and TEM analysis

Fig. 7.3a shows a secondary electron image of the MgO cap layer in plan-view. Note the sharp tile-like microstructure, which is important for subsequent HTS growth. The facets of the tiles are perpendicular to the [002] direction in MgO. Each facet row is about 170 nm wide, including also a fine structure. Fig. 7.3b shows a secondary electron image of an ISD coated conductor sample in cross-section. The columnar ISD MgO layer is about 2.5 µm thick and results from the ISD growth. The MgO columns tend to tilt away from the incoming MgO vapor as can be seen in Fig. 7.3b. The DyBCO layer was found to be 857 nm thick and the Ag top layer had a roughness of about 100 nm.

Author	j_c criterion [$\mu V\ cm^{-1}$]	B [T]	T_c [K]	Growth method	Angle of $j_{c,\,max}$ [°]	Anisotropy value
Holesinger et al. [170]	1	5	75	RABiTS (MOD)	90	21
Holesinger et al. [170]	1	5	75.5	RABiTS (PLD)	90	5.7
Gutierrez et al. [47]	1	1	65	RABiTS (TFA)	90	2.2
This work	7.5	1	77.35	ISD	70	1.8
This work	7.5	5	77.35	ISD	70	12

Table 7.2.: Comparison of anisotropy data of the three different ReBCO growth models.

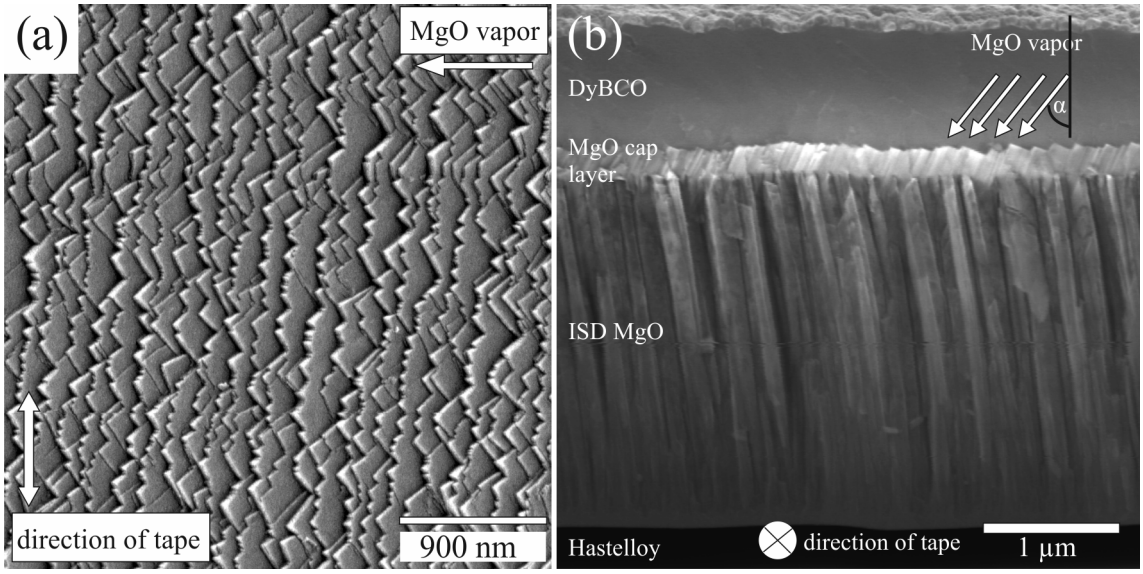

Figure 7.3.: SEM secondary electron image of (a) the MgO cap layer surface in plan-view and (b) the coated conductor layer architecture in cross-section.

Number	Structural feature	Value
1	Thickness of the MgO buffer layers	3085 nm
2	Width of the MgO columnar grains	107 nm
3	MgO facet width	154 ± 37 nm
4	MgO facet height	115 nm
5	MgO facet angle type 1	29 ± 2°
6	MgO facet angle type 2	57 ± 3°
7	DyBCO grain boundary tilt	41 ± 11°
8	Thickness of the DyBCO layer	935 nm
9	Wavelength of the DyBCO/Ag interface	398 ± 200 nm
10	Interface height of the DyBCO/Ag interface	200 nm

Table 7.3.: Structural parameters determined by electron microscopy.

During TEM analysis the sample was tilted and the faceted interface is in projection, i.e. the DyBCO c-axis direction lies in the plane of the image. Only in this tilting position reliable values for the structural parameters such as layer thicknesses and interface properties can be obtained. Fig. 7.4a shows a

low-magnification TEM image of the ISD coated conductor sample in cross section, i.e. a cut perpendicular to MgO facet being present at the tile-like surface. Layer thicknesses extracted from Fig. 7.4a are summarized in Tab. 7.3. The rough and faceted MgO/DyBCO interface can be identified within the image. We calculated an aspect ratio (layer thickness 3085 nm divided by column diameter 107 nm) of 29 for the MgO columnar grains indicating a fast growth of the MgO columns. A schematic drawing of the ISD coated conductor is shown in Fig. 7.4b. The numbers being present correspond to those in the first column of Tab. 7.3. The facets have an average facet width of 154 nm and an average height of 115 nm. An average facet inclination angle (feature #5) of 29° was determined being close to the angle β = 25°. One can assume that the MgO facets have nearly the shape of a right-angled triangle as the value of feature #6 shows. These values are in good agreement with our SEM measurements. Thus, one can state that ISD technology yields samples with reproducible nanostructure.

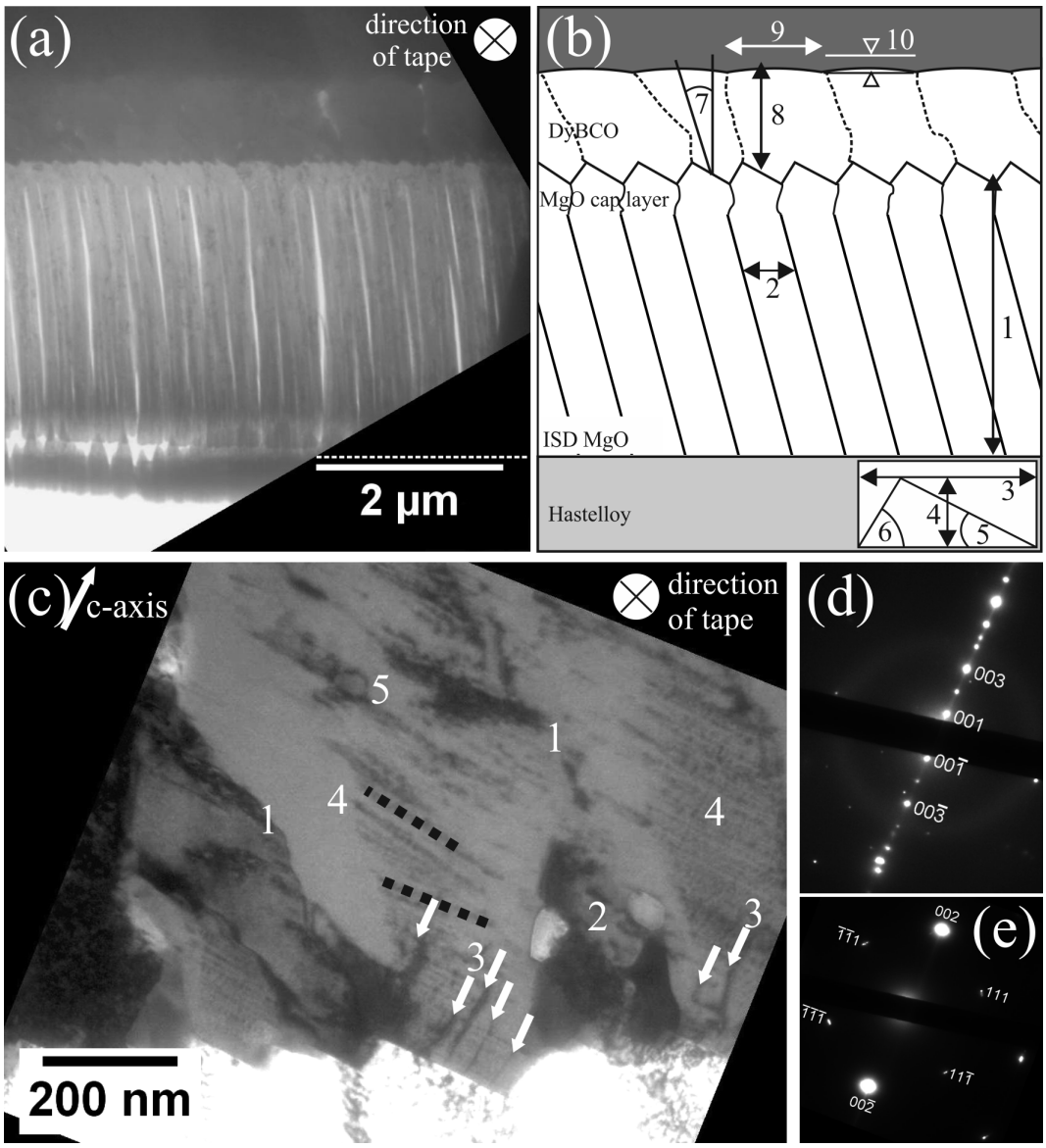

Figure 7.4.: (a) Low-magnification TEM image, (b) schematic layout of (a) including graphical representations of the structural parameters listed in Tab. 7.3. (c) TEM bright-field image at the MgO/DyBCO interface. The numbers indicate the microstructural features addressed in the text. Selected area diffraction pattern of (d) the DyBCO layer and (e) the MgO cap layer.

Fig. 7.4c shows a TEM bright-field image of the MgO/DyBCO interface area. Both, the c-axis orientation

and the tape direction are also indicated. Several microstructural features are addressed by numbers in the image since they are relevant for the pinning behavior: #1 is a grain boundary. In the left grain strain contrast from dislocations was observed and no defects were seen in the right grain under the applied imaging conditions. #2 shows two precipitates of about 100 nm in diameter in the grain. Both show a brighter diffraction contrast than the surrounding grain. #3 marks several threading dislocations by white arrows resulting from the MgO/DyBCO lattice misfit. The threading dislocations are running perpendicular to the MgO/DyBCO interface. Superimposed to the strain contrast of threading dislocations is a strain contrast of sections of dislocation loops lying parallel to the (001) planes of DyBCO in the lower part of the micrograph. This dislocation contrast (#4) is typically about 200 nm long and about 20 nm wide. In the upper part of the grain they are tilted with respect to those in the lower part by an angle of about 12.5° as indicated by the black dotted line. These lines have in most cases a distance to each other, which is smaller than 30 nm. Sometimes it is possible to resolve a fine structure within these lines. The origin of these dislocations is unclear at present time. #5 indicates a dislocation loop of about 70 nm in diameter.

Selected area diffraction patterns along the $[1\bar{1}0]$ zone axis of DyBCO and MgO in the same tilting position are shown in Fig. 7.4d and Fig. 7.4e, respectively. The two diffraction patterns prove that the MgO (001) planes are parallel to the DyBCO (001) planes, i.e. the biaxial texture of the DyBCO film. Characteristic angles can be extracted from TEM selected area diffraction patterns and can be compared to X-ray diffraction results and j_c anisotropy measurements.

The c-axis of the DyBCO encloses an angle of 25° with the surface normal as determined by TEM diffraction. The X-ray measurements provide about the same angle. Both measurements are consistent with the j_c anisotropy measurements shown in Fig. 7.2. EDX spectra were acquired to determine the stoichiometry of the superconducting layer. EDX spectra of two DyBCO grains were quantified by the Cliff-Lorimer method. The results are shown in Tab. 7.4. The Cu mole fraction ratio is larger than expected, which is due to stray radiation from the FIB Cu sample holder and non-stoichiometric powder used for DyBCO growth. Thermal evaporation controls the chemical composition very well and no larger fractions of secondary phases could be identified via EDX within the DyBCO layer. Implanted Ga was not observed in a single EDX spectrum documenting the high sample quality.

Grain	Cu [at%]	Ba [at%]	Dy [at%]
1	55.4	27.2	17.4
2	60.1	26.2	13.7

Table 7.4.: Quantitative X-ray analysis of two DyBCO grains.

7.4. Discussion

A detailed understanding of the structure-property-chemistry relationship in any type of HTS material is the key for upscaling to industrial length scales. In the following the most significant differences of ISD technology compared to well-known technologies, e.g. RABiTS or IBAD are being discussed.

The pinning behavior of HTS coated conductors strongly depends on their microstructure, i.e. defects. It is believed that due the small in-plane coherence length of YBCO (~ 2 nm) point defects such as vacancies or interstitials are able to pin fluxons but also higher-order defects such as grain boundaries, threading dislocations or planar defects suppress the superconducting order parameter due to their strain field such that they are effective pinning centers [179, 46]. According to Gutierrez et al. [179] vacancies and secondary nanophases are pinning isotropically, whereas extended defects such as grain boundaries or threading dislocations pin anisotropically. According to Foltyn et al. [180] also the shape and orientation of defects determines the angular dependence of the critical current. Statistically oriented defects like point defects create “random or isotropic pinning” whereas extended linear or planar defects pin in a “correlated or anisotropic” way, i.e. if the magnetic field is aligned with the defect their pinning potential

has its largest value [180]. In Fig. 7.4c pinning relevant defect types were addressed by the numbers #1 (grain boundaries), #3 (threading dislocations) and #4 (dislocations). All these defects are linearly shaped as for example threading dislocations. Their pinning behavior is thus being anisotropic. The origin of these dislocations is, however, not clear at present time. The grain size in RABiTS deposited superconducting layers is about 40 µm, whereas it is only about 1 µm for DyBCO films prepared by ISD. In addition, the large density of small-angle grain boundaries in ISD samples yields a contribution to pinning and increase the residual resistivity of the films due to the larger amount of electronic scattering centers, i.e. dislocations.

The influence of extended crystal defects on pinning was also discussed by Holesinger et al. [170] yielding significant deviations from random pinning due to twin boundaries and other extended defects if the magnetic field is parallel to the c-axis. In RABiTS or IBAD coated conductors the c-axis is aligned parallel to the substrate normal. Therefore, the maximum in j_c appears if the magnetic field lies in the (001) lattice planes corresponding to an angular value of 90°. Since the DyBCO (001) lattice planes are inclined with respect to the surface normal, for ISD coated conductors this maximum in j_c is shifted by an angle corresponding to the inclination angle (Fig. 7.2b). Due to the tilt of the DyBCO (001) lattice planes the pinning relevant defects (Fig. 7.4c) are also tilted by the same angle. The higher density of small-angle grain boundaries in ISD samples yields additional pinning, which does not appear in RABiTS prepared thin films due to the significantly larger grain size explaining the results summarized in Tab. 7.2.

The MgO/DyBCO interface was found to be strongly faceted. The MgO facets appear to be flat (roughness < 10 nm) and together with diffraction patterns shown in Fig. 7.4d and Fig. 7.4e this indicates epitaxial growth of the DyBCO on the MgO buffer layer. Threading dislocations were observed by diffraction contrast TEM indicating the presence of misfit dislocations at the MgO/DyBCO interface. A more detailed defect analysis as well as a growth model for ReBCO films is presented elsewhere [136].

The observed microstructure is governed by interface and surface energies as well as volume energy due to tensile strain in the film induced by the misfit with respect to the substrate. The strongly faceted inclined MgO surface forces the DyBCO film to grow in an inclined orientation and yields a significantly increased contribution of surface area and energy. This together with the anisotropy of surface energy of DyBCO might be the reason for perfect c-axis growth and suppressed a-axis growth. ISD grown films with different thicknesses offer unique possibilities to study the interplay of surface vs. volume energy contributions and thickness dependent microstructures.

7.5. Summary/Conclusions

DyBCO films grown on biaxially textured MgO buffer layers deposited by ISD technology on Hastelloy substrates were analyzed. ISD coated conductor samples yielded maximum critical current densities up to 2.5 MA cm^{-2} in short samples and 1.2 MA cm^{-2} for tapes exceeding a length of 10 m both measured at 77 K and self-field. The critical current density was measured for different orientations of the magnetic field and showed a significantly different behavior as compared to RABiTS and IBAD prepared films: (i) the maxima of j_c occurred when the magnetic field was perpendicular to the inclined c-axis of the ReBCO film and (ii) the j_c anisotropy was significantly reduced. The MgO buffer layer microstructure and orientation, the MgO buffer layer ReBCO interface, the microstructure and orientation of the superconducting film, and its surface structure were analyzed. The relation of the microstructure and the electric properties was discussed and significantly differences compared to RABiTS and IBAD prepared films were found.

For ISD films the increased surface area due to the sharply faceted MgO surface yields a larger surface energy contribution to the total free enthalpy. Thermal evaporation controls the chemical composition very well and no larger fractions of secondary phases could be identified within the DyBCO layer.

8. $DyBa_2Cu_3O_{7-x}$ coated conductors with critical currents exceeding 1000 A cm^{-1}

8.1. Introduction

$ReBa_2Cu_2O_{7-x}$ (Re: rare earth) coated conductors are up to date the most promising high temperature superconducting (HTS) wires for applications in energy technology [181]. They are the key device for implementing superconductivity in the magnet and energy technology for reducing electrical losses. They consist of biaxially textured HTS thin films deposited on metal substrate tapes using oxide buffer layers [181]. The critical current density, j_c, of coated conductors is in the range of 10^5-10^7 A cm^{-2} and is one key property of the superconducting material used, depending on temperature and magnetic field [182]. Critical currents are relevant for technological applications and are obtained by multiplying j_c with the cross-section of the superconducting film. Note that for coated conductors the critical currents per width of the tape are specified in A cm^{-1}. Coated conductors are being commercialized, however, their maximum critical currents are still limited to about 300-400 A cm^{-1} at 77 K and zero magnetic field [183].

Most of the relevant applications (motors, transformers etc.) for superconducting wires are operated at a magnetic field between 2-6 T. In the presence of a magnetic field the critical current density of superconducting wires decreases due to flux flow [184]. Inserting nano-inclusions into the superconducting material is one possibility to pin magnetic vortices and reach higher critical current densities [185, 47, 186] . Record values of 1010 A cm^{-1} were reported at 75.6 K and self-field for a 2 µm thick film with $BaZrO_3$ nano-rods and Y_2O_3 nano-particles [185]. For another coated conductor with nano-inclusions critical current densities were 1×10^6 A cm^{-2} for a magnetic field of 2 T and 1.8×10^5 A cm^{-2} for 6 T, respectively [47].

The critical current of coated conductors could be increased by increasing the thickness of the superconducting layer. However, a scale-up of the thickness is limited to about 2 µm by fundamental issues related to the thin film growth process of rolling assisted biaxially textured substrates (RABiTS) [187] and ion beam assisted deposition (IBAD) [188, 189, 190, 191]. More recently, PLD deposited $GdBa_2Cu_2O_{7-x}$ thick films [192] and $SmBa_2Cu_2O_{7-x}$ thick films deposited by reactive co-evaporation on IBAD substrates [193] yielded critical currents up to 1000 A cm^{-1}. In this paper we will report results with much thicker DyBCO films grown by ISD [116].

8.2. Experimental

In ISD technology biaxially-textured MgO buffer layers are deposited at room temperature on untextured Hastelloy tapes. MgO is evaporated by an e-gun source and the Hastelloy tape is tilted with respect to the incoming MgO flux (tilting axis parallel to the width of the tape). The anisotropy of the MgO surface energy and the thermally-activated directional diffusion yields the biaxial texture and a faceted surface of the MgO buffer layers [78]. For the sample studied here a 5.9 µm thick DyBCO layer was deposited at 700°C in untilted geometry after MgO buffer layer deposition, the length of the samples was 3 cm.

The ISD MgO buffer layer was grown using standard deposition conditions in our reel-to-reel ISD system on electro-polished Hastelloy substrates. For this special experiment the substrate was not moved

and we used a fixed substrate tilting-angle of 36°. The first 400 nm of the DyBCO layer were grown under untilted conditions and at elevated temperatures with our standard setup and standard deposition conditions in the HTS reel-to-reel system [116, 135]. The deposition temperature of the DyBCO seed layer is hard to measure precisely. It is in the range between 600°C to 800°C. After this an additional layer of DyBCO was deposited in a different HTS chamber yielding a total thickness of 5.9 µm.

For measuring the critical current a 2 mm long and 1.1 mm wide bridge was etched using standard photolithography. We determined the critical current of the sample using a 1 µV mm^{-1} electric field criterion by a four-probe measurement. The usual 1 µV cm^{-1} could not be applied because the signal noise exceeded the threshold voltage of 200 nV for this criterion. However, n values [60] of these materials are about 32 [116] and thus only a small error (about 7%) is introduced with respect to the 1 µV cm^{-1} criterion.

Scanning Electron Microscope (SEM) cross-section samples were prepared by mechanical grinding and polishing. SEM images were acquired with a Jeol 6500F SEM equipped with a backscattered electron (BSE) detector. TEM samples were prepared in cross-section by the Focused Ion Beam (FIB) method using a Zeiss AURIGA® - CrossBeam® Workstation. A thin TEM lamella was cut out by the ion beam, lifted out, and finally attached to a TEM grid. For image acquisition in the TEM, samples were oriented such that the c-axis of the DyBCO was lying in the image plane, i.e. the MgO/DyBCO interfaces were parallel to the electron beam.

Images and diffraction patterns were acquired in a Zeiss 912Ω operated at 120 kV using a 5 or 10 eV energy slit aperture of the Omega energy filter to reduce inelastically scattered electrons contributing to the image background. Diffraction patterns were acquired with a 700 nm selected area electron diffraction (SEAD) aperture. The MgO/DyBCO interface roughness was measured from SEM cross sectional images and the DyBCO surface roughness was measured from TEM cross sectional images.

8.3. Results

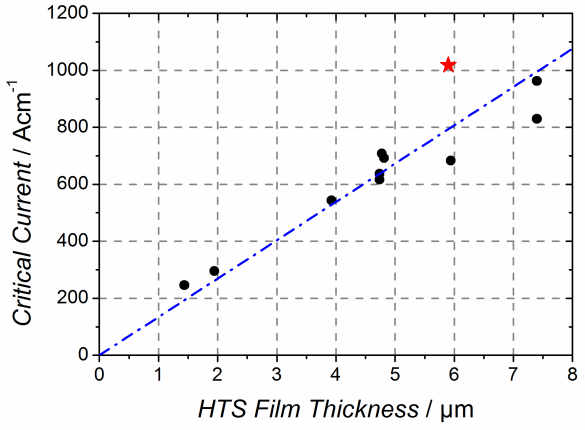

Figure 8.1.: Critical current per cm tape width vs. DyBCO film thickness of ISD coated conductors. The red asterisk indicates the sample investigated by SEM and TEM.

A record critical current of 112 A or 1018 A cm^{-1} was measured at 77 K and self-field for the bridge. As the thickness of the superconducting layer was 5.9 µm, this corresponds to a critical current density of 1.7 MA cm^{-2}. Several coated conductors with increasing film thickness were measured in this way. Fig. 8.1 shows the critical current measured as function of the DyBCO film thickness. An almost linear increase of the critical current with film thickness was observed up to 7.5 µm. The critical current density of DyBCO films with a thickness of 6 µm is close to that of thinner DyBCO films (DyBCO thicknesses up to 2 µm) for which j_c ranges from 1.6 to 2.6 MA cm^{-2}. This indicates the critical current density does not decrease significantly with thickness. A detailed analysis of the microstructure of such coated conductors was carried out for understanding the growth mechanism.

Fig. 8.2a shows a secondary electron image of the MgO surface in plan-view after the ISD deposition of MgO and prior to the deposition of the DyBCO film. The MgO surface consists of sharp and flat facets about 230 nm in size arranged in a tile-like structure, the edges of the facets appear in bright contrast. The

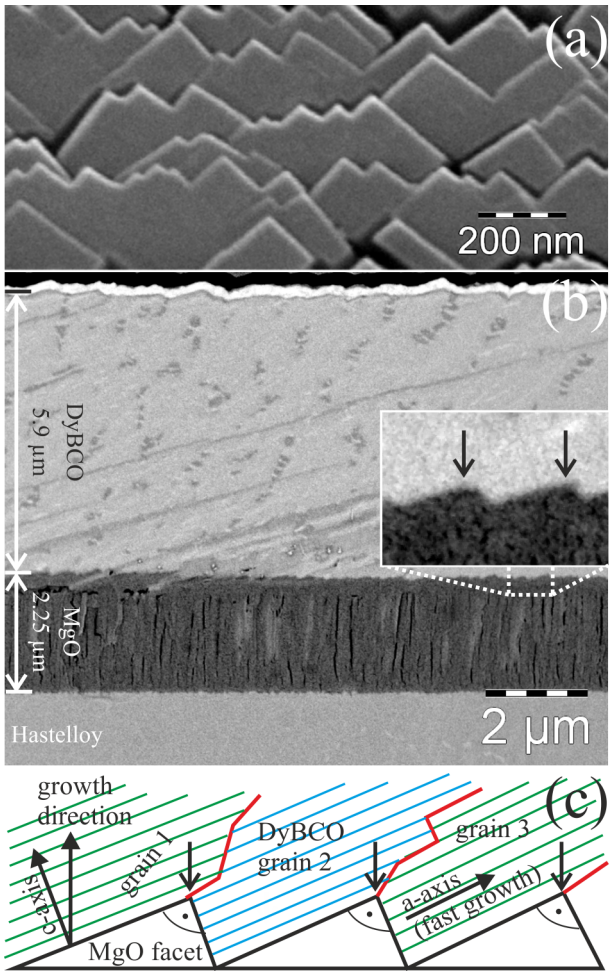

Figure 8.2.: (a) Plan view image of MgO facets prior to DyBCO deposition. (b) Backscattered electron image of the layer structure of a fully processed sample in cross sectional view. In the inset arrows are pointing to the MgO facets. (c) Schematic image showing the facets at the MgO/DyBCO interface.

facets were found to be parallel to (002) planes of the MgO and their surface normal is almost parallel to the direction of the incoming vapor during ISD deposition. Fig. 8.2b shows a BSE image of the layer structure in cross-section after the DyBCO deposition. The MgO layer thickness and the DyBCO film thickness were 2.25 µm and 5.9 µm, respectively. The areas of different contrast are secondary phases namely copper oxides (dark) and dysprosium oxides (bright). These secondary phases appear due to Ba deficient powder used for the DyBCO growth. An enlarged view of the MgO/DyBCO interface is shown in the inset in Fig. 8.2b, some edges of the MgO facets are marked by black arrows. The DyBCO surface had a roughness of less than 200 nm measured over a length of 12 µm of the film. XRD data documenting the biaxial texture of both the ISD and the DyBCO layer are presented elsewhere [135].

A schematic drawing of the MgO/DyBCO interface is shown in Fig. 8.2c based on our results of a large number of cross-sections investigated by TEM [194]. The growth directions as well as the crystallographic axes of the DyBCO film are indicated. The (001) direction of DyBCO encloses an angle of 24° with the substrate normal. As a consequence the growth direction has a non-zero component parallel to the crystallographic (a,b)-plane of the DyBCO for the ISD geometry. Note that the DyBCO (a,b)-plane is parallel to the MgO (200) plane. In Fig. 8.2b arrows point to edges of facets from which grain boundaries emerge into the DyBCO film. The grain size in the lower part of the DyBCO film correlates with the facet size (230 nm). Grain boundaries are tilted with respect to the substrate normal in a direction opposite to the (001) direction of DyBCO.

Fig. 8.3 shows a low-magnification TEM bright-field image of the top part of the DyBCO layer in cross-

section. A DyBCO grain size of 500-600 nm was measured in the upper part of the DyBCO film and a DyBCO surface roughness of 140 nm was determined. Therefore, we observed an increase of the DyBCO grain size with increasing film thickness. The orientation of the DyBCO c-axis was found to be fixed throughout the film thickness. The diffraction pattern is shown in false color to highlight the splitting of reflections due to DyBCO small-angle grain boundaries. The small inset in Fig. 8.3a shows three DyBCO (00l) reflections separated by a maximum angle of 4°. Therefore, the DyBCO grains of the investigated area are separated only by small-angle grain boundaries, this was found to be true for all analyzed areas.

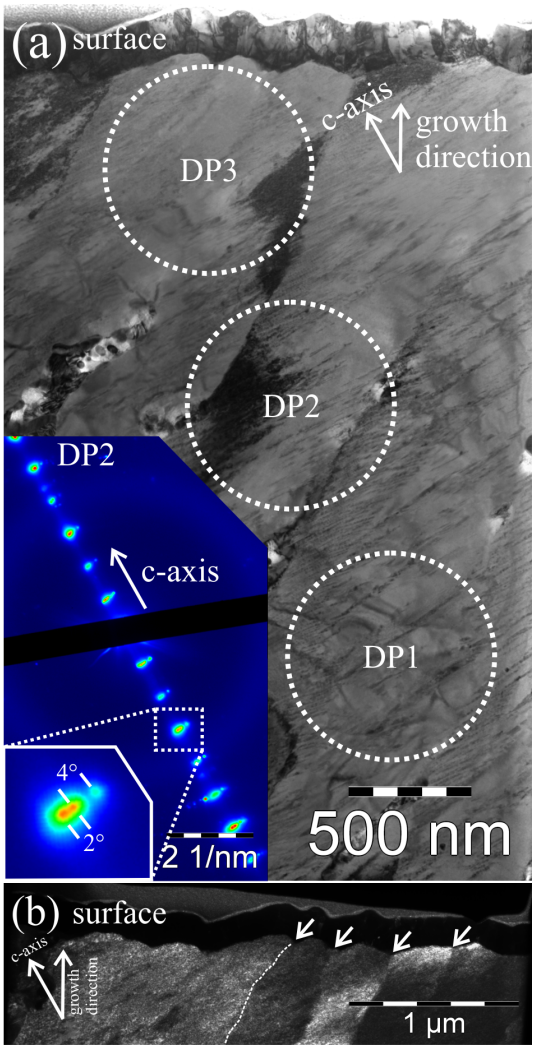

Figure 8.3.: (a) Cross sectional TEM bright-field image of the top 3 µm of a 5.9 µm thick DyBCO film. The inset displays the diffraction pattern DP2 in false color. Diffraction patterns DP1 and DP3 are not shown here. The white circles mark the size of the selected area aperture used for acquiring diffraction patterns. (b) TEM (002) dark-field image of the topmost part of (a). The white arrows indicate DyBCO grain boundaries.

Fig. 8.3b shows a (002) dark-field image of the top part of the DyBCO film close to the surface, grain boundaries are marked by white arrows. Consistent with the schematic drawing (Fig. 8.2c) the DyBCO grain boundaries (Fig. 8.3b) were found to be tilted with respect to the substrate normal opposite to the (001) direction.

8.4. Discussion

It was shown that ISD technology offers unique possibilities to grow monolithic thick films, exceeding 2 µm in thickness. In ISD technology sharp and well-defined MgO (002) facets [164] (their width is about 230 nm) provide a tilted (about 25°) surface for the growth of the superconducting layer. Despite the large lattice misfit (8.5% between MgO and DyBCO), the DyBCO film grows epitaxially on top of the MgO buffer layer, i.e. the (hk0) directions of MgO are parallel to the (hk0) directions of the DyBCO. The DyBCO (001) direction was found to be always parallel to the MgO (002) direction. As a consequence ISD deposited DyBCO films have a non-zero component of the growth direction parallel to the (a,b)-plane of the DyBCO grains, as shown in Fig. 8.2c. This makes the c-axis growth very stable suppressing a-axis growth and yields a perfect transfer of the biaxial texture of the MgO buffer layer into the DyBCO layer. A-axis grains would form large-angle grain boundaries and, therefore, would dramatically reduce the critical current density within the tape [64]. In contrast, the growth direction does not have a component parallel to the (a,b)-plane of $YBa_2Cu_3O_{7-x}$ (YBCO) for the RABiTS and IBAD growth process. As a consequence, thick films grown by these technologies show a-axis growth and porosity (dead layer effect) [187, 191, 170, 83]. Coated conductors fabricated by the RABiTS and IBAD technology can carry the same amount of critical current, however, a more complicated architecture in the superconducting layer is required yielding an increase in processing cost and time.

For ISD technology, the individual grains retained their biaxial texture over the total film thickness (5.9 µm, Fig. 8.3) and neither porosity nor a-axis growth was observed. Critical currents exceeded 1000 A cm^{-1} at a temperature of 77 K and self-field.

8.5. Conclusions

In summary, ISD technology yields significant advantages since (i) DyBCO films can be grown as monolithic thin films avoiding a-axis growth and (ii) yield larger critical currents as compared to IBAD and RABiTS for monolithic films. ISD yields highly biaxially textured DyBCO films at all thicknesses and no significant decrease of the critical current density with film thickness. This is due to the growth process on a faceted MgO surface yielding a non-zero component of the growth direction parallel to the (a,b)-plane of the DyBCO. A maximum critical current of 1018 A cm^{-1} was measured for a DyBCO film with 5.9 µm thickness showing that in ISD technology critical transport currents exceeding 1000 A cm^{-1} can be realized by simply increasing the HTS film thickness.

9. Development of innovative, layered superconductors for energy technology (ELSA)

9.1. Introduction

High-temperature superconductors (HTS) technology is due to its unique properties a key technology of the 21st century. HTS coated conductors are revolutionizing energy-technological applications like motors, generators, transformators, and cables, as well as applications using magnet technology like induction heaters, nuclear magnet resonance (NMR), and magnet resonance imaging (MRI).

Before starting the project there were world-wide intentions to grow $YBa_2Cu_3O_{7-\delta}$ (YBCO) layers using chemical solution deposition (CSD). At that time, the metal-organic decomposition (MOD) by using trifluoroacetate-based precursors (TFA) was applied to grow YBCO layers. It was already proven that by this method YBCO layers may be prepared in long lengths having high critical currents. However, the manufactured lengths were test lengths (few cm to few m) and the industrial length scales are in the range of 100 m to 500 m. Often single layers were deposited by using a physical technology (e.g. e-beam evaporation), which hampered a direct comparison of performances. In 2006 the world-leader in rolling-assisted biaxially textured substrate (RABiTS) coated conductor technology was American Superconductor, which produced RABiTS-based HTS tapes having critical currents exceeding 150 A/cm.

The final goal in coated conductor reasearch was to develop a tape that is grown by solution-based methods under ambient pressure. Several groups in the US, Japan, and Europe tried to develop solution-based deposition methods for buffer layers. However, before project begin all buffer layers except doped $SrTiO_3$ were grown by using vacuum technologies.

The project "Development of innovative, layered superconductors for energy technology (ELSA)" is dealing with the production of coated conductors on basis of epitaxial growth of YBCO HTS thin films on buffered, textured metallic substrates by asing CSD technology. In the ELSA project several groups and institutions were involved: Zenergy Power GmbH (now Deutsche Nanoschicht GmbH and former Trithor GmbH, Rheinbach), the Institute of Bio- and Nanosystems-2 (Forschungszentrum Juelich), the Institute of Electronic Materials II (RWTH Aachen), the Institute of Anorganic Chemistry (RWTH Aachen), GTT Technologies in Herzogenrath, as well as the Institute of Applied Physics (Eberhard Karls University Tuebingen). The project was devided into four main tasks:

1. An appropriate material selection should initially met with computational methods for the basics of innovative buffer layer systems and then be verified in practice.
2. Basic research on high-performance superconducting films for practical applications in magnetic fields carried out by the selection and synthesis of suitable pinning centers and their incorporation into the superconducting layer.
3. The development and optimization of the complex coating process involved the further development of the coating solutions in terms of wetting and drying properties using additives. The Optimization of individual crystallization processes based on thermodynamic and quantum mechanical calculations to stability ranges.
4. The pilot production and testing of the HTS conductor included the scaling of the developed laboratory-scale coatings on lengths of 100 m and more. This includes providing the coating

solutions in suitable quantities and the development of the required reel-to-reel process plant generation. With such a tape should be manufactured and tested finally a coil.

The Institute of Applied Physics focused on structural and chemical analyses of the tapes provided by Zenergy Power GmbH and correlating them to electrical data provided by e.g. the Institute of Bio- and Nanosystems-2 (Forschungszentrum Juelich) in terms of a structure-property-chemistry relationship.

9.2. Experimental

Parameter	Zeiss 912Ω	Jeol 3000F
Electron Source	LaB_6	Field emission
Acceleration Voltage	120 kV	300 kV
Objective lens $C_{S,3}$	2.7 mm	1 mm
Objective lens C_C	2.7 mm	1.8 mm
Point resolution	0.32 nm (elastic), 0.8 nm (inelastic)	0.17 nm
Energy filter type	in-column	post-column
Energy Resolution	max. 1 eV	max. 0.7 eV
STEM unit	no	yes
ADF detector	no	yes

Table 9.1.: Microscope data extracted from the corresponding manuals.

Almost all plan-view samples were analyzed by scanning electron microscopy (SEM) and energy-dispersive X-ray (EDX) analysis. We used a Jeol 6500F equipped with an Oxford EDX detector. Focused ion beam (FIB) cuts were prepared using a Zeiss Auriga Crossbeam system.

In total nine plan-view samples have been prepared successfully by conventional grinding and polishing for transmission electron microscopy (TEM). Out of these nine samples only three samples have been analyzed in great detail. Eleven cross-sectional samples were prepared for TEM. Out of these eleven samples only five samples survived the preparation process including the etching process in a Baltec Res 100 or a Fischione 1010 ion mill. All five samples have been analyzed in detail by using an analytical Zeiss 912Ω transmission electron microscope. However, the TEM results were not satisfying except that of the $La_2Zr_2O_7$ (LZO) sample (no YBCO film on top).

Due to the poor internal connectivity of YBCO layers delamination occured making sample preparation very difficult. The large surface roughness of ELSA samples caused a large glue thickness (10-30 µm), whereas for other technologies the glue thickness was 2 µm at worst. Thus, in the ion etching process the samples were lost or were etched not very smoothly.

Since almost no useful YBCO cross-section sample could be obtained due to poor adhesion, TEM analysis was carried out only for plan-view samples. Two TEM's were used for the characterization: (i) the Zeiss 912Ω and (ii) the Jeol JEM 3000F. The Zeiss 912Ω has only a limited resolution in energy and space (see Tab.9.1) due to the LaB_6 emitter and its objective lens. Thus, only conventional techniques, i.e. diffraction contrast imaging, diffraction, EDX, and energy-loss spectroscopy were applied. For any question beyond this resolution a field emission microscope is necessary. The Jeol 3000F is equipped with a Schottky field emission gun allowing higher spectral and spatial resolution than the Zeiss 912Ω. The Jeol JEM 3000F was used for high-resolution imaging and spectroscopy.

9.3. Results and Discussion

9.3.1. Layer defect analysis by SEM/EDX

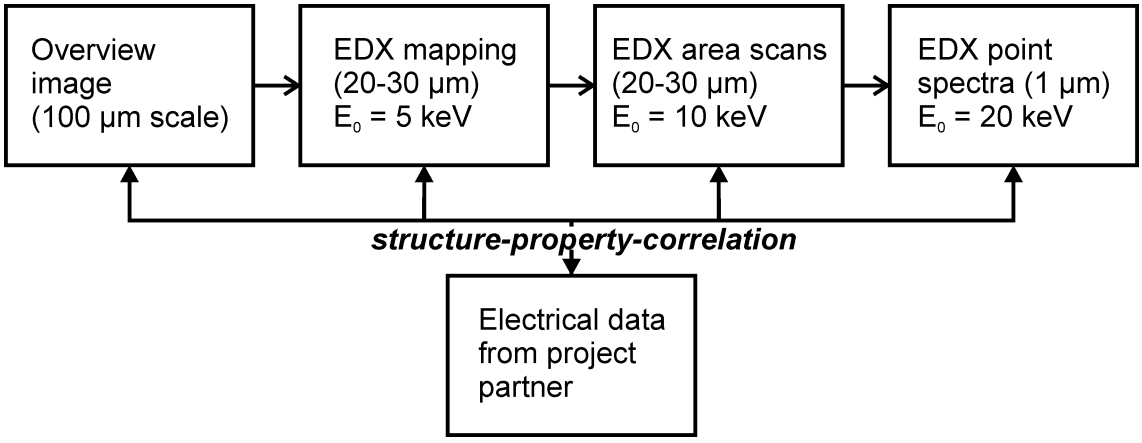

Figure 9.1.: Flow diagram for the SEM analysis of ELSA plan-view samples.

Fig. 9.1 shows the approach for analyzing ELSA plan-view samples in the SEM. Cross-sections are only prepared for specific issues that cannot be answered by the plan-view approach. First overview images are acquired to assess the sample quality on the 100 µm level. In the next step a chemical map is acquired on the 20-30 µm level to indentify the phase distribution. The film quality of CSD-grown films is documented by EDX analyses. This includes the determination of a mean YBCO film thickness by acquiring EDX area scans on a 20-30 µm area as well as the determination of a local YBCO film roughness by EDX point spectra on the 1 µm scale. The difference between an EDX chemical map and an EDX area scan is that in the first a pixel-by-pixel map of EDX spectra is acquired and in the latter an integral spectrum is acquired from an area. Finally, the obtained microstructural and chemical data is compared to electrical measurements carried out by the project partners, yielding a structure-property correlation.

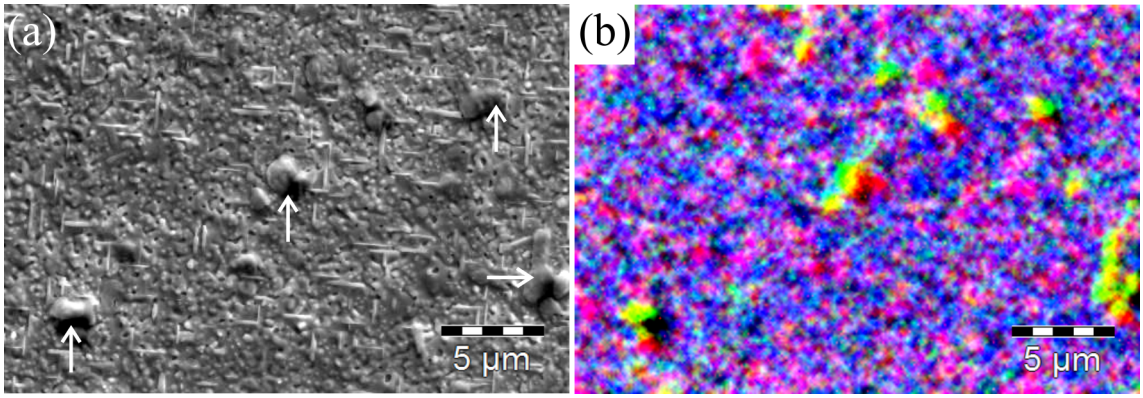

Figure 9.2.: (a) Secondary electron image of a typical CSD YBCO surface and (b) chemical surface map of the same area as imaged in (a) acquired by EDX. The surface map combines three 8 bit gray scale images into one 24 bit color image using the following setting: for the red channel the Ba-L signal is used, for the green one the Cu-L signal, and for the blue one the Y-L signal.

An important technique used for CSD-prepared coated conductors is EDX mapping. It is used to determine the chemistry near the YBCO surface. A crucial parameter is the choice of the primary electron energy. The smaller the energy the better the spatial resolution but the harder the element identification may be, since in the low energy region many X-ray lines can overlap. For CSD coated conductors typical candidates for severe X-ray line overlap are the two pairs Y-L/Zr-L and Ba-L/La-L since both pairs

contain elements that are next to each other in the periodic table. For CSD YBCO 5 keV electron energy was used for all EDX mappings to obtain a good spatial resolution.

Fig. 9.2a shows a typical secondary electron image of the rough YBCO surface. The structures marked by white arrows are copper oxide secondary phases. They have a size of 2 to 3 microns and a density of 0.007 μm^{-2}. In the chemical map in Fig. 9.2b they have a green color. For µm-sized copper oxide particles, shadowing is observed in the map, since they are sticking out the surface so far that they absorb the X-rays emerging from the material behind them in direction towards the detector. Thus, these areas have a black color in the EDX map. A second type of secondary phase can also be observed. In the EDX map in Fig. 9.2b it has a blue color and a size less than 500 nm. Unfortunately, the spatial resolution is not high enough to clearly separate each particle. Together with TEM experiments it was possible to identify those particles as Y_2O_3. The advantage of this method is that secondary phases larger than the typical extension of the excitation volume (here about 1 µm) can be clearly identified since they can be separated from the matrix. For any more advanced analysis of the secondary phases contained in the matrix the TEM is the machine of choice since the spatial resolution is much better than in the SEM.

On a CSD coated conductor surface 30 µm sized defective areas were observed by plan-view SEM (Fig. 9.3a). However, the origin of those defects strongly disturbing the YBCO growth could not be found by plan-view SEM. Therefore, cross-sectional samples were prepared using a FIB system. Fig. 9.3b shows such a defective area from Fig. 9.3a in cross-section. A crater in the Ni substrate of about 3 µm in width and depth is observed. Already the LZO buffer layer is strongly disturbed in this region, i.e. it is untextured in the crater region. As a consequence the growth of the following YBCO layer is disturbed in a significantly larger area (about 30 µm). The origin of the crater-like defects lies in the manufacturing and the processing of the Ni substrate tapes. It was also found out that craters only appear at Ni grain boundaries.

Fig. 9.4a shows a FIB-prepared cross-section of an undamaged sample area of Fig. 9.3a. The large film roughness, i.e. a film thickness difference of 250 nm in the YBCO layer, is documented by two film thickness measurements 500 nm seperated from each other. Ba-L/Cu-K X-ray correlation diagrams (Fig. 9.4b) using the normalized integral counts from the Ba-L and Cu-K peak of EDX point spectra yield a large scatter confirming the observation of a large film roughness in Fig. 9.4a. The Ba/Cu correlation is positive, because both elements are contained in the YBCO layer. Variations in the chemical composition of the YBCO film can be excluded, because they would destroy the linear relationship of the Cu-K/Ba-L ratio and yield uncorrelated agglomerations of points in the Ba-L/Cu-K X-ray correlation diagram. The Ba-L/Cu-K correlation of a sample grown by inclined substrate deposition (ISD) is provided for comparison (Fig. 9.4c), showing significantly less scatter in the data, which indicates a low surface roughness and a homogeneous film thickness.

The YBCO tape showed strong fluctuations in its strucural and superconducting film properties. On a 100 µm length scale coarse inhomogeneities were detected by secondary electron images in the SEM. On 300 µm$\times$300 µm areas EDX area scans were acquired using 10 keV primary electron energy. In area (1), the good area, (see Tab. 9.2a) the standard deviations of the X-ray intensities are in the 1-2% range, whereas in area (2), the poor area, (see Tab. 9.2b) they can reach up to 9%, i.e. significantly larger. Correlation diagrams of X-ray intensities showed that the standard deviations in Tab. 9.2 are due to variations in the film thickness. That means the film homogeneity was poorer in area (2) than in area (1). The inhomogeneities were analyzed by acquiring X-ray point spectra at 20 keV electron primary energy on the µm scale using the same analyzation procedure as for the area scans. It could be shown using this procedure that two length scales exist, which have an influence on the X-ray intensities: (i) 300 µm, (ii) 1 µm. Both can be captured by using SEM-EDX and yield relevant statements on the sample quality correlating with the superconducting properties. The measurement data can be obtained quickly and reliably and allow to probe the layer homogeneity at different length scales, which is of crucial importance for CSD-prepared coated conductors.

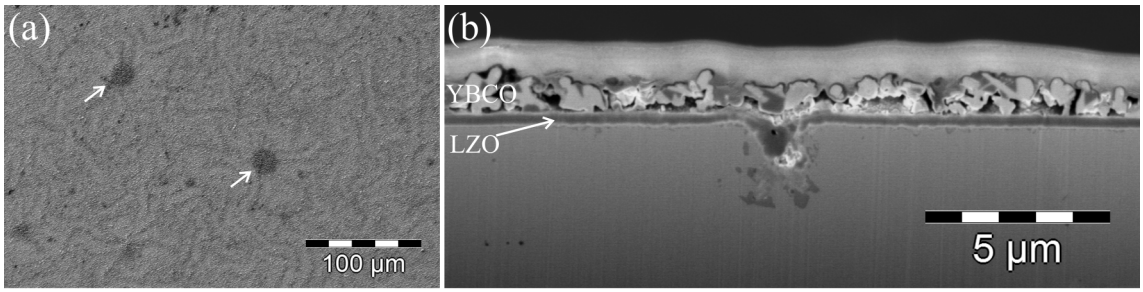

Figure 9.3.: (a) Plan-view SEM image of a CSD-YBCO layer containing defect areas (marked by the white arrows) and (b) Cross-sectional FIB cut across one of the a defective areas marked in (a).

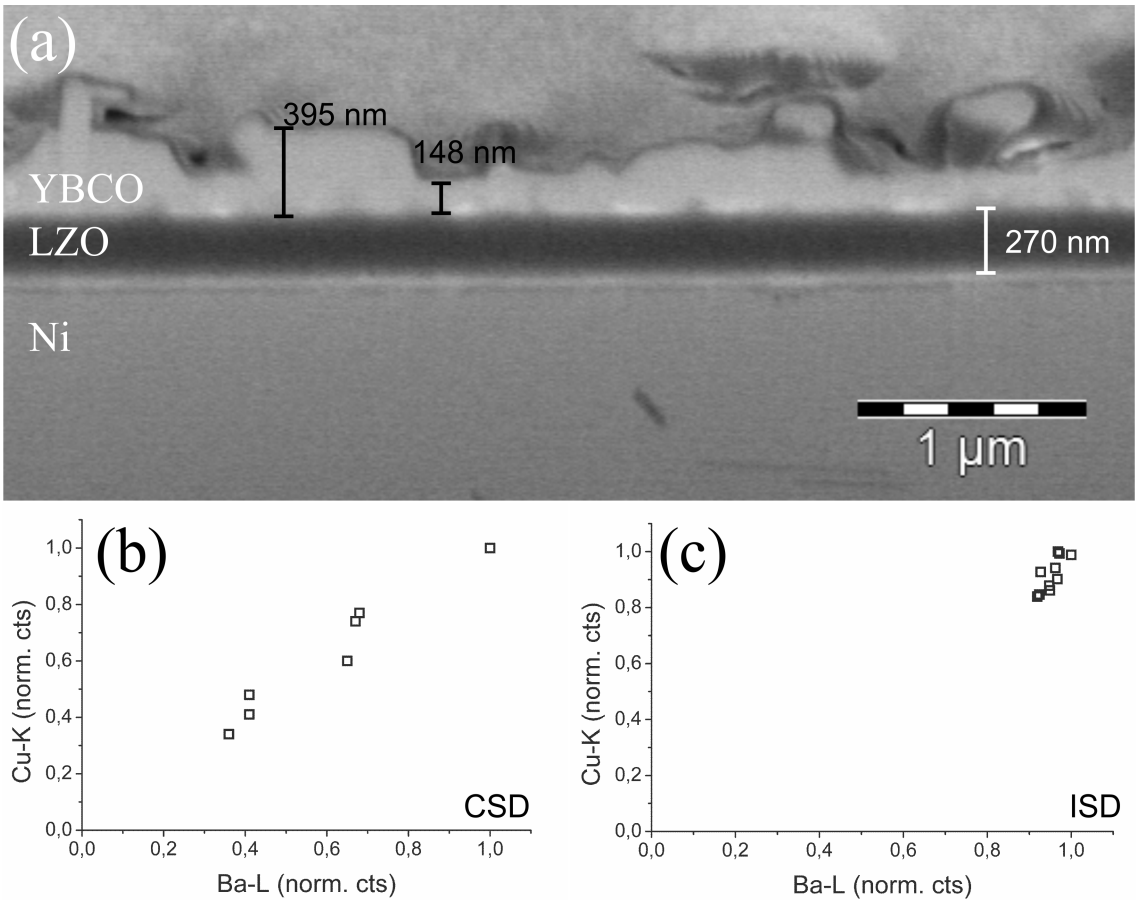

Figure 9.4.: (a) FIB cross-section of an undamaged sample region documenting the large variation in film thickness in CSD coated conductors. Ba-L/Cu-K X-ray correlation diagrams of normalized integral X-ray counts obtained from X-ray point spectra at 20 keV primary electron energy for (b) CSD coated conductors and (c) ISD coated conductors. The large difference in the scatter between the two coated conductor growth methods is clearly visible.

(a) Superconducting area.

	O-K [cts]	Cu-L_α [cts]	Y-L_α [cts]	Ba-L_α [cts]
Mean	4665	3888	1501	872
Std. dev.	53	43	31	7
Norm. mean	0.99	1.01	0.99	1.01
Norm. Std. dev.	*0.01*	*0.01*	*0.02*	*0.01*

(b) Non-superconducting area.

	O-K [cts]	Cu-L_α [cts]	Y-L_α [cts]	Ba-L_α [cts]
Mean	3775	3418	1463	830
Std. dev.	364	290	40	61
Norm. mean	0.94	0.94	0.97	0.93
Norm. Std. dev.	*0.09*	*0.08*	*0.03*	*0.07*

Table 9.2.: X-ray counts acquired in area scans for (a) a superconducting area and (b) a non-superconducting area of a YBCO coated conductor tape. Please note that the standard deviations from the normalized intensities (max. measured intensity equals 1) are significantly smaller in (a) than in (b).

9.3.2. Advanced TEM and STEM analyses

Conventional TEM analyses of LZO buffer layers and EFTEM imaging of CSD YBCO layers with and without artificial pinning centers are summarized in [23].

9.3.2.1. O2p pre-peak spectroscopy on CSD coated conductor samples

The short superconducting coherence length in high-T_c materials makes them extremely sensitive to the strain field introduced by defects on the atomic scale. Perhaps the most important of these defects for large-scale technological applications are grain boundaries [195]. Since STEM and EELS can be acquired simultaneously a direct correlation between the structural images and the local electronic structure information in the spectrum can be achieved. A detailed high-resolution STEM and EELS analysis of grain boundaries has already been carried out in YBCO grown on $SrTiO_3$ bi-crystal substrates [195]. For 2G coated conductors a similar analysis has not been carried out yet. It is known since 20 years that in YBCO the strain field of grain boundary dislocations will lead to a de-oxygenation in the strain field area [64]. The same issue should also hold for other types of defects observed in YBCO coated conductors such as dislocations or precipitate-matrix interfaces. These defects are of great importance for the pinning of magnetic flux lines and thus for applications in magnetic fields up to several Tesla.

EELS can be used to probe the density of states near the Fermi level.$YBa_2Cu_3O_{7-\delta}$ has unoccupied O2p states right above the Fermi level. An increasing oxygen deficiency δ of the YBCO structure decreases the amount of unoccupied O2p states. EEL spectra are highly sensitive to changes of δ and thus to the change in unoccupied O2p states [196]. The oxygen concentration directly influences the superconducting properties of the material. O2p spectroscopy with high spatial and spectral resolution is an excellent method to reveal, e.g. pinning relevant defect structures.

Fig. 1.6b shows the scattering triangle for any type of inelastic scattering. The scattering angle $\mathbf{q}$ has a component parallel $\mathbf{q}_{||}$ and a component perpendicular $\mathbf{q}_{\perp}$ to the incident electron beam. For CSD YBCO plan-view samples the main momentum transfer will be in the (a,b)-plane of YBCO, i.e. in the CuO planes. This determines the form of the EEL spectrum due to the different binding energies of the O1s level of the four different O lattice sites and/or due to the symmetry ($2p_{x,y}$ and $2p_z$) of the O2p final states [197]. In case of total momentum transfer along the YBCO c-axis the O pre-peak is less pronounced in the EEL spectrum than it is if the total momentum transfer is in the (a,b)-plane.

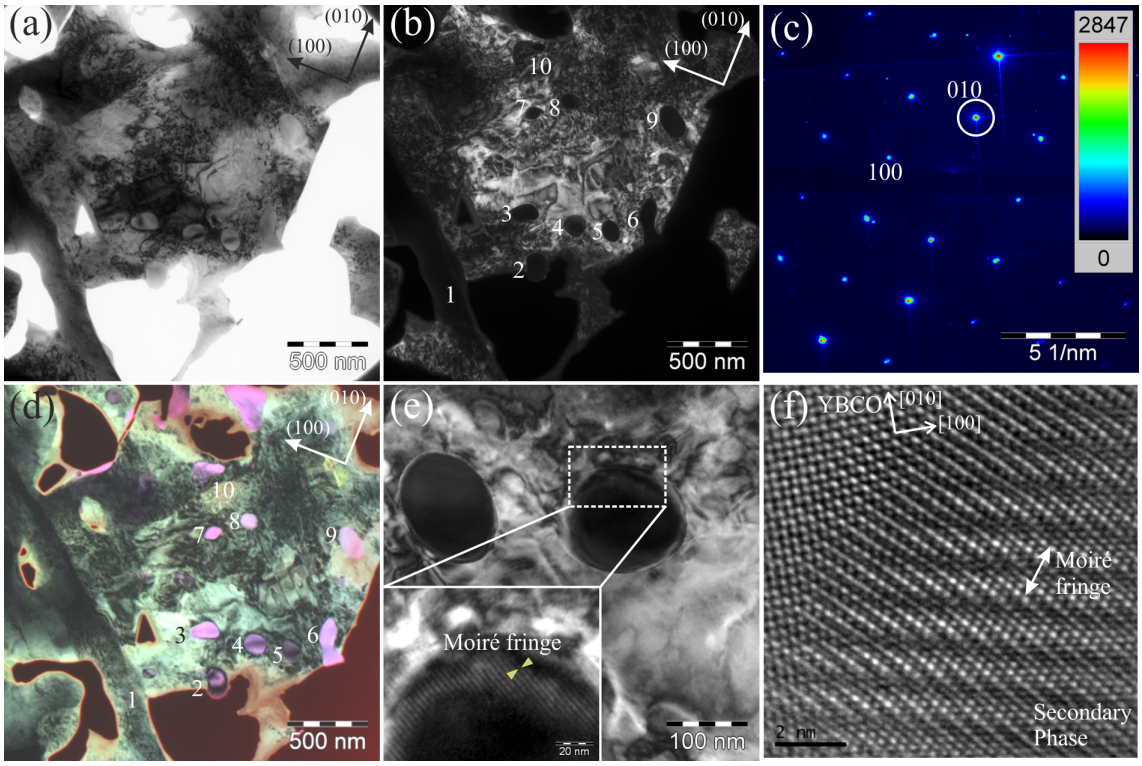

Figure 9.5.: TEM plan-view image in (a) bright-field and (b) dark-field mode. In (b) number 1 indicates an a-axis grain and the numbers 2-10 denote secondary phases. (c) Diffraction pattern in false color. The white circle denotes the reflection used in (b). (d) Plasmon image displaying the secondary phases in a greyish to pink color. The YBCO matrix yields a green color. (e) High magnification dark-field image of a matrix/secondary phase interface showing Moiré contrast. (f) High-resolution phase contrast TEM image in the [001] pole of a similar interface as shown in (e).

High-resolution STEM combined with atomically resolved EELS helps to put forward a structure-property relationship of atomically scaled defects (grain boundaries, dislocations, precipitate-matrix interfaces...) in YBCO coated conductors. A basic characterization of the sample including diffraction contrast imaging, diffraction, EDX, EELS and low-loss EFTEM was carried out using the Zeiss 912Ω. Fig. 9.5a shows a typical YBCO area of a CSD processed sample in bright-field condition. The corresponding dark-field image is shown in Fig. 9.5b. The reflection used for the dark-field image is indicated by the white circle in the diffraction pattern in Fig. 9.5c. A false color table was applied to the diffraction pattern to increase the contrast. In the dark-field image (1) denotes an a-axis grain and the other numbers indicate secondary phases. In dark-field mode secondary phases can be distinguished from the matrix since they do not show diffraction contrast. Fig. 9.5d was obtained by using the plasmon imaging technique. Three energy-filtered images were acquired at energy-losses of 13 eV, 26 eV, and 37 eV using a 5 eV slit aperture. The advantage of this method is that it provides not only a size information but also a chemical fingerprint of the single phases being present in the sample. The YBCO matrix yields a greenish color and the secondary phases appear in pink or pink/gray color due to their different plasmon energy. EDX measurements (not shown here) revealed that pink-colored phases in Fig. 9.5d are Y_2O_3. The Y_2O_3 phase has a typical size of 100-300 nm and a density of ~3 particles per μm^2. Besides the Y_2O_3 and the copper oxide phase also other phases are thermodynamically allowed but were not confirmed here. Fig. 9.5e is a high-magnification dark-field image of a secondary phase. The inset shows a magnified part of the matrix/particle interface region of Y_2O_3 particle #4. Moiré fringe contrast was identified due to the lattice mismatch of the YBCO matrix and the Y_2O_3 particle. A high-resolution phase contrast image (Fig. 9.5f) was also acquired using the Jeol JEM 3000F in the [001] pole showing the same kind of Moiré fringe contrast. The YBCO [100] and [010] directions are indicated within the figure. In the diffractogram of Fig. 9.5f (not shown here) it can be seen that the YBCO and Y_2O_3 reflec-

tions are slightly rotated by about 8° with respect to each other. Thus, the particle is at maximum partially coherent. Pinning relevant defects could not be identified within the image. High-resolution HAADF STEM images should be acquired for projecting interfaces to ease the image analysis and interpretation.

The experiments were carried out using a Jeol JEM 3000F TEM at 300 keV primary electron energy (further details see Tab.9.1). The sample was tilted into the [001] pole. Zero-loss EEL spectra were acquired in the image mode and core-loss EEL spectra in the diffraction mode using the convergent beam electron diffraction (CBED) mode. The STEM unit was not used during these experiments. Further acquisition details for the O2p spectroscopy were:

1. Camera length: 30 cm
2. Spectrometer entrance apertures: 0.6 mm, 2 mm, and 3 mm
3. Energy dispersion: 0.3 eV
4. Acquisition time: 6.4-12.8 s

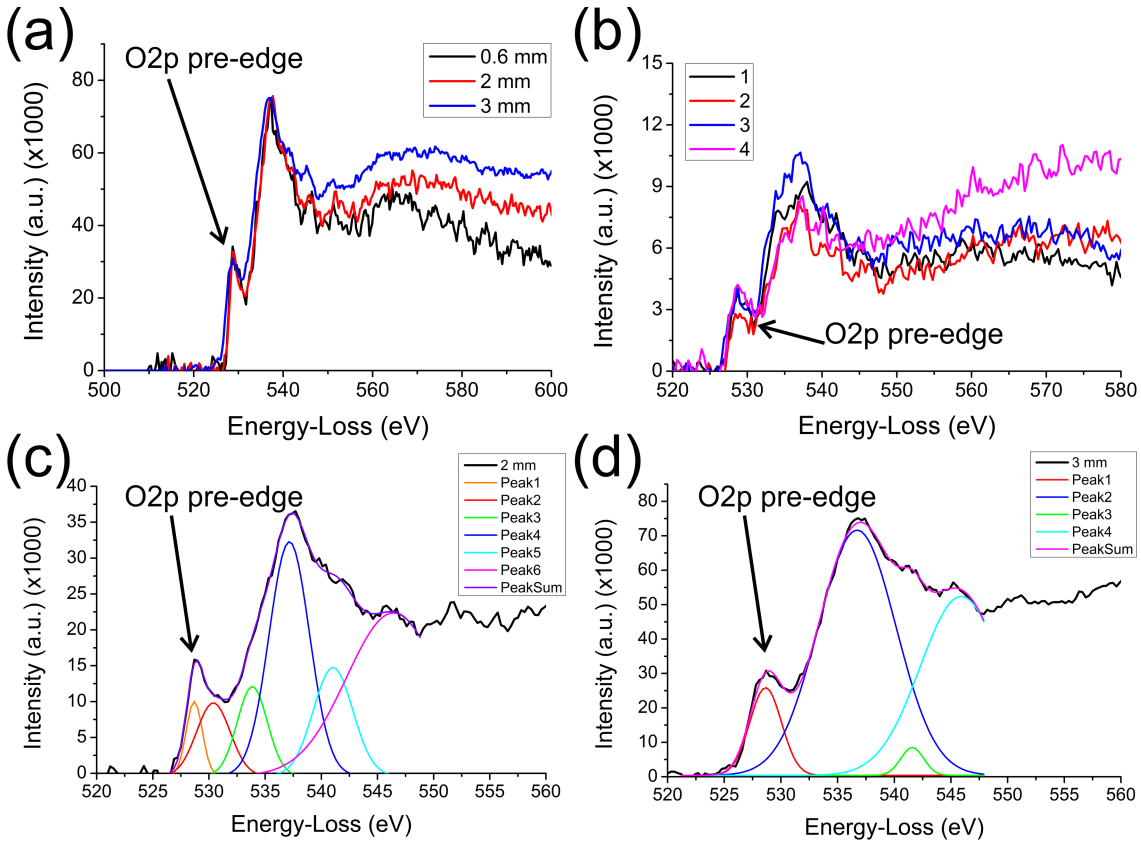

Figure 9.6.: Effect of the (a) used acquisition conditions and (b) sample thickness on the O2p pre-peak. Data evaluation using multi-Gaussian least-square fits for a spectrometer entrance aperture of (c) 2 mm and (d) 3mm.

Please note that a 30 cm camera length and a 3 mm entrance aperture correspond to a collection angle of roughly 10 mrad. This is about 10 times the characteristic angle for the O-K edge at 300 keV primary electron energy. The energy resolution of the O-K EEL spectra was estimated by analyzing the Ba-M_{45} edge (not shown here). An energy resolution of 2.05 eV and 2.56 eV was found for an entrance aperture of 0.6 mm and 3 mm, respectively. The further analysis of the single spectra was carried out considering the following issues:

1. Dependence on the acquisition conditions, i.e. spectrometer entrance aperture
2. Dependence on the sample thickness

3. Results of data evaluation using a Gaussian method similar to that of Browning et al. [198]
4. Evaluation of O2p spectra with respect to beam sensitivity at 300 keV electron energy.

One O-K EEL spectrum was acquired for each spectrometer entrance aperture (Fig. 9.6). The spectra were energetically calibrated such that the center of the O2p pre-peak had a value of 528.5 eV [198]. The intensity of all spectra was normalized on the O-K edge of the 3 mm EEL spectrum. On the one hand, it was found that the spectrum acquired with the 0.6 mm entrance aperture had the best energy resolution, i.e. the O2p pre-peak is separated the farthest from the O-K main edge but had the poorest signal-to-noise ratio and the lowest total counts in the spectrum. On the other hand, the spectrum acquired with the 3 mm entrance aperture showed the poorest energy resolution but the best signal-to-noise ratio and the highest total counts in the spectrum. Furthermore, a fine structure could be identified within the O-K edge. The spectrum acquired with the 2 mm entrance aperture had a similar energy resolution and had a better signal-to-noise ratio as the spectrum acquired with the 0.6 mm aperture. Additionally, the fine structure observed in the 3 mm spectrum was also observed. It is a good compromise between energy resolution, counts, and noise. Thus, for further O2p analysis it is recommended to use the 2 mm spectrometer entrance aperture to obtain high-quality results.

Fig. 9.6b shows four O-K EEL spectra all acquired with a 2 mm spectrometer entrance aperture and at different sample areas. The acquisition time was 6.4 s explaining the low signal-to-noise ratio in these 4 spectra. Spectrum 1, 3, and 4 have a similar height in the O2p pre-peak whereas spectrum 2 has a smaller one. This can either be due to the sample area, i.e. part of the illuminated area is non-superconducting or due to noise in the spectrum. The main O-K edge is for all spectra similar but exact conclusions are hard to state due to the high noise level. Spectrum 4 has an increasing intensity level starting about 20 eV above the O-K edge indicating a thick sample area. All other spectra do not show this feature, i.e. the intensity is almost constant. The O2p pre-peak intensity of spectrum 4 is the same as for spectrum 1 and 3 indicating that there is no thickness dependence of the O2p pre-peak.

Fig. 9.6c and d show two O-K EEL spectra acquired for 12.8 s using a 2 mm and a 3 mm spectrometer entrance aperture, respectively. Both spectra were evaluated using a multi-Gaussian least-square fit. The obtained R^2 value of the resulting sum curve was larger than 0.997 for both spectra. In Fig. 9.6c six Gaussian functions were used due to the higher energy resolution revealing a more extended fine structure than in Fig. 9.6d where only four Gaussian functions were used. The errors of the O2p/O-K ratio were calculated using the propagation of errors. Tab. 9.3 shows the results of the O2p pre-peak data evaluation according to the approach of Browning et al. [198]. Similar values for the O2p/O-K ratio were obtained. If the O2p/O-K ratio is converted into an O stoichiometry value using Fig. 3 of Browning et al. [198] as reference we obtain an oxygen stoichiometry value larger than 6.9 for our sample. However, the errors in our O2p/O-K ratio are quite large for the 2 mm entrance aperture data.

Quantity	**2 mm**	**3 mm**
O2p pre-peak area [cts]	18622 ± 6305	89383.14 ± 3219
O-K edge area [cts]	146898 ± 64202	613128 ± 26004
O2p/O-K	0.13 ± 0.07	0.15 ± 0.01
Corresponding O stoichiometry [198]	> 6.9	> 6.9

Table 9.3.: Evaluation of the O2p pre-peak data evaluation using multi-Gaussian least-square fits.

At 300 keV electron energy it is also reasonable to consider knock-on damage. Especially oxidic samples like YBCO will be affected by a decrease in their oxygen content at high electron energies. Thus, two time series of several O2p EEL spectra were acquired at two different sample areas and evaluated with respect to the O2p/O-K ratio. The following acquisition conditions were used at the Jeol 3000F:

1. Electron energy: 300 keV
2. EELS acquisition mode: diffraction
3. Camera length: 250 mm
4. Illumination mode: TEM
5. GIF aperture: 2
6. EELS dispersion: 0.2 eV
7. EELS acquisition time: 25.6 s
8. Estimated energy resolution: 1 eV

A multi-Gaussian least-square fit was applied to all acquired EEL spectra. The resulting sum curve had always a R^2 value larger than 0.99. O2p and O-K peak areas were calculated from the fit values resulting in the O2p/O-K ratio. The errors of the O2p/O-K ratio were calculated using the propagation of errors. Afterwards, they were plotted according to their acquisition time with respect to the first acquired spectrum. The results are shown in Fig. 9.7. No significant decrease of the O2p/O-K ratio was observed in both graphs indicating that the sample is stable with respect to its oxygen content at these acquisition conditions in contrast to earlier experiments carried out by Browning et al. [198]. However, the amount of sample drift could not be specified and thus, sample drift cannot be excluded.

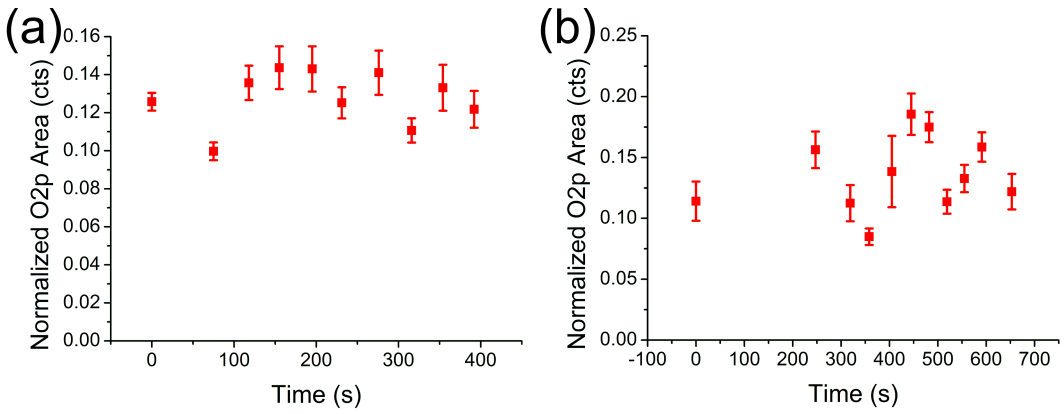

Figure 9.7.: Time series of O2p EEL spectra documenting the stability of the sample against knock-on damage. (a) Area 1 and (b) Area 2.

9.4. Summary

The layer thickness and the homogeneity of CSD coated conductors was determined on different length scales by using SEM-EDX and yielded relevant statements on the sample quality correlating with the superconducting properties. X-ray correlation diagrams showed that the measured effects are mainly due to YBCO film roughness, chemical variations in the layer would yield a decorrelation. Bright-field images revealed that the YBCO layer was heavily twinned and contained a considerable amount of secondary phases. The advanced analysis mainly focused on the determination of the oxygen stoichiometry by O2p EEL spectroscopy. A nearly optimum oxygenation of the sample was found. Another important finding was that there was no knock-on damage at 300 keV primary electron energy up to several minutes, however, the amount of sample drift was not determined.

Appendix

The Product of two infinite sums

Evaluation of the product of two infinite sums is of great relevance for electrons $\Psi(\mathbf{r})$ in a periodic potential $V(\mathbf{r})$ described by the Schrödinger equation:

$$
\begin{aligned}
V(\mathbf{r})\Psi(\mathbf{r}) &= \sum_{\mathbf{g}} U_{\mathbf{g}} \sum_{\mathbf{g}'} C_{\mathbf{g}'}\, e^{2\pi i(\mathbf{k}+\mathbf{g}+\mathbf{g}')\cdot\mathbf{r}} \\
&\overset{\mathbf{g}''=\mathbf{g}+\mathbf{g}'}{=} \sum_{\mathbf{g}''}\sum_{\mathbf{g}'} U_{\mathbf{g}''-\mathbf{g}'} C_{g'}\, e^{2\pi i(\mathbf{k}+\mathbf{g}'')\cdot\mathbf{r}} \\
&\overset{\mathbf{g}'''=\mathbf{g}''-\mathbf{g}'}{=} \sum_{\mathbf{g}'''}\sum_{\mathbf{g}''} U_{\mathbf{g}'''} C_{\mathbf{g}''-\mathbf{g}'''}\, e^{2\pi i(\mathbf{k}+\mathbf{g}'')\cdot\mathbf{r}} \\
&\overset{\substack{\mathbf{g}'''=\mathbf{g}' \\ =\\ \mathbf{g}''=\mathbf{g}}}{=} \sum_{\mathbf{g}'}\sum_{\mathbf{g}} U_{\mathbf{g}'} C_{\mathbf{g}-\mathbf{g}'}\, e^{2\pi i(\mathbf{k}+\mathbf{g})\cdot\mathbf{r}} \\
&= \sum_{\mathbf{g}} e^{2\pi i(\mathbf{k}+\mathbf{g})\cdot\mathbf{r}} \sum_{\mathbf{g}'} U_{\mathbf{g}'} C_{\mathbf{g}-\mathbf{g}'} \\
&= \sum_{\mathbf{g}} e^{2\pi i(\mathbf{k}+\mathbf{g})\cdot\mathbf{r}} \left(U_0 C_g \sum_{\mathbf{g}'\neq 0} U_{\mathbf{g}'} C_{\mathbf{g}-\mathbf{g}'} \right)
\end{aligned}
$$

DTSA-II documentation

Typical input parameters:

Property	Value	Comment
Window	Moxtek AP3.3 manufacture's table	Included in DTSA-II
Elevation angle	35°	
Azimuthal angle	130°	
Optimal working distance	10 mm	
Sample to detector distance	57.5 mm	
Detector area	10 mm^2	
Aluminum layer	20 nm	Estimated
Dead layer	0.1 µm	Estimated
Detector crystal thickness	5 mm	Estimated
Energy resolution (@ Mn-K_α)	133 eV	
# of simulated electrons	10-10000	

Property	Value	Comment
Ionization cross section	Bote et al. [89]	
Mass absorption coefficients	Chantler et al. [105]	
Angular distribution of Bremsstrahlung	Acosta et al. [199]	
Quantitative correction algorithm	PAP – Full $\varphi(\rho z)$	

Typical script of a DTSA-II simulation, here the LZO thickness series:

```
# DTSA-II/NISTMonte script - Michael Duerrschnabel
import java.util as ju
import gov.nist.microanalysis.Utility as ut
import java.lang as ma

scale=1.0e-6
for t_LZO in [0.08e-6,0.134e-6,0.263e-6,0.32506e-6]:
        # Electron primary energy in keV
        for e0 in [10,20,30]:

        # Identify a user defined detector and initialize configuration parameters
        det=findDetector("Pentafet_6500F")  # Detector of Jeol6500F University Tübingen
        det.reset()
        print "Starting: "+"%s"%e0+" kV"
        print "Starting: "+"%s"%t_LZO+" m LZO"
        nTraj=1000 # electrons
        if t_LZO==0.08e-6:
            if e0==30: dose=208 # nA*sec
            if e0==20: dose=141.2 # nA*sec
            if e0==10: dose=64 # nA*sec
        if t_LZO==0.134e-6:
            if e0==30: dose=228 # nA*sec
            if e0==20: dose=153.6 # nA*sec
            if e0==10: dose=66.4 # nA*sec
        if t_LZO==0.263e-6:
            if e0==30: dose=216 # nA*sec
            if e0==20: dose=147 # nA*sec
            if e0==10: dose=66.2 # nA*sec
        if t_LZO==0.32506e-6:
            if e0==30: dose=220 # nA*sec
            if e0==20: dose=152.2 # nA*sec
            if e0==10: dose=73.8 # nA*sec
        # imagesize & scale
        imgSize=512          # pixels
        imgScale=3.0e-6      # m
        # Define the materials
        NiW=epq.Material(epq.Composition([epq.Element.Ni,epq.Element.W],[85.8477,14.1523]),epq
            .ToSI.gPerCC(9.0))
        LZO=epq.Material(epq.Composition([epq.Element.O,epq.Element.Zr,epq.Element.La
            ],[19.571,31.8823,48.5467]),epq.ToSI.gPerCC(6.0))
        # Create a simulator and initialize it
        monte=nm.MonteCarloSS()
        monte.setBeamEnergy(epq.ToSI.keV(e0))
        # Set origin
        origin=epq.SpectrumUtils.getSamplePosition(det.getProperties())
        print "Coordinate-Origin: ["+"%s"%origin[0]+","+"%s"%origin[1]+","+"%s"%origin[2]+"]"
        # Build up the sample
        monte.addSubRegion(monte.getChamber(),NiW,nm.MultiPlaneShape.createSubstrate
            ([0.0,0.0,-1.0],origin))
        monte.addSubRegion(monte.getChamber(),LZO,nm.MultiPlaneShape.createFilm([0.0,0.0,1.0],
            origin,t_LZO))
        # Add event listeners to model characteristic radiation
        xrel=nm.XRayEventListener2(monte,det)
        monte.addActionListener(xrel)
```

```
51          # Add event listeners to model Bremsstrahlung
52          brem=nm.BremsstrahlungEventListener(monte,det)
53          monte.addActionListener(brem)
54          # Determine Electron ranges
55          rSub=epq.ElectronRange.KanayaAndOkayama1972.compute(NiW,epq.ToSI.keV(e0))/NiW.
                getDensity()
56          rObj=epq.ElectronRange.KanayaAndOkayama1972.compute(LZO,epq.ToSI.keV(e0))/LZO.
                getDensity()
57          sc=ma.Math.min(scale,rObj)+ma.Math.max((1.1-scale/rObj)*rSub,rObj/10.0)
58          print "Sc="+"%s"%sc
59          # Produce XRay Emission images
60          ei=nm.EmissionImage.watchDefaultTransitions(xrel,imgSize,2*sc,origin)
61          # Calculate Phi-Rho-Z
62          przs=nm.PhiRhoStats.watchDefaultTransitions(xrel,-0.2*sc+origin[2],sc+origin[2])
63          # Produce trajectory image
64          img=nm.TrajectoryImage(4*imgSize,4*imgSize,sc)
65          img.setXRange(-1.25*sc+origin[0],1.25*sc+origin[0])
66          img.setYRange(-0.75*sc+origin[2],1.75*sc+origin[2])
67          img.setMaxTrajectories(nTraj)
68          monte.addActionListener(img)
69          # Run the electrons
70          det.reset()
71          monte.runMultipleTrajectories(nTraj)
72          # Get the spectrum and assign properties
73          dest=DefaultOutput+PathSep+"%s"%t_LZO+"m LZO"
74          nm.EmissionImage.dumpToFiles(ei,dest+PathSep+"%s"%e0+"kv"+PathSep+"EMIMG")
75          nm.PhiRhoStats.dumpToFiles(przs,dest+PathSep+"%s"%e0+"kv"+PathSep+"PHIRHOZ")
76          img.dumpToFile(dest+PathSep+"%s"%e0+"kv"+PathSep+"Trajektor")
77          spec=det.getSpectrum(dose*1.0e-9/(nTraj*epq.PhysicalConstants.ElectronCharge))
78          # Set spectrum properties
79          props=spec.getProperties()
80          props.setNumericProperty(epq.SpectrumProperties.BeamEnergy,e0);
81          props.setNumericProperty(epq.SpectrumProperties.WorkingDistance, 1.0e3*origin[2]);
                    props.setNumericProperty(epq.SpectrumProperties.LiveTime,dose)
82          props.setNumericProperty(epq.SpectrumProperties.FaradayBegin,1.0)
83          props.setNumericProperty(epq.SpectrumProperties.BeamEnergy,e0)
84          props.setTextProperty(epq.SpectrumProperties.SpectrumDisplayName,"Simulation of LZO-
                film by Script (t_LZO=%s"%t_LZO+", e0=%s"%e0+")")
85          props.setDetector(det)
86          # Write the spectrum to disk and display
87          fos=jio.FileOutputStream(dest+PathSep+"%s"%e0+"kV_Simulation.txt")
88          noisy=epq.SpectrumUtils.addNoiseToSpectrum(spec,1.0)
89          epq.SpectrumUtils.renameSpectrum(spec,"Simulation Skript")
90          ept.WriteSpectrumAsCSV.write(noisy,fos)
91          fos.close()
92          display(noisy)
93      print "-----------------------------------"
94  print "Done!"
```

List of source code files from the EPQ library:

File #	File name	Size [kB]
1	AbsoluteIonizationCrossSection.java	12
2	AbsorptionCorrection.java	7
3	Acosta2002.csv	5
4	AlgorithmClass.java	3
5	AlgorithmUser.java	10
6	Armstrong1982Base.java	6
7	Armstrong1982Correction.java	3
8	Armstrong1982ParticleCorrection.java	36
9	Armstrong1982ParticleMC.java	4
10	AtomicShell.java	24
11	AtomicWeights.csv	1
12	AverageSpectrum.java	4
13	BackscatterCoefficient.java	5
14	BackscatterFactor.java	15

15	BaseSpectrum.java	6
16	BergerSeltzer64.csv	0
17	BergerSeltzer83.csv	1
18	BetheElectronEnergyLoss.java	7
19	Bremsstrahlung.java	21
20	BremsstrahlungAnalytic.java	32
21	BrowningEmpiricalCrossSection.java	3
22	CaveatBase.java	3
23	CharacteristicXRayGeneration.java	4
24	CITZAF.java	65
25	Composition.java	44
26	CompositionFromKRatios.java	27
27	CompositionOptimizer.java	8
28	ComputeZAF.java	7
29	CorrectionAlgorithm.java	31
30	CzyzewskiMottCrossSection.java	11
31	CzyzewskiMottScatteringAngle.java	9
32	DerivedSpectrum.java	5
33	deslattes.csv	163
34	DuaneHuntLimit.java	7
35	EdgeEnergies.csv	6
36	EdgeEnergy.java	15
37	EditableSpectrum.java	6
38	ElectronConfig.csv	6
39	ElectronRange.java	7
40	Element.java	27
41	EPMAOptimizer.java	39
42	EPQException.java	1
43	EPQFatalException.java	1
44	ExtremumSpectrum.java	9
45	FFastEdgeDB.csv	9
46	FFastMAC.csv	895
47	filelist.csv	2
48	FilteredSpectrum.java	8
49	FilterFit.java	40
50	FittingFilter.java	8
51	FlourescenceYield.csv	2
52	Fluorescence.java	19
53	FluorescenceYield.java	23
54	FluorescenceYieldMean.java	9
55	FromSI.java	4
56	Gas.java	4
57	GasMixture.java	5
58	GasScatteringCrossSection.java	6
59	Heinrich Fluorescence.csv	2
60	IonizationCrossSection.java	5
61	IonizationEnergies.csv	1
62	ISpectrumData.java	2
63	ISpectrumTransformation.java	1
64	IterationAlgorithm.java	12
65	ITransform.java	2

66	JumpRatio.java	22
67	Kissel1983.csv	9
68	KRatioOptimizer.java	8
69	KRatioSet.java	14
70	Krause1979.csv	6
71	LeseOrdner.vbs	1
72	LinearSpectrumFit.java	6
73	LineEnergies.csv	28
74	LineWeights.csv	29
75	MACCache.java	3
76	MapImage.java	10
77	MassAbsorptionCoefficient.java	92
78	Material.java	9
79	MaterialFactory.java	39
80	MeanIonizationPotential.csv	1
81	MeanIonizationPotential.java	11
82	MicrocalSpectrumFitter.java	28
83	MuCal.java	31
84	NISTMottScatteringAngle.java	8
85	NISTXRayTransitionDB.java	10
86	NISTxrtdb.csv	3
87	NoisySpectrum.java	3
88	Oz1999.csv	1
89	PandPDatabase.java	4
90	PandPdb.csv	23
91	PAP1991.java	11
92	ParticleSignature.java	8
93	PeakFit.java	13
94	PeakFitter2.java	8
95	PeakIntegral.java	4
96	PeakROISearch.java	12
97	PeakStripping.java	7
98	PhysicalConstants.java	5
99	ProportionalIonizationCrossSection.java	5
100	Proza96Base.java	16
101	Proza96Ext.java	6
102	QualEngine.java	21
103	QuantifySpectrumUsingStandards.java	45
104	RandomizedScatter.java	2
105	RandomizedScatterFactory.java	1
106	Reference.java	18
107	RegionOfInterestSet.java	28
108	relax.csv	898
109	ROISpectrum.java	11
110	SampleShape.java	19
111	ScreenedRutherfordScatteringAngle.java	3
112	SogutEtAl2002.csv	3
113	SogutEtAl2002_Corrected.csv	3
114	SpectrumFitResult.java	16
115	SpectrumFitter8.java	46
116	SpectrumMath.java	6

117	SpectrumProperties.java	75
118	SpectrumSimulator.java	13
119	SpectrumSmoothing.java	9
120	SpectrumUtils.java	90
121	StageCoordinate.java	6
122	StandardsDatabase2.java	18
123	StoppingPower.java	15
124	Strategy.java	5
125	SurfaceIonization.java	8
126	ToSI.java	5
127	TransitionEnergy.java	13
128	TransitionProbabilities.java	11
129	VectorSet.java	9
130	XPP1989Ext.java	7
131	XPP1991.java	17
132	XRayEvents.java	2
133	XRaySource.java	1
134	XRayTransition.java	46
135	XRayTransitionSet.java	38

Atomically resolved high-angle annular dark-field imaging with QSTEM

QSTEM's structure input file [200] Bi8Sb32Te60.cfg of the p-type $(Bi_{0.26}Sb_{0.74})_2Te_3$ bulk compound:

```
Number of particles = 21
A = 1.0 Angstrom (basic length-scale)
//Components of the pseudo-hexagonal lattice vectors
H0(1,1) = 4.395 A
H0(1,2) = 0 A
H0(1,3) = 0 A
H0(2,1) = -2.1975 A
H0(2,2) = 3.80618 A
H0(2,3) = 0 A
H0(3,1) = 0 A
H0(3,2) = 0 A
H0(3,3) = 30.44 A

.NO_VELOCITY. entry_count = 5
// factional coordinates of the single atomic positions inside the unit cell (column 1-3),
    Debye-Waller factor (column 4), and site occupancy (column 5)

127.6 Te // Atomic weight and chemical symbol
0 0 0 0.5 1.0
0.666667 0.333333 0.333333 0.5 1.0
0.333333 0.666667 0.666667 0.5 1.0
0 0 0.7903 0.5 1.0 0 0 0.2097 0.5 1.0
0.666667 0.333333 0.123633 0.5 1.0
0.666667 0.333333 0.543033 0.5 1.0
0.333333 0.666667 0.456967 0.5 1.0
0.333333 0.666667 0.876367 0.5 1.0

208.98 Bi // Atomic weight and chemical symbol
0 0 0.40046 0.5 0.2
0 0 0.59954 0.5 0.2
0.666667 0.333333 0.733793 0.5 0.2
0.666667 0.333333 0.932873 0.5 0.2
0.333333 0.666667 0.067127 0.5 0.2
0.333333 0.666667 0.266207 0.5 0.2

121.76 Sb // Atomic weight and chemical symbol
0 0 0.40046 0.5 0.8
```

```
0  0  0.59954  0.5  0.8
0.666667  0.333333  0.733793  0.5  0.8
0.666667  0.333333  0.932873  0.5  0.8
0.333333  0.666667  0.067127  0.5  0.8
0.333333  0.666667  0.266207  0.5  0.8
```

Screen shot of the QSTEM home screen (upper image) and of the advanced probe configuration window (lower image):

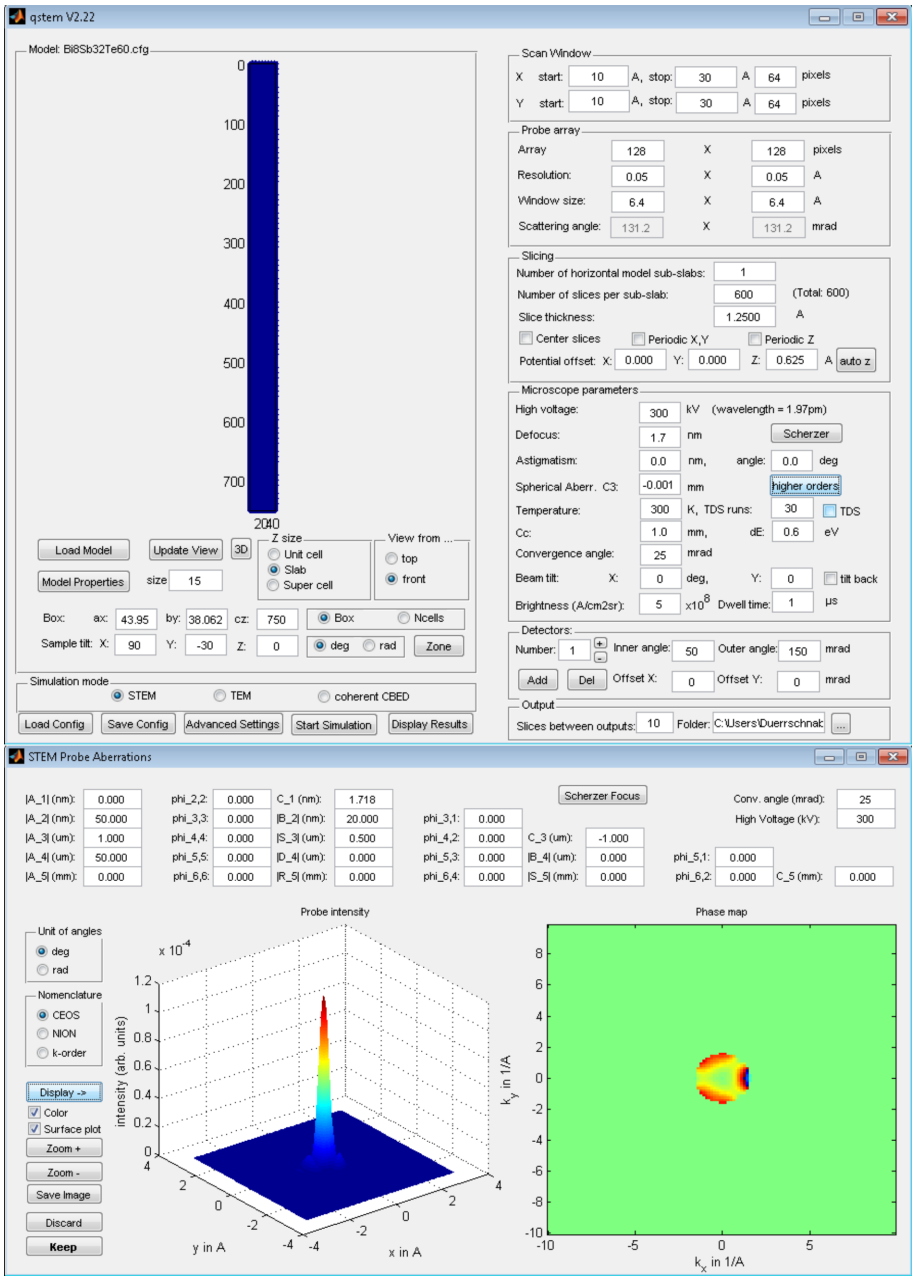

All calculations were carried out without using thermal diffuse scattering (TDS), yielding a calculation time of about 1.2 h for the Bi_2Te_3-related materials. If TDS is included in the QSTEM calculations, then no Debye-Waller factor $f_{DW} = \exp\left(-Bs^2\right)$ will be applied to the atomic potentials, but instead the atoms will be displaced by a 3D Gaussian-distributed position offset u such that $B = 8\pi^2 \langle u^2 \rangle$, where $\langle u^2 \rangle$ is the mean of the squared displacements [11]. This is also known as frozen phonon approximation. However, including TDS yields a dramatic increase of calculation time to several hours or even days, but more accurate results will be obtained with respect to the experiment.

Direct and reciprocal lattices in BoltzTraP

The structural parameters and symmetry operators of Bi_2Te_3 are given in the "Bi2Te3.struct" file, using hexagonal lattice parameters a = 8.28834 bohr and c = 57.63098 bohr. However, symmetry operators in the file "Bi2Te3.struct" as well as the k-point coordinates in the band structure file "Bi2Te3.energyso" are related to the rhombohedral lattice. BoltzTraP reads the "Bi2Te3.struct" file in the subroutine "wien_structfile" in the file "wien_band.f90". Then the subroutine "latgen2" in file "latgen2.f90" is called for calculating the coordinate matrices and the volume of the unit cell as described in [146]. In case of Bi_2Te_3 the following four matrices are generated within the subroutine "latgen2":

Matrix	Name in BoltzTraP	Interpretation
$\begin{pmatrix} a & -\frac{a}{2} & 0 \\ 0 & \frac{\sqrt{3}a}{2} & 0 \\ 0 & 0 & c \end{pmatrix}$	aac_dir	Direct lattice base vectors inside the columns in hexagonal notation with $\mathbf{a}_1 \parallel$ x-axis. All lengths are multiples of the Bohr radius ($\approx$0.53 Å).
$\begin{pmatrix} \frac{2}{3} & -\frac{1}{3} & -\frac{1}{3} \\ \frac{1}{3} & \frac{1}{3} & -\frac{2}{3} \\ \frac{1}{3} & \frac{1}{3} & \frac{1}{3} \end{pmatrix}$	p2c_dir	Converts the direct hexagonal lattice base vectors in aac_dir into trigonal ones.
$\begin{pmatrix} \frac{1}{a} & 0 & 0 \\ \frac{1}{a\sqrt{3}} & \frac{2}{a\sqrt{3}} & 0 \\ 0 & 0 & \frac{1}{c} \end{pmatrix}$	aac_rec	Reciprocal lattice base vectors inside the columns in hexagonal notation. The matrix aac_rec is the inverse of the matrix aac_dir.
$\begin{pmatrix} 1 & -1 & 0 \\ 0 & 1 & -1 \\ 1 & 1 & 1 \end{pmatrix}$	p2c_rec	Converts the reciprocal hexagonal lattice base vectors in aac_rec into trigonal ones.

The trigonal base vectors in matrix form in real space can be calculated by

$$aac\_trig\_dir = aac\_dir \cdot p2c\_dir = \begin{pmatrix} a & -\frac{a}{2} & 0 \\ 0 & \frac{\sqrt{3}a}{2} & 0 \\ 0 & 0 & c \end{pmatrix} \cdot \begin{pmatrix} \frac{2}{3} & -\frac{1}{3} & -\frac{1}{3} \\ \frac{1}{3} & \frac{1}{3} & -\frac{2}{3} \\ \frac{1}{3} & \frac{1}{3} & \frac{1}{3} \end{pmatrix} = \begin{pmatrix} \frac{a}{2} & -\frac{a}{2} & 0 \\ \frac{a}{2\sqrt{3}} & \frac{a}{2\sqrt{3}} & -\frac{a}{\sqrt{3}} \\ \frac{c}{3} & \frac{c}{3} & \frac{c}{3} \end{pmatrix}$$

$$aac\_trig\_rec = aac\_rec \cdot p2c\_rec = \begin{pmatrix} \frac{1}{a} & 0 & 0 \\ \frac{1}{a\sqrt{3}} & \frac{2}{a\sqrt{3}} & 0 \\ 0 & 0 & \frac{1}{c} \end{pmatrix} \cdot \begin{pmatrix} 1 & -1 & 0 \\ 0 & 1 & -1 \\ 1 & 1 & 1 \end{pmatrix} = \begin{pmatrix} \frac{1}{a} & -\frac{1}{a} & 0 \\ \frac{1}{a\sqrt{3}} & \frac{1}{a\sqrt{3}} & -\frac{2}{a\sqrt{3}} \\ \frac{1}{c} & \frac{1}{c} & \frac{1}{c} \end{pmatrix}$$

The reciprocal lattice vectors can be calculated using

$$\begin{aligned} V_{EZh} &= (\mathbf{a}_{1h} \times \mathbf{a}_{2h}) \cdot \mathbf{a}_{3h} = \frac{\sqrt{3}a^2c}{2} \\ \mathbf{a}^*_{1h} &= \frac{\mathbf{a}_{2h} \times \mathbf{a}_{3h}}{V_{EZh}} = \frac{2}{\sqrt{3}a^2c} \begin{pmatrix} \frac{\sqrt{3}ac}{2} \\ \frac{ac}{2} \\ 0 \end{pmatrix} \\ \mathbf{a}^*_{2h} &= \frac{\mathbf{a}_{3h} \times \mathbf{a}_{1h}}{V_{EZh}} = \frac{2}{\sqrt{3}a^2c} \begin{pmatrix} 0 \\ ac \\ 0 \end{pmatrix} \\ \mathbf{a}^*_{3h} &= \frac{\mathbf{a}_{1h} \times \mathbf{a}_{2h}}{V_{EZh}} = \frac{2}{\sqrt{3}a^2c} \begin{pmatrix} 0 \\ 0 \\ \frac{\sqrt{3}a^2}{2} \end{pmatrix} \end{aligned}$$

The matrix p2c_dir can be obtained for the BoltzTraP by using the following construction (trigonal Bi_2Te_3 unit cell (blue) used in BoltzTraP with hexagonal lattice vectors (red)):

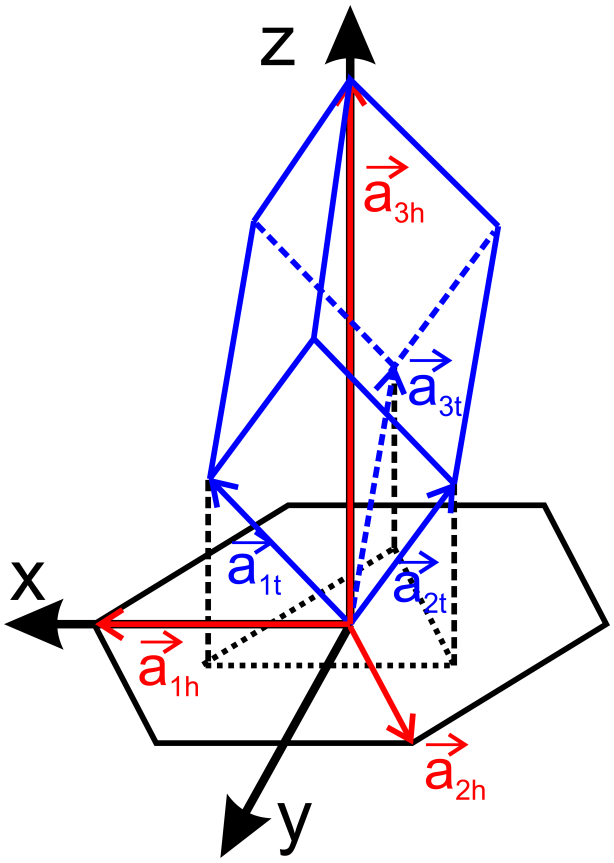

1. Write the hexagonal lattice vectors in terms of the trigonal ones:

$$\begin{aligned} \mathbf{a}_{1h} &= \mathbf{a}_{1t} - \mathbf{a}_{2t} \\ \mathbf{a}_{2h} &= \mathbf{a}_{2t} - \mathbf{a}_{3t} \\ \mathbf{a}_{3h} &= \mathbf{a}_{1t} + \mathbf{a}_{2t} + \mathbf{a}_{3t} \end{aligned}$$

2. Calculated trigonal lattice vectors in dependence of the hexagonal ones:

$$\begin{aligned} \mathbf{a}_{1t} &= \frac{1}{3}\left[2\mathbf{a}_{1h} + \mathbf{a}_{2h} + \mathbf{a}_{3h}\right] \\ \mathbf{a}_{2t} &= \frac{1}{3}\left[-\mathbf{a}_{1h} + \mathbf{a}_{2h} + \mathbf{a}_{3h}\right] \\ \mathbf{a}_{3t} &= \frac{1}{3}\left[-\mathbf{a}_{1h} - 2\mathbf{a}_{2h} + \mathbf{a}_{3h}\right] \end{aligned}$$

3. Get the coefficients from the equations in 2. and write them in form of a matrix. p2c_dir is then just obtained by transposing this very matrix:

$$p2c\_dir = \begin{pmatrix} \frac{2}{3} & \frac{1}{3} & \frac{1}{3} \\ -\frac{1}{3} & \frac{1}{3} & \frac{1}{3} \\ -\frac{1}{3} & -\frac{2}{3} & \frac{1}{3} \end{pmatrix}^T \tag{9.1}$$

The real space lattice gets generated inside the subroutine “gen_lattpoints” in the file “gen_lattpoints.f90”. For the further calculation only the trigonal integer indices are used. These real space lattice vectors are

sorted according to their length and only one vector per length is stored in the lattice field “latt_points”, the others can be obtained using the star function implemented in the subroutine “stern1” in the file “stern1.f90” and are assigned to the first one.

The numerical values for each matrix are:

$$aac\_dir_{hex} = \begin{pmatrix} 8,28833900000000 & -4,14416950000000 & 0 \\ 0 & 7,17791212917731 & 0 \\ 0 & 0 & 57,6309790000000 \end{pmatrix}$$

$$aac\_rec_{hex} = \begin{pmatrix} 0,120651435709857 & 0 & 0 \\ 0,0696581388852007 & 0,139316277770401 & 0 \\ 0 & 0 & 0,0173517788063257 \end{pmatrix}$$

$$aac\_dir_{tri} = \begin{pmatrix} 4,14416950000000 & -4,14416950000000 & 0 \\ 2,39263737639244 & 2,39263737639244 & -4,78527475278487 \\ 19,2103263333333 & 19,2103263333333 & 19,2103263333333 \end{pmatrix}$$

$$aac\_rec_{tri} = \begin{pmatrix} 0,120651435709857 & -0,120651435709857 & 0 \\ 0,0696581388852007 & 0,0696581388852007 & -0,139316277770401 \\ 0,0173517788063257 & 0,0173517788063257 & 0,0173517788063257 \end{pmatrix}$$

Symmetry operators and their interpretation for Bi_2Te_3

ID	Real space symmetry operator in trigonal base	Reciprocal space symmetry operator in trigonal base	Interpretation
1	$\begin{pmatrix} 1 & 0 & 0 \\ 0 & 1 & 0 \\ 0 & 0 & 1 \end{pmatrix}$	$\begin{pmatrix} 1 & 0 & 0 \\ 0 & 1 & 0 \\ 0 & 0 & 1 \end{pmatrix}$	Unity matrix, transfers a point into itself: [u,v,w] ⇒ [u,v,w], (h,k,l) ⇒ (h,k,l)
2	$\begin{pmatrix} -1 & 0 & 0 \\ 0 & -1 & 0 \\ 0 & 0 & -1 \end{pmatrix}$	$\begin{pmatrix} -1 & 0 & 0 \\ 0 & -1 & 0 \\ 0 & 0 & -1 \end{pmatrix}$	Inversion
3	$\begin{pmatrix} 0 & 1 & 0 \\ 1 & 0 & 0 \\ 0 & 0 & 1 \end{pmatrix}$	$\begin{pmatrix} 0 & 1 & 0 \\ 1 & 0 & 0 \\ 0 & 0 & 1 \end{pmatrix}$	Mirror matrix ($m_{[1\text{-}10]}$): [u,v,w] ⇒ [v,u,w], (h,k,l) ⇒ (k,h,l)
4	$\begin{pmatrix} 0 & -1 & 0 \\ -1 & 0 & 0 \\ 0 & 0 & -1 \end{pmatrix}$	$\begin{pmatrix} 0 & -1 & 0 \\ -1 & 0 & 0 \\ 0 & 0 & -1 \end{pmatrix}$	Rotation by 180° (2fold axis), $2_{[1\text{-}10]}$, [u,v,w] [-v,-u,-w], (h,k,l) (-k,-h,-l)
5	$\begin{pmatrix} 1 & 0 & 0 \\ 0 & 0 & 1 \\ 0 & 1 & 0 \end{pmatrix}$	$\begin{pmatrix} 1 & 0 & 0 \\ 0 & 0 & 1 \\ 0 & 1 & 0 \end{pmatrix}$	Mirror matrix ($m_{[01\text{-}1]}$): [u,v,w] ⇒ [u,w,v], (h,k,l) ⇒ (h,l,k)
6	$\begin{pmatrix} -1 & 0 & 0 \\ 0 & 0 & -1 \\ 0 & -1 & 0 \end{pmatrix}$	$\begin{pmatrix} -1 & 0 & 0 \\ 0 & 0 & -1 \\ 0 & -1 & 0 \end{pmatrix}$	Rotation by 180° (2fold axis), $2_{[01\text{-}1]}$, [u,v,w] ⇒ [-u,-w,-v], (h,k,l) ⇒ (-h,-l,-k)

7	$\begin{pmatrix} 0 & 0 & 1 \\ 0 & 1 & 0 \\ 1 & 0 & 0 \end{pmatrix}$	$\begin{pmatrix} 0 & 0 & 1 \\ 0 & 1 & 0 \\ 1 & 0 & 0 \end{pmatrix}$	Mirror matrix ($m_{[-101]}$): [u,v,w] ⇒ [w,v,u], (h,k,l) ⇒ (l,k,h)
8	$\begin{pmatrix} 0 & 0 & -1 \\ 0 & -1 & 0 \\ -1 & 0 & 0 \end{pmatrix}$	$\begin{pmatrix} 0 & 0 & -1 \\ 0 & -1 & 0 \\ -1 & 0 & 0 \end{pmatrix}$	Rotation by 180° (2fold axis), $2_{[-101]}$, [u,v,w] ⇒ [-w,-v,-u], (h,k,l) ⇒ (-l,-k,-h)
9	$\begin{pmatrix} 0 & 1 & 0 \\ 0 & 0 & 1 \\ 1 & 0 & 0 \end{pmatrix}$	$\begin{pmatrix} 0 & 0 & 1 \\ 1 & 0 & 0 \\ 0 & 1 & 0 \end{pmatrix}$	Clockwise Rotation by 120° along the trigonal [1,1,1]-Axis, (u,v,w) ⇒ (v,w,u), (h,k,l) ⇒ (l,h,k)
10	$\begin{pmatrix} 0 & -1 & 0 \\ 0 & 0 & -1 \\ -1 & 0 & 0 \end{pmatrix}$	$\begin{pmatrix} 0 & 0 & -1 \\ -1 & 0 & 0 \\ 0 & -1 & 0 \end{pmatrix}$	Clockwise Rotation by 120° along the trigonal [1,1,1]-Axis + Inversion, (u,v,w) ⇒ (-v,-w,-u), (h,k,l) ⇒ (-l,-h,-k)
11	$\begin{pmatrix} 0 & 0 & 1 \\ 1 & 0 & 0 \\ 0 & 1 & 0 \end{pmatrix}$	$\begin{pmatrix} 0 & 1 & 0 \\ 0 & 0 & 1 \\ 1 & 0 & 0 \end{pmatrix}$	Counterclockwise Rotation by 120° along the trigonal [1,1,1]-Axis, (u,v,w) ⇒ (w,u,v), (h,k,l) ⇒ (k,l,h)
12	$\begin{pmatrix} 0 & 0 & -1 \\ -1 & 0 & 0 \\ 0 & -1 & 0 \end{pmatrix}$	$\begin{pmatrix} 0 & -1 & 0 \\ 0 & 0 & -1 \\ -1 & 0 & 0 \end{pmatrix}$	Counterclockwise Rotation by 120° along the trigonal [1,1,1]-Axis + Inversion, (u,v,w) ⇒ (-w,-u,-v), (h,k,l) ⇒ (-k,-l,-h)

Bibliography

[1] Z. Aabdin, *Structural characterization and structure-property correlation on nanostructured superconducting coated conductors and thermoelectric materials*. PhD thesis, Eberhard Karls University Tuebingen, 2013.

[2] B. Fultz and J. Howe, *Transmission Electron Microscopy and Diffractometry of Materials*. Springer-Verlag, 3rd edition ed., 2007.

[3] D. Williams and C. B. Carter, *Transmission Electron Microscopy*. Springer, 1996.

[4] L. Reimer, *Transmission Electron Microscopy - Physics of Image Formation and Microanalysis*. Springer-Verlag, 1989.

[5] H. Hashimoto, A. Howie, and M. Whelan, "Anomalous Electron Absorption Effects in Metal Foils: Theory and Comparison with Experiment," *Proceedings of the Royal Society of London. Series A. Mathematical and Physical Sciences*, vol. 269, pp. 80–103, 1962.

[6] N. Peranio, *Structural, chemical, and thermoelectric properties of Bi_2Te_3 Peltier materials: bulk, thin films, and superlattices*. PhD thesis, Eberhard Karls Universität Tübingen, 2008.

[7] H. Rose, *Aberration-Corrected Electron Microscopy - Chapter 1: History of Direct Aberration Correction*, vol. 153 of *IMAGING AND ELECTRON PHYSICS*. Elsevier Ltd., 2008.

[8] M. Haider, H. Rose, S. Uhlemann, E. Schwan, B. Kabius, and K. Urban, "A spherical-aberration-corrected 200 kV transmission electron microscope," *Ultramicroscopy*, vol. 75, pp. 53–60, 1998.

[9] J. Spence, *High-resolution Electron Microscopy*. Oxford University Press, 3rd ed., 2003.

[10] D. Muller, "Structure and bonding at the atomic scale by scanning transmission electron microscopy," *Nature Materials*, vol. 8, pp. 263–270, 2009.

[11] C. Koch, *Determination of core structure periodicity and point defect density along dislocations*. PhD thesis, Arizona State University, 2002.

[12] R. Erni, *Aberration-Corrected Imaging in Transmission Electron Microscopy*. Imperial College Press, 2010.

[13] P. Nellist and S. Pennycook, "The principles and interpretation of annular dark-field Z-contrast imaging," *Advances in Imaging and Electron Physics*, vol. 113, pp. 147–203, 2000.

[14] A. Weickenmeier and H. Kohl, "Computation of absorptive form factors for high-energy electron diffraction," *Acta Crystallographica A*, vol. 47, pp. 590–597, 1991.

[15] A. Rosenauer and M. Schowalter, *Microscopy of Semiconducting Materials 2007 chapter STEMSIM - a New Software Tool for Simulation of STEM HAADF Z-Contrast Imaging*. Springer Proceedings in Physics, 2008.

[16] R. Loane, P. Xu, and J. Silcox, "Thermal vibrations in convergent-beam electron diffraction," *Acta Crystallographica A*, vol. 47, pp. 267–278, 1991.

[17] H. Bethe, "Theorie der Beugung von Elektronen an Kristallen," *Annalen der Physik*, vol. 392, pp. 55–129, 1928.

[18] P. Self, M. O'Keefe, P. Buseck, and A. Spargo, "Practical computation of amplitudes and phases in electron diffraction," *Ultramicroscopy*, vol. 11, pp. 35–52, 1983.

[19] P. Stadelmann, "EMS - A software package for electron diffraction analysis and HREM image simulation in materials science," *Ultramicroscopy*, vol. 21, pp. 131–145, 1987.

[20] K. Ishizuka and N. Uyeda, "A new theoretical and practical approach to the multislice method," *Acta Crystallographica Section A*, vol. 33, pp. 740–749, 1977.

[21] J. Cowley and A. Moodie, "The scattering of electrons by atoms and crystals. I. A new theoretical approach," *Acta Crystallographica*, vol. 10, pp. 609–619, 1957.

[22] E. Kirkland, *Advanced Computing in Electron Microscopy*. Springer, 2010.

[23] L. Molina-Luna, *Superconducting Properties and Nonstructure of $YBa_2Cu_3O_{7-\delta}$ Coated Conductors Prepared by Chemical Solution Deposition*. PhD thesis, Eberhard Karls Universität Tübingen, 2010.

[24] R. Egerton, *Electron Energy-Loss Spectroscopy in the Electron Microscope*. Springer US, 1996.

[25] R. Brydson, *Electron Energy Loss Spectroscopy*. Taylor & Francis, 2001.

[26] M. Inokuti, "Inelastic Collisions of Fast Charged Particles with Atoms and Molecules - The Bethe Theory Revisited," *Rev. Mod. Phys.*, vol. 43, pp. 297–347, 1971.

[27] H. Bethe, "Zur Theorie des Durchgangs schneller Korpuskularstrahlen durch Materie," *Ann. Phys.*, vol. 5, pp. 325–400, 1930.

[28] C. Møller, "Zur Theorie des Durchangs schneller Elektronen durch Materie," *Ann. Phys.*, vol. 14, pp. 531–585, 1932.

[29] U. Fano, "Differential inelastic scattering of relativistic charged particles," *Phys. Rev.*, vol. 102, pp. 385–387, 1956.

[30] N. Zaluzec, *K- and L-shell cross sections for x-ray microanalysis in an AEM in* Analytical Electron Microscopy. San Francisco Press, 1984.

[31] L. Reimer, *Scanning Electron Microscopy - Physics of Image Formation and Microanalysis*. Springer, 1998.

[32] W. Buckel and R. Kleiner, *Superconductivity: Fundamentals and Applications*. Wiley-VCH Verlag GmbH & Co. KGaA, 2004.

[33] H. Onnes, "The superconductivity of mercury," *Commun. Phys. Lab. Univ. Leiden*, vol. 120 and 124, 1911.

[34] A. Matthiessen, "On the electric conducting power of the metals," *Philosophical Transactions of the Royal Society of London*, vol. 148, pp. 383–387, 1858.

[35] A. Matthiessen and C. Vogt, "On the influence of temperature on the electric conductive-power of thallium and iron," *Philosophical Transactions of the Royal Society of London*, vol. 153, pp. 369–383, 1863.

[36] A. Matthiessen and C. Vogt, "On the influence of temperature on the electric conductive-power of alloys," *Philosophical Transactions of the Royal Society of London*, vol. 154, pp. 167–200, 1864.

[37] W. Meissner and R. Ochsenfeld, "Ein neuer Effekt bei Eintritt der Supraleitfähigkeit," *Die Naturwissenschaften*, vol. 21, pp. 787–788, 1933.

[38] H. London and F. London, "The Electromagnetic Equations of the Supraconductor," *Proceedings of the Royal Society of London. Series A*, vol. 149, pp. 71–88, 1935.

[39] V. Ginzburg and L. Landau, "On the theory of superconductivity," *Zhurnal Eksperimental'noi i Teoreticheskoi Fiziki*, vol. 20, p. 1064, 1950.

[40] J. Bardeen, L. Cooper, and J. Schrieffer, "Theory of Superconductivity," *Phys. Rev.*, vol. 108, pp. 1175–1204, 1957.

[41] C. Kittel, *Introduction to Solid State Physics* . Wiley John + Sons, 2004.

[42] J. Nagamatsu, N. Nakagawa, T. Muranaka, Y. Zenitani, and J. Akimitsu, "Superconductivity at 39 K in magnesium diboride," *Nature*, vol. 410, pp. 63–64, 2001.

[43] A. Sleight, J. Gillson, and P. Bierstedt, "High-temperature superconductivity in the $BaPb_{1-x}Bi_xO_3$ systems," *Solid State Communications*, vol. 17, pp. 27–28, 1975.

[44] J. Bednorz and K. Müller, "Possible high T_c superconductivity in the Ba-La-Cu-O system," *Zeitschrift für Physik B Condensed Matter*, vol. 64, pp. 189–193, 1986.

[45] M. Wu, J. Ashburn, C. Torng, P. Hor, R. Meng, L. Gao, Z. Huang, Y. Wang, and C. Chu, "Superconductivity at 93 K in a new mixed-phase Y-Ba-Cu-O compound system at ambient pressure," *Physical Review Letters*, vol. 58, pp. 908–910, 1987.

[46] D. Larbalestier, A. Gurevich, D. Feldmann, and A. Polyanskii, "High-T_c superconducting materials for electric power applications," *Nature*, vol. 414, pp. 368–377, 2001.

[47] J. Gutierrez, A. Llordes, J. Gazquez, M. Gibert, N. Roma, S. Ricart, A. Pomar, F. Sandiumenge, N. Mestres, T. Puig, and X. Obradors, "Strong isotropic flux pinning in solution-derived $YBa_2Cu_3O_{7-x}$ nanocomposite superconductor films," *Nature Materials*, vol. 6, pp. 367–373, 2007.

[48] P. J. Lee, "Engineering Critical Current Density vs. Applied Field - http://www.magnet.fsu.edu/magnettechnology/research/asc/plots.html." webpage, 04 2012.

[49] S. Maekawa and M. Sato, *Physics of High-Temperature Superconductors*. Springer-Verlag Berlin and Heidelberg GmbH & Co. KG, 1992.

[50] J. Jorgensen, B. Veal, A. Paulikas, L. Nowicki, G. Crabtree, H. Claus, and W. Kwok, "Structural properties of oxygen-deficient $YBa_2Cu_3O_{7-\delta}$," *Phys. Rev. B*, vol. 41, pp. 1863–1877, 1990.

[51] S. Tsurumi, M. Hikita, T. Iwata, K. Semba, and S. Kurihara, "High T_c Superconductivities of $A_2Ba_4Cu_6O_{14+y}$," *Jpn. J. Appl. Phys.*, vol. 26, pp. L856–L857, 1987.

[52] G. Chryssikos, E. Kamitsos, J. Kapoutsis, A. Patsis, V. Psycharis, A. Koufoudakis, C. Mitros, G. Kallias, E. Gamari-Seale, and D. Niarchos, "X-ray diffraction and infrared investigation of $RBa_2Cu_3O_7$ and $R_{0.5}Pr_{0.5}Ba_2Cu_3O_7$ compounds (R = Y and lanthanides)," *Physica C*, vol. 254, pp. 44–62, 1995.

[53] G. van Tendeloo and T. Krekels, *Characterization of High T_c Materials and Devices by Electron Microscopy*. Cambridge University Press, 2006.

[54] Z. Cai and Y. Zhu, *Microstructures & Structural Defects in High-Temperature Superconductors*. World Scientific Publishing Co Pte Ltd, 1998.

[55] M. Cyrot and D. Pavuna, *Introduction to Superconductivity and High-T_c Materials*. World Scientific Publishing Co. Pte. Ltd., 1992.

[56] B. Birajdar, *Correlation of superconducting properties and microstructure in MgB_2 using SEM, EPMA and TEM*. PhD thesis, Eberhard Karls Universität Tübingen, 2008.

[57] P. Schmitt, L. Schultz, and G. Saemann-Ischenko, "Electrical properties of $Bi_2Sr_2CaCu_2O_x$ thin films prepared in situ by pulsed laser deposition," *Physica C*, vol. 168, pp. 475–478, 1990.

[58] J. Claassen, M. Reeves, and R. S. jr., "A contactless method for measurement of the critical current density and critical temperature of superconducting films," *Rev. Sci. Instrum.*, vol. 64, pp. 996–1004, 1990.

[59] G. Grimaldi, M. Bauer, H. Kinder, W. Prusseit, U. Gambardella, and S. Pace, "Magnetic imaging of YBCO coated conductors by Hall probes," *Physica C*, vol. 372-376, pp. 1009–1011, 2002.

[60] H. Edelman and D. Larbalestier, "Resistive transitions and the origin of the n value in superconductors with a Gaussian critical-current distribution," *J. Appl. Phys.*, vol. 74, pp. 3312–3315, 1993.

[61] W. Read, *Dislocations in Crystals*. McGraw-Hill, 1953.

[62] D. Dimos, P. Chaudhari, and J. Mannhart, "Superconducting transport properties of grain boundaries in $YBa_2Cu_3O_7$ bicrystals," *Phys. Rev. B*, vol. 41, pp. 4038–4049, 1990.

[63] O. Eibl, "Superconductivity: Materials and Applications - Lecture Notes." Lecture Notes, June 2006.

[64] M. Chisholm and S. Pennycook, "Structural origin of reduced critical currents at $YBa_2Cu_3O_{7-\delta}$ grain boundaries," *Nature*, vol. 351, pp. 47–49, 1991.

[65] R. Cava, "Structural Chemistry and the Local Charge Picture of Copper Oxide Superconductors," *Science*, vol. 247, pp. 656–662, 1990.

[66] O. Eibl, "Electron Microscopy - Lecture Notes," 2006.

[67] X. D. Wu, S. R. Foltyn, P. Arendt, J. Townsend, C. Adams, I. H. Campbell, P. Tiwari, Y. Coulter, and D. E. Peterson, "High current $YBa_2Cu_3O_{7-\delta}$ thick films on flexible nickel substrates with textured buffer layers," *Appl. Phys. Lett.*, vol. 65, p. 1961, 1994.

[68] Y. Iijima, N. Tanabe, O. Kohno, and Y. Ikeno, "In-plane aligned $YBa_2Cu_3O_{7-x}$ thin films deposited on polycrystalline metallic substrates," *Applied Physics Letters*, vol. 60, pp. 769–771, 1992.

[69] K. Knoth, *Chemisch abgeschiedene LZO-Pufferschichten auf technischen Substraten zur Realisierung von YBCO-Bandleitern*. PhD thesis, Technische Universität Dresden, 2006.

[70] A. Goyal, D. Norton, J. Budai, M. Paranthaman, E. Specht, D. Kroeger, D. Christen, Q. He, B. Saffian, F. List, D. Lee, P. Martin, C. Klabunde, E. Hartfield, and V. Sikka, "High critical current density superconducting tapes by epitaxial deposition of $YBa_2Cu_3O_x$ thick films on biaxially textured metals," *Applied Physics Letters*, vol. 69, pp. 1795–1797, 1996.

[71] B. Ahn, V. Lee, R. Beyers, T. Gür, and R. Huggins, "Quaternary phase relations near $YBa_2Cu_3O_{6+x}$ in reduced oxygen pressures," *Physica C*, vol. 167, pp. 529–537, 1990.

[72] K. Knoth, S. Engel, C. Apetrii, M. Falter, B. Schlobach, R. Hühne, S. Oswald, L. Schultz, and B. Holzapfel, "Chemical solution deposition of $YBa_2Cu_3O_{7-x}$ coated conductors," *Current Opinion in Solid State and Materials Science*, vol. 10, pp. 205–216, 2006.

[73] E. Specht, A. Goyal, D. Lee, F. List, D. Kroeger, M. Paranthaman, R. Williams, and D. Christen, "Cube-textured nickel substrates for high-temperature superconductors ," *Superconductor Science and Technology*, vol. 111, pp. 945–949, 1998.

[74] J. Eickemeyer, D. Selbmann, R. Opitz, H. Wendrock, E. Maher, U. Miller, and W. Prusseit, "Highly cube textured Ni-W-RABiTS tapes for YBCO coated conductors," *Physica C: Superconductivity*, vol. 372-376, pp. 814–817, 2002.

[75] M. Falter, W. Häßler, B. Schlobach, and B. Holzapfel, "Chemical solution deposition of $YBa_2Cu_3O_{7-x}$ films by dip coating," *Physica C: Superconductivity*, vol. 372-376, pp. 46–49, 2002.

[76] H. Rogalla and P. Kes, eds., *100 Years of Superconductivity*. Taylor & Francis, 2011.

[77] M. Bauer, R. Semerad, and H. Kinder, "YBCO films on metal substrates with biaxially aligned MgO buffer layers ," *IEEE Transactions on Applied Superconductivity*, vol. 9, pp. 1502 –1505, 1999.

[78] M. Bauer, R. Metzger, R. Semerad, P. Berberich, and H. Kinder, "Inclined substrate deposition by evaporation of magnesium oxide for coated conductors," *MRS Online Proceedings Library*, vol. 35, p. 585, 1999.

[79] Y. Xu, C. Lei, B. Ma, H. Evans, H. Efstathiadis, M. Rane, M. Massey, U. Balachandran, and R. Bhattacharya, "Growth of textured MgO through e-beam evaporation and inclined substrate deposition," *Supercond. Sci. Technol.*, vol. 19, pp. 835–843, 2006.

[80] W. Prusseit, M. Bauer, V. Große, R. Semerad, and G. Sigl, "Working around HTS thickness limitations - towards 1000+ A/cm-class coated conductors," in *EUCAS 2011 Proceedings*, 2012.

[81] W. Prusseit, C. Hoffmann, R. Nemetschek, G. Sigl, J. Handke, A. Lumkemann, and H. Kinder, "Reel to Reel Coated Conductor Fabrication by Evaporation," *IEEE T. Appl. Supercon.*, vol. 16, p. 996, 2006.

[82] D. Hazelton, F. Roy, and P. Brownsey, "Recent Developments in 2G HTS Coil Technology," tech. rep., SuperPower, Inc., 2011.

[83] K. J. Leonard, A. Goyal, D. M. Kroeger, J. W. Jones, S. Kang, N. Rutter, M. Paranthaman, D. F. Lee, and B. W. Kang, "Thickness dependence of microstructure and critical current density of $YBa_2Cu_3O_{7-\delta}$ on rolling-assisted biaxially textured substrates," *Journal of Materials Research*, vol. 18, pp. 1109–1122, 2003.

[84] M. Duerrschnabel, Z. Aabdin, M. Bauer, R. Semerad, W. Prusseit, and O. Eibl, "$DyBa_2Cu_3O_{7-x}$ superconducting coated conductors with critical currents exceeding 1000 A cm^{-1}," *Superconductor Science and Technology*, vol. 25, p. 105007, 2012.

[85] N. Ritchie, "Spectrum Simulation in DTSA-II," *Microscopy and Microanalysis*, vol. 15, pp. 454–468, 2009.

[86] D. Joy, *Monte Carlo Modeling for Electron Microscopy and Microanalysis*. Oxford University Press, 1995.

[87] V. Scott and G. Love, *Quantitative Electron-probe Microanalysis*. Ellis Horwood Ltd., 1983.

[88] E. Casnati, A. Tartari, and C. Baraldi, "An empirical approach to K-shell ionisation cross section by electrons," *Journal of Physics B: Atomic and Molecular Physics*, vol. 15, pp. 155–167, 1982.

[89] D. Bote, F. Salvat, A. Jablonski, and C. Powell, "Cross sections for ionization of K, L and M shells of atoms by impact of electrons and positrons with energies up to 1 GeV: Analytical formulas," *Atomic Data and Nuclear Data Tables*, vol. 95, pp. 871–909, 2009.

[90] C. Campos, M. Vasconcellos, J. Trincavelli, and S. Segui, "Analytical expression for K- and L-shell cross sections of neutral atoms near ionization threshold by electron impact," *Journal of Physics B: Atomic, Molecular and Optical Physics*, vol. 40, pp. 3835–3841, 2007.

[91] M. Gryzinski, "Classical Theory of Atomic Collisions. I. Theory of Inelastic Collisions," *Physical Review*, vol. 138, pp. A336–A358, 1965.

[92] M. Gryzinski, "Two-Particle Collisions. II. Coulomb Collisions in the Laboratory System of Coordinates," *Physical Review*, vol. 138, pp. A322–A335, 1965.

[93] C. Jakoby, H. Genz, and A. Richter, "A semi-empirical K-shell ionization cross section by electron impact," *Le Journal de Physique Colloques*, vol. 48, pp. C9–487, 1987.

[94] M. Krause, "Atomic radiative and radiationless yields for K and L shells," *Journal of Physical and Chemical Reference Data*, vol. 8, pp. 307–327, 1979.

[95] W. Bambynek, B. Crasemann, R. Fink, H.-U. Freund, H. Mark, C. Swift, R. Price, and P. Rao, "X-Ray Fluorescence Yields, Auger, and Coster-Kronig Transition Probabilities," *Reviews of Modern Physics*, vol. 44, pp. 716–813, 1972.

[96] V. Kostroun, M. Chen, and B. Crasemann, "Atomic Radiation Transition Probabilities to the 1s State and Theoretical K-Shell Fluorescence Yields," *Physical Review A*, vol. 3, pp. 533–545, 1971.

[97] E. McGuire, "K-Shell Auger Transition Rates and Fluorescence Yields for Elements Ar-Xe," *Physical Review A*, vol. 2, pp. 273–278, 1970.

[98] D. Walters and C. Bhalla, "Nonrelativistic K-shell auger rates and matrix elements for $4 < z \leq 54$," *Atomic Data and Nuclear Data Tables*, vol. 3, pp. 301–315, 1971.

[99] J. Campbell, "Fluorescence yields and Coster-Kronig probabilities for the atomic L subshells," *Atomic Data and Nuclear Data Tables*, vol. 85, pp. 291–315, 2003.

[100] . Sögüt, E. Büyükkasap, A. Kücükönder, M. Ertugrul, O. Dogan, H. Erdogan, and . Simsek, "Fit values of M subshell fluorescence yields and Coster-Kronig transitions for elements with $20 \leq Z \leq 90$," *X-Ray Spectrometry*, vol. 31, pp. 62–70, 2002.

[101] R. Castaing and J. Descamps, "Sur les bases physiques de l'analyse ponctuelle par spectrographie X," *Journal de Physique et le Radium*, vol. 16, pp. 304–317, 1955.

[102] D. Newbury and K. Heinrich, *Electron Probe Quantitation*. Springer, Berlin, 1991.

[103] G. Bastin, J. Dijkstra, and H. Heijligers, "PROZA96: an improved matrix correction program for electron probe microanalysis, based on a double Gaussian $\phi(\rho z)$ approach," *X-ray Spectrometry*, vol. 27, pp. 3–10, 1998.

[104] G. Bastin, P. Oberndorff, J. Dijkstra, and H. Heijligers, "Extension of PROZA96 to conditions of non-perpendicular incidence of the electron beam," *X-Ray Spectrometry*, vol. 30, pp. 382–387, 2001.

[105] C. Chantler, "Detailed Tabulation of Atomic Form Factors, Photoelectric Absorption and Scattering Cross Section, and Mass Attenuation Coefficients in the Vicinity of Absorption Edges in the Soft X-Ray (Z=30-36, Z=60-89, E=0.1 keV-10 keV), Addressing Convergence Issues of Earlier Work," *Journal of Physical and Chemical Reference Data*, vol. 29, pp. 597–1056, 2000.

[106] G. Zschornack, *Handbook of X-ray data*. Springer, 2007.

[107] D. Joy and S. Luo, "An Empirical Stopping Power Relationship for Low-Energy Electrons," *Scanning*, vol. 11, pp. 176–180, 1989.

[108] E. Segre, ed., *Experimental Nuclear Physics Vol. 1*. John Wiley & Sons, 1953.

[109] F. Bloch, "Bremsvermögen von Atomen mit mehreren Elektronen," *Z. Physik*, vol. 81, pp. 363–376, 1933.

[110] R. Wilson, "Range and Ionization Measurements on High Speed Protons," *Physical Review*, vol. 11, pp. 749–753, 1941.

[111] K. F. J. Heinrich and H. Yakowitz, "Quantitative electron probe microanalysis: Uncertainty in the atomic number correction," *Mikrochimica Acta*, vol. 58, pp. 123–134, 1970.

[112] J. Ruste and M. Gantois, "A quantitative analysis of very light elements by the electron probe microanalyser," *Journal of Physics D: Applied Physics*, vol. 8, pp. 872–890, 1975.

[113] S. Seltzer and M. Berger, "Evaluation of the collision stopping power of elements and compounds for electrons and positrons," *The International Journal of Applied Radiation and Isotopes*, vol. 33, pp. 1189–1218, 1982.

[114] R. Sternheimer, M. Berger, and S. Seltzer, "Density effect for the ionization loss of charged particles in various substances," *Atomic Data and Nuclear Data Tables*, vol. 30, pp. 261–271, 1984.

[115] S. Sathyamurthy, M. Paranthaman, H. Zhai, S. Kang, T. Aytug, C. Cantoni, K. Leonard, E. Payzant, H. Christen, A. Goyal, U. S. X. Li, T. Kodenkandath, and M. Rupich, "Chemical Solution Deposition of Lanthanum Zirconate Barrier Layers Applied to Low-Cost Coated-Conductor Fabrication," *Journal of Materials Research*, vol. 19, pp. 2117–2123, 2004.

[116] W. Prusseit, R. Nemetschek, C. Hoffmann, G. Sigl, A. Lümkemann, and H. Kinder, "ISD process development for coated conductors," *Physica C: Superconductivity*, vol. 426-431, pp. 866–871, 2005.

[117] R. Nemetschek, W. Prusseit, B. Holtzapfel, J. Eickemeyer, B. deBoer, U. Miller, and E. Maher, "Continuous YBCO - Tape Coating by Thermal Evaporation," *MRS Online Proceedings Library*, vol. 689, p. E9.2, 2001.

[118] J. Doster and R. Gardner, "The complete spectral response for EDXRF systems - calculation by Monte Carlo and analysis applications. 1 - homogeneous samples," *X-Ray Spectrometry*, vol. 11, pp. 173–180, 1982.

[119] S. Pennycook and L. Boatner, "Chemically sensitive structure-imaging with a Scanning Transmission Electron Microscope," *Nature*, vol. 336, pp. 565–567, 1988.

[120] P. Batson, "Simultaneous STEM imaging and Electron Energy-loss Spectroscopy with atomic-column sensitivity," *Nature*, vol. 366, pp. 727–728, 1993.

[121] P. Batson, N. Dellby, and O. Krivanek, "Sub-angstrom resolution using aberration corrected electron optics," *Nature*, vol. 418, pp. 617–620, 2002.

[122] P. Voyles, D. Muller, J. Grazul, P. Citrin, and H. Gossmann, "Atomic-scale imaging of individual dopant atoms and clusters in highly n-type bulk Si," *Nature*, vol. 416, pp. 826–829, 2002.

[123] Z. Aabdin, N. Peranio, O. Eibl, W. Toellner, K. Nielsch, D. Bessas, R. Hermann, M. Winkler, J. Koenig, H. Boettner, V. Pacheco, J. Schmidt, A. Hashibon, and C. Elsaesser, "Nanostructure, Excitations, and Thermoelectric Properties of Bi_2Te_3-based Nanomaterials," *Journal of Electronic Materials*, vol. 41, pp. 1792–1798, 2012.

[124] D. Medlin, Q. Ramasse, C. Spataru, and N. Yang, "Structure of the (0001) basal twin boundary in Bi_2Te_3," *Journal of Applied Physics*, vol. 108, p. 043517, 2010.

[125] S. Pennycook and D. Jesson, "High-resolution Z-contrast imaging of crystals," *Ultramicroscopy*, vol. 37, pp. 14–38, 1991.

[126] S. V. Aert, J. Verbeeck, R. Erni, S. Bals, M. Luysberg, D. V. Dyck, and G. V. Tendeloo, "Quantitative atomic resolution mapping using high-angle annular dark field scanning transmission electron microscopy," *Ultramicroscopy*, vol. 109, pp. 1236 – 1244, 2009.

[127] M. Heidelmann, J. Barthel, and L. Houben, "StripeSTEM, a technique for the isochronous acquisition of high angle annular dark-field images and monolayer resolved electron energy loss spectra," *Ultramicroscopy*, vol. 109, pp. 1447–1452, 2009.

[128] D. Rowe, *CRC Handbook of Thermoelectrics*. CRC Press, 1995.

[129] N. Peranio, O. Eibl, and J. Nurnus, "Structural and thermoelectric properties of epitaxially grown Bi_2Te_3 thin films and superlattices," *J. Appl. Phys.*, vol. 100, p. 114306, 2006.

[130] N. Peranio and O.Eibl, "Quantitative EDX microanalysis of Bi_2Te_3 in the TEM," *Phys. Status Solidi A*, vol. 204, pp. 3243–3255, 2007.

[131] N. Peranio and O. Eibl, "Structural modulations in Bi_2Te_3 materials," *J. Appl. Phys.*, vol. 103, p. 024314, 2008.

[132] N. Peranio and O.Eibl, "Gliding dislocations in Bi_2Te_3 bulk materials," *Phys. Status Solidi A*, vol. 206, pp. 42–49, 2009.

[133] N. Peranio, Z. Aabdin, W. Toellner, M. Winkler, J. Koenig, O. Eibl, K. Nielsch, and H. Boettner, "Low loss EELS and EFTEM study of Bi_2Te_3 based bulk and nanomaterials," *MRS Proceedings*, vol. 1329, p. 1238, 2011.

[134] D. Eyidi, D. Maier, O. Eibl, and M. Westphal, "Chemical Composition and Crystal Lattice Defects of Bi_2Te_3 Peltier Device Structures," *Physica Status Solidi (a)*, vol. 187, pp. 585–600, 2001.

[135] W. Prusseit, C. Hoffmann, R. Nemetschek, G. Sigl, J. Handke, A. Lumkemann, and H. Kinder, "Long length coated conductor fabrication by inclined substrate deposition and evaporation," *Journal of Physics: Conference Series*, vol. 43, pp. 215–218, 2006.

[136] Z. Aabdin, M. Duerrschnabel, M. Bauer, R. Semerad, W. Prusseit, and O. Eibla, "Growth behavior of superconducting $DyBa_2Cu_3O_{7-x}$ thin films deposited by inclined substrate deposition for coated conductors," *Acta Materialia*, vol. 60, pp. 6592–6600, 2012.

[137] R. Kilaas, "Optimal and near-optimal filters in high-resolution electron microscopy," *Journal of Microscopy*, vol. 190, pp. 45–51, 1998.

[138] T. Malis, S. C. Cheng, and R. F. Egerton, "EELS log-ratio technique for specimen-thickness measurement in the TEM," *Journal of Electron Microscopy Technique*, vol. 8, no. 2, pp. 193–200, 1988.

[139] Z. Aabdin, N. Peranio, and O. Eibl, "Switching of the natural nanostructure in bi2te3 materials by ion irradiation," *Advanced Materials*, vol. 24, no. 34, pp. 4605–4608, 2012.

[140] G. S. Nolas, J. L. Cohn, G. A. Slack, and S. B. Schujman, "Semiconducting Ge clathrates: Promising candidates for thermoelectric applications," *Applied Physics Letters*, vol. 73, no. 2, pp. 178–180, 1998.

[141] K. Schwarz, P. Blaha, and G. Madsen, "Electronic structure calculations of solids using the WIEN2k package for material sciences," *Computer Physics Communications*, vol. 147, pp. 71–76, 2002.

[142] G. Madsen and D. Singh, "BoltzTraP. A code for calculating band-structure dependent quantities," *Computer Physics Communications*, vol. 175, pp. 67–71, 2006.

[143] D. Koelling and J. Wood, "On the Interpolation of Eigenvalues and Resultant Integration Scheme," *Journal of Computational Physics*, vol. 67, pp. 253–262, 1986.

[144] P. Blaha, K. Schwarz, and P. Sorantin, "Pull-Potential, Linearized Augmented Plane Wave Programs For Crystalline Systems," *Computer Physics Communications*, vol. 59, pp. 399–415, 1990.

[145] W. Pickett, H. Krakauer, and P. Allen, "Smooth Fourier Interpolation of periodic functions," *Physical Review B*, vol. 38, pp. 2721–2725, 1988.

[146] G. Giacovazzo, ed., *Fundamentals of crystallography*. Oxford University Press, third edition ed., 2011.

[147] G. Madsen, "Boltztrap - ICAMS (http://www.icams.de/content/departments/ams/madsen/ams_madsen.html)," 06 2012.

[148] N. Peranio, M. Winkler, M. Duerrschnabel, J. Koenig, and O. Eibl, "Assessing Antisite Defect and Impurity Concentrations in Bi_2Te_3 Based Thin Films by High-Accuracy Chemical Analysis," *Adv. Funct. Mater.*, vol. 23, no. 39, pp. 4969–4976, 2013.

[149] B. Huang and M. Kaviany, "Ab initio and molecular dynamics predictions for electron and phonon transport in bismuth telluride," *Phys. Rev. B*, vol. 77, p. 125209, 2008.

[150] T. Scheidemantel, C. Ambrosch-Draxl, T. Thonhauser, J. Badding, and J. Sofo, "Transport coefficients from first-principles calculations," *Physical Review B*, vol. 68, p. 125210, 2003.

[151] P. Larson, "Effect of $p_{1/2}$ corrections in the electronic structure of Bi_2Te_3 compounds," *Physical Review B*, vol. 68, p. 155121, 2003.

[152] H. Goldsmid, "The Electrical Conductivity and Thermoelectric Power of Bismuth Telluride," *Proc. Phys. Soc.*, vol. 71, p. 633, 1958.

[153] M. Winkler, X. Liu, J. König, S. Buller, U. Schürmann, L. Kienle, W. Bensch, and H. Böttner, "Electrical and structural properties of Bi_2Te_3 and Sb_2Te_3 thin films grown by the nanoalloying method with different deposition patterns and compositions," *J. Mater. Chem.*, vol. 22, pp. 11323–11334, 2012.

[154] J. Fleurial, L. Gailliard, R. Triboulet, H. Scherrer, and S. Scherrer, "Thermal properties of high quality single crystals of bismuth telluride - Part I: Experimental characterization," *J. Phys. Chem. Solids*, vol. 49, pp. 1237–1247, 1988.

[155] V. Sokolovsky, V. Meerovich, V. Beilin, and I. Vajda, "Applications of an HTS thin film switching element in the inductive current limiter," *Physica C*, vol. 386, p. 480, 2003.

[156] P. Corsaro, M. Bechis, P. Caracino, W. Castiglioni, G. Cavalleri, G. Coletta, G. Colombo, P. Ladie, A. Mansoldo, R. Mele, S. Montagner, C. Moro, M. Nassi, S. Spreafico, N. Kelley, and C. Wakefield, "Manufacturing and commissioning of 24 kV superconducting cable in Detroit," *Physica C-Superconductivity and Its Applications*, vol. 378, pp. 1168–1173, 2002.

[157] W. Prusseit, G. Sigl, R. Nemetschek, C. Hoffmann, J. Handke, A. Lumkemann, and H. Kinder, "Commercial coated conductor fabrication based on inclined substrate deposition," *IEEE T. Appl. Supercon.*, vol. 15, p. 2608, 2005.

[158] D. Smith, M. Cohen, and G. Weiss, "Oblique-Incidence Anisotropy in Evaporated Permalloy Films," *J. Appl. Phys.*, vol. 31, p. 1755, 1960.

[159] U. Balachandran, B. Ma, M. Li, B. Fisher, R. Koritala, D. Miller, and S. Dorris, "Development of coated conductors by inclined substrate deposition," *Physica C*, vol. 392-396, p. 806, 2003.

[160] K. Hasegawa, N. Hobara, Y. Nakamura, T. Izumi, and Y. Shiohara, "Preparation of MgO films on metal substrate as a buffer layer for liquid phase epitaxy processed RE123 coated conductor," *Physica C*, vol. 354, p. 424, 2001.

[161] M. Bauer, *Herstellung Und Charakterisierung Von YBCO-Schichten Und Biaxial Texturierten Pufferschichten Auf Technischen Substraten*. PhD thesis, Technische Univerisität München, 1998.

[162] D. Mitchell, "DiffTools: Electron diffraction software tools for DigitalMicrograph™," *Microsc. Res. Techniq.*, vol. 71, p. 588, 2008.

[163] A. Goyal, D. P. Norton, D. K. Christen, E. D. Specht, M. Paranthaman, D. M. Kroeger, J. D. Budai, Q. He, F. A. List, R. Feenstra, H. R. Kerchner, D. F. Lee, E. Hatfield, P. M. Martin, J. Mathis, and C. Park, "Epitaxial superconductors on rolling-assisted biaxially-textured substrates (RABiTS): A route towards high critical current density wire," *Applied Superconductivity*, vol. 4, pp. 403–427, 1996.

[164] R. Koritala, M. Chudzik, Z. Luo, D. Miller, C. Kannewurf, and U. Balachandran, "Transmission electron microscopy investigation of texture development in magnesium oxide buffer layers," *IEEE T. Appl. Supercon.*, vol. 11, pp. 3473–3476, 2001.

[165] R. E. Koritala, M. Beihai, D. J. Miller, L. Meiya, B. L. Fisher, and U. Balachandran, "exture development of MgO buffer layers grown by inclined substrate deposition," *IEEE Transactions on Applied Superconductivity*, vol. 13, pp. 2691–2694, 2003.

[166] A. van der Drift, "Evolutionary selection, a principle governing growth orientation in vapour-deposited layers," *Philips Research Reports*, vol. 22, pp. 267–288, 1967.

[167] J. M. Thijssen, "Simulations of polycrystalline growth in 2+1 dimensions," *Physical Review B*, vol. 51, pp. 1985–1988, 1995.

[168] Paritosh and D. J. Srolovitz, "Shadowing effects on the microstructure of obliquely deposited films," *Journal of Applied Physics*, vol. 91, pp. 1963–1972, 2002.

[169] C. Tang, S. Alexander, R. Bruinsma, and B. E. Shaw, "Scaling theory for the growth of amorphous films," *Physical Review Letters*, vol. 64, pp. 772–775, 1990.

[170] T. G. Holesinger, L. Civale, B. Maiorov, D. M. Feldmann, J. Y. Coulter, J. Miller, V. A. Maroni, Z. J. Chen, D. C. Larbalestier, R. Feenstra, X. P. Li, M. B. Huang, T. Kodenkandath, W. Zhang, M. W. Rupich, and A. P. Malozemoff, "Progress in nanoengineered microstructures for tunable

high-current, high-temperature superconducting wires," *Advanced Materials*, vol. 20, pp. 391–407, 2008.

[171] B. Ma, M. Li, R. E. Koritala, B. L. Fisher, A. R. Markowitz, R. A. Erck, R. Baurceanu, S. E. Dorris, D. J. Miller, and U. Balachandran, "Pulsed laser deposition of YBCO films on ISD MgO buffered metal tapes," *Superconductor Science & Technology*, vol. 16, pp. 464–472, 2003.

[172] O. Eibl and B. Roas, "Microstructure of $YBa_2Cu_3O_{7-x}$ thin films deposited by laser evaporation," *Journal of Materials Research*, vol. 5, pp. 2620–2632, 1990.

[173] L. Molina, K. Knoth, S. Engel, B. Holzapfel, and O. Eibl, "Chemically deposited $La_2Zr_2O_7$ buffer layers for YBCO-coated conductors: film growth and microstructure," *Superconductor Science & Technology*, vol. 19, pp. 1200–1208, 2006.

[174] L. Molina, T. Thersleff, C. Mickel, S. Menzel, B. Holzapfel, and O. Eibl, "TEM sample preparation of YBCO-coated conductors: conventional method and FIB," in *EMC 2008 14th European Microscopy Congress*, pp. 355–356, 2008.

[175] R. Nemetschek, W. Prusseit, B. Holzapfel, J. Eickemeyer, B. DeBoer, U. Miller, and E. Maher, "Continuous $YBa_2Cu_3O_7$-tape deposition by thermal evaporation," *Physica C-Superconductivity and Its Applications*, vol. 372, pp. 880–882, 2002.

[176] S. Furtner, R. Nemetschek, R. Semerad, G. Sigl, and W. Prusseit, "Reel-to-reel critical current measurement of coated conductors," *Superconductor Science & Technology*, vol. 17, pp. S281–S284, 2004.

[177] R. Herzog and J. E. Evetts, "Low-Temperature 2-Axis Goniometer with Accurate Temperature Control," *Review of Scientific Instruments*, vol. 65, pp. 3574–3576, 1994.

[178] W. Prusseit, G. Sigl, R. Nemetschek, C. Hoffmann, J. Handke, A. Lümkemann, and H. Kinder, "Commercial Coated Conductor Fabrication Based on Inclined Substrate Deposition," *IEEE Transactions on Applied Superconductivity*, vol. 15, pp. 2608–2610, 2005.

[179] J. Gutierrez, T. Puig, and X. Obradors, "Anisotropy and strength of vortex pinning centers in $YBa_2Cu_3O_{7-x}$ coated conductors," *Applied Physics Letters*, vol. 90, p. 162514, 2007.

[180] S. R. Foltyn, L. Civale, J. L. Macmanus-Driscoll, Q. X. Jia, B. Maiorov, H. Wang, and M. Maley, "Materials science challenges for high-temperature superconducting wire," *Nature Materials*, vol. 6, pp. 631–642, 2007.

[181] A. Malozemoff, S. Fleshler, M. Rupich, C. Thieme, X. Li, W. Zhang, A. Otto, J. Maguire, D. Folts, J. Yuan, H.-P. Kraemer, W. Schmidt, M. Wohlfart, and H.-W. Neumueller, "Progress in high temperature superconductor coated conductors and their applications," *Supercond. Sci. Technol.*, vol. 21, p. 034005, 2008.

[182] J. Mannhart, *Physics of High-Temperature Superconductors*. Springer-Verlag, 1992.

[183] V. Selvamanickam, Y. Chen, I. Kesgin, A. Guevara, T. Shi, Y. Yao, Y. Qiao, Y. Zhang, Y. Zhang, G. Majkic, G. Carota, A. Rar, Y. Xie, J. Dackow, B. Maiorov, L. Civale, V. Braccini, J. Jaroszynski, A. Xu, D. Larbalestier, and R. Bhattacharya, "Progress in Performance Improvement and New Research Areas for Cost Reduction of 2G HTS Wires," *IEEE T. Appl. Supercon.*, vol. 21, pp. 3049–3054, 2011.

[184] A. Kilic, K. Kilic, S. Senoussi, and K. Demir, "Influence of an external magnetic field on the current-voltage characteristics and transport critical current density," *Physica C*, vol. 294, pp. 203–216, 1998.

[185] D. Feldmann, T. Holesinger, B. Maiorov, H. Zhou, S. Foltyn, J. Coulter, and I. Apodoca, "1000 A cm^{-1} in a 2 μm thick $YBa_2Cu_3O_{7-x}$ film with $BaZrO_3$ and Y_2O_3 additions," *Supercond. Sci. Technol.*, vol. 23, p. 115016, 2010.

[186] J. L. MacManus-Driscoll, S. R. Foltyn, Q. X. Jia, H. Wang, A. Serquis, L. Civale, B. Maiorov, M. E. Hawley, M. P. Maley, and D. E. Peterson, "Strongly enhanced current densities in superconducting coated conductors of $YBa_2Cu_3O_{7-x}$ + $BaZrO_3$," *Nature Materials*, vol. 3, pp. 439–443, 2004.

[187] K. Leonard, S. Kang, A. Goyal, K. Yarborough, and D. Kroeger, "Microstructural characterization of thick $YBa_2Cu_3O_{7-\delta}$ films on improved rolling-assisted biaxially textured substrates," *J. Mater. Res.*, vol. 18, pp. 1723–1732, 2003.

[188] S. Foltyn, Q. X. Jia, P. Arendt, L. Kinder, Y. Fan, and J. F. Smith, "Relationship between film thickness and the critical current of $YBa_2Cu_3O_{7-\delta}$-coated conductors," *Applied Physics Letters*, vol. 75, pp. 3692–3695, 1999.

[189] T. Holesinger, S. Foltyn, P. Arendt, Q. X. Jia, P. Dowden, R. DePaula, and J. Groves, "A comparison of buffer layer architectures on continuously processed YBCO coated conductors based on the IBAD YSZ process," *IEEE T. Appl. Supercon.*, vol. 11, pp. 3359–3364, 2001.

[190] T. G. Holesinger, S. R. Foltyn, P. N. Arendt, H. Kung, Q. X. Jia, R. M. Dickerson, P. C. Dowden, R. F. DePaula, J. R. Groves, and J. Y. Coulter, "The microstructure of continuously processed $YBa_2Cu_3O_y$ coated conductors with underlying CeO_2 and ion-beam-assisted yttria-stabilized zirconia buffer layers," *Journal of Materials Research*, vol. 15, pp. 1110–1119, 2000.

[191] T. Holesinger, B. Maiorov, O. Ugurlu, L. Civale, Y. Chen, X. Xiong, Y. Xie, and V. Selvamanickam, "Microstructural and superconducting properties of high current metal-organic chemical vapor deposition $YBa_2Cu_3O_{7-\delta}$ coated conductor wires," *Supercond. Sci. Technol.*, vol. 22, p. 045025, 2009.

[192] M. Igarashi, K. Kakimoto, T. Hayashida, Y. Hanada, S. Fujita, K. Morita, N. Nakamura, S. Hanyu, Y. Sutoh, H. Kutami, Y. Iijima, and T. Saitoh, "High-speed deposition of RE123 film with large current capacity by hot-wall type PLD system," *Physica C*, vol. 470, pp. 1230–1233, 2010.

[193] H.-S. Ha, J.-H. Lee, R.-K. Ko, H.-S. Kim, H.-K. Kim, S.-H. Moon, C. Park, D.-J. Youm, and S.-S. Oh, "Thick SmBCO/IBAD-MgO Coated Conductor for High Current Carrying Power Applications," *IEEE T. Appl. Supercon.*, vol. 20, pp. 1545–1548, 2010.

[194] Z. Aabdin, M. Duerrschnabel, M. Bauer, R. Semerad, V. Große, W. Prusseit, and O. Eibl, "Growth behavior of $DyBa_2Cu_3O_{7-\delta}$ thin films deposited by inclined substrate deposition for coated conductors," *Physics Procedia*, vol. 36, pp. 1445–1449, 2012.

[195] N. Browning, J. Buban, C. Prouteau, G. Duscher, and S. Pennycook, "Investigating the atomic scale structure and chemistry of grain boundaries in high-T_c superconductors," *Micron*, vol. 30, pp. 425–436, 1999.

[196] N. Nuecker, J. Fink, J. Fuggle, P. Durham, and W. Temmerman, "Evidence for holes on oxygen sites in the high-T_c superconductors $La_{2-x}Sr_xCuO_4$ and $YBa_2Cu_3O_{7-y}$," *Phys. Rev. B*, vol. 37, pp. 5158–5163, 1988.

[197] N. Nucker, H. Romberg, X. X. Xi, J. Fink, B. Gegenheimer, and Z. X. Zhao, "Symmetry of Holes in High-T_c Superconductors," *Physical Review B*, vol. 39, pp. 6619–6629, 1989.

[198] N. Browning, J. Yuan, and L. Brown, "Determination of the local oxygen stoichiometry in $YBa_2Cu_3O_{7-\delta}$ by electron energy loss spectroscopy in the scanning transmission electron microscope," *Physica C*, vol. 202, pp. 12–18, 1992.

[199] E. Acosta, X. Llovet, and F. Salvat, "Monte Carlo simulation of bremsstrahlung emission by electrons," *Applied Physics Letters*, vol. 80, pp. 3228–3230, 2002.

[200] C. Koch, "Qstem data formats," October 2013.

List of publications

Publications during Ph.D. thesis

Peer-reviewed journal papers

[1] **M. Duerrschnabel**, Z. Aabdin, M. Bauer, R. Semerad, W. Prusseit, O. Eibl, "$DyBa_2Cu_3O_{7-x}$ superconducting coated conductors with critical currents exceeding 1000 A cm^{-1}," *Superconductor Science and Technology*, **25** (2012) pp. 105007. This article has been selected by the editors of *Superconductor Science and Technology* for inclusion in the "***Highlights of 2012***" collection. doi: 10.1088/0953-2048/25/10/105007

[2] Z. Aabdin, **M. Duerrschnabel**, M. Bauer, R. Semerad, W. Prusseit, and O. Eibl, "Growth behavior of superconducting $DyBa_2Cu_3O_{7-x}$ thin films deposited by inclined substrate deposition for coated conductors," *Acta Materialia*, **60** (2012), pp. 6592-6600. doi: 10.1016/j.actamat.2012.08.025

[3] N. Peranio, M. Winkler, **M. Duerrschnabel**, J. Koenig, and O. Eibl, Assessing antisite defect and impurity concentrations in Bi_2Te_3 based thin films by high-accuracy chemical analysis, *Advanced Functional Materials*, **23** (2013), pp. 4969-4976. doi: 10.1002/adfm.201300606

Peer-reviewed conference papers

[1] **M. Duerrschnabel**, Z. Aabdin, M. Bauer, T. Rudolf, R. Semerad, W. Prusseit, O. Eibl, "$DyBa_2Cu_3O_{7-x}$ thick films deposited on coated conductors with I_c exceeding 1000 A cm^{-1}," *Physics Procedia*, **36** (2012), pp. 1649-1654. doi: 10.1016/j.phpro.2012.06.323

[2] **M. Duerrschnabel**, Z. Aabdin, M. Bauer, V. Große, G. Sigl, O. Eibl, "Growth of biaxially-textured MgO buffer layers by inclined substrate deposition," *Physics Procedia*, **36** (2012), pp. 1546-1551. doi: 10.1016/j.phpro.2012.06.208

[3] Z. Aabdin, **M. Duerrschnabel**, M. Bauer, R. Semerad, W. Prusseit, and O. Eibl, "Growth behavior of $DyBa_2Cu_3O_{7-x}$ thin films deposited by inclined substrate deposition for coated conductors," *Physics Procedia,* **36** (2012), pp. 1445-1449. doi: 10.1016/j.phpro.2012.06.240

[4] Z. Aabdin, **M. Duerrschnabel**, M. Bauer, V. Große, R. Semerad, and O. Eibl, "Microstructure of $BaZrO_3$-doped $DyBa_2Cu_3O_{7-x}$ coated conductors deposited by inclined substrate deposition," *Physics Procedia*, **36** (2012), pp. 1655-1660. doi: 10.1016/j.phpro.2012.06.324

[5] W. Prusseit, M. Bauer, V. Große, R. Semerad, G. Sigl, **M. Duerrschnabel**, Z. Aabdin, O. Eibl, "Working around HTS thickness limitations – towards 1000+ A cm^{-1} class coated conductors," *Physics Procedia*, **36** (2012), pp. 1417-1422. doi: 10.1016/j.phpro.2012.06.146

[6] R. Hoenig, **M. Duerrschnabel**, W. van Mierlo, Z. Aabdin, J. Bernhard, J. Biskupek, O. Eibl, U. Kaiser, J. Wilde, F. Clement, D. Biro, "The Nature of Screen Printed Front Side Silver Contact - Results of the Project MikroSol", *Energy Procedia*, **43** (2013), pp. 27-36. doi: 10.1016/j.egypro.2013.11.085

Conference abstracts

[1] **M. Duerrschnabel**, Z. Aabdin, R. Hoenig, F. Clement, D. Biro, and O. Eibl, "Structure-property correlation of industrial Si solar cells with screen-printed front side contacts", *Microscopy and Microanalysis Conference*, Indianapolis, August 2013.

[2] Z. Aabdin, **M. Duerrschnabel**, O. Eibl, "High-Performance $DyBa_2Cu_3O_{7-x}$ Superconducting Coated Conductors Grown by Inclined Substrate Deposition with I_c Exceeding 1000 A cm^{-1}", *Microscopy and Microanalysis Conference*, Indianapolis, August 2013.

[3] **M. Duerrschnabel**, R. Hoenig, Z. Aabdin, J. Elia, F. Clement, O. Eibl, and D. Biro, "Microscopical and spectroscopical analysis of front side metallization interfaces in Si solar cells", *EMRS Spring Meeting*, Strasbourg, May 2012.

[4] Z. Aabdin, **M. Duerrschnabel**, and O. Eibl, "Structure-property correlation of $DyBa_2Cu_3O_{7-x}$ coated conductors with critical currents exceeding 1000 A cm^{-1}", *EMRS Spring Meeting*, Strasbourg, May 2012.

[5] **M. Duerrschnabel**, J. Elia, and O. Eibl, "Metallisierungschichten für kristalline Si Solarzellen: mikroskopische und spektroskopische Analytik", *2. Photovoltaik Symposium*, Bitterfeld-Wolfen, 2011.

[6] **M. Duerrschnabel** and O. Eibl, "Multilayer thin films: energy-dispersive X-ray spectroscopy and Monte Carlo simulations," *MC Proceedings*, M4.P569 (ISBN: 978-3-00-033910-3), Kiel, August 2011.

[7] **M. Duerrschnabel**, Z. Aabdin, and O. Eibl, "Biaxial texture and nanostructure of MgO buffer layers grown by inclined substrate deposition for superconducting coated conductors," *MC Proceedings*, M4.P570 (ISBN: 978-3-00-033910-3), Kiel, August 2011.

[8] Z. Aabdin, **M. Duerrschnabel**, and O. Eibl, "Microstructure of $DyBa_2Cu_3O_{7-x}$ coated conductors deposited by inclined substrate deposition," *MC Proceedings*, M4.P571 (ISBN: 978-3-00-033910-3), Kiel August 2011.

[9] Z. Aabdin, **M. Duerrschnabel**, T. Rudolf, W. Dreher, and O. Eibl, "TEM specimen preparation for superconducting coated conductors grown by inclined substrate deposition," *MC Proceedings*, IM7.P189 (ISBN: 978-3-00-033910-3), Kiel, August 2011.

[10] **M. Duerrschnabel**, J. Handke, W. Dreher, W. Prusseit, and O. Eibl, "ISD-grown superconducting DyBCO coated conductors investigated by TEM", *MC Proceedings*, M6.P374 (ISBN: 978-3-85125-062-6), Graz, August 2009.

[11] L. Molina-Luna, **M. Duerrschnabel**, M. Falter, M. Baecker, and O. Eibl, "Structure-property correlation of CSD processed coated conductors at different length scales", *MC Proceedings*, M6.P402 (ISBN: 978-3-85125-062-6), Graz, August 2009.

[12] **M. Duerrschnabel**, J. Handke, W. Prusseit, W. Dreher, and O. Eibl, "Superconducting and structural properties of ISD-grown DyBCO CC's", *9th European Conference on Applied Superconductivity*, P-144, Dresden, September 2009.

Miscellaneous

[1] One talk on high-Performance $DyBa_2Cu_3O_{7-x}$ superconducting coated conductors grown by Inclined Substrate Deposition with I_c Exceeding 1000 A cm^{-1} presented at the *Microscopy and Microanalysis conference* 2013 in Indianapolis, IN, USA.

Publications during diploma thesis

Peer-reviewed papers

[1] L.D. Yao, D. Weissenberger, **M. Duerrschnabel**, D. Gerthsen, I. Tischer, M. Wiedenmann, M. Feneberg, A. Reiser, and K. Thonke, Structural and cathodoluminescence properties of ZnO nanorods after Ga-implantation and annealing, *Journal of Applied Physics*, **105** (10), (2009) p. 103521. http://link.aip.org/link/doi/10.1063/1.3132865

[2] D. Weissenberger, **M. Duerrschnabel**, D. Gerthsen, F. Perez-Willard, A. Reiser, G. M. Prinz, M. Feneberg, K. Thonke, and R. Sauer, Conductivity of single ZnO nanorods after Ga implantation in a focused-ion-beam system, *Applied Physics Letters*, **91** (13), (2007) p. 132110. http://link.aip.org/link/doi/10.1063/1.2791006

[3] S.B. Thapa, J. Hertkorn, T. Wunderer, F. Lipski, F. Scholz, A. Reiser, Y. Xie, M. Feneberg, K. Thonke, R. Sauer, **M. Duerrschnabel**, L.D. Yao, D. Gerthsen, H. Hochmuth, M. Lorenz, M. Grundmann, MOVPE growth of GaN around ZnO nanopillars, *Journal of Crystal Growth*, **310** (23), (2008) pp. 5139-5142. http://dx.doi.org/10.1016/j.jcrysgro.2008.07.009

Conference contributions

[1] **Michael Dürrschnabel**, Daniel Weissenberger, Dagmar Gerthsen, Anton Reiser, Günther Prinz, Martin Feneberg, Klaus Thonke, and Rolf Sauer, Structural properties of ZnO Nanorods before and after Ga-Implantation in a Focused-Ion-Beam-System, *Verhandlungen zur DPG Frühjahrstagung*, Berlin, 2008.

[2] Daniel Weissenberger, **Michael Dürrschnabel**, Dagmar Gerthsen, Fabián Pérez-Willard, Anton Reiser, Günther Prinz, Martin Feneberg, Klaus Thonke, and Rolf Sauer, Conductivity of single ZnO Nanorods after Ga-Implantation in a Focused-Ion-Beam System, *Verhandlungen zur DPG Frühjahrstagung*, Berlin, 2008.

[3] F. Scholz, S.B. Thapa, M. Fikry, J. Hertkorn, T. Wunderer, F. Lipski, A. Reiser, Y. Xie, M. Feneberg, K. Thonke, R. Sauer, **M. Duerrschnabel**, L.D. Yao, and D. Gerthsen, Epitaxial growth of coaxial GaInN-GaN hetero-nanotubes, in SEMICONDUCTOR NANOSTRUCTURES TOWARDS ELECTRONIC AND OPTOELECTRONIC DEVICE APPLICATIONS II (SYMPOSIUM K, EMRS 2009 SPRING MEETING), ser. IOP Conference Series-Materials Science and Engineering, Notzel, R, Ed., vol. 6, EMRS. DIRAC HOUSE, TEMPLE BACK, BRISTOL BS1 6BE, ENGLAND: IOP PUBLISHING LTD, 2009, Proceedings Paper, Symposium K on Semiconductor Nanostructures Towards Electronic and Optoelectronic Device Applications II at the *EMRS Spring Meeting*, Strasbourg, Juni 2009.

[4] S.B. Thapa, J. Hertkorn, T. Wunderer, F. Lipski, F. Scholz, A. Reiser, Y. Xie, M. Feneberg, K. Thonke, R. Sauer, **M. Duerrschnabel**, L.D. Yao, D. Gerthsen, H. Hochmuth, M. Lorenz, and M. Grundmann, MOVPE growth of GaN around ZnO nanopillars, JOURNAL OF CRYSTAL GROWTH, vol. 310, no. 23, pp. 5139-5142, NOV 15 2008, *14th International Conference on Metal Organic Vapor Phase Epitaxy*, Metz, Juni 2008.

Acknowledgments

A Ph.D. thesis can never be written without the support of others. Therefore, I would like to thank

- **Prof. Dr. O. Eibl** for providing me the possibility to obtain a Ph.D. degree, for teaching me material science, superconductivity, and multiple aspects of electron microscopy. Furthermore, for his intensive guidance through the projects *Highway*, *ELSA*, *MikroSol*, and *SPP1386*. I benefited a lot from his broad knowledge in many aspects of physics and how to organize things. Last but not least, I'd like to thank him for providing me the possibility to set up a simulation environment in his group including band structure calculations, electron transport coefficients, and electron microscopic imaging and spectroscopy.
- **Prof. Dr. R. Kleiner** for his acceptance to be 2nd reviewer for my thesis and the possibility to use the Jeol 6500F SEM machine.
- **Prof. Dr. D. Kern** and **Prof. Dr. M. Oettel** for joining the thesis defense committee.
- for **financial support**:
  - The **Bundesministerium für Wirtschaft und Technologie** (BMWi), the projects HIGHWAY (FK 0327489C) and ELSA (FK 0327433A).
  - The **Baden-Wuerttemberg Stiftung**, project "MikroSol (U23)"
  - The **DFG SPP1386**
- my colleagues at the **Institute of Applied Physics** at the University of Tübingen for providing a good working atmosphere and support during my stay at the institute, especially **Dr. Z. Aabdin, Dr. N. Peranio, Dr. L. Molina-Luna, Ms. E. Lohmann, Dr. G. Bertsche, Dipl. Ing. B. Degel, Dr. A. Biesemeier, Dr. M. Künle**, **Dr. W. Engelhart**, **Dipl. Phys. M. Weiler, Mr. S. Schleehauf, Mr. S. Schlipf, Mrs. S. Kurzenberger, Mrs. P. Katz,** and **Mrs. G. Thomas.**
- the **Theva Dünnschicht GmbH** in Ismaning, especially **Dr. M. Bauer, Dr. W. Prusseit, Dr. R. Semarad, Dr. D. Sanchez**, and **Mr. V. Große**, for providing the ISD coated conductor samples, the **Zenergy Power GmbH** (now **Deutsche Nanoschicht GmbH**) in Rheinbach, especially **Dr. M. Falter** and **Dr. M. Bäcker** for providing the CSD coated conductor samples, and the **Fraunhofer Institute for Solar Energy Systems (ISE)**, especially **Dipl. Ing. R. Hönig, Dr. F. Clement**, and **Dr. D. Biro** for providing the Si solar cell samples.
- **Dr. M. Luysberg** (Ernst-Ruska center Jülich) for acquiring the atomically resolved HAADF STEM images and the StripeSTEM data on Bi_2Te_3- related materials.
- **Dr. L. Molina-Luna** for acquiring the atomically resolved HAADF STEM images of DyBCO and the O2p EEL spectra in YBCO at the EMAT Antwerp and for helping me to start my thesis at the University of Tuebingen.
- the **NMI Reutlingen** for preparing the FIB samples.
- **PD Dr. T. Wenzel** from the Mineralogy & Geodynamics department (Petrology group) for the possibility to access the Jeol Superprobe 8900 RL EPMA machine.
- **Dr. N. Peranio, Dr. Z. Aabdin, Prof. Dr. K. Dürrschnabel,** and **my mother** for proof reading the thesis.
- My **parents, family**, and **friends** for their patience and moral support.